Analysis of Textile Deformation during Preforming for Liquid Composite Moulding

by

Joram Wiggers

thesis submitted to the University of Nottingham for the

Degree of Doctor of Philosophy, July 2007

Abstract

Fibre Reinforced Plastics offer several advantages over other materials such as decreased part counts, weight savings, and flexibility. The obstacles to the further expansion of composites use, particularly in cost-conscious industries such as the car industry, include volume, cost, and quality. Liquid Composite Moulding, where the dry textile reinforcement is shaped prior to application of the plastic matrix, offers to address these drivers by offering potential for automation, speed, and quality control. However, the preforming of the dry reinforcement is rarely automated, and its results are variable and hard to predict or control.

This thesis aims to facilitate better preforming process design and control. The dominant deformation mechanism that allows reinforcements to conform to a 3D surface is trellis shear. Work is therefore presented on shear characterisation of textile reinforcements using the picture frame and the bias extension tests. Several approaches to normalising these tests to achieve method-independent shear data are proposed, and compared. Of these, a normalisation technique for the bias extension test based on energy considerations appears to be the most appropriate. A constitutive modelling approach, based on the meso-mechanical deformation mechanisms identified in the reinforcement, is developed for characterising the asymmetric shear properties exhibited by non-crimp fabrics. The results from this model are compared with experimental data. Finally, an energy minimising kinematic drape method is developed to account for the use of automated reinforcement blank-holders, and methods for modelling process variability using the code are investigated.

Acknowledgements

The author would like to thank the following organisations for their support: Engineering & Physical Sciences Research Council, Dowty Propellers, ESI Software, Ford Motor Company, Formax UK Ltd, Rolls Royce.

Thanks to Prof. Rudd, Prof. Long, and Dr. Harrison for their guidance as tutors during this research. Their experience and direction has been invaluable.

Thanks to the technical staff for their assistance in the technical work - G. Tomlinson, R. Smith and D. Smith.

The rest of the team at the University of Nottingham who made it an enjoyable place to work, including C. Wong, F. Robitaille, A. Ragondet, N. Lorenco, J. Crookston, T. Bailey, M. Sherburn, P. Schubel. The discussions and cross-fertilisation of ideas was vital.

Special thanks to Dr. P. Anstice for his support and encouragement.

Finally and most importantly thanks are due to my wife, Katherine, and my children, Esther and Grace, who have been patient and long-suffering. Their love and support make it all worthwhile.

Contents

List of Tables

List of Figures

Nomenclature

A	(m^2)	Area of sample region to be sheared. Subscript 0 denotes initial area, subscripts A B g (gauge) s (unit stitch) denote different regions, page 55
A_{BH}	(m^2)	Blank-holder contact area, page 150
a_i	(N/m)	nth order fit constant for L_3 normalised bias extension extensive force curve, page 81
b_i	(N/m)	nth order fit constant for normalised bias extension power curve, page 81
C_1		Constant depending on initial point of interest in tow crossover - also C_2, page 123
cr		crossover number, page 76
d	(m)	Cross-head displacement. Numbered subscripts or i refer to different tests, page 52
D_{BH}	(m)	Linear distance textile pulled through blank-holder, page 150
$\dot{d}$	(m/s)	Rate of cross-head displacement, page 53
E_f	(N/m^2)	Reinforcement fibre Young's modulus, page 120
E_s	(N/m^2)	Stitch Young's modulus, page 113
f		frame number, page 76
F	(N)	Cross-head force. Numbered subscripts or i refer to different tests, page 52
F_{BH}	(N)	Blank-holder force, page 150
F_s	(N)	Shear force, page 52
h_0	(m)	initial bias extension sample height, page 66
k_1	(s^{-1})	picture frame side length normalised displacement rate constant, page 54
k_2	(s^{-1})	Shear test normalised force and power proportionality constant, page 55
l		crossover marking line number, page 76

L	(m)	Picture frame side length, or equivalent for bias extension. Numbered subscripts or i refer to different tests, page 52
N		Total number of courses in lapping sequence, page 109
N	(N/m)	Line force, or force per unit length. Subscripts L, X, and Y refer to direction it is resolved in, s is shear force per unit length, page 83
P	(W)	Power to extend the cross-head in a picture frame or bias extension test. Numbered subscripts denote different tests, page 53
px		pixel number along line l of crossover cr at frame f, page 76
s_A	(m^2)	Stitch cross-section, page 113
s_Δ	(m)	Stitch extension, page 113
s_g	(m)	Stitch spacing - determined by gauge, page 106
s_L	(m)	Total unit stitch length, page 109
s_l	(m)	Initial (manufactured) stitch length, page 106
s_{node}	(m)	Node spacing in a pin jointed net (fixed), page 71
s_{oi}	(m)	Stitch length parameter: length of ith overlapping, page 106
S_s	(N)	Average stitch tension, page 113
s_t	(m)	Stitch length parameter: length of through-thickness section, page 108
s_u	(m)	Stitch length parameter: length of underlapping, page 106
t	(s)	Time, page 123
t_A	(m^2)	Tow cross-sectional area, page 108
t_t	(m)	Tow thickness, page 108
t_w	(m)	Tow width, page 108
U	(J)	Energy of deformation or forming. Subscripts refer to source: s, stitch; e, stitch friction; X, tow crossover friction;f, blank-holder friction, page 113
V_0	(m^3)	Initial volume fraction, page 120
V_0	(m^3)	Initial volume of sample to be sheared, page 55

V_a	(m^3)	Available volume fraction, page 120
V_f		Tow fibre volume fraction, page 120
w_0	(m)	initial bias extension sample width, page 66
X	(m)	X-axis position coordinate, page 123
Y	(m)	Y-axis position coordinate, page 123
α		Fibre angle relative to a global axis, $\alpha = \frac{\pi}{2} - \phi$, page 83
β		Reinforcement fibre crimp factor, page 120
$\dot{\gamma}_t$		In-plane shear strain rate in tow, page 123
ΔA_{BH}	(m^2)	Segment blank-holder contact area, page 152
ΔF_{BH}	(N)	Equivalent, per-segment, blank-holder force, page 150
ΔU_f	(J)	Segment blank-holder energy contribution, page 152
ϵ_s		Global stitch strain, page 110
θ		Shear angle. Subscripts A or B denote the shear angle in different shear regions, page 52
$\dot{\theta}$	$(°/s)$	Shear rate. Subscript A or B denote different shear regions, page 54
κ		generic bias extension sample aspect ratio factor that allows for non orthogonal fabrics, page 66
λ		bias extension sample aspect ratio, page 18
μ		Coefficient of friction. Subscript denotes source: s stitch, X tow crossover, BH blank-holder, page 118
$\vec{\nu}_{vel}$	(m/s)	Relative velocity field between the crossovers, page 123
σ	(N/m^2)	Stress values / tensor, page 82
σ_b	(N/m^2)	Tow bulk (lateral) stress, page 120
τ	(Nm)	Shear torque. Subscripts s (stitch) denote shear source, page 114

ϕ		Picture frame or blank-holder angle. Subscripts denote: 0 initial, picture frame angle; other number or i, different blank-holder or bias extension tests; *segment*, blank-holder segment angle, page 52
ω	(s^{-1})	Relative angular shear rate of two tows in crossover, page 123
ψ	(W/m^2)	Power to extend the cross-head P_i normalised by initial sample area A_0. Subscripts A or B denote different shear regions, page 55

Chapter 1

Introduction

This thesis concerns itself with the manufacture of fibre reinforced plastics (FRP). Specifically, it looks to model the effects observed around the dry fabric preforming of fibrous textiles for liquid composite moulding processes.

The thesis aims to achieve a greater understanding of this aspect of FRP manufacture. Increased process understanding can facilitate increased speed, accuracy, and decreased costs in the design, manufacture, and analysis stages of a product life cycle. Furthermore, it can aid accurate predictions of those downstream manufacturing steps that are affected by the preform fibre architecture.

1.1 Overview

A composite material consists of the combination of constituents, such that they do not dissolve or merge completely into each other. Composites typically consist of a combination of two materials where the composite gains some of the most advantageous characteristics of each constituent. Some example not covered in this thesis include chip board, which combines wood chips with a polymer to make a cheap boarding; nano-composites, in which (for example) nano-clays are dispersed into a polymer matrix to improve the tensile and flexural strength and modulus, heat distortion, water sensitivity, permeability, and so on; reinforced concrete, which combines the bulk low cost and high compressive modulus of concrete with the high tensile modulus of steel; sandwich structures, which use a low cost filler sandwiched between high tensile strength skins which bear the bulk of the load.

The FRP industry arose almost a century ago as essentially a craft industry, and large parts of it remain so even today. Parts are carefully hand manufactured by skilled workers, with nothing more technical than some shears, a bucket of resin, and a brush or roller. This is sometimes even the case for composites destined for the highest technological applications. The low tech nature of the manufacturing process allows for very easy and low cost low volume manufacture when compared to steel or other metals. It does however provide barriers for medium to higher volume applications in terms of per-part cost, time etc.

Many varieties of continuous fibre reinforced plastic composites have for some time been adopted in those areas of the engineering world where the performance and weight advantages outweigh the traditionally high cost. This includes the space exploration and aerospace industries, high performance motoring, and competition boating, cycling and motorcycling. The relatively low tooling costs in many composite manufacturing processes outweighs the higher component manufacture costs for low volumes, so that they are found in many low volume or prototyping examples. However, there has for some time been interest in the use of fibre reinforced plastics in higher volume, low cost applications such as the mainstream automotive industry. In order for them to be viable in such industries, they *must* become more predictable, reliable, and substantially cheaper to manufacture at high volumes.

The motive for this thesis is to further the understanding of the composite manufacturing process with a view to streamline the process for low cost, automated manufacturing techniques. In particular, the mechanics of dry textile draping in liquid composite moulding processes is focussed on. The final fabric layup has to be taken into account when modelling the resin infusion process. These two process steps are subsequently required to accurately predict the mechanics of the formed component, failure characteristics, etc. As the models for textile preforming become more comprehensive and complete, they allow the forming process and component performance to be more accurately predicted. This allows tighter safety factors to be adopted, less design iterations to be required, and a shorter prototyping and testing phase. All of these factors currently limit the potential for the use of composites in high volume, low cost per part processes. A reliable textile constituent model, that adequately predicts the forming characterisation of a textile from its meso-mechanical geometric description, also offers the possibility of designing fabric architecture for a specific application, broadening the possible uses of composites.

1.2 Liquid composite moulding processes and textile forming

There are many different processes used in the composites manufacturing industry. The dominant approach within the aerospace industry involves the forming of a textile that has already been pre-impregnated with a thermoset resin. This is shaped to the single sided mould, covered with an impermeable bag on which a vacuum is drawn, and placed to set in an autoclave at a raised temperature and pressure. Some approaches take a thermoplastic matrix already combined with the textiles in the form of a solid sheet or in the form of commingled constituent fibres. These are heated, formed into the desired shape, and pressed to consolidate. Another approach is to conform the dry fibrous reinforcement to the desired shape using a single mould, and then to paint on the resin with a brush or a roller. This is one of the oldest approaches, and apart from being labour intensive, presents many quality and health and safety issues. A further approach shapes the dry reinforcement to the desired shape using a single or pair of moulds, and then imposes a pressure differential to infuse the liquid thermosetting resin into the fibres in the mould. This is given a number of different names including Resin Transfer Moulding (RTM), RTM-light, and vacuum infusion (VI). Whilst the work in this thesis is relevant to any processes that preform the fabric in an unimpregnated state, the focus of enabling greater automation is more biased to RTM-like processes.

RTM, resin transfer moulding, holds the pre-formed fibrous sheet between opposing moulding tool faces, which are held in a press while resin is injected into the component at a high pressure. RTM-light requires less rigid tooling, typically the tooling itself will be made from a fibre reinforced composite. The resin is injected under pressure only slightly above ambient, the process being aided by simultaneously applying a vacuum to the resin outlet. Unlike RTM, which requires an expensive press to counteract the high force exerted by the pressurised resin over the face of the tool, RTM-light tools are commonly held together by a double vacuum seal around the edge of the tool - it becomes apparent that in order to maintain the tool closed, the force applied by the injection pressure must be less than the force applied by the sealing vacuum. For this reason RTM-light resin is usually injected at half an atmosphere relative pressure or less. Vacuum infusions only use one moulding tool face, and injection of the resin is entirely through the vacuum on the resin outlet. In place of an opposing tool, the process is sealed with a bag which is sucked by the vacuum to the shape of the component. This process is particularly suited to very large components such as boat hulls, but is less suitable for components that require two accurately positioned or cosmetic faces.

There are advantages and disadvantages to each of the above methods, not to mention variants of these methods and other methods that fall in this category. RTM, due to the high pressure that can be applied to the resin, can be faster than the other methods. The injection pressure that can be applied is however affected by the size of the press in relation to the size of the tool. Moreover, the cost of the tooling and press required for this process becomes prohibitive for lower volume applications.

VIs are more suited to low volume and particularly large applications. The tooling can be made relatively quickly and easily as it does not need to withstand high injection pressures. However, the process can be fairly slow, and a good surface finish on both faces of the component cannot be achieved.

RTM-light, also called VI-RTM, performs the compromise between the two extremes. Like vacuum infusion, the primary pressure differential is created by drawing a vacuum, and tools are also held together with a vacuum so that no press is required. Associated with this is a slower process speed. However, like RTM, two tool faces are available to control surface quality.

The difference between all these processes tends to involve the method for infusion with resin. The textile preforming process, in contrast, remains very similar. The textile is typically placed by hand onto one of the tool faces. In the cases where the textile cannot deform in-plane sufficiently to conform to the tool contours, it will bridge and / or wrinkle. Wrinkles are undesirable: They create delamination zones where failure is likely, they create resin rich and depleted zones, and they ruin the cosmetic aspects of the part. Likewise, bridging, where the fabric does not follow an indentation but cuts across it, is clearly not acceptable. One solution to avoid wrinkling commonly used in the industry involves the cutting of excess fabric from areas prone to wrinkling. This may compromise the structural capacity of the component, affect the cosmetic appearance, as well as being more labour intensive.

1.2.1 Fabric response to draping for composite manufacture

A textile does not need to deform in order to conform to a flat surface. The textile can also easily conform to a surface with single curvature, such as a half cylinder, by bending of the fibres in the textile. A geometry whose curvature cannot be described by rotation of a flat plane around a series of parallel axes is described as having double curvature. In most cases, certain regions of an initially flat textile must undergo a change in surface area in order to conform to a surface with double curvature. The location and size of these regions and the magnitude of change in surface area depends on the textile structure and the surface geometry.

Typically, a surface with very sharp radii of curvature, or one that has a deep "draw" - that is, it is very deep compared to its other dimensions - requires the greatest change in surface area. Textiles for fibre reinforced polymers typically utilise fibres with extremely high tensile moduli in order to produce a part with high strength and stiffness to weight ratio. In this case, the required change in surface area cannot be accommodated by the tensile elongation of the fibres in the textile: This is not only a very high energy deformation mechanism due to the high moduli, but typical fibres used such as glass and carbon also tend to be brittle. Another option for changing surface area is for some fibres to longitudinally compress, resulting in undesirable wrinkles. A further mechanism is fibre slip - however, this does not allow a very large change in surface area, and moreover is not observed very much in most existing reinforcement textiles [30]

The remaining deformation mechanism *other* than buckling (that is, wrinkling) is termed trellis shear. Trellis shear resembles engineering shear in many ways. However, the extreme anisotropy of the textiles undergoing shear means that there are also distinct differences. Trellis shear must always occur in reference to the fibre or tow directions in the fabric, a tow being composed of a bundle of roughly aligned fibres with which the fabric is manufactured. (Tows can also consist of twisted fibres, which hold together better, but this reduces the longitudinal stiffness advantages that are typical in FRPs.) For example, a woven textile with two distinct and uniform initial tow directions will only shear in reference to those two directions. As a result the trellis deformation of textiles, being the dominant deformation mechanism in conformance of technical textiles to component geometries with double curvature, is of primary interest in the study of dry textile preforming.

1.2.1.1 Non Crimp Fabrics

Traditionally, liquid transfer moulding has utilised Continuous Filament Mat (CFM - randomly oriented continuous fibres with a typically low fibre volume fraction), Woven textiles, and unidirectional textiles (UD) for reinforcements. CFM is often easier to drape than woven textiles or UDs. However, it is often unsuitable in high performance applications. UDs can present a draping challenge, adding to the time taken to preform the component, but allow fibres to be laid in the direction most needed. Woven fabrics are in many ways easier to drape than UDs, and present consistent fibre directions allowing them to be used in higher performance applications. However, unlike UDs, the tows in the textiles are crimped by the weave pattern. This can result in textile tensile moduli that are lower than the fibre moduli, as the tows un-crimp before placing the fibres under direct tension. Additionally, there is a weight limit to woven textiles.

Non-crimp fabrics claim to overcome some of these limitations of woven fabrics. A common example of non-crimp fabrics, knitted reinforcement textiles, is manufactured by laying tow mats in between one and four layers, and knitting the mats together using texturised polyester thread. these textiles are often much more conformable than woven equivalents in that they can shear to higher angles before locking and wrinkling. Their manufacturing method allows them to be manufactured at greater weights, which can be very helpful in manufacturing large composite components such as boat hulls and aircraft bodies. Finally, as their namesake suggests, the tows are not crimped by the manufacturing process, allowing for a greater transfer of the component load to the reinforcement fibres.

Much of this thesis concentrates on the forming behaviour of knitted non-crimp fabrics.

1.2.2 Drape modelling

The term “Drape” refers to the process of conforming a textile to a 3D geometry. Drape modelling approaches fall broadly into two categories. The first approach models the textile as a “pin-jointed net” (PJN). This net consists of inflexible, inextensible ‘rods’ attached at each end with pin joint nodes. The nodes are laid so that they coincide with the surface geometry, according to the constraint that they must remain a fixed distance from adjacent nodes. From this, it becomes apparent that given the position of nodes along two intersecting lines representative of the two tow directions, all other nodes can be calculated by geometric constraints. For very simple geometries such as a hemisphere the geometric equations can be directly solved to predict the forming pattern. For the vast majority of geometries, however, a numerical solution is required. Many solvers now exist that are able to model fabric forming using this approach.

At the other extreme of the analysis spectrum is finite element modelling (FEM). This attempts to model as many as are possible of the physical characteristics of the fabric, the mould, the ambient conditions, and the process sequence in order to attempt to replicate chronologically the entire forming process. Accurate FEM requires in-depth understanding of the modelling technique, the software tools that utilise it, and the material models that underpin it.

Each of these two extremes offers advantages and disadvantages. The former is relatively easy to use, and in many cases gives good results, which it generates very quickly. However, in many other cases it cannot model accurately. This is for a number of reasons, the most important of which is that the position of the original two intersecting lines is determined geometrically. This does not take into account the shear behaviour of the specific fabric or its interaction with the tools. Conversely, the detailed interactions of the fabric, tools, and process modelled by FEM requires detailed data on their mechanical, rheological and temperature related behaviour. It requires substantial user competence to enter the data, to interpret the results, and to gauge their accuracy. It can take many days to input this data, and also long times to run the model – although with improving material data and the increasing power of computers these times are continually decreasing.

Some models attempt to find a middle ground between these two extremes. One model, borrowed from the apparel industry, models the fabric as a series of interconnected energy nodes. The drape is optimised to minimise the energy of the nodes, that are subject to gravity, elastic interactions, and so on. A similar method more adapted to the composites industry advances the pin-jointed-net concept by introducing an energy minimisation routine [60].

The energy required to shear each of the units of the pin jointed net is calculated from the measured shear behaviour for the specific material under question (See Section 2.2.1 for methods of measuring the shear behaviour of textiles). The positions of the two lines which geometrically constrain the entire drape solution are then chosen in such a way as to minimise the total shear energy of the fabric. The difference between this approach and the PJN approach can be most easily seen in non-symmetric fabrics that preferentially shear in one direction rather than the other. In these cases, the increased accuracy of the energy minimised PJN is very apparent. Furthermore, it requires substantially less user skills than FEM, and only takes a few minutes to solve the model, as compared to the few seconds the PJN method requires, or the hours or days that the FEM takes. It does, however, require shear behaviour characteristics to be available for the specific fabric.

This model, in allowing for the textile architecture-specific response to be modelled in a relatively fast manner, provides the potential for analysis of statistical variations to be conducted, although this is not yet implemented. It also does not model the effects of the interactions between the textile and the mould or other automated tools such as a blank-holder(similarly to those found in the metal stamping industry, a composite blank-holder holds the undeformed textile while the male geometry is inserted, thus facilitating automated draping). Finally, it only provides limited support for the modelling of multi-layer preforms, in which multiple textile layers have been formed onto the geometry.

1.3 Conclusions

The aspiration in terms of lower cost, high volume RTM components is a greater degree of automation, repeatability, and quality. The design process should be streamlined, with the use of more accurate modelling tools and process understanding assisting the reduction of design iterations and prototyping. Commonly within the industry the effects of fabric architecture and part geometry on drape, resin infusion, and component performance is simplified at best and ignored at its worst. The critical process parameters should be well understood and controlled, with a variability control strategy that minimises scrap rates and predicts confidence limits.

The current composite manufacturing processes require development before they can be undertaken in this sort of environment. Technology exists that automates the spreading and cutting of textiles, their loading into the mould, and textile "blank-holders" that hold the textile in tension while the mould is closed (currently blank-holders are only implemented in thermoplastic prepreg stamping processes, however). The injection process can be automatically controlled, with sensors in place to monitor infusion progress and modelling tools that can correct the injection strategy to ensure successful resin transfer on a real time basis. Not all of these technologies are mature, and very few, if any, current manufacturing operations combine all of them for a high efficiency manufacturing line.

In terms of a more robust and efficient design cycle, the forming modelling tools available provide complementary roles in the design process. PJN tools allow very fast forming approximations for very early design iterations. Energy based PJN tools assist further on when the fabric choice and other parameters are taken into consideration. Finally, near the end of the design cycle, FEM tools can be used to validate and refine the chosen design parameters. This allows an optimal process whereby initial design cycles can be conducted very fast and with a minimal amount of resource and effort, while the final design is robustly tested and validated.

To further these goals, this thesis concentrates on the shear behaviour of bi-directional fabrics for fibre reinforced composites, and development of the energy minimised PJN modelling approach for that forming process. It attempts to quantify and understand the shear behaviour of some interesting industrially available textile reinforcements, both in terms of experimental and mathematical characterisation. It tries to further the understanding of the experiments most commonly used in measuring the shear response of textiles. The shear behaviour of reinforcement textiles is important for accurate modelling of both FEM and energy-minimised PJN forming models.

Pursuing the energy-minimised PJN forming models, this thesis attempts to extend the model to incorporate other forming phenomena so far neglected, such as fabric and forming variability, and the edge effects of automated forming blank-holders.

It is expected that as each of these aspects of preform manufacture is better understood, and tools begin to be integrated so that forming predictions inform infusion models, and both of these inform mechanical models, then the accuracy and versatility of predicted performance will improve. In this way the composites industry can move from black art to science, and thereby significantly expand its acceptance in the mainstream.

Chapter 2

Literature Review

2.1 Introduction

The context of the work presented in this thesis is in the modelling and prediction of preforming of dry textiles to aid the product and process design within the continuous fibre reinforced plastics industry. This necessarily builds on previous textile forming work, which originates from the apparel industry, looking at the deformability of textile clothing. Whilst the apparel modeling work was taken as the starting point in this field, and a significant number of aspects of the work are still in common across the fields, the work has nevertheless diverged due to the different technical, aesthetic, and economic drivers found within the two industries.

The materials of choice within the textiles industry must primarily reach a certain standard of comfort. Further criteria that vary according to the specific application include aesthetics, price, durability, colour fastness, heat retention characteristics, ease of cleaning, and more. In contrast, a primary driver for reinforcement textiles is the composite performance: Without a performance advantage, other materials will dominate. Again, other applicable criteria depend on the application, but include price, deformability, processability, recyclability, and aesthetics. The textile performance, deformability and processability (including handling and resin transfer properties) are highly dependent on its drape characteristics. Most textiles show extremely low resistance to bending. Whilst elegant folds are often an advantage in the textile industry, these significantly reduce processability and performance in the composites field. Also, seams and joins are common in apparel, to ensure good fit to shape. In contrast, they can significantly affect performance in composites. Finally, the high modulus fibres that provide the performance advantages in the composites industry result in textiles with very high tensile moduli in comparison to other preform deformation mechanisms. Tensile deformation is in contrast of much more importance in the apparel industry.

Due to this difference in motivations, composite textile modelling concentrates on shear deformations. Textile shear allows a textile to conform to complex surfaces with two degrees of curvature without wrinkling (low energy but undesirable), tensile extension (very high moduli and low ultimate strains are typical), or requiring tailoring operations. Thus, preform reinforcements and their forming operations are specifically designed to maximise shear deformation, suppress wrinkles, and minimise tailoring. In order to understand the preforming operation, textile shear must be first understood.

The work therefore, and the literature reviewed that forms the background to the work, concentrates first on the characterisation and modelling of the shear behaviour of continuous fibre reinforcements. Second, work done on modelling of textile preforming is reviewed.

2.2 Fabric shear characterisation

Before fabric shear is modelled or measured, its nature must be understood. The word shear should be used with care, as textile shear, whilst sharing some important characteristics with engineering shear, is a complex phenomenon involving many different deformation mechanisms.

Homogeneous engineering shear is defined as a force applied tangentially to the surface on which it is acting, so that the shear stress (τ) is defined as the tangential force divided by the surface area over which the force acts. The material deformation response to shear stress is the shear strain (ε_{xy}), such that for small angles shear strain is approximately equal to the shear angle in radians, θ.

Textile shear also refers to the action of a force parallel to the surface on which it acts. Textiles, however, are heterogeneous materials so that the shear force of interest must act parallel to one of the fibre directions. Shear deformation in biaxial fabrics can often extend to 50 or more degrees, causing the reference axes (parallel to fibres) to be no longer even approximately perpendicular. As the reference axes must rotate with the fibres, textile shear, sometimes referred to as trellis shear, must not therefore be confused with engineering shear.

2.2.1 Experimental characterisation

Shear response data allow textile preforming simulations to predict the effects of textile structure on the draped pattern. This is vital in the prediction and control of the resin injection process, and the modelling and design of the composite mechanical properties. It would be beneficial to be able to predict textile shear response based on its structure, and previous work as well as work in this thesis makes progress toward this goal. For these reasons, shear response measurements are important to textile preforming science. They allow forming models to be developed *in parallel* to shear models, and they provide essential validation for shear models.

Much work has been carried out to measure the shear characteristics of fabrics, first in the textiles industry, and latterly in many other contexts including the manufacture of fibre reinforced polymer composites. The many variations of shear experiments can be classified into three broad types, illustrated in Figure 2.1:

1. Direct shear force
2. Bias extension
3. Picture frame

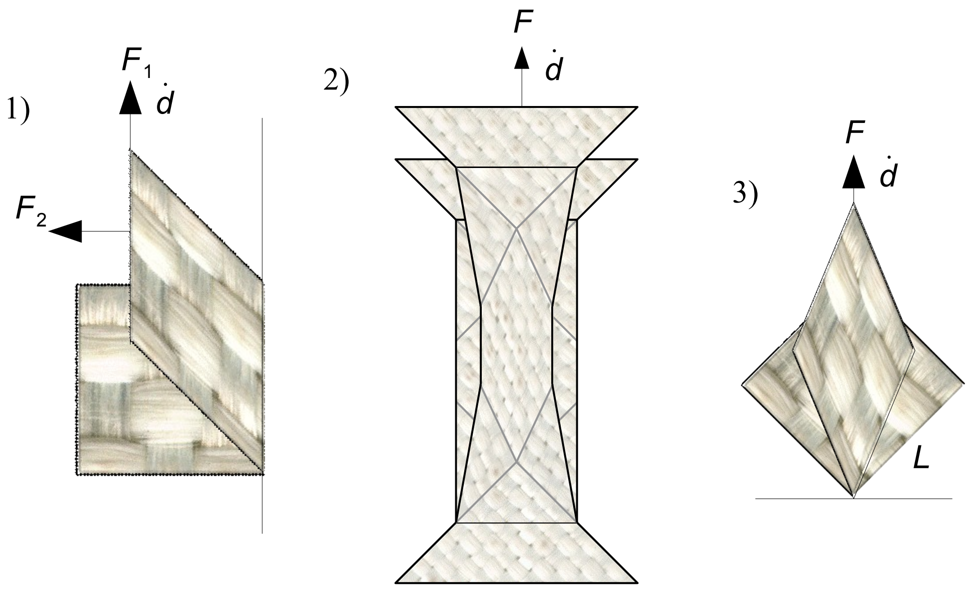

Figure 2.1: Three methods for measuring the shear properties of a textile.

All three test methods are summarised in the following sections, and more detailed descriptions of the latter two can be found in Section 3.3.1 and Section 3.4.1 respectively.

2.2.1.1 Direct shear measurement

As has been discussed, direct shear force experiments originate from the textile industry [61]. Opposite sides of a rectangular specimen are clamped parallel to one of the fibre directions. Displacement of one of the clamped edges is in the direction of the fibres, so that a direct shear force is exerted. A force is applied normal to the fibre direction in order to keep the fabric taut. This ensures that shear rather than wrinkling is measured.

This was adapted for engineering fabrics by the likes of Kawabata [27], who used a biaxial testing machine to measure the direct shear response. Force was applied in one direction to keep the specimen taut, while a centre clamp applied the shear stress in the other direction. Later variations [24] on this method included more than one specimen pulled by the central clamp so that out of plane reactions would cancel. This also allows, with careful placement of the specimens, measurement of shear strain in only one direction, an important factor in textiles that exhibit different shear characteristics according to the shear direction. Kawabata's work led to the Kawabata Evaluation System for Fabrics (KES-F), now available commercially for fabric characterisation, and is used for the characterisation of technical textiles including reinforcements [38].

The KES-F system presents difficulties as a shear measurement system for reinforcements. It is very expensive and hard to obtain and is limited to the low shear strains and loads characteristic to the textiles industry. Furthermore, Hu and Zhang [23] suggested that the specimen in the KES-F was not subjected to pure shear. Their finite element simulation of the shear test suggested a shear distribution from zero at the corners to a maximum at the centre of the specimen.

2.2.1.2 Bias extension

In the bias extension test the sample is cut and extended along an axis half-way between the fibre directions, illustrated in Figure 2.1b (see Figure 3.16 for a biaxial test setup).

The uniaxial bias extension method has been used for some time [62, 53] and is popular as it requires little more than standard tensile testing apparatus. The test requires grips wide enough to hold the top and bottom of most textile samples, however, these are of very simple design for dry textiles. Also, it is relatively repeatable compared to the other tests. Wang et al. [68] demonstrated that, as only the central part of the sample undergoes pure shear, sample dimensions are important, and suggested that sample aspect ratios λ such that the sample height is greater than twice its width were desirable so that the uniform deformation area dominates the sample response:

$$\lambda > 2 \tag{2.1}$$

Ideal deformation within the test allows the central shear area shear angle to be related to the extension (Equation 3.19), however the boundary conditions of the test mean that as the shear angle approaches the locking angle (that is, the maximum shear angle that the textile will allow, often the angle at which the fabric begins to wrinkle), the sample begins to deform by slip rather than shear. As a consequence it is best to measure the shear angle from direct observation of the central shear area.

Despite its popularity, the complex shear distribution over the sample, the lack of control of boundary conditions and the slip deformation mechanisms reduce the quantitative usefulness of the test.

The biaxial bias extension test [57] uses a cruciform sample cut in the bias direction. Ideally such a test would match the X-axis extension to the Y-axis extension according to the ideal shear deformation of the sample, or instead set one axis to exert a constant force. Such a setup would minimise tow slip and allow tow tension to be induced during shear. However, in the example of Sharma et al. [57] both axes are extended at a constant rate and the subsequent slip induced in the cruciform tabs is ignored by solely considering the stress fields in the central shear area.

2.2.1.3 Picture frame

In this method the sample is cut in a cruciform with axes aligned with tow directions. It is then clamped into a square frame with corner hinges whose centre of rotation is aligned with the clamping edges. Two opposite corners of the picture frame are extended, so that so long as the sample is properly aligned [5], pure shear is induced. Except for the fibre bending induced at the clamp edges, this test induces pure shear throughout the sample.

Tension in the tows prior to shearing can be induced with the use of a pre-tensioning device [7, 60]. As well as allowing the fabric shear behaviour under tension to be examined, this has been found to improve repeatability of results, as it helps alignment of the sample within the frame. The test is extremely sensitive to fabric misalignment. Misalignment causes either premature buckling or increasing tensile loading of the tows, which due to their inextensibility subsequently dominate results. The effects of tension on the fabric shear behaviour is of importance, for example in forming utilising a blank-holder to hold the preform. Some research has indicated that tension can alter the shear behaviour of the textiles [60, 69, 32], such as increased low angle shear resistance and increased locking angle. This might allow a challenging part to be draped without wrinkles. Most tests did not however measure the change in tension during shear, thus limiting the validity of the data. Launay et al. [32] demonstrated that this varies significantly during shear, so that a single shear test with a given pre-tension measures the shear response at different pre-tension for different shear angles.

Another proposed solution to the generally low repeatability found in this test is termed mechanical conditioning [10]. This proposes that the sample be sheared and unsheared several times before test results are taken. Any misaligned tows in the sample are pulled straight in the first few tests so that the recorded test concerns a more predictably aligned sample. The results are indeed more repeatable, however, in conditioning the sample the fabric no longer resembles that which comes off the roll, and so its shear behaviour may no longer be representative of the material which is actually formed. For example, after conditioning many fabrics exhibit thinner tows with larger gaps, indicating some permanent compaction of the tows. Such deformations are therefore no longer present in the recorded data, to the detriment of its applicability.

2.2.1.4 Benchmarking

In an attempt to understand the differences between the different tests conducted by different researchers, a web based forum (`http://nwbenchmark.gtwebsolutions.com/`) was established to standardise and benchmark the international efforts to characterise materials and simulate the forming processes. The aim of the material characterisation forum was to attempt to compare different shear tests to establish normalisation strategies and better understand the factors that affect the results.

The work is presented by Gorczyca-Cole et al. [15] and compares the different techniques used to conduct the picture frame test. The benchmark chose three textiles donated by Saint-Gobain to be tested - two of these, numbered 1 and 3 in the benchmarking exercise, are the same fabrics tested, whose shear results are presented in Section 3.3.3 and Section 3.4.5. These were all dry, commingled fibreglass-polypropylene woven-composite materials. In order to compare the results from different picture frame sizes and setups, it was necessary to present the results in such a way that they were independent of sample size.

Early work on the relationship between shear force and sample size suggested that shear force should be normalised by sample area [59]. This was later modified by Harrison et al. [18], who suggested that shear *energy* should be normalised by sample area, and showed that if this was the case then the shear force should be normalised by the sample side length. Peng et al. [50] developed this work to account for samples whose central shear area is substantially less than the picture frame side length, where their normalisation formula simplified to Harrison et al.'s in the case where the central shear region side length is equal to the picture frame side length. Peng et al.'s work is relevant for picture frame tests where the unclamped tows in the tabs are removed: However, where only the tow at the edge of the central shear region is removed, or where no tows are removed, the tabs between the central shear region and the picture frame clamps also shear, albeit under different boundary conditions. In these cases the shear contribution of the tabs should be allowed for, and the normalisation length should be equal to the square root of the area of fabric inside the picture frame clamps.

Gorczyca-Cole et al. [15] compared the results from different tests around the world normalised both by fabric area and according to Peng et al.'s technique. Whilst agreement improved after normalisation, there was still a wide amount of scatter between different tests. The normalisations did not account for the differences between those tests that removed tows from the tabs and those that did not. Furthermore, the differences in boundary conditions were not taken into account. Some of the tests were placed into the frames under tension, whilst some were not. One test rig had the facility to measure and vary the tension during shear. Clamping arrangements varied, as did actuation. Some experiments mechanically conditioned the material before the test by shearing and un-shearing it a few times. Whilst this substantially improves repeatability, the material that is tested can be visually seen to be different to the virgin material. This shows that the picture frame test is very sensitive to differences in the testing conditions. This is further borne out in the difficulties in achieving repeatable results in the same picture frame by the same researcher. Nevertheless, it is important that techniques for normalisation of results continue to be developed in order to facilitate the comparison of different tests. This allows the effects of other factors on the test results to be explored and understood.

2.2.1.5 Discussion on experimental data

Typically, shear measurements find a number of factors that affect the shear resistance of dry textiles:

- Weave pattern strongly affects shear compliance [60]. Patterns that induce large amounts of tow crimp, such as plain weave, show less shear compliance, whereas patterns with very little crimp, such as some satin weaves, show much greater shear compliance.

- Due to their uncrimped nature, biaxial non-crimp fabrics exhibit very low shear resistance. The presence of the stitching can cause them to preferentially shear in one direction.
- Greater fibre density increases shear resistance.
- Greater shear resistance usually translates to a smaller locking angle.

2.2.2 Modelling approaches

The shear deformation of textiles is key to understanding their forming behaviour. As in the modelling approaches to forming, the meso-mechanical shear deformation of textiles falls into two categories: idealised empirical modelling; and Finite Element modelling. Finite Element approaches provide an important facet to the understanding of textile shear, but even these need an understanding of the underlying mechanisms involved to model the textile behaviour correctly. The FE approach to shear modelling is still in its early stages and suffers from deficiencies such as difficulties in modelling large deformations and appropriate tow compressive stiffness [58, 3]. As a result, the material behaviour is approached from an idealised, constitutive modelling approach herein.

2.2.2.1 Meso-mechanical deformation modelling

In order to model the shear behaviour of a textile, the meso-mechanical processes that facilitate and resist the shearing must be defined and understood. It is the interaction of all of these separate phenomena that results in the behaviour actually observed. Typically, empirical shear models have concentrated on the shear behaviour of plain-weave fabrics. The primary deformation mechanism concentrated on has been the frictional resistance experienced at tow cross-overs. Other factors modelled have included the effects of tow tension, crimp, bending, compaction, and torsion. However, these secondary effects have often been modelled to evaluate their effects on the frictional forces experienced at the tow cross-overs. When considering Non Crimp multiaxial Fabrics (NCFs), this will be shown to be an inappropriate approach, so that an energy based approach, in which the energy contributions from each of these effects are added irrespective of their significance.

Plain-weave tensile modelling

An important contribution to the understanding of textile deformation comes from Kawabata [25, 26, 27], who presented his work in three parts, the first two of which modelled biaxial and uniaxial deformation along the fibre direction. His models introduced the saw-tooth approximation for plain weave tow paths, illustrated in Figure 2.2. The first paper [25] introduced the interrelation between the tow contact forces F_c at crossover and the tow tensile forces in the plane of the textile F_i where both tow directions were subjected to tensile stresses. For the saw-toothed geometry to maintain equilibrium, the contact force was given as

$$F_c = 2F_i \cos\phi_i \qquad (2.2)$$

where i referred to the warp and weft tows, and ϕ_i is the angle of crimp of the tows in the saw-toothed model. Two resultant expressions were created from Equation 2.2, for each of the two tows, and the equilibrium solution was determined graphically so

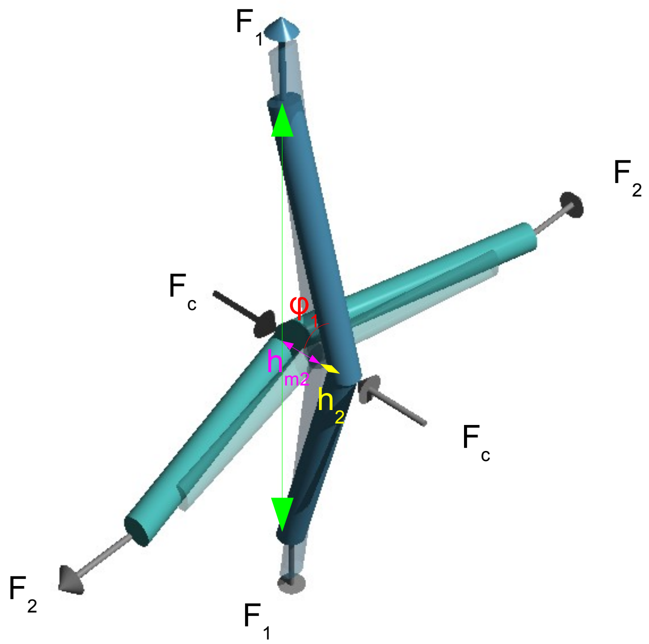

Figure 2.2: The saw tooth model for a plain-weave crossover under biaxial loading. The tows are illustrated in the unstressed (solid) and stressed (transparent) states.

that these two were equal. The tension in the direction of the tows was subsequently calculated as

$$F_i = \frac{F_c \epsilon_i y_{0i}}{4(h_{mi} - h_i)} \tag{2.3}$$

where ϵ_i is the strain in the i direction, and h_{mi} and h_i represent the crimp amplitudes for the i-direction tow before and after deformation, as illustrated in Figure 2.2.

Validation of this model was made using a biaxial tensile testing machine. Given good experimental tensile and compaction data for the yarns, the model corresponded closely with the biaxial measurements, particularly for higher stresses.

The second paper [26] allowed for the uniaxial stress scenario, where in order to model the reaction of the tows in the unstressed direction a first order approximation based on the bending and shear forces within the tow was created. The contact force was determined as the sum of tow bending and shear forces,

$$F_c = F_{cs} + F_{cb} \tag{2.4}$$

where F_{cs} is the tow shear force

$$F_{cs} = \frac{2\mu_f d_f}{l_{02}} \left(h_2 \frac{dF_c}{dh_2} + F_c \right) \tag{2.5}$$

and F_{cb} is the tow bending force

$$F_{cb} = 2n_f \frac{192 E_f I_f}{8 l_{02}^3} h_2 \tag{2.6}$$

Again, this work provided accurate results when compared to experimental tests for higher stresses. It seems likely that in both the biaxial and the uniaxial models the discrepancies at low stresses were a result of the lack of modelling for the lateral compaction of the tow(s) under tension. Another possible effect not modelled is the bending of the tow under tension.

Plain-weave shear modelling

Whilst the fabric behaviour under tensile loads is of limited interest due to the tendency to deform by shear, it is important that such behaviour is understood in order to understand some of the meso-mechanical shear mechanisms. The third paper by Kawabata [27] attempted to model the shear behaviour of the plain-weave fabric by allowing the tows in the bi-axial saw-tooth model to rotate relative to each other. The torque needed to rotate a crossover was approximated as

$$T = T_0 + C_1 F_c + C_2 \theta + C_4 F_c \theta \tag{2.7}$$

where C_1, C_2, and C_4 were derived from shear measurement apparatus. Not surprisingly, the results using Equation 2.7 showed good correlation with the model. Kawabata did however propose a mechanical model for the torque required to shear the fabric:

$$T = \frac{2}{3} \mu_{cr} \frac{D_{eff}}{2} F_c \tag{2.8}$$

where μ_{cr}, the crossover frictional coefficient, was taken to be 0.3, D_{eff} was the effective diameter of a circular crossover area with diameter equal to the width of the tow, and F_c was calculated using Equation 2.2. This value was noted to be similar to the C_1 values measured for Equation 2.7, so that C_2 and C_4 were thought to be due to elastic effects in the contact region.

In another early approach to modelling shear resistance, Skelton [59] hypothesised that the shear stiffness can be related to the area normalised shear torque:

$$S = \frac{T/A}{\theta_s} \tag{2.9}$$

where T in the torque required to shear a sample of area A by an angle of θ_s degrees. By defining shear torque as

$$T \approx \frac{\mu_{cr} F_c D_{eff}}{2} \tag{2.10}$$

where $\mu_{cr} = 0.3$ is the crossover frictional constant, D_{eff} is the effective radius of rotation for an elliptical crossover contact area of dimensions a in the minor axis and b in the major so that

$$D_{eff} = \sqrt{\frac{a^2 + b^2}{2}} \tag{2.11}$$

and F_c is related to the flexural rigidity of the yarn, B_y

$$F_c \approx \frac{8B_y \sin\psi}{T_s} \tag{2.12}$$

This pointed to the relative contribution of shear deformation in a textile, as the model, although incomplete, suggested that shear strain could be many orders of magnitude greater than the tensile strain at similar stresses. Skelton demonstrated this with experimental data comparing low angle shear stiffness for polymeric fibre textiles to that of metallic sheet materials, which supported the findings. Most work on textile deformation relies on this phenomenon.

Skelton [59], with further work by Prodromou and Chen [54], also proposed a simple prediction for the textile locking angle from the initial values for tow spacing and width:

$$\cos\theta_{li} = \frac{T_s}{T_w} \tag{2.13}$$

where T_s is the tow spacing and T_w is the width of the tow. This suggests that the locking angle occurs when adjacent tows contact each other. The prediction of the locking angle is important, as it is often used as a factor in predicting the onset of wrinkling. However, later work by Souter [60] found that whilst visual observations of experiments confirmed that the textile locked soon after adjacent tows came into contact, this consistently occurred at a greater shear angle than predicted by Equation 2.13. This might suggest that the tows may compact in-plane *prior* to coming in contact with each other, possibly due to the crimping effect of the crossover tows, or perhaps due to a strong increase in in-plane tension near locking angle [32]. Souter's work in shear modelling, however, modelled the tows as compacting after contact, and specific experiments to validate this showed no tow compaction prior to contact. More work is required in assessing the sources of tow compaction in different weave structures, as well as different textiles.

Another model based on the saw tooth model was by Leaf et al. [34]. The tensile, compressive and bending strain energies of the yarns were modelled in order to predict the initial tensile behaviour of the textile, based on Castigliano's theorem. In a further paper, Leaf et al. [35] attempted to model plain-weave bending, again using Castigliano's theorem. The approach essentially derived an empirical formula, for which constants related to the contact geometry were altered to fit experimental data. This did however highlight the importance of the yarn geometry, in particular at the contact regions. Leaf et al. also attempted to model shear behaviour for a plain-weave textile [33], but by constraining the rotation of the tows around the crossover, so that shear was resisted by the tow bending. The ends of the tows were modelled as free ends of a cantilever beam constrained at the crossover, such that the shear angle θ was related to the end deflection δ_i and the free fibre length a_{ci}, where i once again refers to warp and weft, as

$$\tan\frac{\theta}{2} = \frac{\delta_i}{a_{ci}} \tag{2.14}$$

This approach required two fitting parameters to model the initial shear modulus, although these were refined to just one later. The fitting parameter proved to be constant for every (apparel) textile tested, although it was acknowledged that more yarn types needed to be tested before a universal fitting constant could be declared.

McBride [45] built on these increasingly complex unit cell description by modelling the yarn geometry in a plain-weave fabric during shear with sinusoidal curves, the coefficients of which were determined from the tow width, spacing, and textile thickness. The model was specifically aimed at predicting shear behaviour. Textile thickness was taken to be constant, as was confirmed from experimental measurements. Similarly, tow spacing was assumed to remain constant. The variation of tow width with shear was measured experimentally and an equation constructed to fit the measurements. His model produced good correlation with measured data, however, much of the data, such as the variation of tow width with shear angle, required experimental input. McBride's model made good progress in modelling a more realistic unit cell geometry, however the nature of the geometric description restricts his model to plain weave fabrics.

It should be noted that while most work agrees that the thickness of textiles remains relatively constant, some does not. Kutz measured the variation of thickness of textiles under a blank-holder before and after partial deformation over a hemispherical tool [29]. This was made in response to findings that the use of a single-piece blank-holder caused the textile to pull more at some points than at others. Kutz observed that as the fabric sheared in some places but not others, it must thicken at those and experience a greater blank-holder resistance than elsewehere. His findings showed that both non-crimp fabrics and woven textiles showed a thickness increase, of up to 9% in some cases.

One factor in the uncertainty over the variation of fabric thickness with shear is the different approaches to measuring it. While Kutz measured the displacement of a blank-holder during one-sided forming around a hemisphere, McBride [45] used a light block resting on the sheared textile, and Souter [60] painted a sheared textile in resin, and cast cross-sections in potting resin for measurements. The latter two tests did however agree that woven textiles maintain relatively constant thicknesses until they approach the locking angle. Kutz has suggested that thickness does not become a factor until the tows approach their compaction limits. As his blank-holder approach measures the thickness of the thickest (by inference, the most sheared) sections of the textiles around the circumference, it is thus more likely to record thickness variation at higher angles. Moreover, it does not specify the angle at which the thickness is measured. However, one aspect of his results that may be of interest is the variation of thicknesses at different blank-holder pressures.

This highlights an important difference of boundary conditions between the experimental shear tests and the shear deformation in a forming operation. In press or vacuum forming, the textile must deform under pressure on its faces, a factor that cannot be replicated by any of the shear test methods.

Generic weave shear models

Souter [60] expanded the work of McBride by extending the geometric description to weave patterns other than the plain-weave, and by similarly using the geometric description for these weave patterns as a basis for a mechanical shearing model. Souter's approach modelled the unit cell tow paths using a lenticular basis, in which crimp is defined by sections of circular arcs and straight segments. This allowed him to geometrically model unit cells other than plain-weave. He also took a much more sophisticated approach to defining tow cross-section, allowing it to vary along the tow length depending on its contact with other tows and the crimp structure. He maintained constant tow height and crimp angle, after taking experimental measurements that confirmed previous findings that textiles maintain relatively constant thickness up to the locking angle. Souter maintained constant tow width up to the point at which adjacent tows came into contact, after which he varied tow width with the cosine of the shear angle (see Equation 2.13) This corresponded very well to experimental measurements taken of a plain weave glass reinforcement. By balancing the flexural stiffness of the tow fibres with the compaction stresses, Souter found a way to predict the initial textile thickness. This did not correspond to experimental measurements and was not reflected in his *geometric* models, but was used solely to allow him to develop a value for the contact force at the crossover.

The description of tow path, cross-sectional shape, width and thickness, allowed Souter to determine the effective radius of rotation for each crossover in the unit cell, similar to Kawabata's concept [27]. It also allowed Souter to calculate the compaction of the tow at the crossover (see Section 2.2.2.2, below), from which he could calculate the force applied over the parallelogram crossover area. The shear forces predicted corresponded well to measured values for a number of different weave structures including plain weave, 4 harness satin weave, and 2:2 twill weave [60].

Souter's shear model was specifically developed for woven textiles, and could not model other structures such as 3D textiles or non-crimp fabrics. The lateral compaction model was used to determine the crossover contact force for frictional resistance, rather than being modelled as a source of shear resistance in and of itself. However, the model corresponded well with experimental results, suggesting that compaction as a direct shear effect is less significant in woven fabrics. Moreover, the effects of tow tension on crossover friction and compaction was only briefly alluded to. The effects of the stitch on non-crimp fabrics were discussed but not modelled. It was suggested that lateral tow compaction may have more influence on shear behaviour for non-crimp fabrics than for woven fabrics, but this was not explored.

A similar model to Souter's was developed by Lomov and Verpoest [37] that took account of a more comprehensive list of mechanical effects. This included tow tension, friction, bending (and unbending) vertical and lateral compression, torsion, and vertical displacement. Lomov's model exhibited good agreement with experimental data for woven fabrics, although it required extensive measurements of tow mechanical properties. Creech and Pickett [11] presented FE simulations of non-crimp fabrics based on meso-mechanical work presented by Long et al. [43], but using solid orthotropic elements to model the tows and beam elements with zero compressive stiffness to model the stitches. The material properties were tuned to provide good agreement with experimental data for picture frame and bias extension tests.

2.2.2.2 Compaction modelling

A vital part of modelling the shear behaviour of fabrics is the tow compaction behaviour. Tow compaction behaviour is affected by many factors, including the constituent fibre materials, crimp and twist. As in shear modelling, there are three common approaches to predicting tow compaction:

- Empirical models - these attempt to fit empirical equations to the compaction curves [56];
- Mechanical models - these attempt to model the behaviour of the constituent fibres, using mechanical and / or statistical equations to relate the fibre deformations to the tow deformations;
- FE models - as above, but fibre deformations and interactions are modelled using a finite element approach [58].

The compaction models covered herein mostly treat the fibres within the tows as beams which are forced to deform in compaction through their contact with other fibres [67].

Early work attempted to model a random fibre assembly for the compressibility of wool as fibres in Kirchoff bending. Van Wyk [67] proposed

$$\sigma_b = \frac{K E_f m^3}{\rho_f^3} \left(\frac{1}{V_f^3} - \frac{1}{V_0^3} \right) \tag{2.15}$$

Where K was experimentally determined, E_f is the Young's modulus of the fibres, m is the mass of fibres in the fibre bundle, ρ_f is the density of the fibre bundle, V_f is the fibre volume fraction, and V_0 is the minimum volume fraction of the fibre bundle.

Further work treated the fibre assembly as a set of fibre sections, the section length being determined by the probability of contact with other fibres. Komori et al. [28] concentrated on the distribution of fibre contact points, by modelling the fibres as straight cylinder segments of diameter d_f and length λ, with distance between points of contact b. A distribution function, $\Omega(\theta, \phi)$, was developed to predict the orientation of a segment. Fibre contact was treated statistically, so that a volume was defined such that there was 100% probability of contact between two fibres of orientation (θ, ϕ) and (θ', ϕ') with a randomly distributed centre of mass. The probability of the fibres contacting in a volume V, then, is given as

$$p = \frac{v'}{V} = \frac{2d_f\lambda^2 \sin\chi}{V} \tag{2.16}$$

where χ is the angle between the two fibres. This allowed mean b values to be derived

$$b = \frac{V}{2d_f L I_c} \tag{2.17}$$

where

$$I_c = \int_0^\pi d\theta \int_0^\pi d\phi J(\theta, \phi)\Omega(\theta, \phi) \sin\theta \tag{2.18}$$

and

$$J(\theta, \phi) = \int_0^\pi d\theta' \int_0^\pi d\phi' \Omega(\theta', \phi') \sin\chi(\theta, \phi, \theta', \phi') \sin(\theta') \tag{2.19}$$

Lee and Lee [36] used this to calculate the initial compressive moduli and Poisson's ratios for the fibre assembly. To do this the fibre geometry was analysed in each of the principal directions, to develop an expression for the projected mean free fibre lengths in each direction. The force transmitted through each contact point was calculated along the direction of each of the principal axes. No allowance was made for the formation of new contact points (hence the *initial* moduli etc.). This allowed the fibre segments to be treated similarly to Van Wyk, as simple beams bending with free ends. The deformation δ_{jk} of each fibre segment allowed the deformation of the fibre bundle to be defined as

$$\bar{\delta}_{jk} = \pm \frac{2C_j b^3}{3E_f I_f} M_{jk} (+; j \neq k, -; j = k) \quad (2.20)$$

where M_{ij} accounts for the stresses and deformations projected along each of the principal axes.

Pan and Carnaby [48, 49] modified the work using beams with constrained ends, ensuring continuity of curvature along fibre segments. Thus,

$$\bar{\delta}_{jk} = \pm \frac{C_j b^3}{6E_f I_f} M_{jk} \quad (2.21)$$

They then extended the work to model the compressive hysteresis of fibre bundles [9], by considering the inter-fibre slip during compression. The friction between fibres due to relative motion during compression allowed a critical angle of the contact force, relative to the normal to the contact points, above which slipping occurs.

The use of a fibre distribution function Ω means that in theory any fibre assembly could be modelled. However, such a model for aligned fibres has not yet been developed. Instead, Cai and Gutowski [8] developed a model specifically aimed at (lubricated) aligned fibre assemblies. In many ways it is cruder and makes more assumptions than other models, but work by McBride [45] adapted the technique to dry fibre bundles and fit the resulting curve extremely well to experimental data. The ease of implementation, the good fit to experimental data, and the availability of fit parameters make this a useful model for the purposes of this thesis.

Rather than straight beams, the fibres were modelled as simple arches, illustrated in Figure 2.3, with a single contact point at the apex of the arch. Thus the length

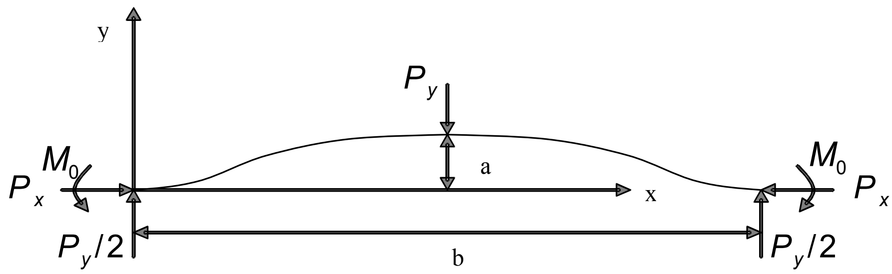

Figure 2.3: Cai and Gutowski modelled a fibre as an arch, under a centre point load, with applied moments and axial end loads.

to height ratio of the arches determined the number of contact points in the bundle. The deflection of the arch in the x and y directions were evaluated using beam theory:

$$\begin{Bmatrix} \Delta x \\ \\ \Delta y \end{Bmatrix} = \begin{bmatrix} \left(\dfrac{a^2 b}{8E_f I_f} + \dfrac{b}{E_f A_F}\right) & \left(-\dfrac{ab^2}{4\pi^2 E_f I_f}\right) \\ \left(-\dfrac{ab^2}{4\pi^2 E_f I_f}\right) & \left(\dfrac{b^3}{192 E_f I_f}\right) \end{bmatrix} \begin{Bmatrix} P_x \\ \\ P_y \end{Bmatrix} \tag{2.22}$$

The fibre was assumed to occupy a cell volume $a^2 \times b$ (Figure 2.4), with the lengthways stress acting on the end faces and the so-called bulk stress acting on the other faces. The forces P_x and P_y could thus be related to the axial stress along the fibre length and the compressive stress lateral to the fibre assembly respectively, and similarly for the strains. Given then the volume fraction V_f, the minimum volume fraction (at zero bulk stress) V_0, the maximum volume fraction V_a, and the ratio of a to b, β, the lateral, or bulk, strain, was defined as

$$\epsilon_b = 1 - \sqrt{\frac{V_f}{V_0}} \tag{2.23}$$

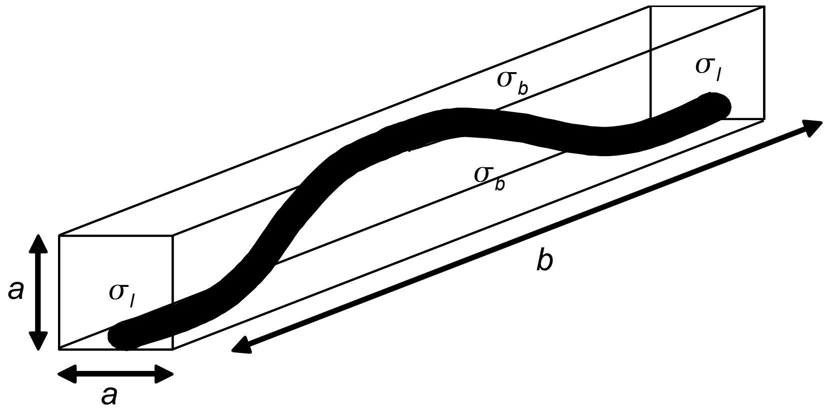

Figure 2.4: Conversion of fibre stresses to bulk tow stresses require a cell to be constructed around the fibre.

and a compliance matrix could be determined

$$\begin{Bmatrix} \epsilon_l \\ \\ \epsilon_b \end{Bmatrix} = \begin{bmatrix} B_{ll} B_{lb} \\ \\ B_{bl} B_{bb} \end{bmatrix} \begin{Bmatrix} \sigma_l \\ \\ \sigma_b \end{Bmatrix} \tag{2.24}$$

B_{ll}, $B_{bl} = B_{lb}$, and B_{bb} are defined as

$$B_{ll} = \frac{4}{\pi E_f} \zeta^2 \left[1 + 2(\zeta - 1)^2\right] \tag{2.25}$$

$$B_{bl} = B_{lb} = -\frac{16\beta^2}{\pi^3 E_f} \zeta(\zeta - 1)^3 \tag{2.26}$$

$$B_{bb} = \frac{\zeta^4}{3\pi E_f} (\zeta - 1)^4 \tag{2.27}$$

and

$$\zeta = \sqrt{\frac{V_a}{V_f}} \tag{2.28}$$

McBride developed this model into a sixth order compliance matrix, and tested it against many different load cases, allowing him to derive accurate values for the fit parameters. One load case for the smaller compliance matrix of interest to shear is that of zero axial strain

$$\sigma_b = \frac{\epsilon_b B_{ll}}{B_{bb} B_{ll} - B_{bl}^2} \tag{2.29}$$

2.2.3 Discussion

The ideas for shear mechanisms that were initially formulated by Skelton and others have developed to become fairly accurate shear prediction tools for woven textiles. The effects encountered in non-crimp fabrics, however, have not yet been modelled. As a consequence, only the effects of crossover shear have been modelled so far, despite indications that other factors may become more important in different textile structures and towards the extremes of woven shear. The next steps to a more complete shear resistance model, therefore, are proposed to be to identify other shear resistance mechanisms, and to allow them to be added to shear models by taking an energy based approach.

2.3 Forming modelling for resin transfer moulding (RTM)

The formed state of continuous fibre textile reinforcement is important in many different ways:

- It allows an accurate blank shape to be predicted. This helps in automated cutting systems and textile scrap minimisation.
- It may predict wrinkles, allowing challenging geometric features to be assessed early on in the design process, and altered if necessary.

- It may allow the lay-up or forming process to be optimised, reducing or eliminating defects such as wrinkles.
- It facilitates accurate resin flow modelling [39]. Textiles can allow resin to preferentially flow in some directions. Also, the variation in fibre volume fraction around the part caused by the varied deformation creates potential dry spots.
- It allows for more accurate mechanical analysis of the formed part [12]. The mechanical response of composites is substantially weaker normal to the fibre direction. Thus, the weakest tensile direction at any point is along the greatest angle from any fibres (45° in the case of two, orthogonal fibre directions). Thus, the prediction of the direction of the fibres along the formed parts forms an important factor in the design performance of that part.

Forming simulations have generally taken two approaches. The first, termed kinematic analysis, is typically fast and requires minimal user input for results. However, it does not make allowances for the shear characteristics of the textiles being used, or for manufacturing conditions. This range of characteristics make it very useful for early design stages, when fast solutions allow initial design decisions to be made. Such approaches can provide very accurate solutions for hand lay-up of fabric or prepreg.

The second approach is a full Finite Element solution of the proposed process. These model the entire physical sequence of events during the draping of the part over the tool, modelling the textile according to its characteristics and allowing for effects such as bridging (where the textile runs clear of the tool between two high points) and process effects such as those created by blank holders. However, these tools require a large amount of computational power, not to mention user training and experience. They are very dependant on accurate process description, which can require extensive data on material characteristics. These factors make it suitable for final design validation steps, where most design decisions have been taken, few further design iterations are required, and accurate results become more vital.

Note that for simple geometries with shear-symmetric textiles kinematic and FE analyses produce the same geometric results.

2.3.1 Empirical modelling approaches

The first attempts to model textile forming took an empirical approach over surfaces of revolution [44]. They suggested that threads be treated as straight and inextensible, pivoting around crossover points with no slippage. Further, each crossover is in contact with the geometry, whose smallest radius of curvature is larger than the yarn spacing. These assumptions have proved to be the basis for all subsequent so-called "Pin-Jointed Net" approaches [53, 55, 41]. It should be pointed out that whilst they claim to be more physically appropriate, many mechanical finite element approaches also make some of these assumptions.

Robertson et al. [55] applied this concept to a hemisphere. Due to symmetry, he modelled only one quadrant, with the warp and weft tows constrained to the edge of the quadrant. Solving the intersection of the geometry and two spheres with radius equal to the fibre spacing, he found that all other nodes (crossovers) on the PJN could be calculated. Comparisons with experimental results for the draping of a woven cloth on a hemisphere were favourable. Van West [66, 65] extended this approach to any geometry that can be represented as a collection of bicubic patches. At this point the limitations of the approach became apparent. These are related to the assumptions stated above, regarding tow slippage, surface radii, etc. Another problem presented itself, the placement of the initial "generator paths". The placement of these had been obvious in the hemisphere problem, but was now less so for generic geometries.

Many people have proposed largely similar solutions for kinematic drape algorithms over generic geometries, including several commercial offerings. One other example was Long et al. [41], who modelled the drape over a surface comprised of flat elements, which provided a particularly fast calculation procedure.

2.3.2 Modified kinematic modelling approaches

With generic geometries, two geometric path placement options emerged: Projection, and geodesics. In projection, the paths were placed so that when viewed from directly above they followed a straight line at 90° to each other. In geodesics, the shortest distance between two points on a surface was calculated. This ensured that at the generator paths the tensile forces acted directly along the tow - this was shown to improve accuracy in many cases [63, 64].

Other path placement options were explored, that tried to be more sensitive to the process occurring. Bergsma [1] offered an iterative scheme whereby the position of generator paths were set to minimise the change in surface area from flat to draped sheet. Bergsma concluded that whilst projecting the paths provided a quick and accurate prediction for axi-symmetric parts, for others the shear minimisation approach should be utilised.

Ye and Daghyani [70], rather than minimising shear, minimised shear energy.

They took Kawabata's [27] expression for torque required to rotate a crossover, and integrated it with respect to shear angle to obtain a shear energy (similar to Equation 4.14). Although Ye and Deghyani's torque model did not reflect any real reinforcement, their approach suggested a method by which real textiles could be modelled within the kinematic frame.

Souter [60] took this idea further, by measuring actual shear torques for textiles and using these as the basis for an energy minimisation algorithm based on Long's [41] kinematic code. This allowed Souter to model asymmetric drape effects encountered when using certain non-crimp fabrics [42].

Lai and Young [30] tried to modify the kinematic procedure to account for inter-yarn slip. The process first predicted a kinematic drape pattern. The in-plane bending at each crossover was then calculated. At nodes of high bending angle, the in-plane radius of curvature was calculated so that the bending angle was smoothed out over adjacent nodes. This minimised large changes in shear angle, which corresponds to Wang et al.'s finding that significant slip was found where there was a large change in shear angle [68]. An iterative process is then used to determine the fibre spacings at which the in-plane bending angles match the smoothed out set. Results corresponded well to experiments using very loose plain weaves, in which inter-yarn slip could be reliably measured. Comparisons to tighter weaves were not made.

2.3.3 Finite element modelling approaches

As discussed before, FE simulations were primarily introduced to model effects neglected in the kinematic approach. These included the interactions between the tools and the material, rate effects, and non shear textile deformations such as slip and buckling. Because they could model this, these tools proved particularly useful for prepreg modelling, in which rate, temperature, and pressure are all important. As this thesis concentrates on dry fabric forming, this work will not be covered in detail.

In modelling the stresses experienced by the textile during the forming process, accurate deformation mechanics must be included into the elements. Several approaches to replicate the behaviour of textiles in contrast to isotropic materials have been proposed.

Bergsma [1] modelled the textile as a collection of one-dimensional beams that deform by shear, stretching and buckling only. His approach allowed wrinkling to be predicted, although not yarn slip. Results against a single geometry corresponded well to experimental results.

Boisse et al. [4] tested a textile on a biaxial tensile testing machine, and used the data in a fabric model for a non-linear finite element analysis. The textile was allowed to shear but shear properties were not modelled as they were several factors lower than the tensile moduli. This predicted fibre patterns adequately, but in order to accurately predict fibre buckling (wrinkling), it was found that shear data became important [6].

Blanlot [2] presented a finite element formulation based on constitutive equations formulated to an objective rigid-body rotation frame. This allowed the textile to be modelled by, after each incremental deformation step, updating the principal directions of strain to correspond to the directions of warp and weft yarns.

Bergsma and Boisse, together with many since such as Yu et al. [71], have consistently found that increasing blank-holder force improves the draping of the textiles. Yu et al. aimed to allow for the assymetric shear behaviour of non-crimp fabrics and also the effects of blank-holder on forming. He adapted a tensile model originally developed for woven fabrics, and added a shear stiffness constitutive equation developed from experimental shear data to successfully demonstrate the shear asymmetry observed with this material on a hemisphere, and the reduction of that effect with increased blank-holder forces.

Increased complexity in the FE model should be treated with care, however. DeLuca et al. [14] modelled specialised viscous-friction and contact constraints as separate layers. The increase in the degrees of freedom associated with the number of layers modelled led to huge FE overheads. Lamers et al. [31] simplified this approach and modelled the various effects in a single element layer, incleding friction between layers.

2.3.4 Forming implications from drape models

Whilst all drape models have aimed to predict the draped pattern in advance, the variety of modelling approaches has highlighted the vast number of possible drape patterns available on any given geometry. Considering the kinematic approaches, the result depends on the point of initial drape, together with the path plotted for each generator tow. The shear energy minimisation path placement approaches recognise that some shear distributions are less energetically favourable than others, and favours the result requiring the least shear deformation energy. This seems a reasonable strategy when modelling dry reinforcements that are automatically draped, or are draped over simple geometries.

The shear angle minimisation approach, in contrast, aims to determine the drape pattern least likely to wrinkle, regardless of the shear energy that might be required to achieve it. Hancock and Potter [16] first suggested a method by which forming models could be used to inform processing to optimise the formed pattern according to the shear angle minimisation approach for the hand lay-up of tacky pre-pregs. The generic application of this principle would allow a pattern to be draped without wrinkles even when the draping process to achieve it is not intuitive or shear energy minimised.

The different deformation operations required to drape the material over the geometries were discussed, and categorised into four types: No manipulation, Warp manipulation, Weft manipulation, and Bias manipulation. These four categories correspond to areas where there is very little warp or weft in-plane curvature, substantially greater Weft than Warp in-plane curvature, or proportional amounts of both Warp and Weft curvature respectively. An analysis of the geometry identified regions for which each of these manipulations were recommended to achieve the required draped pattern. The in-plane curvature vectors were also used to create a manipulation vector that allowed the different manipulation regions to be linked sequentially to form an order of drape.

This work allowed a geometry to be moulded that had previously proved impossible to mould both by diaphragm forming trials and hand lay-up. The basis of this work is to show that modified kinematic models can be used to intelligently inform forming methods to achieve acceptable results over challenging geometries. This work, and subsequent work creating automated tools to generate the hand lay-up instructions [17], has however concentrated on the specific (and challenging) case of tacky pre-preg hand lay-up, which cannot move relative to the tool once it has been applied. Similar work needs to follow on with suggestions on the control of automated forming techniques to minimise wrinkling, and also to address the different issues encountered with dry textiles.

2.3.5 Discussion

Kinematic, modified kinematic and mechanical approaches to drape simulations have been proposed. Whilst Kinematic and mechanical approaches occupy very different complementary niches in the design cycle, both leave much to be done when compared to, for example, sheet metal forming models. Important mechanisms such as shear and tensile stress responses have been modelled, and also blank-holder effects and wrinkling in FE models. However, process and textile variability have yet to be treated.

Modified kinematic models such as Souter's energy minimising kinematic approach and Lai and Young's fibre slip models are important in increasing understanding early in the design process. It would be advantageous to also have an approach to modelling wrinkling or blank-holder effects in an equally simple and less computationally intensive manner.

Chapter 3

Experimental Shear Characterisation of Fabric Reinforcements

3.1 Introduction

Simulation of forming processes offers the potential to substantially reduce costs by reducing the number of prototype iterations, performance tests and process revisions. In order to accurately predict the response of the material to the forming process its forming characteristics must be taken into account.

Experimental characterisation of technical fabrics for engineering composites has two immediate purposes that are within the context of this thesis: To generate material data for forming simulations, and for validation of material behaviour models. Material behaviour models, in turn, are developed with a view to automatically generate material data for forming simulations. For this reason trellis shear deformation, which is the dominant deformation mechanism in the textile preforming process, is the focus both of the deformation models (which require validation) and material input data.

Two such characterisation experiments, specifically designed for measurements of large in-plane shear and wrinkling, include the picture frame (PF - see Section 2.2.1.2) and bias extension (BE - see Section 2.2.1.3) test methods. The original concept behind these and other similar in-plane shear tests can be traced back to research in textile drape and fabric forming [13, 61, 62].

Table 3.1 outlines the materials tested in the line of this work. Results are presented later in this chapter, in Section 3.3.3 comparing the picture frame test at different pre-tension, in Section 3.4.5 on the comparison of different bias extension normalisation techniques, and in Section 3.5 on the comparison of the two test techniques. Further results can be found in Appendix B, with additional test data in Appendix C.

Table 3.1: Materials tested for shear response

Material name	**Material**	**Description**
Bentley mat1	E-glass	±30° non-crimp fabric, double stitched with a (+1,0,-1,0) stitching pattern.
Bentley mat2	E-glass	3D E-glass woven fabric from 3Tex
EBXhd-936	E-glass	936gm^{-2}, ±45° non-crimp fabric from Vetrotex, with a tricot (+1,-1) stitching pattern, 6-gauge, stitch length 2mm
FGE 106hd	E-glass	950gm^{-2}, ±45° non-crimp fabric from Formax, with a tricot (+1,-1) stitching pattern, 6-gauge, stitch length 2.5mm
FGE 106hd:1.65 (special)	E-glass	950gm^{-2}, ±45° non-crimp fabric from Formax, with a tricot (+1,-1) stitching pattern, stitch length 1.65mm
FGE 106hd:5 (special)	E-glass	950gm^{-2}, ±45° non-crimp fabric from Formax, with a tricot (+1,-1) stitching pattern, stitch length 5mm
Twintex^{TM} 1	Co-mingled E-glass/PP	1816gm^{-2} Twintex^{TM} unbalanced 2/2 twill weave fabric from Vetrotex
Twintex^{TM} 3	Co-mingled E-glass/PP	743gm^{-2} Twintex^{TM} balanced plain weave fabric from Vetrotex

3.2 Comparison of experiments

In order to be of generic use, material characteristics should be presented in such a way that they only reflect the nature of the material. They should therefore be independent of the test method, rate, sample dimensions, etc. Such data can be generated by the normalisation of an individual test's raw output. The materials treated in this thesis are non-viscous and therefore mostly independent of shear rate [46]. As a result, it is unnecessary to normalise with respect to rate. Normalisation of data depends on sample shape, size, shear distribution, and boundary conditions. Shear distribution and boundary conditions are primarily affected by the test method, whereas size and shape are factors that also affect same-method tests.

Picture frame experiments are simpler to normalise as compared to bias extension as the entire sample undergoes uniform shear. Normalisation of bias extension test data is complicated by the non-uniform strain profile occurring in the sample. One method of avoiding this complication is to measure the strain field in a gauge section of the deforming sample. This requires that tests are conducted on samples with a length / width ratio greater than two. However, tests on such specimens can increase difficulties associated with handling the fabric, particularly when dealing with loose fabrics that tend to disintegrate easily. Large sample length / width ratios also mean that edge effects [62] and intraply slip [20, 51] may become more significant and can influence the deformation kinematics within a sample. Finally, use of a length / width ratio of two can decrease the amount of material required for testing. For these reasons, an alternative BE test normalisation procedure has been developed. The main advantage of this method is that results from BE tests using samples with an initial length / width ratio of just two (or greater) can be treated. An analogous normalisation method on shear rate dependent, pre-impregnated viscous continuous fibre reinforced composite (CFRC) has been presented previously [18].

In the following sections, different normalisation procedures for each of picture frame and bias extension tests are developed and discussed. Normalised results using different methods are compared for bias extension, and finally normalised results from different tests are also compared.

3.3 Picture frame experiments

3.3.1 Experimental method

The picture frame apparatus used for this thesis is illustrated in Figure 3.1, and is typical for this test.

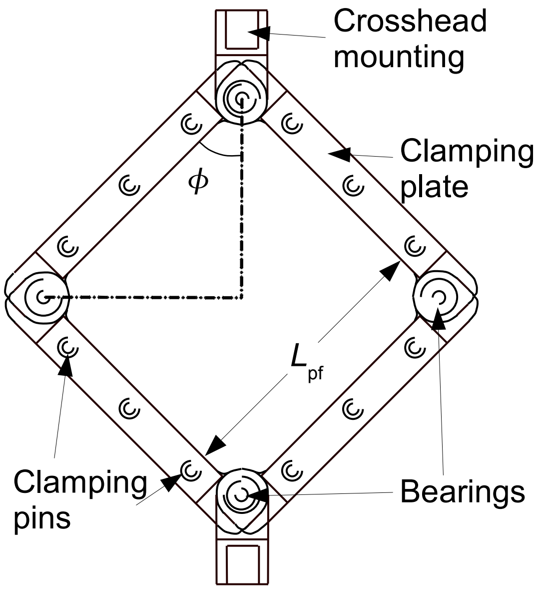

Figure 3.1: The picture frame shear rig

The apparatus is designed to impose pure trellis shear deformation onto the sample. In order to do this, the inside edge of each clamping plate must be aligned with the centre of the bearings at either end. Also the distance between bearing centres must be equal for opposite clamping plates. For the purposes herein it will be assumed that this distance, called the picture frame side length (L_{pf} in Figure 3.1), is equal on all sides, so that when the faces are orthogonal the frame is square. Finally, the frame sides must be aligned with the textile fibre directions. The sample is fixed into the picture frame so that it cannot move relative to the frame. The result of aligning the clamps with the fibre directions means that, for a $\pm 30°$ textile for example, the angle between the frame sides ($2\phi_p f$, or 2ϕ) before deformation (subscript 0 denotes initial, $2\phi_0$) must be $60°$. Figure 3.2 shows a close up of the picture frame with a textile clamped in and sheared.

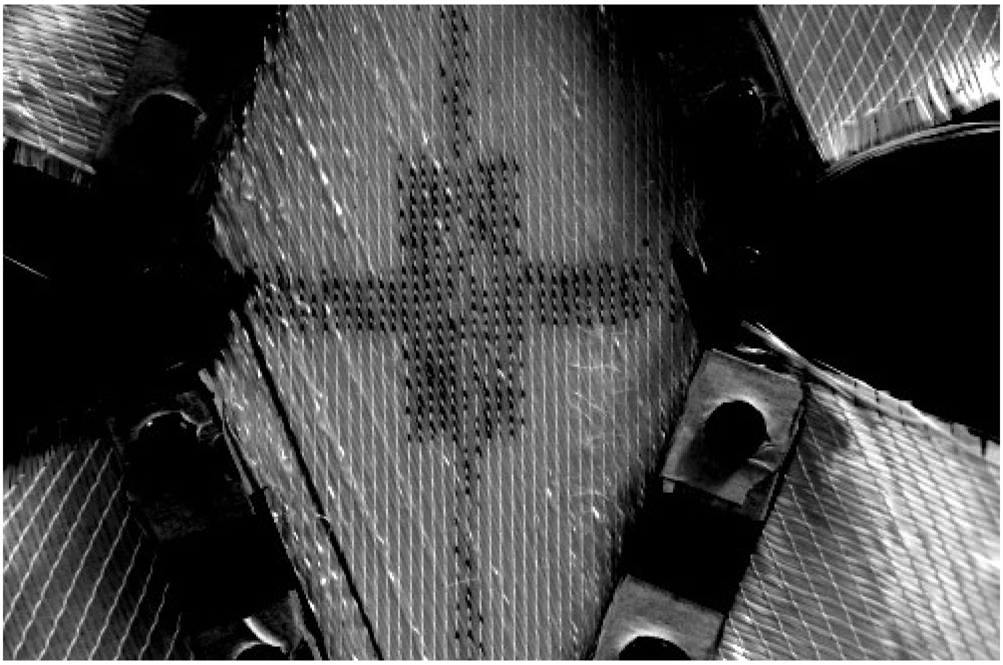

Figure 3.2: Close up of picture frame with a textile clamped in and sheared.

In the example presented herein, the side length of the picture frame was 145mm, with as little of the corners cut out as possible, so that the central area had a side length of 115mm. To ensure consistency the size of the samples was determined in terms of the crossovers for woven textiles. Thus, a sample with 4 tows per cm would be measured to have a central area 46 tows wide. This ensures that the cutting follows the direction of the tows and any handling does not affect the alignment. Initially, the EBXhd-936 non-crimp fabric was cut out using a stamp cutting die. However, this proved hard to align with the fibre directions, as discussed later in Section 3.3.3. Subsequently for FGE 106hd the dimensions were determined by following the stitches with reference to the manufacturing data. Thus, to mark a diagonal line on FGE 106hd, which has 6 stitches per inch in the weft direction and a stitch length of 2.5mm, the line would follow 6 stitch spacings in the weft direction for every 10 stitch lengths in the warp, which would constitute the 45° fibre direction before handling.

The clamps are composed of ridged plates that are bolted to the picture frame sides through three holes. Rubber strips on the inside of the clamping plates and frame sides ensure that a good grip on the fabric is maintained (see Figure 3.3). Tapered-ended bolts are used to minimise damage to the fibres when they were inserted through the textile - the converse problem this causes is the potential re-alignment of fibre angles as they are pushed around the bolt shanks.

The test is very sensitive to misalignment of the fibres within the picture frame. A slight misalignment causes progressive compression or extension to be applied to the fibres, causing premature wrinkling in the former case, and very high fibre tension (due to their high modulus) in the latter. The fibres' length-ways compressive, shear and extensive moduli differ by orders of magnitude, resulting in a large scatter where exact alignment of the fibres cannot be assured. In order to minimise misalignment, a pre-tensioning rig can be used, illustrated in Figure 3.3. This applies tension to the

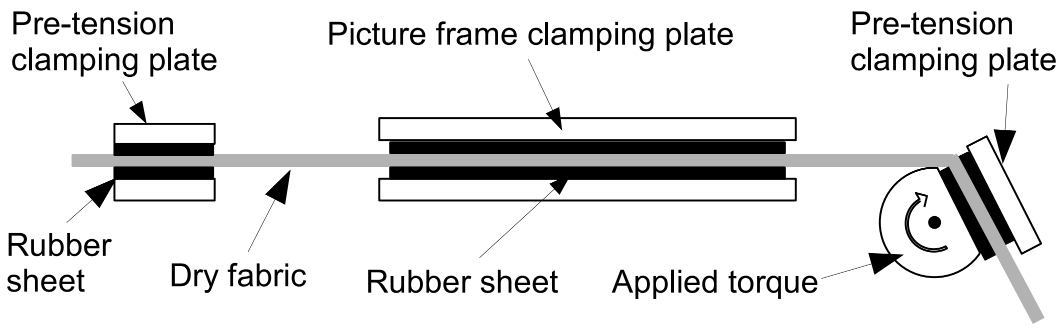

Figure 3.3: Picture frame pre-tensioning device

fibres before they are clamped into the picture frame, aligning them with each other and therefore making it easier to align them with the rig. The torque is applied by hanging weights from an arm attached to the Pre-tensioning plate. The arm position was adjusted to remain horizontal to ease torque calculations. Pre-tensions were applied at four levels: 0N, 62N, 375N, and 1300N.

Note that textile misalignment in the pre-tensioner could result in uneven tension in the tows, as well as limited improvement in alignment in the picture frame. It is also important to remember that the tension applied before deformation does not necessarily remain constant during shear.

The cross-head is extended in a line away from the diagonally opposite corner of the rig, and the force exerted in that direction, F_1 (see Figure 3.4), is recorded against displacement, d_1.

The shear force is calculated using

$$F_s = \frac{F_1}{2\cos\phi} \tag{3.1}$$

This is best plotted against shear angle,

$$\theta = 2(\phi_0 - \phi) \tag{3.2}$$

Given the geometry of the picture frame, and presuming a square frame, the cross-head displacement can be related to the picture frame$\angle\phi$:

$$d_1 = 2L_1\cos\phi - 2L_1\cos\phi_0 \tag{3.3}$$

which, together with Equation 3.2, gives displacement in terms of shear angle,

$$d_1 = 2L_1\left(\cos\left(\phi_0 - \frac{\theta}{2}\right) - \cos\phi_0\right) \tag{3.4}$$

or the shear angle in terms of displacement:

$$\theta = 2\left(\phi_0 - \arccos\left(\cos\phi_0 + \frac{d_1}{2L_1}\right)\right) \tag{3.5}$$

Using crosshead displacement in tensile tests often results in inaccurate results occurring due to small amount of slip of the specimen in the jaws. This is not an issue in the picture frame test as the frame is fully constrained within the machine, and cannot slip. Issues of textile slipping within the frame are considered later in the chapter.

3.3.2 Normalisation of results

A simple argument is used to justify normalisation of picture frame test results by the side length of the picture frame rig. A similar argument was presented by Harrison et al. [18, 19]. For clarity and in later sections, the derivation is repeated here.

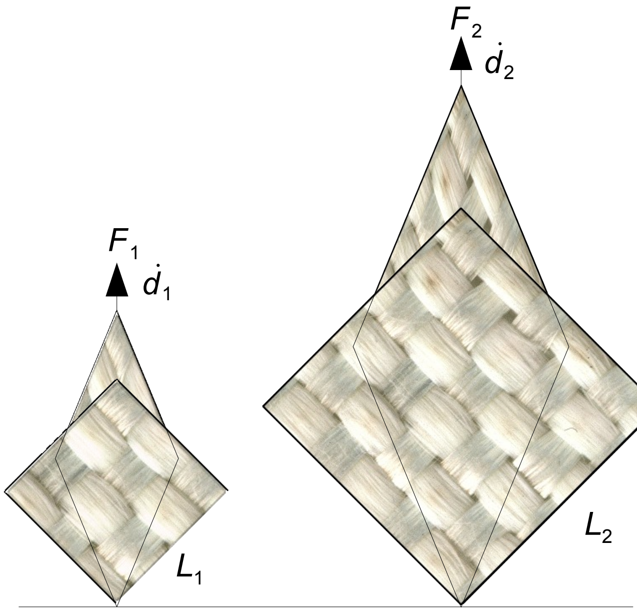

Figure 3.4: Two picture frame experiments with sample sizes L_1 and L_2.

Figure 3.4 shows two idealised picture frame experiments of the same material with different sample side lengths L_1 and L_2. The power required to extend the picture frame is:

$$P_i = F_i \dot{d}_i \tag{3.6}$$

where F_i is the measured extensive force for test i ($i = 1$ or 2 for the two tests in Figure 3.4), and $\dot{d}_i$ is the cross-head displacement rate.

Differentiating Equation 3.4 gives

$$\dot{d}_i = \dot{\theta} \sin\left(\phi_0 - \frac{\theta}{2}\right) L_i \tag{3.7}$$

This can be re-written as

$$\dot{d}_i = k_1 L_i \tag{3.8}$$

where as long as the extension rate in tests 1 and 2 is such that their angular shear rate $\dot{\theta}$ is the same, then k_1 is the same in both tests,

$$k_1 = \dot{\theta} \sin\left(\phi_0 - \frac{\theta}{2}\right) \tag{3.9}$$

Substituting Equation 3.8 into Equation 3.6 gives

$$P_i = k_1 F_i L_i \tag{3.10}$$

The material can be assumed to be relatively homogeneous (with respect to shape and size of sample, rather than directionality of properties) if the sample size is at least an order of magnitude larger than the material's unit cell. Taking that assumption, then, the power required to deform a given material at a given deformation and deformation rate increases linearly with its initial volume. However, the thickness of the material (regardless of its compressibility) at that same deformation state can be assumed to be independent of the initial volume. Given these assumptions, the power required to extend the picture frame *at that deformation state* increases linearly with the initial sample *area*, which for a square sample is to say:

$$P \propto V_0 \propto A_0 \propto L^2 \tag{3.11}$$

where V_0 and A_0 are the initial volume and area of material respectively. The proportionality constant for this material, ψ, is the power normalised by initial area,

$$\psi = \frac{P_i}{A_0} = \frac{P_i}{L_i^2 \sin 2\phi_0} \tag{3.12}$$

and is a function of θ and $\dot{\theta}$.

Equation 3.12 can be substituted into Equation 3.10 to give

$$\psi L_i \sin 2\phi_0 = k_1 F_i \tag{3.13}$$

Defining a new constant k_2

$$k_2 = \frac{k_1}{\sin 2\phi_0} = \frac{\sin\left(\phi_0 - \dfrac{\theta}{2}\right)}{\sin 2\phi_0}\dot{\theta} \tag{3.14}$$

allows Equation 3.13 to be rearranged to give

$$\frac{\psi}{k_2} = \frac{F_i}{L_i} \tag{3.15}$$

so that

$$\frac{F_1}{L_1} = \frac{\psi}{k_2} = \frac{F_2}{L_2} \tag{3.16}$$

where ψ/k_2 is a constant for the a given material at a given θ and $\dot{\theta}$. Given that compressible material shear response tends to be rate independent, any two picture frame tests for these materials can be compared according to this principle, comparing F at any angle θ.

3.3.3 Results

Table 3.2 lists the fabrics tested with the picture frame. In the case of non-crimp fabrics, the gauge refers to the spacing of the stitch, being the number of stitching threads per inch. A (+1, -1) tricot stitch, following a terminology proposed by

Souter [60], describes a stitch where the overlaps (see Section 4.3.1.1, and Figure 4.2), extend diagonally one stitch spacing per stitch length, and then back.

Non-crimp fabrics exhibit different shear response depending on the direction of shear. The reasons for this are explored in Chapter 4. It becomes necessary to define directions of shear. Positive shear is defined as shear such that the fabric is extended in the stitch direction, Negative shear being such that the fabric is extended normal to the stitch direction.

Table 3.2: Materials tested for shear response according to the picture frame test method

Material name	**Material**	**Description**
EBXhd-936	E-glass	936gm^{-2}, ±45° non-crimp fabric from Vetrotex, with a tricot (+1,-1) stitching pattern, 6-gauge, stitch length 2mm
FGE 106hd	E-glass	950gm^{-2}, ±45° non-crimp fabric from Formax, with a tricot (+1,-1) stitching pattern, 6-gauge, stitch length 2.5mm
Twintex^{TM} 1	Co-mingled E-glass/PP	1816gm^{-2} Twintex^{TM} unbalanced 2/2 twill weave fabric from Vetrotex
Twintex^{TM} 3	Co-mingled E-glass/PP	743gm^{-2} Twintex^{TM} balanced plain weave fabric from Vetrotex

The woven twintex fabrics in Figures 3.6 to 3.9 show a significant increase in low angle shear force with pre-tension. This tendency has been indicated in past work [70], although the poor repeatability of the test has made it difficult for others to concur [60]. The possible sources for this increase include fibre bending at the clamps [22], and increased inter-tow friction [60]. The latter source is supported by the non-decisive difference that pre-tension seems to make in an non-crimp fabric tested at different pre-tensions, as can be seen in Figures 3.10 and 3.11 , in which high pre-tension seems to increase conformability for positive shear (Conformability is the ease with which a textile will conform to a shape with double curvature). Section 4.3.2.2 will demonstrate that inter-tow friction is not significant in the shear response of non-crimp fabrics, unlike in woven fabrics.

It is interesting to note the sudden spikes in the curves such as can be seen in the highest pre-tension curve in Figure 3.11. These correspond to the breaking of the stitching, a phenomenon that is observable during the test both visually and audibly. In Chapter 4 the stitching is modelled until breaking point, however beyond that it becomes difficult to predict how the material will behave. The curves show that the tension in the stitching is not suddenly and catastrophically released, but that friction retains the stitching in the fabric. As the fabric does not disintegrate on stitch failure, and the stitch has no role in the mechanical behaviour of the composite, this demonstrates that high shear leading to stitch failure is unlikely to be detrimental to the component performance.

The results, particularly for the non-crimp fabrics, show a high degree of variability, this is one of the prime weaknesses of the picture frame test method. This is particularly demonstrated in Figures 3.12 and 3.13 . Non-crimp fabrics in particular are very difficult to align in a picture frame rig. This is because the tow directions are not immediately apparent in many non-crimp fabrics. Figure 3.5 illustrates this problem. The dashed line marks the apparent tow direction on the textile. To determine the actual tow direction, lines have been drawn across the textile, and then a small bundle of fibres have been pulled. The points where the lines have shifted have shown the actual fibre direction, which was marked in as a dot-dashed line. This illusory tow direction is created by the stitching, which pierces the tows and creates channels where the fibres have been re-routed. These channels appear to form lines

Figure 3.5: Marked sample of FGE 106hd illustrating the difficulties in ascertaining tow direction in a non-crimp fabric.

that mark the tow edges. However, their direction is determined by the stitch length and spacing, which in this case is 2.5mm and 4.23mm respectively. As the tows are laid at 45° to the stitch direction during manufacture, the channels from stitching points closest to 45° with respect to each other appear to match up. In this case, this is for channels that are two stitch lengths and one stitch width apart - however, these create an apparent tow angle of almost 50°. Added to this, the tension in the stitch tends to shear the textile so that it is often loaded into the frame a few degrees sheared, and the challenge in properly aligning the sample becomes readily apparent.

The effects of fibre misalignment manifest differently depending on the direction of misalignment. If the initial fibre angles are greater than ϕ_0 then the fibres will undergo compressive strain during shear and the sample will wrinkle prematurely. Where this occurred the test results were discarded and the misaligned shear response has not been presented. Alternatively, if the initial fibre angles are less than ϕ_0, the fibres are placed under increasing tension during the test. This can not be observed visually, so that it is likely that despite best attempts to align the fibres in the frame, some misaligned samples have been included in the results. The high modulus of the fibres means that they cannot strain significantly enough under tension, and so they feed through the picture frame clamp. The greatest amount of extension per degree of shear in misaligned fibres occurs at the start of the test, so that the effect of misalignment on the measured response can be expected to be greatest at the start of the test. This may explain the hump observed in many picture frame results such as those in Figure 3.13. As misaligned samples with lower shear force have already been discarded due to premature wrinkling, it seems likely that the best results are close to the bottom of the distribution.

The remaining picture frame test results can be found in Section B.1

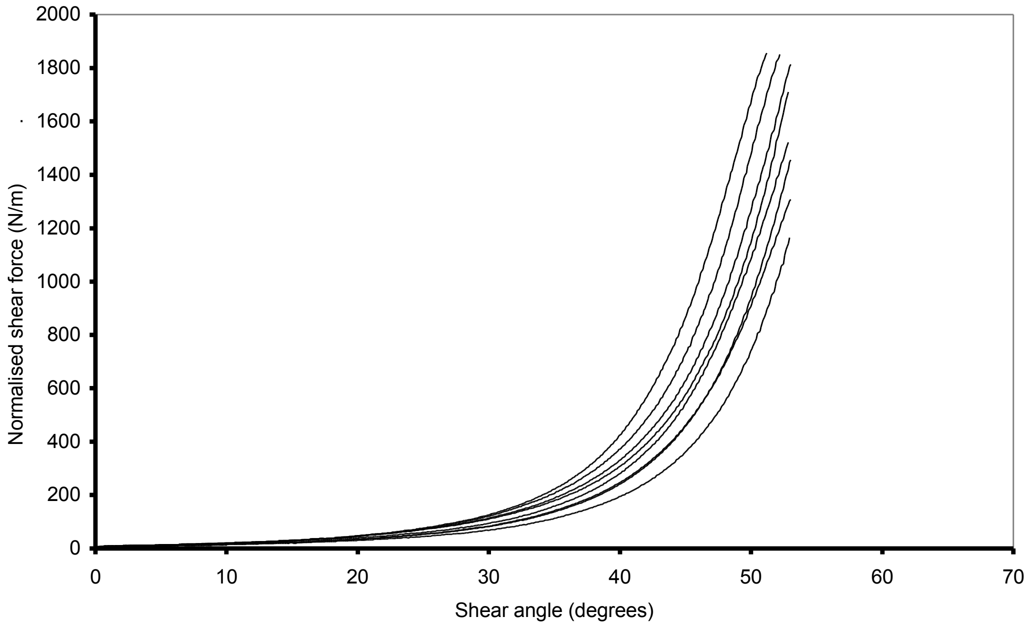

Figure 3.6: Twintex^{TM} 1 at 0N pre-tension

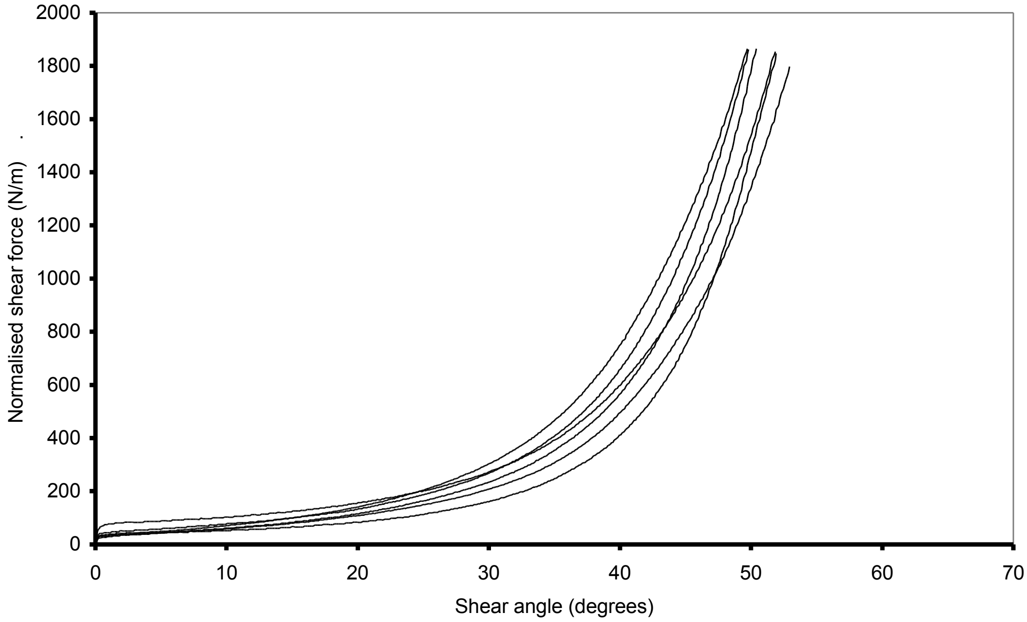

Figure 3.7: Twintex^{TM} 1 at 375N pre-tension

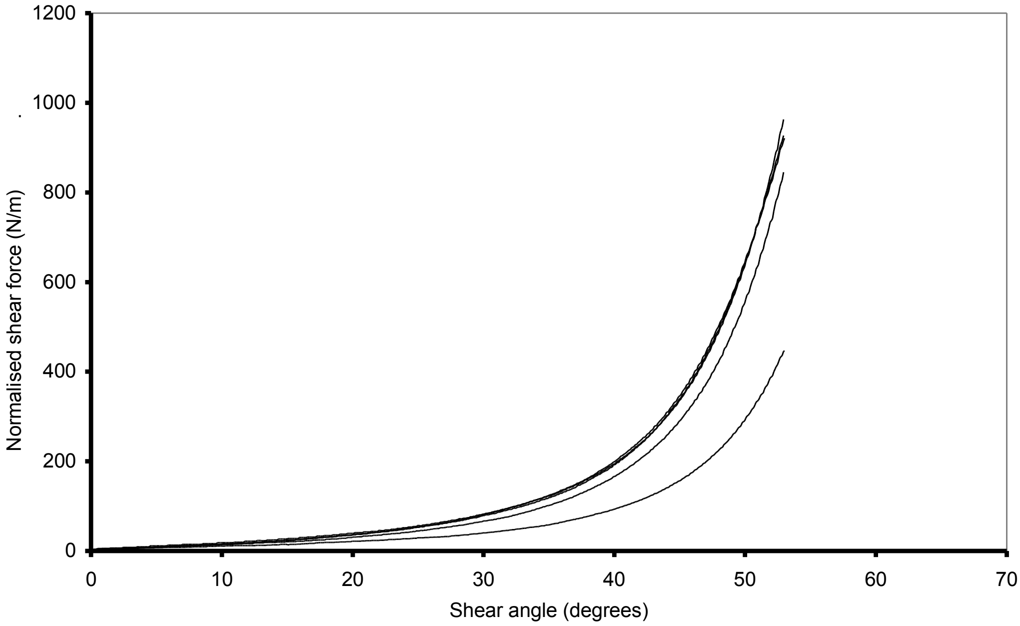

Figure 3.8: Twintex^{TM} 3 at 0N pre-tension

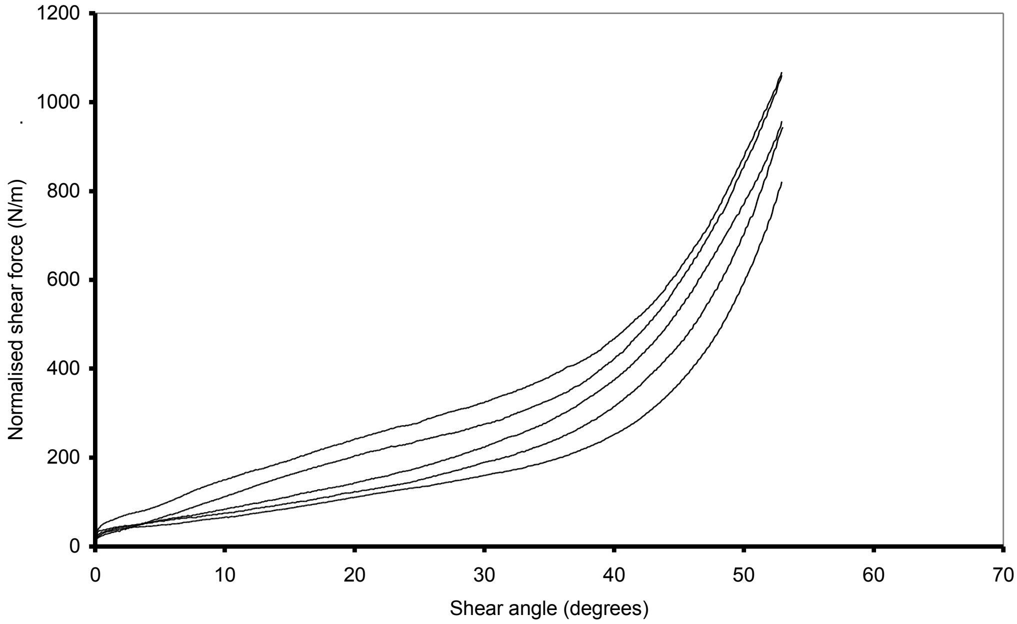

Figure 3.9: Twintex^{TM} 3 at 375N pre-tension

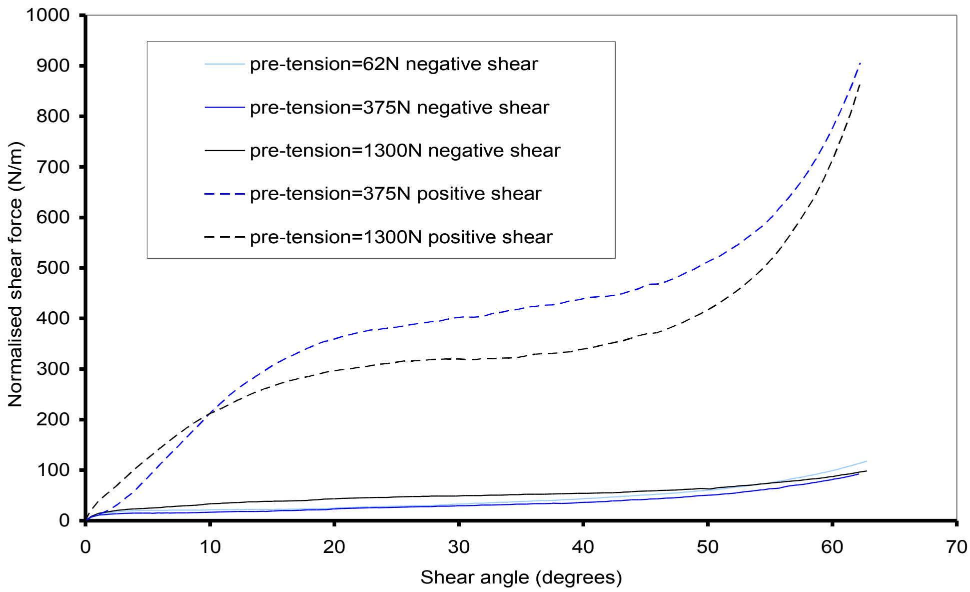

Figure 3.10: Comparison of EBXhd-936 tested at different pre-tensions, at negative and positive shear. Each curve is selected from 3 or 4 visually acceptable repeats, except for at 62N pre-tension, for which only one test was conducted.

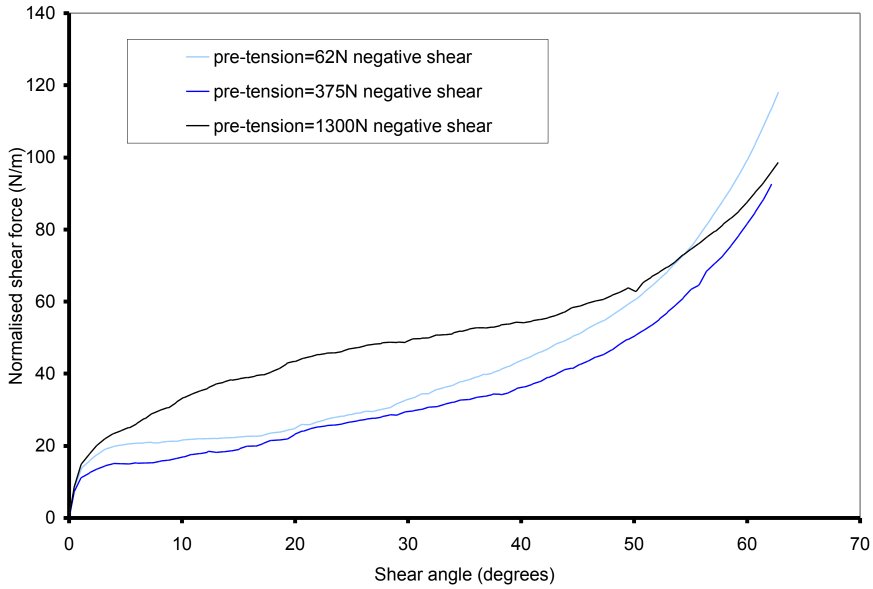

Figure 3.11: Comparison of EBXhd-936 tested at different pre-tension, at negative shear.

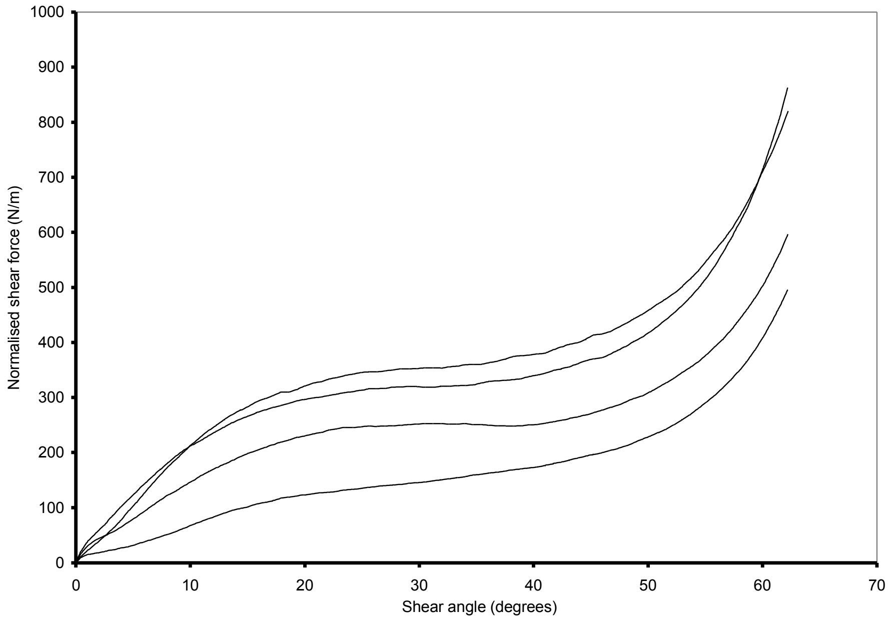

Figure 3.12: EBXhd-936 at 1300N pre-tension, sheared in the positive direction, demonstrating the large amount of scatter observed in testing non-crimp fabrics in the picture frame.

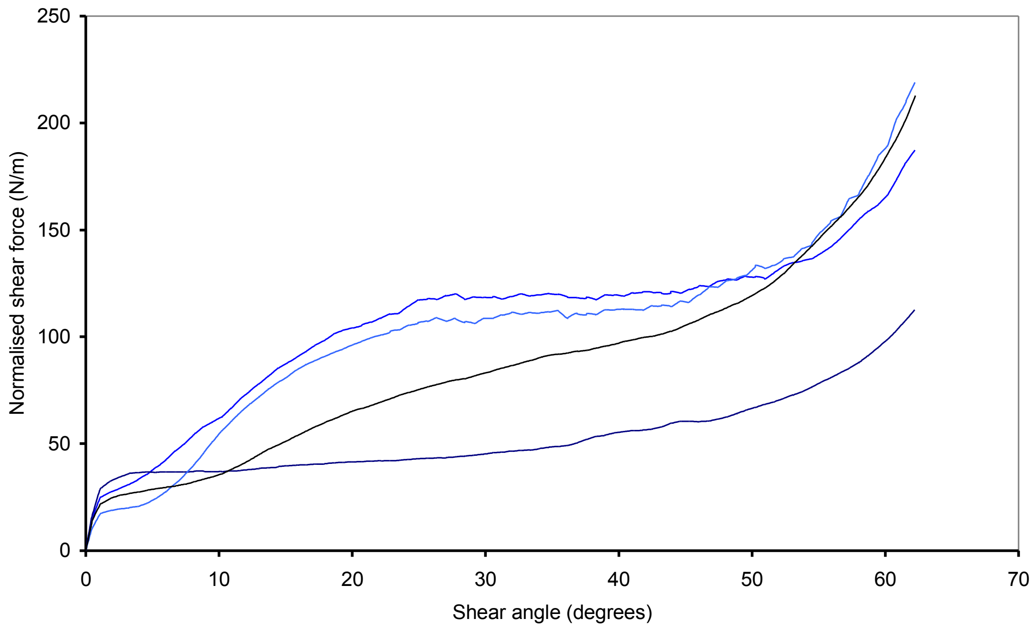

Figure 3.13: FGE 106hd at 1300N pre-tension, sheared in the negative direction, demonstrating the large amount of scatter observed in testing non-crimp fabrics in the picture frame.

3.4 Bias extension experiments

3.4.1 Experimental method

In the bias extension test the sample is cut so that its Y-axis is at an angle ϕ_0 to the fibre angles - this is the bias direction. The bias extension test is commonly proposed due to its improved repeatability compared to the picture frame test. This is because it is much more impervious to sample angle misalignment than the picture frame test. However, care must be taken with lengthways alignment, as this can cause a fairly large apparent discrepancy in the curves, so that it is prudent to ensure that the fabric is unsheared and the actual sample aspect ratio is recorded. Nonetheless, in contrast to the effects of angle misalignment in the picture frame test, which causes the test to record a combination of fabric shear and fibre extension or buckling, a lengthways misalignment in bias extension tests causes a simple shift in the shear response curves, so that ways of allowing for misalignment can be proposed.

Uniaxial test

An idealised uniaxial bias extension test is shown in Figure 3.14.

In order to induce shear deformation in orthogonal fabrics the sample dimension ratio $\lambda = h_0/w_0$ must be greater than 1. If the sample ratio is less than this constraint then some fibres will be clamped in both top and bottom clamps, placing them under tension. However, the ratio is normally constrained to $\lambda \geq 2$. This ensures that a larger proportion of the sample is at uniform shear, and also that the sample allows a reasonable amount of extension before full shear is reached. The illustrations in Figure 3.14 separate the samples into different shear regions marked A, B, and C, assuming idealised kinematics (i.e. pin-jointed behaviour):

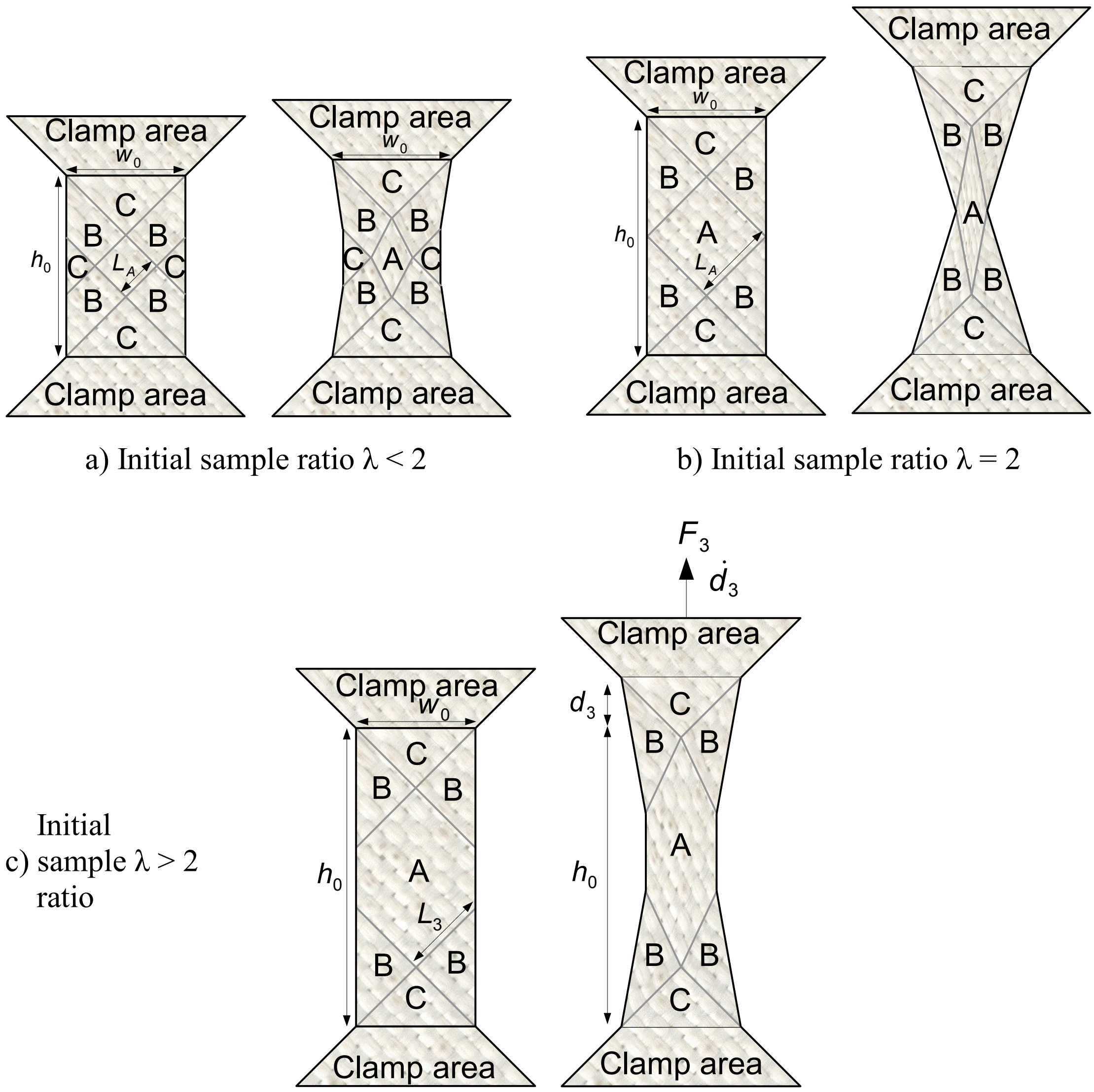

Figure 3.14: Idealised bias extension tests at different sample ratios, $\lambda = h_0/w_0$. Each test is shown before extension (left) and after (right).

A) shears similarly to material in picture frame test.

B) shears at a half the angle (and therefore half the rate) of material in A.

C) does not shear at all.

Considering that material in region A would reach locking angle first, it is desirable for the bias extension response to be dominated by fabric deformation in region A.

The constraints $\lambda > 1$ or $\lambda \geq 2$ have no relevance for non-orthogonal fabrics, for which sample dimension constraints also depend on the initial fibre angle ϕ_0. To allow for this a ϕ_0-dependant sample ratio parameter κ must be defined

$$\kappa = \lambda \tan \phi_0 = \frac{h_0}{w_0} \tan \phi_0 \tag{3.17}$$

For the most common case where $\phi_0 = 45°$, $\kappa = \lambda$, the sample aspect ratio. Thus, for consistency, all bias extension sample ratios will be quoted in terms of κ rather than λ.

The fabric ratio is subsequently constrained by $\kappa > 1$ or $\kappa \geq 2$ for a material with initial fibre angle $0° < \phi_0 < 90°$.

Given an ideal bias extension sample with initial fibre angle ϕ_0 and $\kappa \geq 2$, similar to that in Figures 3.14 b and 3.14 c, geometric constraints allow the cross-head displacement to be related to the shear angle:

$$d_3 = 2(\kappa - 1)L_3 \left(\cos\left(\phi_0 - \frac{\theta}{2}\right) - \cos \phi_0 \right) \tag{3.18}$$

or the shear angle in terms of displacement:

$$\theta = 2\left(\phi_0 - \arccos\left(\cos \phi_0 + \frac{d_3}{2(\kappa - 1)L_3}\right)\right) \tag{3.19}$$

Note that for $\kappa = 2$ these equations are equivalent to Equations 3.4 and 3.5 for the picture frame. In practice, unlike the picture frame test, using the crosshead displacement to calculate shear angle is likely to result in large errors, as the sample is not so constrained and other deformation mechanisms such as slip in the grips, tow slip, etc can dominate. It is therefore very important to directly measure the actual shear deformation during the test.

Figure 3.15 shows the two pairs of clamps that were used in the bias extension tests presented here. The first comprises of steel, serrated clamps which bolt together. Samples of approximately 90mm width with 50mm high tabs were used in these clamps - as for the picture frame, sample widths were determined by a fixed number of crossovers for woven fabrics and a fixed number of stitch length or widths for non-crimp fabrics. The tabs were inserted into the jaws with 10mm excess clear of the edge, which subsequently fed into the jaws as they were closed, causing the clamped fabric to crimp. It was found that using these clamps caused unnecessary difficulties when the simpler pair were adequate for use in testing dry textiles.

The second pair of clamps used consisted of flat, rubber-lined faces which were also bolted shut. This allowed easier clamping and release of the samples, as well as bigger sample dimensions. Orthogonal materials tested in these jaws were approximately 100mm wide, with 50mm tabs again. One material tested in these jaws, however, is a $\pm 30°$ non-crimp fabric, for which sample dimensions must be treated with care. A 90mm wide sample at $\kappa = 2$ contains a central shear region A (Figure 3.14) with area a little over 4000mm^2. From Equation 3.17, to test a $\pm 30°$ sample at $\kappa = 2$ with a similar central shear area would require sample dimensions of 70mm width and 242mm height in one shear direction, and 120mm width and

139mm height in the other shear direction. The clamps would not hold a width greater than 120mm.

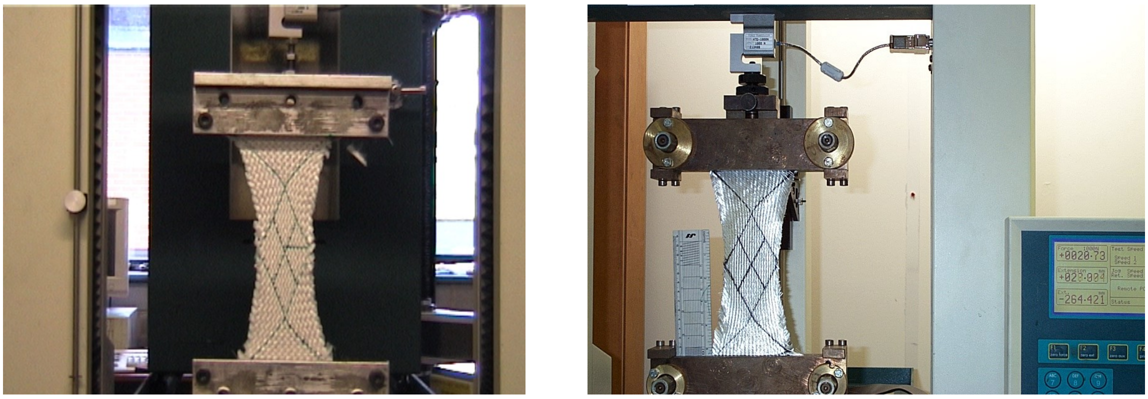

Figure 3.15: The two clamp types that were used in the bias extension tests presented. Left are the rubber-lined faces, right are the serrated faces.

Biaxial test

Note that no biaxial tests are presented in this thesis. The method is presented here for completeness only.

The gauge section in a bias extension test is defined as that part of the sample which experiences uniform shear across the full width of the sample. For most fabrics this is at ±45° to the fibre directions. The test can be carried out as either a uniaxial test, or a biaxial test.

A biaxial bias extension test, like that illustrated in Figure 3.16, *must* have a gauge section, so that its uniaxial-equivalent sample ratio parameter

$$\kappa = \frac{w_g}{h_g + 2h_{tab}} \tan\phi_0 \tag{3.20}$$

must be *greater* than two. In this case it is perhaps better to specify that the test must have gauge dimensions $w_g > 0$ and $h_g > 0$. The tabs must then have

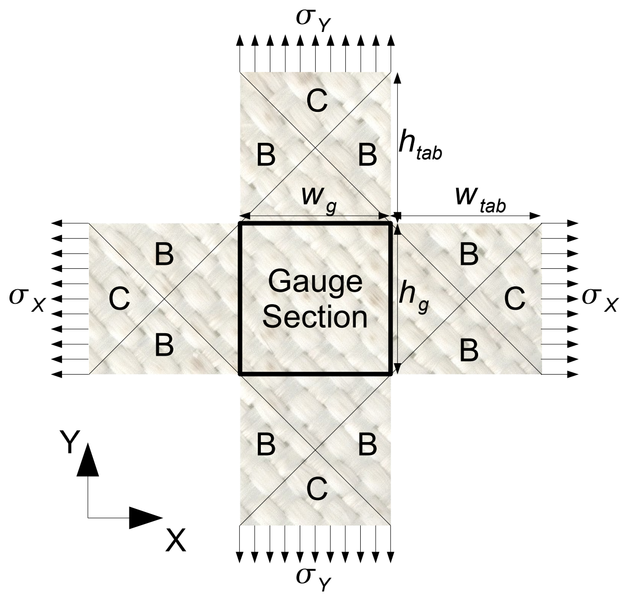

Figure 3.16: A generalised biaxial bias extension test with $\kappa = 3$.

$\kappa_{tab} \geq 1$, with the X-axis tabs having height h_g and the Y-axis tabs having width w_g. In order to allow the material to shear without fibre slip, the Y-axis extension should be geometrically matched to the X-axis extension (or vice-versa) according to pin-jointed behaviour constraints. This, together with the relative rarity of bi-axial testing machines, makes the test very difficult to perform, and it very rarely is. No biaxial test results are presented in this thesis.

Otherwise the biaxial test is very similar to the uniaxial, and the equations for θ and d_3 hold. The displacement d_3 in the biaxial bias extension test can be applied in either the X or the Y axes, bearing in mind that Equation 3.19 will always return a positive angle in the direction of d_3.

3.4.2 Assumptions and limitations

Several assumptions affect the validity of the method for measuring the trellis shear response of the material. The method is only valid while the material deforms according to idealised deformation. Deviation from the idealised pin-jointed deformation is dependant on many factors including the material, the sample size and ratio. As a result it is important to monitor the test for conformance. In order to do this, a digital video was taken of the tests and analysed using purpose-written code (described in Section 3.4.3). There are several ways in which the deformation can deviate from the idealised case.

Misalignment

Despite being relatively impervious to angular misalignment, the response is fairly sensitive to any lengthways misalignment caused while clamping the sample, which alters the sample aspect ratio. The same effect can be caused by any pre-shearing of the material, so that the zero-shear sample ratio is different to the perceived ratio cut out. Similar slack in generic tensile tests is often allowed for by setting a pre-load in the test machine, so that data is not recorded until the measured load exceeds the set pre-load. However, the low loads caused by fabric shear, the low gradient of the curves at lower extensions, and a high ambient load "noise" at the start of the test renders this method unsuitable. Such factors, however, should only cause a shift in the curves rather than a change in their shape, so that the visual analysis can also be used to allow for them.

Fibre slip

At a point where shear deformation forces become too high, fibre slip sets in. The transition from pure shear to pure slip deformation regimes is gradual, so that a cut-off point has to be set after which the test is deemed non-ideal. This may a good indicator, however, of the fabric locking angle, so that the angle at which the deformation leaves ideal kinematics tends to tally well with the angle at which the same fabric wrinkles in drape tests.

Fibre slip can occur both along the length of the tow and transverse. Lengthways slip occurs due to tension overcoming the friction holding the tow in the textile. This is not so much of an issue in woven fabrics, in which the crimp develops increasing frictional resistance with increasing tension. Transverse slip occurs where the tow under tension experiences a sudden change in angle. This effect has been modelled in forming by Lai and Young [30], but applies equally in the bias extension test. In essence, it is the result of the need for a compaction force to counter the net transverse force caused by a bent tow under tension. In fact, the first form of slip observable in many bias extension tests is exactly of this form, occurring around the tip of the "C" areas, causing them to elongate. This can be observed in both samples presented in Figure 3.15.

Non-ideal shear distribution

Finally, the fabric can deform by pure shear, and yet the shear distribution vary from the ideal distribution. This may however cause an overall increase in predicted shear deformation energy. Some factors that might cause a non-ideal shear distribution include pre-shear due to handling, and other deformation energy factors not allowed for in the idealised case, such as fibre bending. To demonstrate this effect a spreadsheet bias extension simulation has been created that allows the nodes along the centre line in the central deformation region A to have varying separation. Some results are shown in Figure 3.18.

In the spreadsheet the relative positions of all the nodes along the centre line of region A (which runs along the bias direction) are manually set, as well as those along the clamp edges. The relative node positions along the clamped edges remain fixed, from which it becomes apparent that all the nodes in the top and bottom regions C remain fixed in relation to each other (hence no shear can occur there). However, the relative x and y positions of consecutive nodes along the centre line of region A can be varied within the constraints of pure trellis shear — that the node spacing along the fibre directions remains a constant. Given these nodes, then, all remaining node positions can be calculated by geometric constraints. The entire sample remains on the x-y plane, so that, given two adjacent node positions $\bar{p}_{0,n}$ and $\bar{p}_{0,n+2}$ on Figure 3.17, along the clamp edge or the centre line of region A, the solution for the next node, being constrained to a distance s_{node} from both $p_{0,n}$ and $p_{0,n+2}$, simplifies from the generic case to

$$\left\{ \begin{array}{c} x \\ y \end{array} \right\}_{1,n+1} = \frac{1}{2} \left\{ \begin{array}{c} x_{0,n} + x_{0,n+2} \\ y_{0,n+2} + y_{0,n} \end{array} \right\} + \frac{f_1}{2} \left\{ \begin{array}{c} y_{0,n+2} - y_{0,n} \\ x_{0,n} - x_{0,n+2} \end{array} \right\} \tag{3.21}$$

$$\text{where } f_1 = \sqrt{\frac{4s_{node}^2}{(y_{0,n} - y_{0,n+2})^2 + (x_{0,n} - x_{0,n+2})^2} - 1}$$

Given the positions of the nodes along the clamp edges, which, with Equation 3.21 gives the nodes in region C, and also given the node positions along the centre line

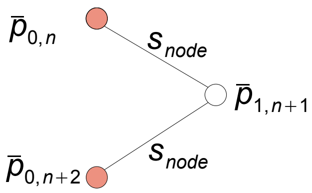

Figure 3.17: Adjacent nodes on a 2D surface. The nodes on the left have been fixed, and the node on the right is constrained to a distance of s_node from those on the left.

of region A, all other node positions can subsequently be calculated. The sum of the y-axis separation of these centre nodes yields the total sample extension.

However, even this simple demonstration does not cover the possible scenarios of pure-shear deviation from ideal deformation. There could for example be some pre-shear (uniform or otherwise) in the sample before clamping, so that areas of sheared material remain fixed in their sheared state in the regions C.

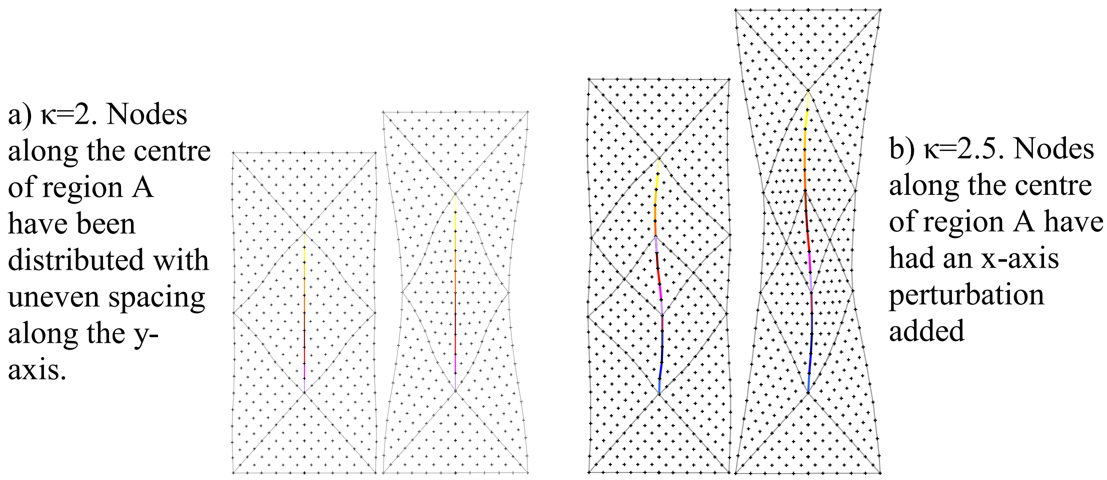

Figure 3.18: Two non-ideal pure shear bias extension test simulations, each before (left) and after extension (right).

3.4.3 Test monitoring

To measure the cut-off point for ideal kinematics, photographs can be taken periodically through some tests. Prior to the test, the samples are marked along the borders of the different shear regions A B and C, as well as a central cross - all lines follow tow directions. The photographs are then analysed for central shear angle and compared to expected shear angle. At a point at which measured shear angle differs substantially from expected, the cut-off point for the shear test validity is set. The maximum angle measured is indicative of the locking angle.

It was estimated that during the course of a test only about seven to ten photographs can be taken, which subsequently require laborious analysis to measure the shear angle, measure the extension, and calculate the expected shear angle. To improve on this process, for later tests a digital video was taken of the tests. C++ code was written to automatically analyse the shear angle and extension at each frame, requiring only the original markings to be highlighted on the starting frame. This gave a lot more information about the deformation field, as well as allowing less errors when measuring extension and shear angle than when doing so by hand. Finally, it also allows any initial pre-shearing of the sample to be corrected for.

Figure 3.19 illustrates the graphical user interface for the program, which was based on the Microsoft® Foundation Classes (MFC). The figure shows the program analysing a black twintex sample with white markings, with the lines it tracks displayed in green, and the start, end and crossovers of the lines displayed as red crosses.

The use of the software is shown in the flow diagram in Figure 3.20. In all

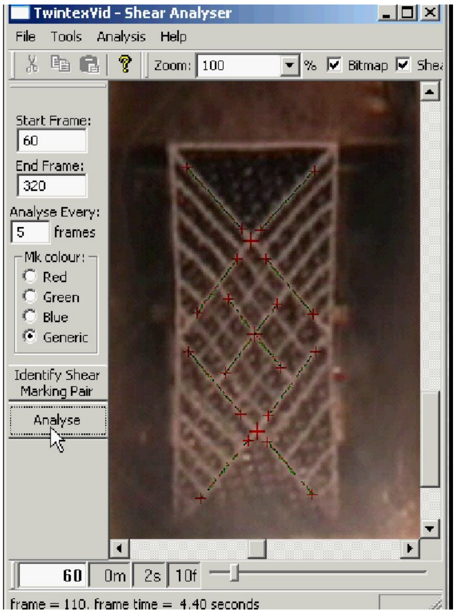

Figure 3.19: The user interface for the bias extension automated video analysis software

results presented in this thesis, the test was analysed in every frame (25 frames per second). It is important to note from Figure 3.19 that the lines' starting and end points can be anywhere. In the top crossover being tracked, they start and end above the crossover, so that the crossover is outside the limits of the lines. In the centre crossover, however, the line start and end points have been indicated so that the crossover point is approximately half way along the limits. It would be just as feasible to have the crossover point on one of the lines but beyond the other. It is also important to note that the shear angle measured will vary depending on which side of the crossover the lines are taken. To understand this, consider again the top crossover indicated in Figure 3.19. The crossover is tracked twice: Once from the two lines above, and once from the two lines below. As the two lines above the crossover are on the edge of region C (using the notation introduced in Figure 3.14), they should record no shear during the test. However, the two lines *below* the same crossover are on the edge of region A, and thus should measure the full theoretical shear angle. If the two lines to the left or the right of the crossover had been tracked, they should measure a half of the full theoretical shear angle.

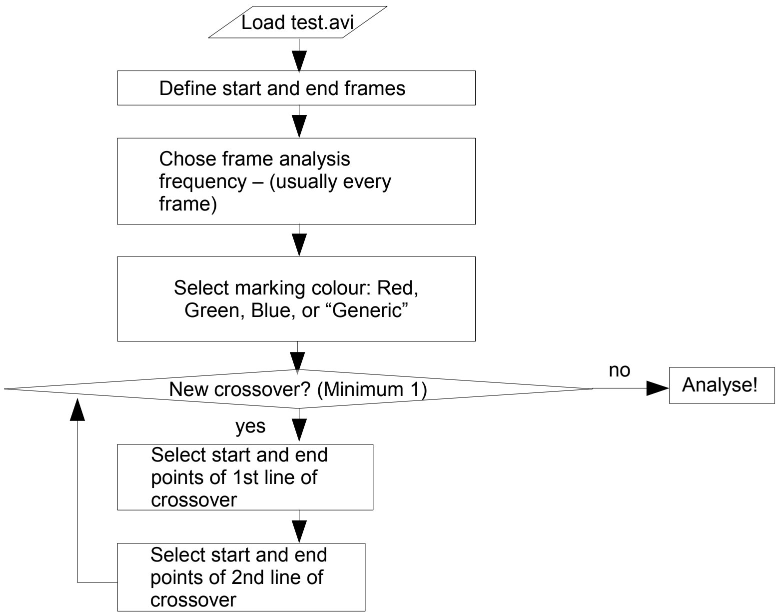

Figure 3.20: Flow diagram showing the user sequence for analysing a bias extension video

The program tracks the crossovers indicated by the user according to the flow diagram indicated in Figure 3.21. The figure explains how the line is found if it is marked as being red, green, or blue. In the "Generic" choice, the program scans the search line at each pixel twice: On the first scan it calculates an average value of red, green, and blue; on the second, it finds the pixel for which the sum of the absolute differences of the r, g and b values from the averages is greatest. Typically, each line being tracked is between 20 and 50 pixels long, giving 20 to 50 search points. As explained, the "search line" is set perpendicular to the most recent position of the line being tracked, and the pixel most like the line being tracked along the search line is noted in what is essentially an edge finding algorithm. The resolution of the edge finding algorithm is kept at a one pixel level, due to the existence of many "edges" in the non uniform texture of most textiles. A new pixel to match the line definition is stored for each pixel along the old line, and the new line is determined by a least squares fit through the new points.

The output from the program is a series of three points for each crossover at each frame number analysed.

The program writes to a tab delimited file, recording for each frame number analysed three coordinates (the farthest point on each line and the intersection) and a shear angle for each crossover. This is pasted into a Microsoft® Excel spreadsheet, which allows a full analysis to be made of the bias extension test. Consider Figure 3.19. The top and bottom line pairs are at the edge of areas C, which will not shear while the bias extension specimen deforms ideally. The top crossover, then, initially extends at exactly the same rate as the test machine crosshead. A straight line fit to the plot of this point against time (as calculated from frame number) allows the spreadsheet to calculate two important values. The first, corresponding to the intersection of the best fit line with the x-axis, allows the spreadsheet to determine the test start point (the camera is activated before the test commences). The second, corresponding to the gradient of the best fit line, when compared with the extension rate of the test, allows the spreadsheet to accurately determine the scale of the video in mm/pixel. As the scale is determined not from a single measurement but from several tens or hundreds of data points, this should be a more reliable value than that determined from placing a reference distance next to the test piece.

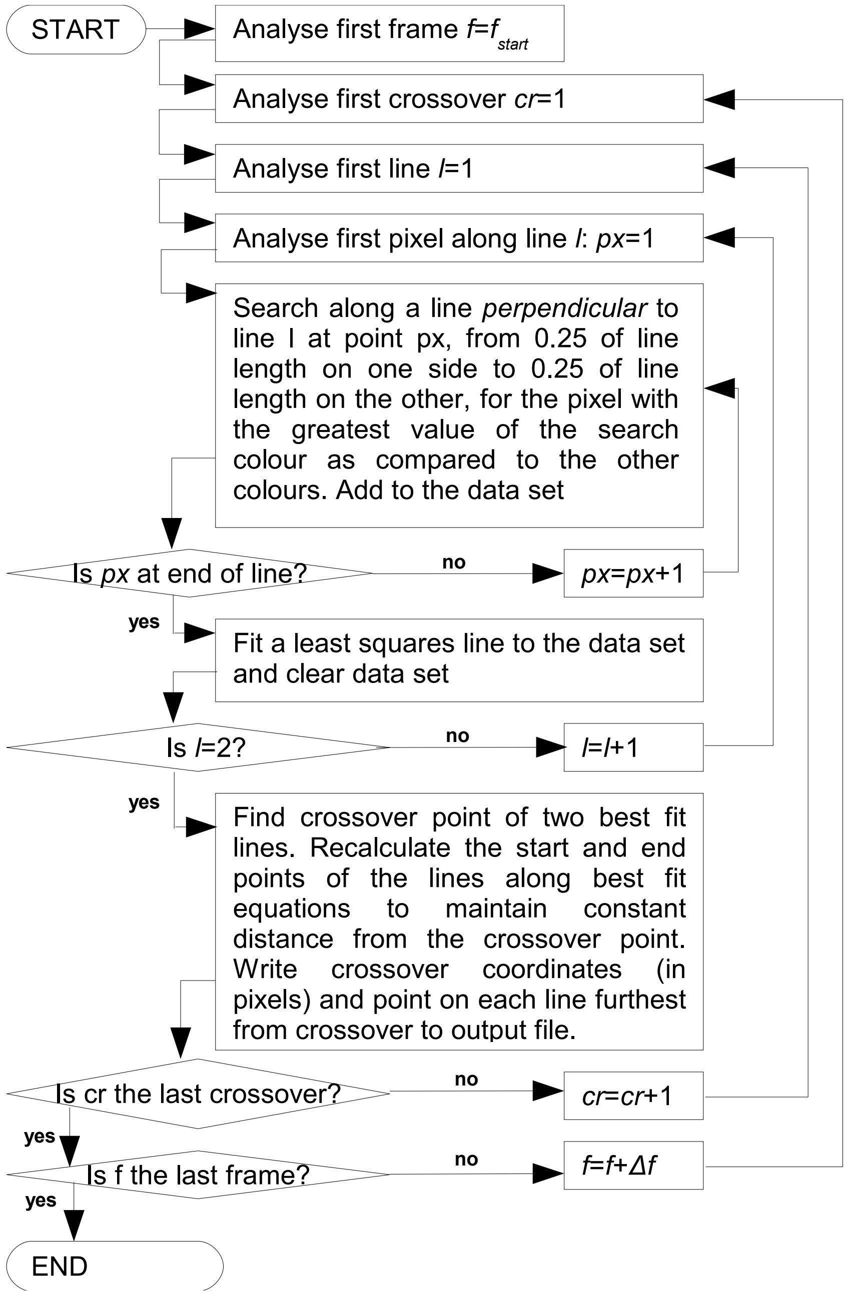

Figure 3.21: Flow diagram showing the sequence used by the program to keep track of marked crossovers on a bias extension video. f denotes the current frame, cr the current crossover, l the current line, px the current pixel along the line l, Δf the frame analysis frequency (see Figure 3.20)

The spreadsheet can also of course calculate the local shear angle at each crossover, and this value can be compared with the expected angle to determine the locking angle of the textile, and how much of the test corresponds to pure and idealised shear. Finally, the plot of the shear angle against extension allows one more factor to be calculated. If the sample is at all pre-sheared through handling or due to its own weight as it hangs vertically in the test machine, it can shift the curve a little along the x-axis. Due to the shape of the shear curves, this can correspond to a very large apparent unrepeatability in the measured shear response. The initial very low load gradients also preclude the use of a set pre-load to match the curves. However, any pre-shear can be noted in the measured vs expected shear angle curves as a *shift* of the ideal linear portion. Thus, to correct for pre-shear, the x-intercept of a linear fit of the measured vs expected shear angle curves can be used to shift the shear force curves appropriately.

It is very important to measure and understand the limits of the bias extension test in terms of shear deformation. Beyond the point at which measured shear substantially differs from idealised pin-jointed shear, the shear behaviour of the textiles is no longer being measured. Instead, a combination of shear and slip is recorded. Thus, the graphs are only valid as shear response curves up to the point at which the ideal shear angle corresponds well to the actual shear angle. The shear response graphs are presented against theoretical shear, which corresponds to the measured shear for the valid proportion of the graph. It is however very important to remember that these graphs may not be valid shear response values beyond shear angles substantially less than 70°, depending on the material. The measured shear allows the cut off point for shear response validity to be determined.

3.4.4 Normalisation of results

Normalisation of results for a bias extension test is not as straight forward as that for the picture frame. Bias extension tests with the same κ value but in a different scale can be compared by dividing the extensive force by a characteristic length (say, L_3 or w_0 in Figure 3.14c). However, the non-uniform shear distribution means that results from different ratio tests or comparison with picture frame results requires more careful treatment. Several approaches to a more robust bias extension normalisation procedure are presented here. Because they all take different assumptions, it is worthwhile to compare and contrast them. The relative merits of these approaches to normalising bias extension data will be examined in Section 3.4.5 and discussed in Section 3.5.

3.4.4.1 Energy normalisation method

Energy arguments similar to those developed for the picture frame test can also be used to normalise the bias extension test. However, the more complex deformation distribution in the bias extension test makes for a more involved analysis. In order to normalise the bias extension test using energy arguments the energy contributions from the different shear regions in the sample must be separately accounted for. The approach is therefore only valid when the observed bias extension deformation is similar to the idealised bias extension test.

First, geometric constraints reveal that, for $\kappa \geq 2$ (Figure 3.14 c), the areas of regions A and B are:

$$A_A = L_3^2(2\kappa - 3)\sin 2\phi \tag{3.22}$$

$$A_B = 2L_3^2 \sin(\phi_0 + \phi) \tag{3.23}$$

so that the initial area ratio of the regions is:

$$A_B(\phi_0) = \left(\frac{2}{2\kappa - 3}\right) A_A(\phi_0) \tag{3.24}$$

Also,

$$\theta_B = \frac{\theta_A}{2} \tag{3.25}$$

where θ_A and θ_B are the shear angles in regions A and B respectively. [Where a subscript is ommited for the bias extension test, the shear angle θ can be assumed to be referring to that in the centre region A, $\theta = \theta_A$.] Differentiating Equation 3.25 gives the relative angular shear rates of the regions:

$$\dot{\theta}_B = \frac{\dot{\theta}_A}{2} \tag{3.26}$$

Now the picture frame extensive power definition, Equation 3.6, is equally true for the bias extension test. Differentiating Equation 3.18 gives $\dot{d}_3$,

$$\dot{d}_3 = \dot{\theta} \sin\left(\phi_0 - \frac{\theta}{2}\right) (\kappa - 1) L_i \tag{3.27}$$

so that the bias extension test equivalent to Equation 3.8 is:

$$\dot{d}_3 = (\kappa - 1) k_1 L_3 \tag{3.28}$$

where k_1 is defined in Equation 3.9. This leads to the equivalent to Equation 3.10:

$$P_3 = (\kappa - 1) k_1 F_3 L_3 \tag{3.29}$$

The two-phase shear distribution of the bias extension test means that the shear power relationship has *two* parts. Given Equation 3.12 for the material at a given shear angle θ, and bearing in mind the amount of material in the different shear regions given in Equations 3.22 and 3.23 , the power for the bias extension sample to deform can be written as

$$P_3 = L_3^2 \sin 2\phi_0 \left((2\kappa - 3)\psi_A(\theta) + 2\psi_B(\theta)\right) \tag{3.30}$$

where ψ_A and ψ_B are the shear power per unit initial area for regions A and B respectively (see Equation 3.12), and are functions of θ and $\dot{\theta}$.

Assuming that these power terms are directly proportional to the local shear rates $\dot{\theta}_A$ and $\dot{\theta}_B$, and given the relative shear angles and rates in regions A and B in Equations 3.25 and 3.26 , ψ_B evaluated at (θ) can be related to ψ_A at $\left(\frac{\theta}{2}\right)$:

$$\psi_B(\theta) = \frac{\psi_A(\theta/2)}{2} \tag{3.31}$$

Substituting Equation 3.31 into 3.30 gives

$$P_3 = L_3^2 \sin 2\phi_0((2\kappa - 3)\psi_A(\theta) + \psi_A(\theta/2)) \tag{3.32}$$

and equating this $P3$ with Equation 3.29 and rearranging gives

$$\frac{\psi_A}{k_2} = \frac{\kappa - 1}{2\kappa - 3}\frac{F_3}{L_3} - \frac{\psi_A(\theta/2)}{(2\kappa - 3)k_2} \tag{3.33}$$

where the left hand side is the same as that in Equation 3.16 — the normalised force. Note, however, that the right hand side of the equation includes the normalised force at $\theta/2$, so that in order to *calculate* the normalised force an iterative scheme must be followed.

The iterative scheme proposed is very simple. An initial approximation for ψ_A is taken as

$$(\psi_A(\theta))_{i=0} = \frac{\kappa - 1}{2\kappa - 3}\frac{k_2 F_3}{L_3} \tag{3.34}$$

This can be used to evaluate subsequent iterations

$$(\psi_A(\theta))_{n+1} = \frac{\kappa - 1}{2\kappa - 3}\frac{k_2 F_3}{L_3} - \frac{\left(\psi_A\left(\frac{\theta}{2}\right)\right)_n}{(2\kappa - 3)} \tag{3.35}$$

until the solution converges.

Alternatively, if an nth order least squares fit is taken for the F_3/L_3 vs θ curve,

$$\frac{F_3}{L_3} = \sum_{i=0}^{n} a_i \theta^i \tag{3.36}$$

then an nth order ψ_A/k_2 curve,

$$\frac{\psi_A}{k_2} = \sum_{i=0}^{n} b_i \theta^i \tag{3.37}$$

can be derived. Substituting Equations 3.36 and 3.37 into Equation 3.33, rearranging, and comparing θ^i parameters gives the b_i values in terms of the a_i values:

$$b_i = \left(\frac{\kappa - 1}{2\kappa - 3 + 2^{-i}}\right) a_i \tag{3.38}$$

The normalised extensive force curve is therefore approximated by

$$\frac{\psi_A}{k_2} = (\kappa - 1)\sum_{i=0}^{n}\left(\frac{a_i \theta^i}{2\kappa - 3 + 2^{-i}}\right) \tag{3.39}$$

Both methods will be presented and compared.

3.4.4.2 Gauge method - Stress tensor rotation

This approach to normalising the material response from a bias extension test, adapted from that suggested by Sharma et al. [57], is simple and is more consistent with materials testing in general. *However, it must be remembered that these methods were developed for engineering shear, which is a different quantity to trellis shear.*

The strain for a gauge section in which the shear is uniform is measured in order to calculate θ, and the measured stress tensor is then transformed into the appropriate coordinates. This approach is relevant in uniaxial tests where κ is greater than 2, as well as in biaxial tests, for example those in Figure 3.14c or Figure 3.16. Figure 3.16 illustrates the gauge section (a uniaxial test would be similar, without the horizontal tabs) and the global X and Y axes. In these cases the applied extensive forces parallel to the X and Y axes are the same at the clamp edges as they are at the gauge section boundaries. As deformation in the gauge section is assumed to be uniform, the resulting stresses over the whole of the gauge section can also be assumed to be uniform.

The principal applied stresses are in the X and Y axes, so that the stress tensor can be written as

$$\sigma_{ij} = \begin{bmatrix} \sigma_{XX} & 0 \\ 0 & \sigma_{YY} \end{bmatrix} \tag{3.40}$$

This can be rotated by angle α:

$$\sigma'_{ij} = \begin{bmatrix} \sigma_{XX}\cos^2\alpha + \sigma_{YY}\sin^2\alpha & (\sigma_{YY} - \sigma_{XX})\cos(\alpha)\sin(\alpha) \\ (\sigma_{YY} - \sigma_{XX})\cos(\alpha)\sin(\alpha) & \sigma_{XX}\sin^2\alpha + \sigma_{YY}\cos^2\alpha \end{bmatrix} \tag{3.41}$$

The angle α is defined so that the rotated X'-axis is parallel with one of the fibre directions (Figure 3.22):

$$\alpha = \frac{\pi}{2} - \phi_0 + \frac{\theta}{2} \tag{3.42}$$

Estimates of the applied stress depend on the material thickness, which is very hard to estimate. Because of this it is better to refer to the "line force", the force

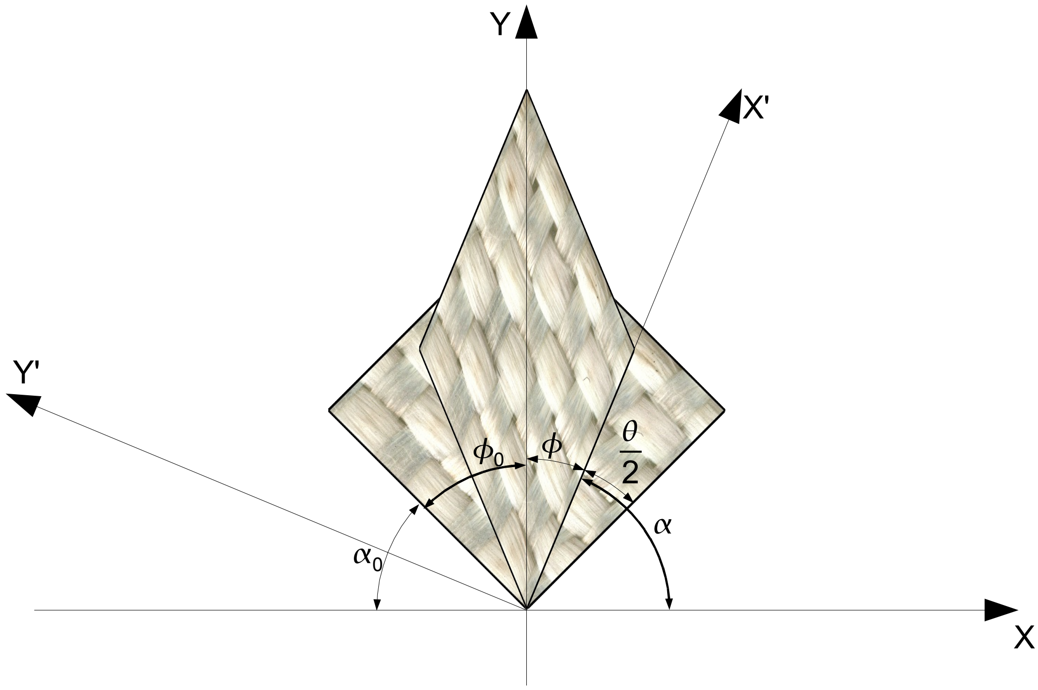

Figure 3.22: Global and rotated orthogonal axes. The value of rotation, α, depends on the shear angle, θ.

per unit length:

$$N = \sigma t \tag{3.43}$$

where t is the current thickness of the material. As this treatment assumes that stress and deformation (and therefore thickness) are uniform throughout the gauge section at any given deformation state, Equations 3.41 and 3.43 can be combined to find

$$N_L = N_X \cos^2 \alpha + N_Y \sin^2 \alpha \tag{3.44}$$

where $N_{subscript}(N/m)$ is the line force, subscripts X and Y refer to the global X and Y directions, and L refers to the fibre direction: hence N_L is the normalised fibre tension. Note that N_X and N_Y are normalised by the material dimensions they act on, $h_g(\theta)$ and $w_g(\theta)$ respectively, which are dependent on shear angle.

Similarly, Equations 3.41 and 3.43 also imply

$$N_s = (N_Y - N_X) \cos \alpha \sin \alpha \tag{3.45}$$

where $N_s(N/m)$ is the normalised shear force acting along the fibre directions. This shear force can be directly compared with that of Equation 3.1 derived for the picture frame test. Finally, in the case of a uni-directional bias extension test, the value N_X is set to zero so that the normalised shear force N_s becomes

$$N_s = N_Y \cos \alpha \sin \alpha \tag{3.46}$$

3.4.4.3 Gauge method - picture frame equivalence

The approach outlined in Section 3.4.4.2 gives rise to a third approach, which is by far the simplest. This attempts to be more sensitive to the difference between engineering shear and fabric trellis shear.

Considering the gauge section only, the material can be seen to be deforming by pure trellis shear, very similarly to that in the picture frame test. The method relies on the assumption that where a material is deforming uniformly and only by trellis shear, the sample response is not dependant on the shape, but on the initial volume of the sample. Furthermore, assuming that a given material at a given shear angle and shear rate has a uniform thickness T that is independent of the sample shape, the shear response is therefore only dependant on the initial *area* of the sample. Other differences that are not taken into account are the different boundary conditions and tensile stresses generated by the different test methods. If, therefore, the equivalent picture frame test of the same material with an initial sample volume equal to that in the gauge section can be specified, then the measured X and Y axis forces should also be the same.

Consider a picture frame test similar to those in Figure 3.4, but with side length L_g such that the sample has the same area as that of the gauge section in Figure 3.14c. Note also, that for a biaxial equivalent, a force would be exerted on the side hinges along the X axis. The initial area of the bias extension gauge section is

$$A_g(\theta_0) = \left(h_0 - \frac{2w_0}{tan\phi_0}\right) w_0 \tag{3.47}$$

and using Equation 3.17, h_0 can be substituted to give

$$A_g(\theta_0) = (\kappa - 2)\frac{w_0^2}{\tan\phi_0} \tag{3.48}$$

The initial area of the picture frame sample, on the other hand, is given by

$$A_0 = L_g^2 \sin 2\phi_0 \tag{3.49}$$

Equating the two and rearranging gives

$$L_g = \sqrt{\frac{1}{2}(\kappa - 2)} \left(\frac{w_0}{\sin \phi_0} \right) \tag{3.50}$$

The equivalent picture frame experiment would have side length as calculated using Equation 3.50, so that the picture frame shear force is calculated as

$$N_s = \frac{F_Y}{2L_g \cos \phi} - \frac{F_X}{2L_g \sin \phi} \tag{3.51}$$

where θ is calculated using Equation 3.19 and the method is valid for as long as the material in the gauge section follows idealised pin-jointed deformation.

The biaxial treatment has only been included here for completeness, as no biaxial test results are presented in this thesis. It does, however, give rise to the approach for the uniaxial test. The differences give rise to a simpler solution.

The uniaxial bias extension test has no force in the X direction, $F_X = 0$. As a result, the section to be considered must be w_0 wide, but can have a *range* of heights greater than 0. The restraints on the gauge section dimensions are that it must be a segment of the sample experiencing a uniform stress field with known boundary stresses, so that in the uniaxial test the height of the gauge section for normalisation purposes could be any value up to h_g,

$$0 < h'_g \leq h_g \tag{3.52}$$

This suggests that the bias extension force, when plotted against *shear angle*, is independent of the gauge section height. It is therefore *only* dependant on the sample width w_0, leaving the normalised extensive force as

$$N_d = \frac{F_Y}{w_0} \tag{3.53}$$

where the normalised shear force is calculated similarly to Equation 3.1.

This method works to some extent for initially orthogonal fabrics. However, a little more thought is required for non-orthogonal fabrics. In these cases the sample dimensions for a given κ and L_3 vary according to the shear direction being tested. Thus, if the sample is only being normalised by the sample width, it would be normalised by different amounts according to the shear direction. A better approach would be to take account of the number of crossovers across the width - this is a constant regardless of shear direction. A length value representative of this is the width at $\phi = 45°$, which is to say, $\sqrt{2}L_3$.

3.4.5 Results

Table 3.3 outlines the materials that were tested using the bias extension method.

Table 3.3: Materials tested for shear response according to the bias extension test method

Material name	Material	Description
Bentley mat1	E-glass	±30° non-crimp fabric, double stitched with a (+1,0,-1,0) stitching pattern.
Bentley mat2	E-glass	3D E-glass woven fabric from 3Tex
FGE 106hd	E-glass	950gm^{-2}, ±45° non-crimp fabric from Formax, with a tricot (+1,-1) stitching pattern, stitch length 2.5mm
FGE 106hd:1.65 (special)	E-glass	950gm^{-2}, ±45° non-crimp fabric from a tricot (+1,-1) stitching Formax, with pattern, stitch length 1.65mm
FGE 106hd:5 (special)	E-glass	950gm^{-2}, ±45° non-crimp fabric from Formax, with a tricot (+1,-1) stitching pattern, stitch length 5mm
Twintex^{TM} 1	Co-mingled E-glass/PP	1816gm^{-2} Twintex^{TM} unbalanced 2/2 twill weave fabric
Twintex^{TM} 3	Co-mingled E-glass/PP	Twintex^{TM} balanced plain weave fabric 1816gm^{-2} fabric

3.4.5.1 Comparing the energy normalisation techniques - Iterative vs least squares

The two suggestions for solving Equation 3.33 offer advantages and disadvantages. The results presented here are chosen to highlight such advantages and disadvantages. The two curves presented in Figure 3.23 have been generated using the two solutions outlined by Equations 3.34 to 3.39 .

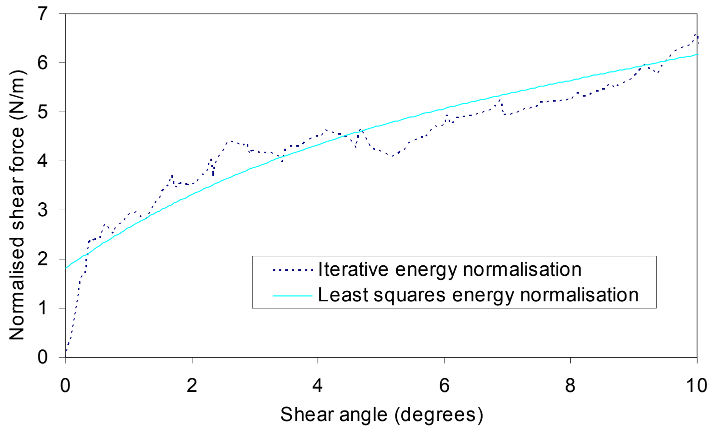

Figure 3.23: Advantages and disadvantages of the two energy minimisation solutions are highlighted at the beginning of this curve. The material tested is the Twintex^{TM} 3 fabric, for a $\kappa = 2$ sample.

To ensure a good fit, the sixth order fit for the curve used in Figure 3.23 has not been forced to pass through the origin. Whilst this is inaccurate at the start, it is possibly more physically appropriate, as the jump is caused by frictional energy losses, so that if the test had started at negative shear the jump would not have been observed. The multiple use of previous data in the iterative solution causes sudden jumps in raw force (such as those caused by the discretisation of the load cell or that at the start of the curve) to propagate up the curve. This can be seen in the jagged nature of the iterative curve, caused by sudden jumps in the digital load output. It can also be observed in the way that it oscillates first above and then below the fit curve, caused by the sudden increase in load at the onset of shear.

Other than the differences caused by these limitations, however, the two approaches agree closely for all materials tested. This confirms that a high enough order was chosen for the fitted curve approach, and also that numerical errors are not significant in the iterative process.

3.4.5.2 Shear angle curves

The bias extension tests conducted proved to have poor repeatability. However, the use of the video analysis to offset the curves according to the predicted angle vs measured angle offsets improved repeatability. After visually calculated offsets had been corrected, curves were offset a second time to coincide at the average value at a given force - the curves mostly coincided perfectly for angles below the locking angle. It is important to present the results of the video analysis software, to understand the range of applicability of the bias extension tests.

The angles measured appear to be subject to a lot of noise, as can be seen in Figure 3.24. This is caused by the fitted line being affected by outlying points, however, if a frame by frame angle measurement was made by hand, a similar error would be observed. By having such a density of measured data, the average can be taken as a more reliable measure than the few points that can be measured manually, with the scatter providing a useful indicator of confidence limits of the measurement method. Therefore the results are presented as a moving average with standard deviation error bars in the following graphs.

One thing that can be examined is the effects of the sample aspect ratio on the

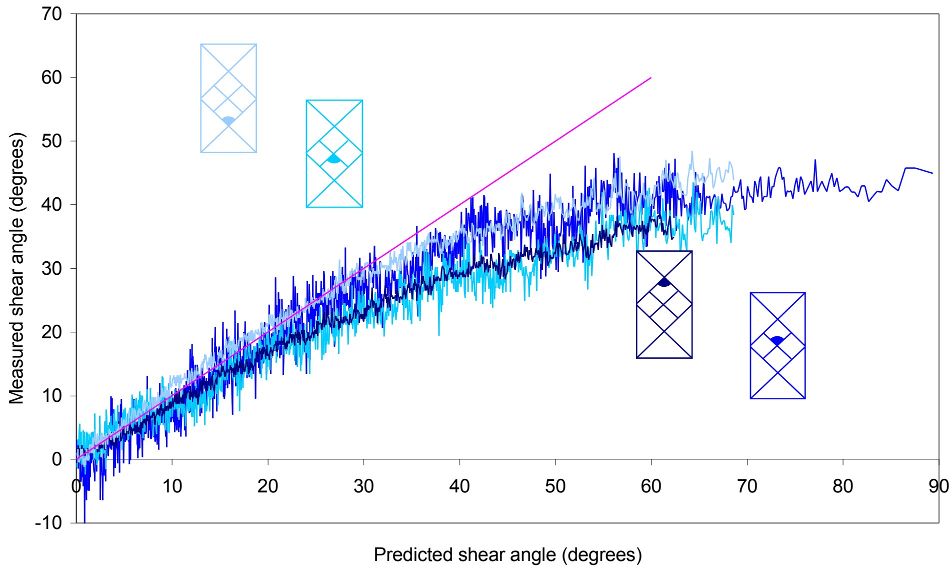

Figure 3.24: Angles measured from video taken of a bias extension test of Twintex^{TM} 1 with sample ratio factor $\kappa = 2$.

angles. Figures 3.25 to 3.27 demonstrate the differences. It is apparent that the aspect ratio, within the range tested, have minimal effect on the locking angle, and the onset of non pin-jointed behaviour. The tests appear to be relevant for the first 35 degrees, with the sample locking at just over 40 degrees. Observations conclude that the first cause of the onset of non-linear behaviour is transverse fibre slip at the tips of the C regions. Secondly the material begins to buckle, and finally it rips apart as the tows pull out of the textile. This does not include the effects of non-uniform behaviour, as described at the end of Section 3.4.2

Examination of the figures also shows the variation of shear angles measured at different regions, within the central shear area. This is typically 2-5°, but can be as much as 10°. Shear angle figures for other materials and at other ratios can be found in Appendix C. This includes 9 different results for Twintex^{TM} 3 at $\kappa = 2$.

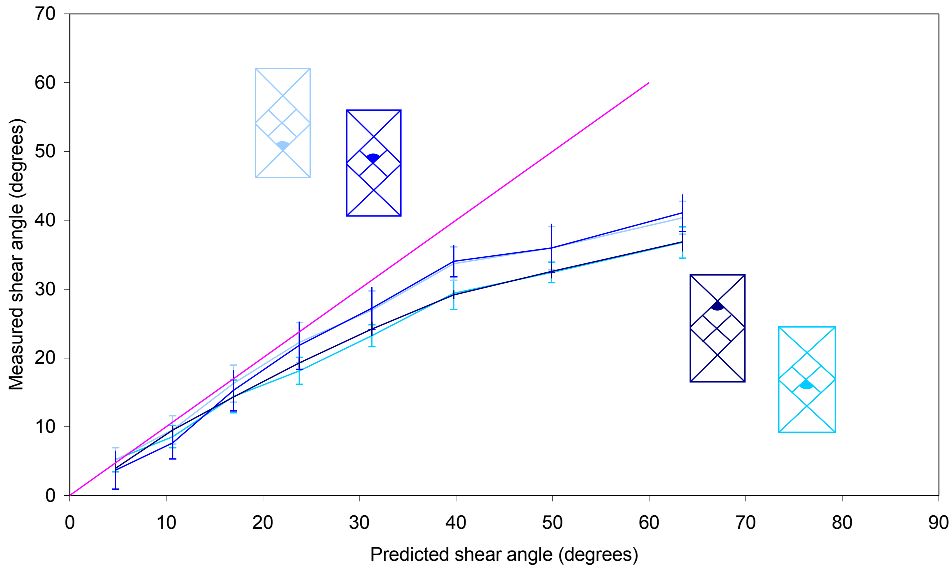

Figure 3.25: Angles measured from video taken of a bias extension test of Twintex$^{\mathrm{TM}}$ 1 with sample ratio factor $\kappa = 2$.

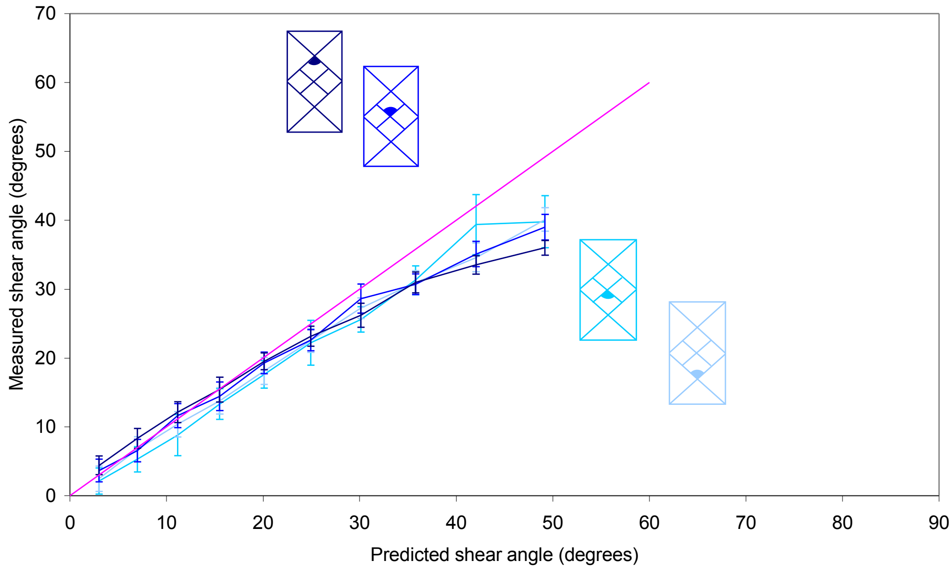

Figure 3.26: Angles measured from video taken of a bias extension test of Twintex$^{\mathrm{TM}}$ 1 with sample ratio factor $\kappa = 2.5$.

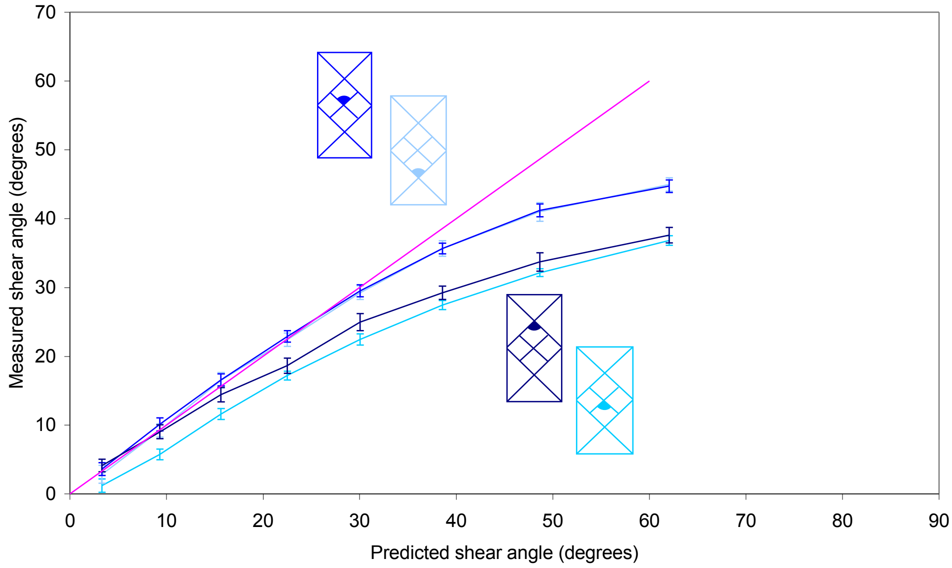

Figure 3.27: Angles measured from video taken of a bias extension test of Twintex™ 1 with sample ratio factor $\kappa = 3$.

Examination of these shows that whilst the majority of the samples exhibited lower shear angles at the top of theoretically constant shear region A than at the bottom, this trend is not universal. The shear irregularities are probably caused by the low shear modulus of the textiles. This creates a very low shear penalty to irregular shear distributions, and weak interactions between different shear areas. Other causes of shear irregularities include the transverse slip described above, which distort the shear angle measured near the tips of the C regions. Thus, measurements taken from the centre of the sample are likely to be reliable for a greater proportion of the test.

Finally, it is important to observe the reliability of the video analysis tool. Comparison of Figures 3.25and 3.26 with Figure 3.27 shows that the analysis observes less scatter in some cases. This is affected by the resolution of the video, which is dependant on the size of the sample and the zoom setting of the video. It is also affected by the colour of the textile, the choice line colour, the ambient lighting, the textile structure, and the manner in which the textile deforms. Additionally, as the textile moves away from ideal shear, the markings curve, so that a straight line fit is no longer appropriate.

3.4.5.3 Bias extension normalisation comparison

The energy approach, whilst being the more complicated, takes the most thorough account of the test conditions, and so the results should be taken as the most reliable available. Given that, it is of interest to investigate how the other, more simple normalisation techniques compare to it and to each other.

The results are presented for a representative test for each material in Table 3.3, at each sample ratio that was tested for that material. Results not directly discussed can be found in Section B.2.

For initially orthogonal fabrics, the stress-tensor rotation approach tends to agree very closely with the energy minimisation at low shear angles. This is expected, as the model is only accurate whilst the rotated stress tensor aligns with both fibre directions - i.e. while the fibres are orthogonal. This effect is highlighted by the $\pm 30°$ material results. In Figures 3.28 and 3.29 the stress-tensor rotation approach does not agree with other methods even at relatively low shear angles in both shear directions. However, in the negative shear direction it crosses the other curves near the point at which the fibres are orthogonal.

Looking at the results for different bias extension aspect ratios presented for Twintex^{TM} 1 in Figures 3.30 to 3.32 , the picture frame equivalence approach appears to work best at $\kappa = 2.5$ (see also Figure B.15), whereas it consistently over-predicts at $\kappa = 2$, and under-predicts at $\kappa = 3$. The $\kappa = 2.5$ ratio is notable in that at this ratio the area of central shear region A is equal to the square of the sample width w_0 (for initially orthogonal fabrics). The approach seems to frequently over-predict at low shear angles when compared to the other methods. This may indicate that in the initial few degrees of shear the whole sample undergoes deformation, not necessarily just shear. This is because the sample must show some tension along the direction of the tows. Thus the initial tensile loading of the tows could cause the normalisation methods to differ at low shear angles.

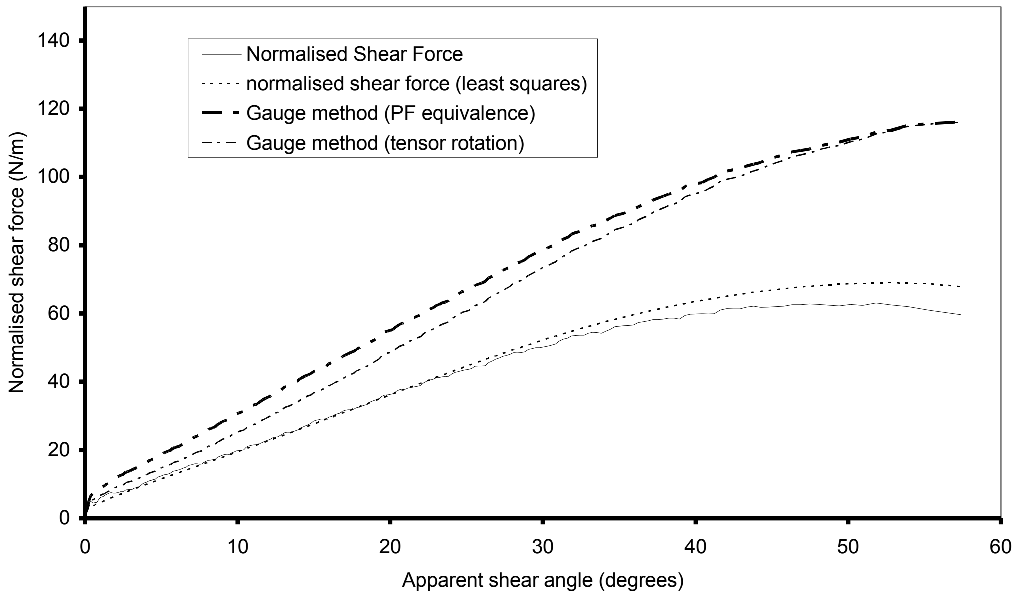

Figure 3.28: Bentley mat1 at $\kappa = 2$, positive shear direction. Sample width = 120mm, rate of extension = 80mm/min.

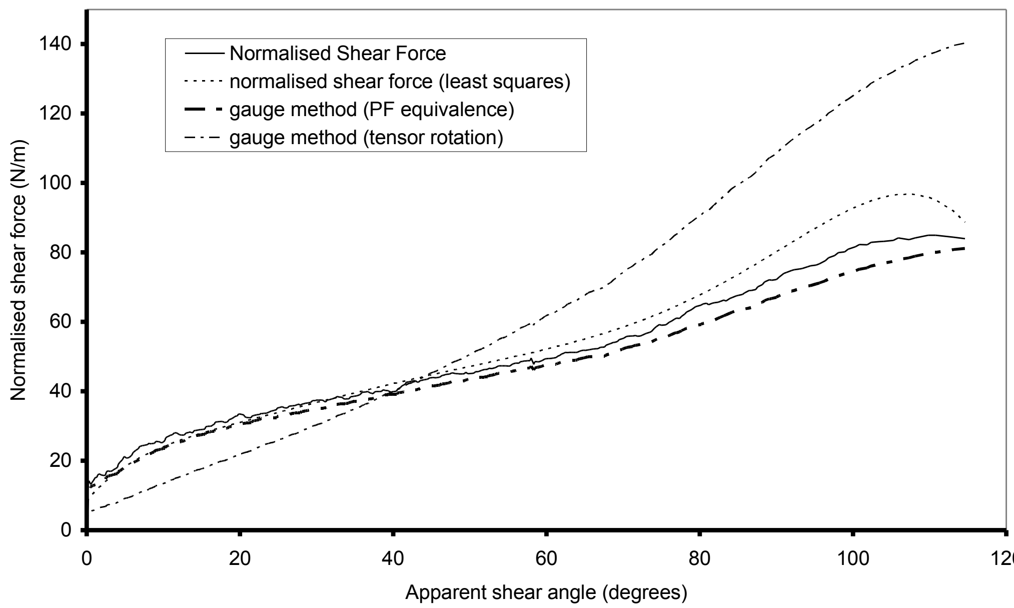

Figure 3.29: Bentley mat1 at $\kappa = 2$, negative shear direction. Sample width = 70mm, rate of extension = 80mm/min.

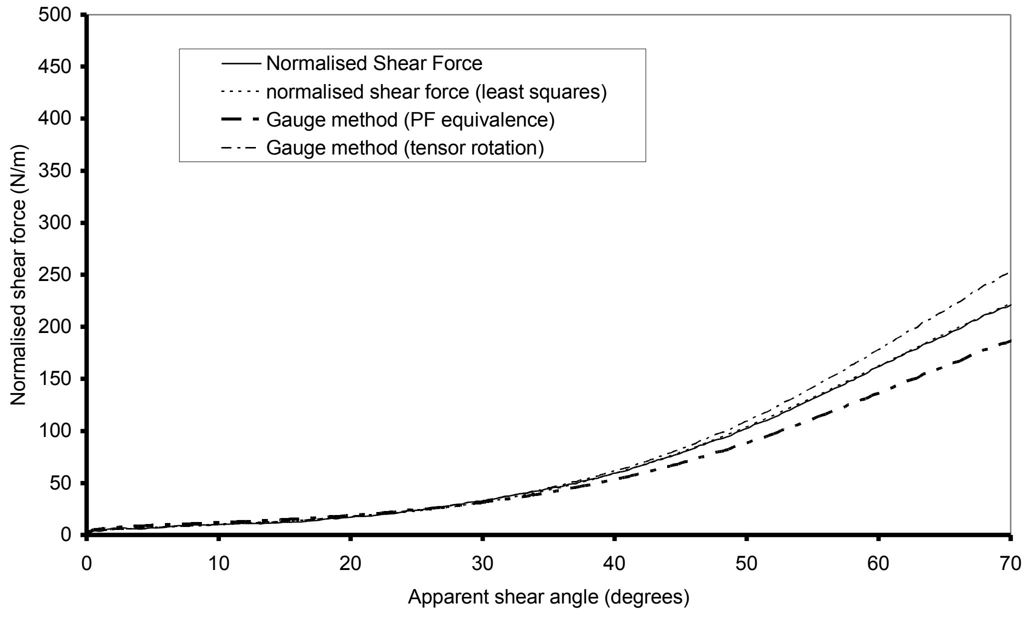

Figure 3.30: Twintex^{TM} 1 at $\kappa = 2$. Sample width = 99mm

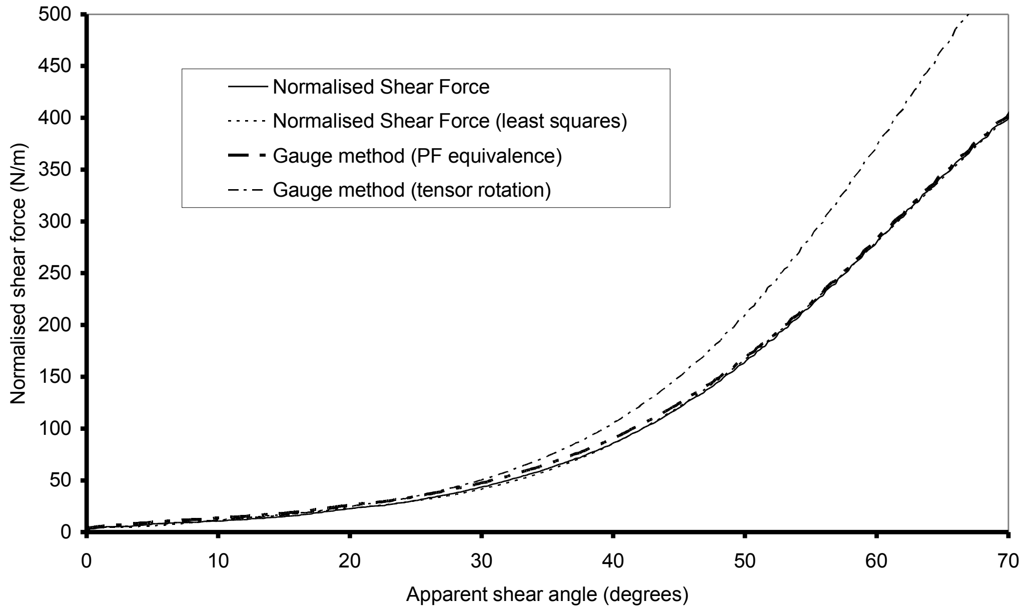

Figure 3.31: Twintex^{TM} 1 at $\kappa = 2.5$. Sample width = 99mm

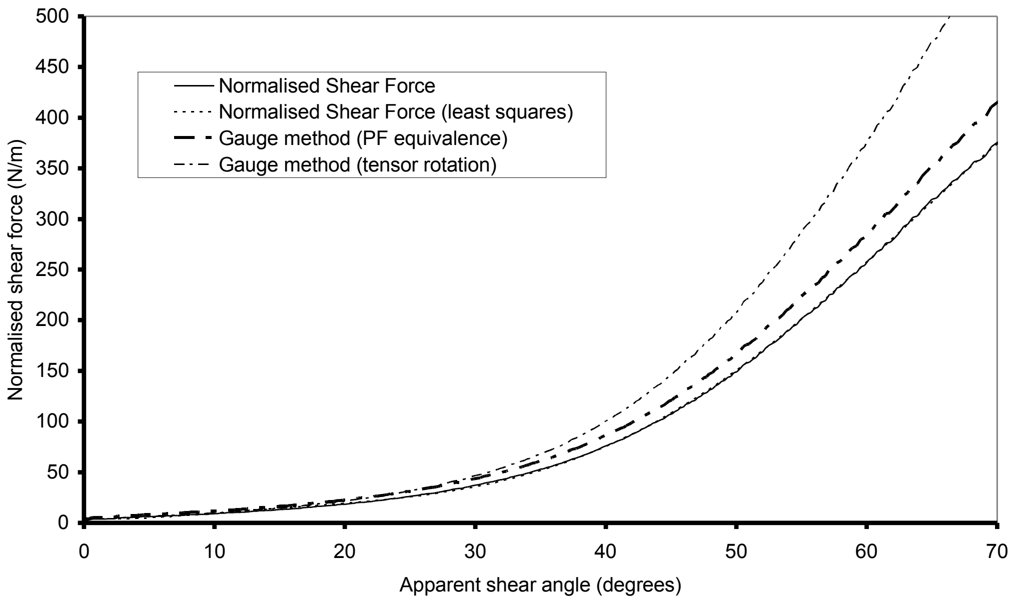

Figure 3.32: Twintex^{TM} 1 at $\kappa = 3$. Sample width = 99mm

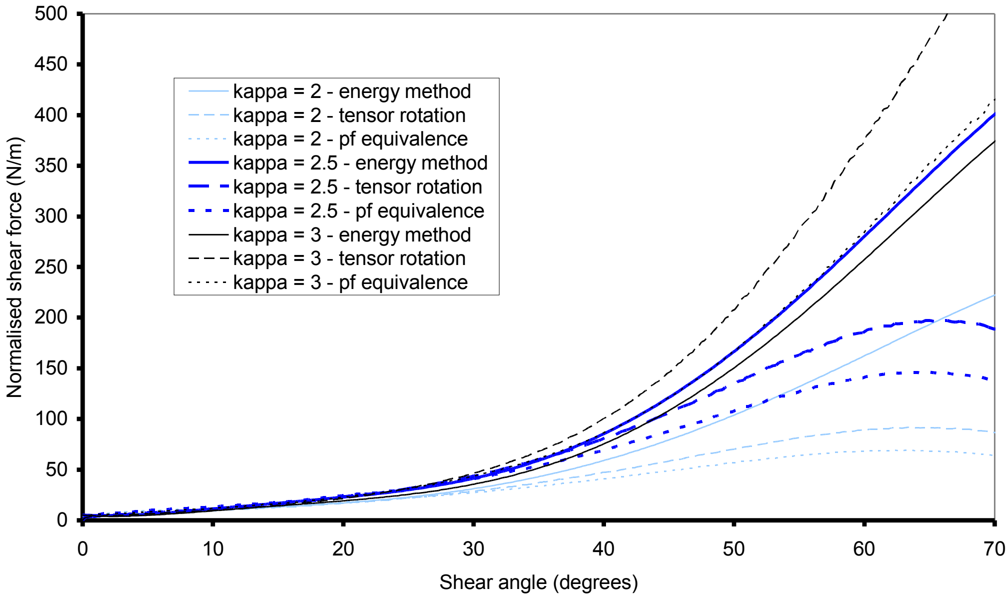

Figure 3.33: Twintex$^{\text{TM}}$ 1 compared for $\kappa = 2$, 2.5, and 3.

3.5 Comparison of normalised results - bias extension vs picture frame

If the differences in boundary conditions of different types of test (BE or PF) had minimal impact on the test results, and assuming that the normalisation approach is correct, then the normalised shear curves should coincide. The normalised results using the energy normalisation arguments are therefore compared here - full results can be found in Section B.3 It is proposed that the different boundary conditions imposed by the different tests are at least partly responsible for differences in the normalised test results.

From consideration of Figures 3.34 and 3.35 , it can be seen that the picture frame test always records a higher shear force than the bias extension. This suggests

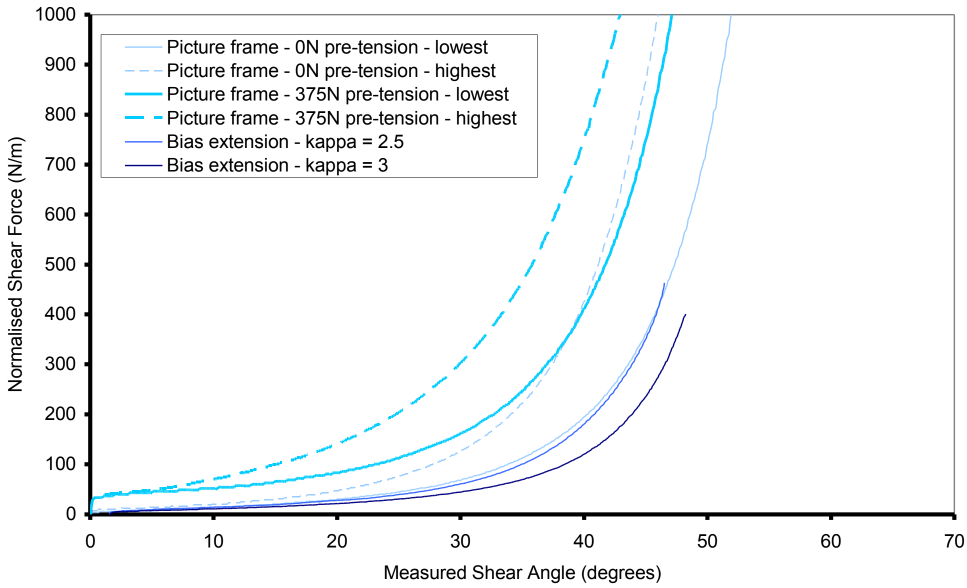

Figure 3.34: Comparison of picture frame (at 0N and 375N pre-tension) and bias extension ($\kappa = 2$, 2.5 and 3) normalised test results for Twintex^{TM} 1. Four samples per test condition.

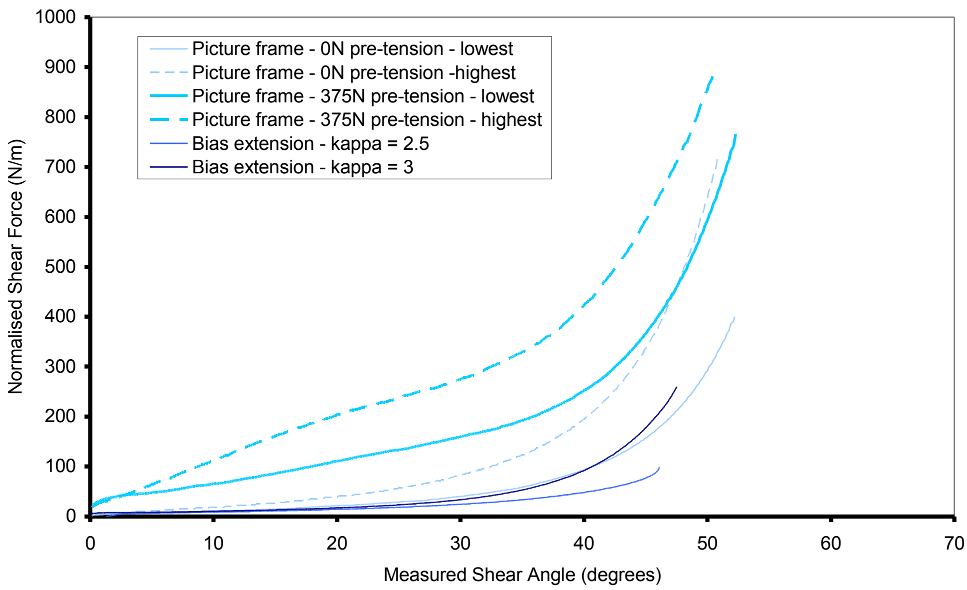

Figure 3.35: Comparison of picture frame (at 0N and 375N pre-tension) and bias extension ($\kappa = 2$, 2.5 and 3) normalised test results for Twintex^{TM} 3. Four samples per test condition.

that the strong end clamping that the picture frame test imposes has a significant effect on the shear response of a textile. Mechanisms that contribute to this are the fibre deformation at the clamping edge, tension developed during shear (either directly due to crimp, or indirectly due to lateral compaction), and the lack of freedom for lateral tow slip. However, consideration of the stresses developed in the bias extension test sample suggest that the tows must develop a certain degree of tension during shear - or they would pull apart. For this reason, the 0 pre-tension tests, whilst often suffering the least repeatability, should be regarded as the most comparable to bias extension test results. In Figures 3.34 and 3.35 they certainly seem to agree to a close degree, comparing the highest bias extension result with the lowest 0 pre-tension picture frame result. Comparison with bias extension indicates that the lowest of the curves at zero pre-tension that did not wrinkle prematurely (as observed by eye) probably gives the most accurate response. This is because fibre misalignment in one direction causes very high picture frame response, but in the other direction results in premature wrinkling, the latter being immediately discarded from the results as obviously misaligned. However, shear response under tension may be important in modelling more accurate forming simulations with a blank-holder. For this to be adequate, tension should be monitored throughout the test.

Ultimately, the different boundary conditions imposed by the different tests renders comparison between them of limited use, and they are different again from those imposed on the material during forming. Thus, it may prove that the results from picture frame tests are more pertinent to forming using a blank-holder, whereas bias extension test results are more appropriate for diaphragm and hand forming operations.

3.6 Conclusions

Experimental characterisation has been undertaken using both the bias extension method at different aspect ratios and picture frame testing method at different pretensions. The difficulties with picture frame boundary conditions continue to produce highly variable results of limited usability. Bias extension tests at small aspect ratios also suffer from some variability, however this variability is mostly due to curve offsets. A method for visually analysing bias extension tests to show offset effects has been developed. This does not consistently eliminate offset variability for all materials, but is nonetheless a useful tool in analysing bias extension results.

Bias extension and picture frame test data analysis has been generalised to allow for non-orthogonal textiles, and a $\pm 30°$ textile has been tested to demonstrate the changes. Several normalisation approaches for bias extension results have been proposed, and the experimental results compared for the varying approaches, and to normalised picture frame results. The $\pm 30°$ material has particularly effectively demonstrated the weaknesses of applying an isotropic stress rotation technique to an anisotropic material. Overall, it is proposed that the energy based bias extension normalisation technique is the most appropriate, as it takes into account the actual deformation within the samples, without making assumptions about the detailed (and probably complex) stress field within the sample. This is further supported by the agreement observed for all materials for tests at $\kappa = 2.5$ and 3 using this normalisation method.

It is curious that the picture frame equivalence normalisation approach agrees so well with the energy approach at $\kappa = 2.5$. Furthermore, at $\kappa = 3$, it is an almost constant 10% less than the energy approach. More work should be carried out to investigate the cause of this, if any. This could include comparison at higher ratios such as 3.5, 4 or above. If the discrepancy could be understood then this would make a modified picture frame equivalence normalisation technique the preferred method due to its great simplicity, and the ease with which it could be applied to past test data.

Bias extension and picture frame results do not agree well even after normalisation. However, the lowest of visually acceptable picture frame results correspond to the highest of bias extension results, suggesting that the differences between the results arise from differences in boundary conditions. Whilst these inherent differences in the tests may render attempts to compare the results a little misleading, the comparison presented here demonstrates that the exercise increases the understanding of both tests as well as the inherent mechanisms that affect sheared textiles. Normalisation may allow for a rational approach to deal with the large amount of variability of results. For example, the strong agreement between the highest bias extension results and the lowest 0 pre-tension picture frame results suggest that these should be taken as the most appropriate results rather than the average. In the case of the picture frame test, it suggests that higher shear forces are the result of misalignment, while in the bias extension test, non ideal shear and fibre slip cause lower than expected forces.

Chapter 4

Shear Modelling of Fabric Reinforcements

4.1 Introduction

As has been outlined in Section 2.2.1, the dominant and most desirable deformation mechanism for technical textiles draped around features with double curvature is trellis shear. The shear modulus shown by a typical biaxial textile is many orders of magnitude smaller than the tensile modulus along either of the tow directions. The energy associated with wrinkling is often at least an order of magnitude lower again than that associated with trellis shear: However, this is an undesirable effect in the vast majority of composite applications, so that the forming process is designed to avoid wrinkling.

Forming simulation with any level of sophistication subsequently requires fabric deformation data, the most relevant of which is its trellis shear behaviour. In order to accurately predict the forming results of a specific fabric its shear behaviour must be measured or predicted. It is unlikely that experimental shear characterisation will ever be rendered entirely redundant. However, shear modelling complements shear experiments in several vital ways.

Firstly, it helps in the validation of results. Shear characterisation of technical textiles is notoriously difficult, particularly with certain emerging classes of textiles such as knitted non-crimp fabrics. Poor repeatability of results must be addressed either by improving the test method or by the use of more robust criteria for the exclusion of outlying curve data. Shear modelling allows the trellis shear phenomenon to be understood better, both highlighting the weaknesses in test methods and therefore facilitating their improvement, and also allowing the results to be understood better so that irregularities can be better identified and discarded. Furthermore, understanding of the trellis shear process may ultimately allow the effects of test result repeatability issues and material variability to be untangled. This way, not only confidence in test results can improve, but quality control of fabric variability can be managed to maximise process success.

As discussed in Chapter 3, many fabrics exhibit some variability in their shear and forming behaviour, which produces some challenges for shear measurement experiments. FE shear models already show some promise in modelling the effects of fabric variability on shear behaviour [58] - however, the slow analysis restricts the number of repeats that can be realistically made for full statistical analyses. It may be that as constitutive shear models mature that methods are proposed for allowing fabric variability to be modelled, and the speed of the evaluation of these methods would subsequently allow large data sets to be developed for different factors.

FE shear modelling approaches for dry textiles, based on unit cell models are still, like constitutive models, quite a way from maturity. In many ways, however, conducting an FE shear characterisation is not unlike conducting an experimental shear characterisation. In both cases, a fundamental understanding of the underlying deformation mechanisms is required in order to generate accurate, trustworthy results. To this end this thesis has concentrated on the constitutive modelling of the trellis shear process, expanding current models to include non woven textiles such as non-crimp fabrics.

Finally, it is important to point out the relative benefits of the direct output of constitutive shear models. The results of such models can be generated in a fraction of the time and at a subsequent fraction of the cost of FE results or experimental measurements. Considering the bewildering and ever increasing array of technical textile choices facing a would-be composite manufacturer, such simple models have the potential to allow quick, cost effective evaluation of the shear behaviour (and therefore the forming behaviour) of many different, even not yet existent textiles.

Much work has been done in determining the shear energy elements in woven fabrics, as outlined in Section 2.2.2. Less however has been done for non-crimp fabrics. In order to create a generic modeller the peculiarities of these fabrics must also be modelled. Some approaches to modelling the effects of the stitching on the non-crimp fabric's shear behaviour are proposed, and the results are compared to experimental results.

4.2 Sources of shear resistance in fabrics

A typical engineering fabric consists of a complex arrangement of component materials, each of which contributes to the overall material response. When considering the shear response of fabrics to deformation, it becomes necessary to categorise the shear resistance according to the different mechanisms that the fabric undergoes during shear. Obvious categories for each component within the fabric include the component material strain responses and the component interfaces.

Each component category requires prioritising according to the magnitude of its contribution to the overall material response. The energy contributions from the greatest of these can then be summed to give an approximation for the energy contribution of the fabric.

Such a categorisation is illustrated in Table 4.1. The categories can be used as required for a specific fabric. A woven fabric, for example, will not have stitching, so that the energy contribution for that category is zero. A non-crimp fabric, on the other hand, has stitching but will experience little tow bending and torsion.

Each of the element categories in Table 4.1 may be applied more than once within a fabric, according to its structure. For example, a fabric might have both glass and carbon tows, in which case the relevant material properties for each tow have to be taken into account.

4.3 Shear resistance in non-crimp fabrics

4.3.1 Stitch effects

The stitch constitutes a structurally unimportant part of the fabric structure, with its tensile modulus typically being many magnitudes smaller than that of the tows. However, the stitch strain response *is* on a comparable magnitude to the fabric shear response — and so is an important factor in shear. This is seen in many stitched fabrics' unusual shear behaviour.

Of the two dominant energy factors outlined in Table 4.1, the stitch extension is considered most important, and so is treated first.

4.3.1.1 Stitch extension

In order to understand the stitching pattern in a warp-knit non-crimp fabric, the warp-knitting process must be briefly described. The tows are laid in a mat that is held and moved through the machine by moving hooks at the edges. These hooks move the mat into the knitting bars, which knit the mats together. The knitting machine has a row of guides positioned above the tow mat, with a stitch threaded through a hole in each guide, and a row of needles below the tow mat, illustrated in Figure 4.1 The guides and needles are evenly spaced, according to the gauge, a measure that defines the number of needles per inch.

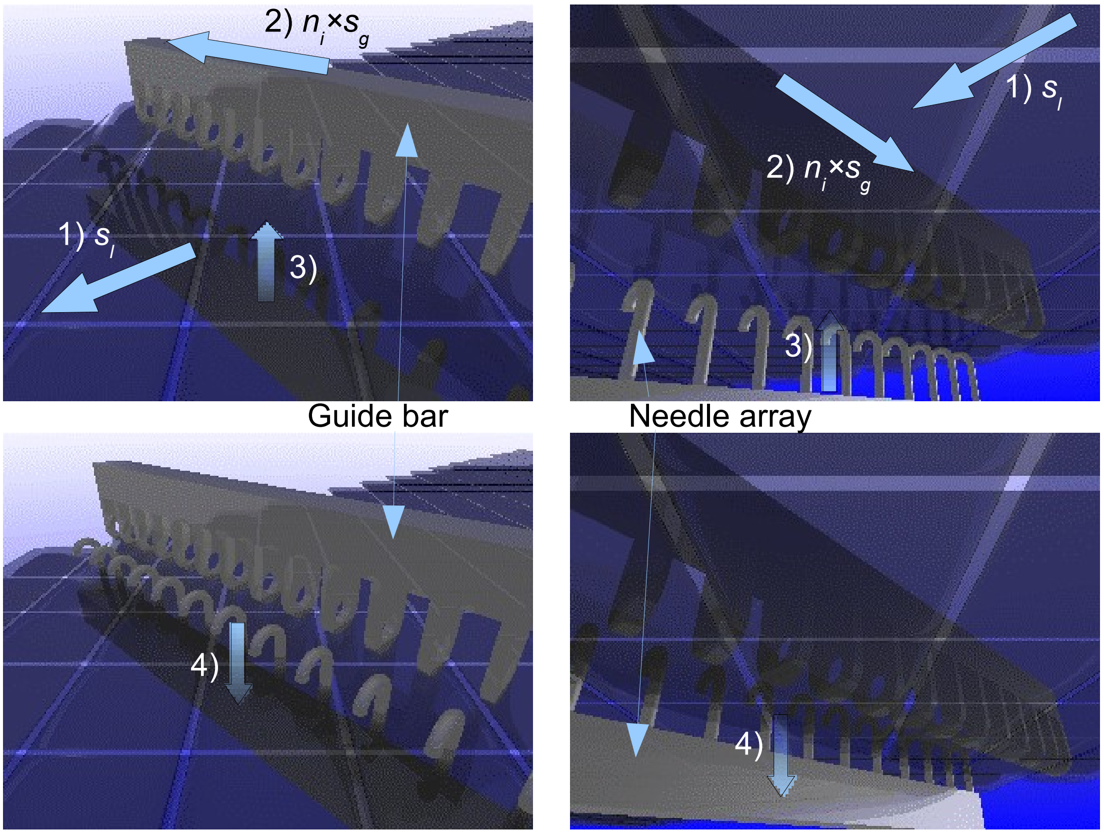

Figure 4.1: A conceptual illustration of the warp-knitting process – the stitching thread has been omitted for clarity. An example stitching pattern can be found in Figure 4.2.

The pattern is produced by a sequence of stitch cycles, where on a generic ith stitch cycle, a sequence of events occur, numbered 1-4 in Figure 4.1, as follows:

1. The tow mat advances by the stitch length distance, s_l.

2. At the same time, the guide bar indexes a multiple n_i of the stitch separation s_g to the left or right.

3. The needle array pushes through the tow mat.

4. Each needle hooks a loop of stitching thread from the guide above it and pulls it through the tow mat and previous loop, completing the cycle.

A stitching cycle is normally referred to as a course.

The lapping sequence, which is the series of guide array index values n_i, determines the stitching pattern. An example of one stitching pattern that repeats over two courses, a tricot stitch, is illustrated in Figure 4.2. At the top of the fabric, the overlaps consist of a single stitch thread that runs in a diagonal with dimensions s_l in the warp direction and $n_i \times s_g$ in the weft direction, where n_i can be a positive or negative integer, or zero. At the bottom, the underlaps consist of a chain of stitch loops running in the warp direction, each loop being constrained by the subsequent loop, which passes through it. The sum of the guide array index sequence $\sum n_i$ must be zero, in order that the guide bar ends up in the same position at the end of the sequence as at the beginning. Typically the guide bar rarely strays more than two or three stitch spacings from its starting position.

Figure 4.2 separates the stitch into a sequence of three classes of segments: Through-thickness, overlapping, and underlapping. As the fabric shears, the geometric development of each of these segments can be treated separately, and the

Table 4.1: Shear energy dissipation categories for generic shear fabrics.

Element	**dominant energy type**	**constrained by**
Tow	extension	BCs, Adj/Cross Tow, Stitch
	lateral compaction	BCs, Adj/Cross Tow, Stitch
	shear	BCs, Adj/Cross Tow, Stitch
	bending	BCs, Adj/Corss Tow, Stitch
	torsion	BCs, Adj/Cross Tow, Stitch
	friction	BCs, Adj/Cross Tow, Stitch
Stitch	extension	Adj Tow, Stitch
	friction	BCs, Adj Tow, Stitch

key

BCs	Boundary Conditions (e.g. mould, picture frame)
Adj Tow	Adjacent Tow
Cross Tow	Crossover Tow
Stitch	Adjacent Stitch

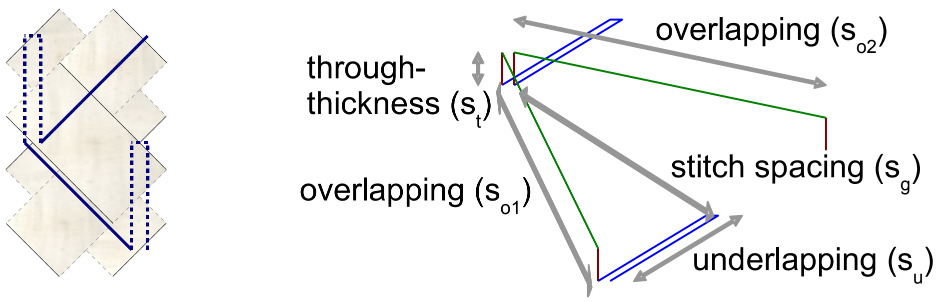

Figure 4.2: An example warp-knit stitch, a tricot stitch.

effects added together.

underlapping

If a particular segment of the stitch is not colinear with either tow direction, trellis shear will cause that segment to extend or compress. For a fabric with initial tow angles $\pm\phi_0$ the underlapping length s_u is related to the initial stitch length s_l and the shear angle θ by

$$s_u(\theta) = \frac{\cos\phi}{\cos\phi_0} s_l \tag{4.1}$$

where $\phi = \phi_0 - \theta/2$.

overlapping

Similarly, the ith overlap length s_{oi} in the lapping sequence is given by

$$s_{oi}(\theta) = \sqrt{\frac{\cos^2\phi}{\cos^2\phi_0} s_l^2 + \frac{\sin^2\phi}{\sin^2\phi_0} n_i^2 s_g^2} \tag{4.2}$$

where s_g is the stitch spacing and n_i is the ith index in the lapping sequence.

through-thickness

Finally, in order to model the through-thickness segments, the fabric thickness must be considered, for which tow compaction is a factor. Consider Figure 4.3 in which a tow is shown before and after shear. In the figure, and in the segmentation of the stitch, a rectangular tow cross-section is assumed. This is mostly for convenience: However, sections taken by Souter [60] suggest a rectangular tow cross-section is a reasonable assumption for non-crimp fabrics. The tow lateral cross-sectional area t_A

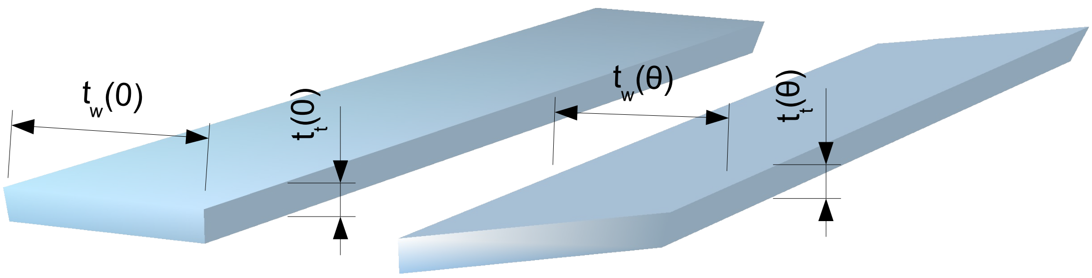

Figure 4.3: A tow with rectangular cross-section before (left) and after (right) shear.

is given by

$$t_A(\theta) = t_t(\theta) t_w(0) \frac{\sin 2\phi}{\sin 2\phi_0} \tag{4.3}$$

so that the tow thickness is given by

$$t_t(\theta) = \frac{t_A(\theta) \sin 2\phi_0}{t_w(0) \sin 2\phi} \tag{4.4}$$

Now the through-thickness is the sum of the tow thicknesses, so that for a fabric with the same tows in both directions,

$$s_t(\theta) = \frac{2 \sin 2\phi_0}{t_w(0) \sin 2\phi} t_A(\theta) \tag{4.5}$$

where s_t is the length of the through-thickness stitch section.

Pre-pregs retain a constant cross-sectional area such that $t_A(\theta) = t_A(0)$, whereas dry fabrics retain a relatively constant thickness $t_t(\theta) = t_t(0)$ (see Section 2.2.2.1, McBride or Souter [45, 60]. These represent the two possible extremes for the thickness behaviour of the fabric. This thesis concentrates on dry fabrics, so that the latter scenario is of more interest. However, it is worth noting that there is a limit to the compressibility of dry fabrics. Figure 4.4 plots the tow fibre volume fraction vs shear angle for a constant thickness fabric. Also shown on the graph is a limiting volume fraction for the tows based on hexagonal packing. As the material shears the volume fraction increases, and as it approaches the limit the material must either thicken or wrinkle.

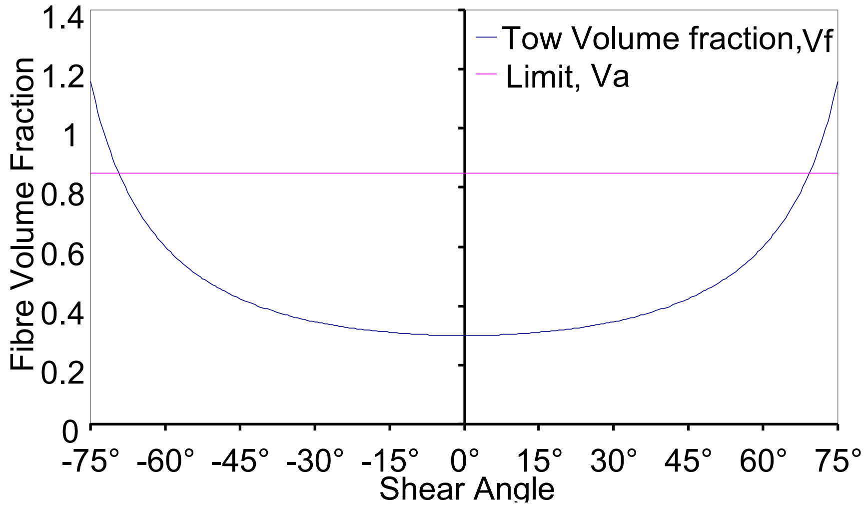

Figure 4.4: Variation of a tow's volume fraction with shear angle

Total stitch length

Summing the stitch segment lengths over the entire lapping sequence of N courses gives the sequence stitch length s_L. This is called the unit stitch, as it is the smallest repeatable unit when considering the stitch pattern *in isolation*.

$$s_L = \sum_{i=1}^{N} (2s_u + 2s_t + s_{oi}) \tag{4.6}$$

Substituting Equations 4.1, 4.2 and 4.5 into Equation 4.6 gives

$$s_L = 2N\frac{\cos\phi}{\cos\phi_0}s_l + \frac{4N}{t_w(0)\cos\theta}t_A(\theta) + \sum_{i=1}^{N}\sqrt{\frac{\cos^2\phi}{\cos^2\phi_0}s_l^2 + \frac{\sin^2\phi}{\sin^2\phi_0}n_i^2 s_g^2} \tag{4.7}$$

Evaluating at θ=0, such that $\phi = \phi_0$, gives

$$s_L(0) = 2Ns_l + \frac{4N}{t_w(0)}t_A(0) + \sum_{i=1}^{N}\sqrt{s_l^2 + n_i^2 s_g^2} \tag{4.8}$$

This becomes useful when calculating stitch strain.

Stitch constraints

Global stitch strain is given by

$$\epsilon_s = \frac{s_L(\theta) - s_L(0)}{s_L(0)} \tag{4.9}$$

However, this value presumes that the stitch is at uniform tension throughout. Except for the simplest stitching pattern, the chain stitch, different segments of the stitch could experience different changes in length during shear, so that the stitch would have to pass relatively freely from one segment to another in order to remain at uniform tension. It is important to establish whether this is the case.

In order to investigate this a tricot stitch sample was sheared. Prior to shearing, the overlaps at the centre of the sample were marked black, but the underlaps were left white. The sample was mounted into a picture frame and the picture frame was extended in stages. At each stage a photograph taken of the underside of the fabric. The photographs were analysed using ImageTool[1], an image analysis program, to measure the proportion of the underlaps that was white, and that which was black.

If the stitching is entirely constrained at the end of the segments, then the underlaps would have remained white, with the stitching accommodating the increase in length entirely by strain. If, on the other hand, the stitching is free to move from one segment to the other, then the underlaps would have gradually shown more black stitching as thread from the compressing overlaps was passed to accommodate the extending underlaps.

[1]http://ddsdx.uthscsa.edu/dig/itdesc.html

Figure 4.5 shows a photograph of the sample after some shearing. Figure 4.6 illustrates the average proportion of black and white thread observed in a sample of the underlap photographs. As can be seen, the extension was almost entirely accommodated by thread passing through from the overlaps. This confirms that the stitching is relatively unconstrained, so that the tension is essentially uniform throughout its length.

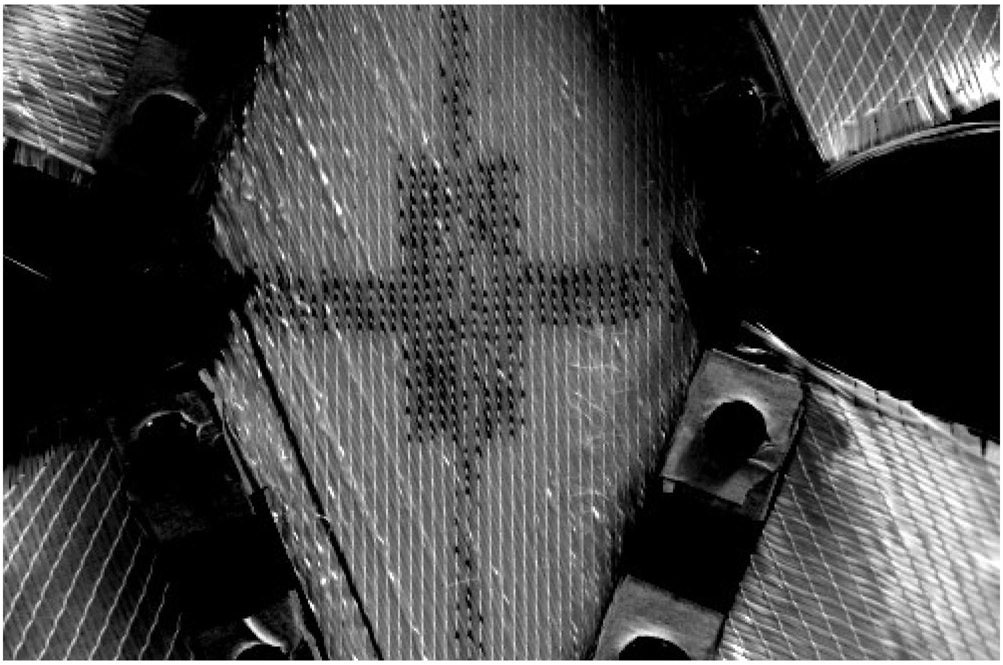

Figure 4.5: Sheared non-crimp fabric sample (underside) (FGE 106hd, see Table 3.3), in which the stitch overlaps were marked black before shearing

It should be noted that, when tested, the stitch failed at 17% strain. This corresponds to the point at which the stitch begins to break at places. The stitch has been observed in both picture frame and bias extension tests to break at high shear angles. However, the stitch failure points cannot be predicted, and it is difficult to assess how much of the tension would subsequently be released beyond failure.

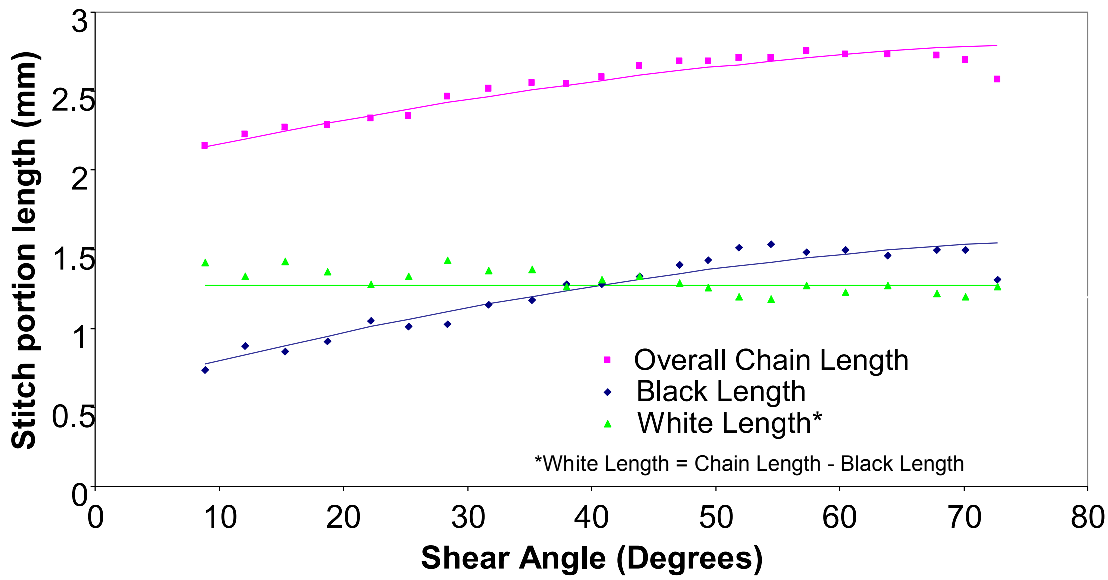

Figure 4.6: Average lengths of white and black thread segments in the underlaps during shear

Visual observation suggests that some tension remains, which is related to the stitch friction within the structure. Due to this complicated scenario, the stitch contributions are only modelled up to failure, beyond which they are presumed to no longer contribute to the shear behaviour. As the stitch does not catastrophically unravel after failure, but the material remains mostly intact, this failure mechanism is unimportant to the pre-forming process, except in that it affects the shear behaviour and could therefore affect the forming results of the textile. In practice, the stitch has not been observed to fail in experimental forming, as in order to do so it would probably require extreme boundary conditions.

Stitch energy

The stitching is typically made of texturised polyester yarn, for which micro mechanical deformation behaviour is more akin to that of the tows than of a homogeneous substance. This stitching material is broadly used in the non-crimp fabric industry. The texturising process, whereby the yarn is twisted, heated close to its melting temperature, cooled, and then untwisted, results in fibres that are permanently crimped and thus substantially increasing the amount of extension that the stitch yarn will undergo. This first part of the stitch extension, in which the fibres are uncrimping, is very hard to model, as relatively negligible application of tension results in very large extensions – in fact, it is very hard to establish the zero extension point. Beyond the point at which the fibres in the stitch yarn have aligned, the stitch exhibits a fairly linear stress / strain curve, as can be seen in Figure 4.7, which was obtained from experimental tensile testing of stitch samples taken from FGE 106hd stitch yarn. As a first approximation of the stitch behaviour, only the linear portion of the tension/extension curve for the stitch is considered in the model.

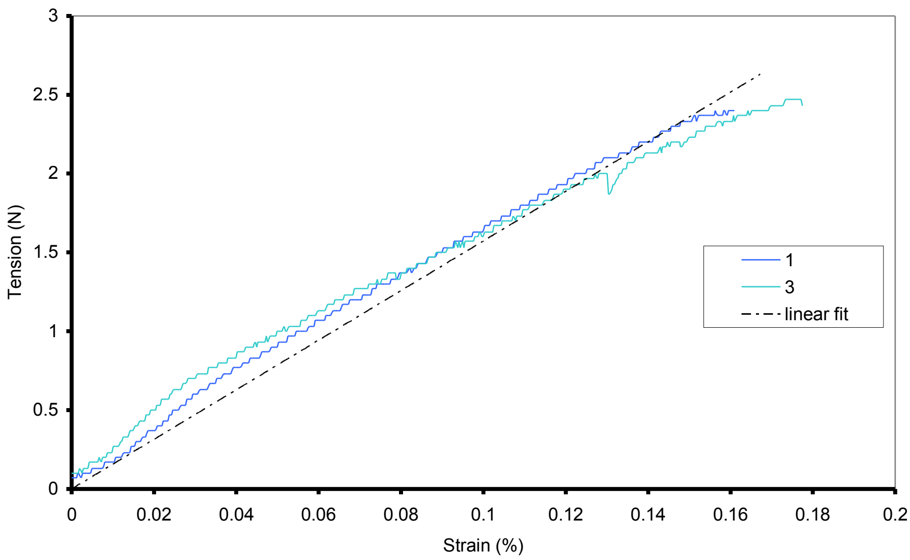

Figure 4.7: Two sample stitch tensile curves with best fit lines.

Let the stitch, then, have an effective modulus E_s and cross-section s_A such that their multiple is the gradient of the best fit line. For the stitch found in Figure 4.7, $E_s s_A = 15.725$N. In that case, the average tension in the stitch during trellis shear is given by

$$S_s = E_s s_A \epsilon_s = E_s s_A \frac{s_L(\theta) - s_L(0)}{s_L(0)} \tag{4.10}$$

It must be remembered however that E_S and s_A have not been assigned *individual* values, and so are meaningless on their own.

Given the stitch extension $s_\Delta = s_L(\theta) - s_L(0)$, the energy U_s expended in extending the stitch can be defined as

$$\begin{aligned} U_s &= \int S_s ds_\Delta \\ &= \frac{E_s s_A}{2s_L(0)} s_\Delta^2 \\ &= \frac{E_s s_A}{2s_L(0)} \left(s_L(\theta) - s_L(0)\right)^2 \end{aligned} \tag{4.11}$$

This is normalised by the fabric area that the unit stitch occupies,

$$A_s = N s_l s_g \tag{4.12}$$

to give

$$\frac{U_s}{A_s} = \frac{E_s s_A}{2N s_l s_g s_L(0)} (s_L(\theta) - s_L(0))^2 \tag{4.13}$$

Shear force

Differentiating the normalised stitch extension energy with respect to the shear angle θ yields the normalised shear torque,

$$\frac{\tau_s}{A_s} = \frac{1}{A_s}\frac{dU_s}{d\theta} = \frac{E_s s_A}{2N s_l s_g s_L(0)} \frac{d}{d\theta} \left[(s_L(\theta) - s_L(0))^2 \right] \tag{4.14}$$

from which the normalised shear force N_s can be easily calculated

$$N_s = \frac{\tau_s}{A_s \cos\theta} \tag{4.15}$$

Now

$$\frac{d}{d\theta}\left[(s_L(\theta) - s_L(0))^2\right] = 2(s_L(\theta) - s_L(0))\frac{ds_L}{d\theta} \tag{4.16}$$

and

$$\frac{ds_L}{d\theta} = 2N\left(\frac{ds_u}{d\theta} + \frac{ds_t}{d\theta}\right) + \sum_{i=1}^{N}\frac{ds_{oi}}{d\theta} \tag{4.17}$$

So, differentiating Equation 4.1

$$\frac{ds_u}{d\theta} = \frac{s_l}{\cos\phi_0}\sin\phi \tag{4.18}$$

taking the assumption of constant fabric thickness gives

$$\frac{ds_t}{d\theta} = 0 \tag{4.19}$$

and differentiating Equation 4.2,

$$\frac{ds_{oi}}{d\theta} = \frac{s_l^2\tan\phi_0 - \dfrac{n_i^2 s_g^2}{\tan\phi_0}}{\sqrt{\dfrac{\cos^2\phi}{\cos^2\phi_0}s_l^2 + \dfrac{\sin^2\phi}{\sin^2\phi_0}n_i^2 s_g^2}} \tag{4.20}$$

Finally, substituting Equations 4.14, 4.17 and 4.18-4.20 into Equation 4.15, gives

$$N_s = \frac{E_s s_A \epsilon_s \tan\theta}{N s_l s_g}\left[\frac{2Ns_l}{\cos\phi_0} + \sum_{i=1}^{N}\frac{s_l^2\tan\phi_0 - \dfrac{n_i^2 s_g^2}{\tan\phi_0}}{\sqrt{\dfrac{\cos^2\phi}{\cos^2\phi_0}s_l^2 + \dfrac{\sin^2\phi}{\sin^2\phi_0}n_i^2 s_g^2}}\right] \tag{4.21}$$

where ϵ_s is defined using Equations 4.7-4.9 .

The stitch is fed into the knitting process under tension, which is determined by a factor called the stitch run-in, quoted as the length of thread in mm fed out over 480 courses. The stitch run-in is controlled through the rotational speed of the stitch reel. Geometric considerations are taken into account in terms of the radius at which the thread is coming off the reel so that the rotation of the reel maintains the run-in specified. It is relatively easy to incorporate this into the above value, by redefining the stitch strain ϵ_s as

$$\epsilon_s = \frac{s_L(\theta) - s_{L0}}{s_{L0}} \tag{4.22}$$

where s_{L0} is different to $s_L(0)$ in that it is the length of the unit stitch at zero tension, and can be defined as

$$s_{L0} = \frac{N}{480000} \times \text{run-in} \tag{4.23}$$

However, using the stated stitch run-in for one fabric gives a stitch strain at $\theta = 0$ as 36%, which is approximately double the breaking strain. This is clearly a result of ignoring the stress free extension portion of the stitch graph, as is discussed earlier. For the sake of the characterisation of the stitch the stress-free length was taken to be at the base of the linear portion of the stress-strain curve, however, the stitch can be in an unbuckled state at shorter lengths than this, and may well be so in the reels. Also, the approximations taken in calculating run-in are likely to be erroneous, as they certainly do not need to be accurate from a manufacturing point of view, as long as they are consistently applied. The best way to determine the starting point of the stress-strain curve is to mark the start and end of a known number of stitches within a fabric, remove the stitching, and test it. The path of the stitching when still in the textile will yield the initial length value $S_L(0)$, and the stitching can be loaded into the tensile test at this length. The resulting stress-strain curves could be applied as if $S_{L0} = S_L(0)$.

4.3.1.2 Stitch friction

Given that, as found in Section 4.3.1.1 the stitch passes from one segment to another during shear, the frictional losses due to this process must be modelled.

This model requires a point along the stitch to be identified where the stitch experiences equal extension on both sides. In the case of the tricot stitch, for example, this can be found at the apex of any underlap (Figure 4.8), as the sequence of stitch segments either side of that point is symmetrical: underlap segment, through-thickness, overlap with index magnitude 1, through-thickness, underlap. The cross-

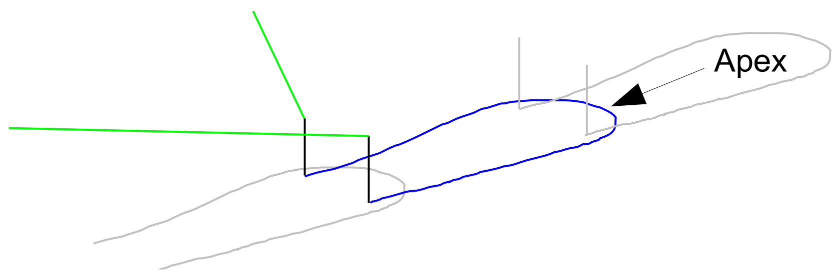

Figure 4.8: A close up of a tricot stitch with the apex of the underlapping. The apex is taken to be at the bottom of the through-thickness segment.

over points, at which frictional losses occur, are taken to be at the apexes, the normal force causing the friction being the tension in the stitch.

From this point of symmetry, working along the stitch, each point passing through an apex must be assessed to determine any frictional loss arising from stitch passing through. Firstly, for each segment, the length of the stitching from the symmetry point to each pass-through point must be assessed. For the example where the point of symmetry is on the apex, the lengths to the three pass-through points in each segment up to segment N are given by:

$$L_{st\to i1}(\theta) = s_u + \sum_{j=st}^{i-1} (2s_u + 2s_t + s_{oj}) \tag{4.24}$$

$$L_{st\to i2}(\theta) = s_u + 2s_t + s_{oi} + \sum_{j=st}^{i-1} (2s_u + 2s_t + s_{oj}) \tag{4.25}$$

$$L_{st\to i3}(\theta) = 2s_u + 2s_t + s_{oi} + \sum_{j=st}^{i-1} (2s_u + 2s_t + s_{oj}) \tag{4.26}$$

and for the segments before the starting point:

$$L_{st\to i1}(\theta) = s_u + \sum_{j=i+1}^{st} (2s_u + 2s_t + s_{oj}) \tag{4.27}$$

$$L_{st\to i2}(\theta) = s_u + 2s_t + s_{oi} + \sum_{j=i+1}^{st} (2s_u + 2s_t + s_{oj}) \tag{4.28}$$

$$L_{st\to i3}(\theta) = 2s_u + 2s_t + s_{oi} + \sum_{j=i+1}^{st} (2s_u + 2s_t + s_{oj}) \tag{4.29}$$

Next, the actual change in the stitch length up to that point is subtracted from the change in the stitch path length,

$$\begin{aligned} e_{st\to ip}(\theta) &= \Big| (L_{st\to ip}(\theta) - L_{st\to ip}(0)) - L_{st\to ip}(0)\epsilon_s \Big| \\ &= \Big| L_{st\to ip}(\theta) - (\epsilon_s + 1)L_{st\to ip}(0) \Big| \end{aligned} \tag{4.30}$$

for each of the three pass-through points $p = 1, 2, 3$. Note the absolute signs, as the direction that the stitch passes through is immaterial.

The energy taken to pass the stitch through these points $U_{e_{ip}}$ is given by the multiple of the frictional force and the distance pulled through. The frictional force is calculated from the stitch frictional constant μ_s and the force normal to the contact area, which will be assumed to be equal to the stitch tension S_s (Equation 4.10).

$$F_{e_{ip}} = \mu_s S_s \tag{4.31}$$

So that

$$U_{e_{ip}}(\theta) = \mu_s \int_0^{e_{st\to ip}(\theta)} S_s de_{st\to ip} \tag{4.32}$$

This can be summed for all contact points,

$$U_{eT}(\theta) = \sum_{i=1}^{N} \sum_{p=1}^{3} U_{e_{ip}}(\theta) \tag{4.33}$$

The energy due to stitch friction can be normalised by the same area in Equation 4.12, added to the normalised stitch tension energy, differentiated with respect to shear angle, and converted to a normalised shear force. Note that for generic functions $f(\theta)$ and $g(\theta)$,

$$\frac{d}{d\theta}(f + g) = \frac{df}{d\theta} + \frac{dg}{d\theta} \tag{4.34}$$

so that it is equally valid to add the individual shear torque (and therefore shear force) contributions as it is to add the energy contributions. Both the integration in Equation 4.32 and the subsequent differentiation were numerically carried out using the trapezium rule for the results presented in this thesis.

4.3.2 Tow effects

The tows contribute the bulk of the structural behaviour of the finished composite. However, their shear contribution is not so straightforward. In non-crimp fabrics the tow bending, extension and torsion due to pure trellis shear are negligible, as these effects arise mostly due to the crimped tow paths caused by the weaving process. As a result, the tow effects concentrated on are the tow compaction and friction.

As the fabric shears, the tows will experience in-plane compaction due to the reduction in surface area associated with shear. At the same time they may be subjected to some out of plane lateral compaction from the other tow layers. Finally, they will experience a frictional resistance to any change in profile due to the complex lateral compaction forces acting on them. As well as this, the tows will experience a number of other frictional resistances. Lateral compaction will require either internal shear or lateral friction with adjacent tows, or a combination of both. Rotation with respect to other tow layers will create friction, depending on the level of internal in-plane shear and compaction experienced.

In many NCFs the needles pierce the tows during the knitting process so that the tows effectively become redefined around the stitching. The stitch length s_l and gauge separation s_g are also often not in a ratio corresponding to the tow angle ϕ_0, so that the points at which the tows are pierced vary along the tow direction. Thus the tow layer becomes a mat of aligned glass fibres with periodic piercings causing fibre placement disturbances. This is important when assessing tow friction and shear, but is relatively unimportant for in-plane lateral compaction, which can be considered independent of these effects.

4.3.2.1 Lateral compaction

The model adapted by Cai and Gutowski [8] gives a sufficiently good fit to experimental data, and is therefore used for this shear model (See Section 2.2.2.2). As the fabric shears the tows may be forced to shear with it, and also to compact to accommodate the change in surface area.

The first step is to predict the volume compaction associated with fabric shear. In-plane lateral compaction is caused by the variation of the tow mat width, which varies proportionally to $\frac{\sin 2\phi}{\sin 2\phi_0}$. Hence, from Equation 4.3, and remembering that pure trellis shear creates zero strain along the tow directions, the fibre volume fraction varies according to

$$V_f(\theta) = \frac{t_t(0)}{t_t(\theta)} \frac{\sin 2\phi_0}{\sin(2\phi_0 - \theta)} V_f(0) \tag{4.35}$$

Note that if $\phi_0 \neq 45°$ then at some point the volume fraction will be smaller than that before shear $V_f(0)$. In this case, while the overall volume fraction will obey Equation 4.35, depending on the stitch architecture, the tow mat may develop large gaps rather than decreasing local (tow) volume fraction.

Using McBride's compaction models outlined in Section 2.2.2 with his suggested values for β, V_0, V_a and E_f, the volume fraction can be used to calculate bulk strain and therefore lateral compaction stress.

In order to transform the lateral compaction stress to a fabric shear stress, consider Figure 4.9. Equating the boundary stresses vertically for the top half of the sample reveals that

$$N_s = \frac{2\sigma_b t_t}{\sin 2\phi} \tag{4.36}$$

As outlined at the end of Section 4.3.1.2, appropriately normalised shear forces from different sources can be added as legitimately as shear energies.

Other tow mechanical properties are not included in the model. Possibly the most important of those not modelled is the tow shear stiffnesses G_{12} and G_{13}. This

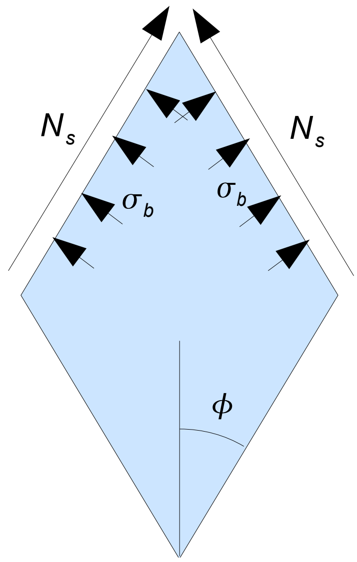

Figure 4.9: A shearing fabric sample of unit length with internal bulk stress σ_b, and the resulting line shear stress N_s.

may be a significant source of textile shear resistance depending on the scale on which it occurs during textile shear.

4.3.2.2 Inter-tow Friction

Crossover friction model

Crossover shear energy dissipation has been discussed previously with regard to viscous textile composites [19]. In collaboration with Harrison [21] a method was developed to determine the energy dissipation due to shearing between crossovers in a dry fabric. The main difference is that for viscous composites, the energy dissipation is related to the instantaneous rate of shearing in the film of viscous matrix fluid separating tows at the crossover. For dry fabrics, tows are considered to be in direct contact at the crossovers and therefore energy dissipation is related to relative displacement rather than the rate of relative displacement. This point is elaborated in the following analysis, in which the mechanism of crossover shear energy dissipation is most conveniently explained in terms of the fabric architecture of woven fabrics rather than NCFs. Nevertheless, the crossover shearing mechanism is also shown to be relevant to energy dissipation in NCFs. During shear, the in-plane shear rate of tows is rarely as high as the overall in-plane shear rate across the composite sheet [19, 52]. This produces a non-uniform displacement profile across the fabric, as shown in Figure 4.10.

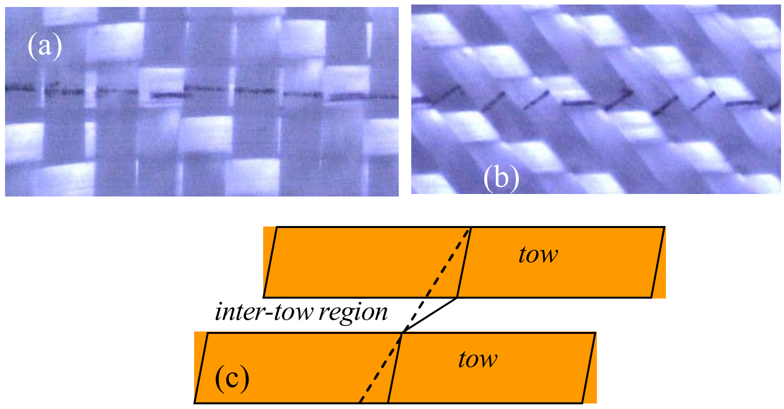

Figure 4.10: 4-harness satin weave glass fibre fabric, (a) black line marked in ink before shear (b) after 40 degrees of shear the black line is clearly broken (c) Shear of two tows and separating inter-tow region. Continuous-line shows local displacement profile across tow and inter-tow regions, dashed-line shows average displacement profile across the fabric sheet.

If the strain profile were uniform then the straight line marked on the fabric in Figure 4.10a would remain straight following shear. The subsequent idealised strain profile due to this heterogeneous shear across the fabric is illustrated in Figure 4.10c. The heterogeneous shear profile across the sample implies relative shear between tow crossovers. In [19] the relative 2-D kinematics occurring between crossovers was derived as

$$\vec{\nu}_{vel} = \{(\dot{\gamma}_t - \omega)(1 - \sin\theta)Y\}\,\hat{\imath} + \{(\omega - \dot{\gamma}_t)(1 - \sin\theta)X\}\,\hat{\jmath} \tag{4.37}$$

where $\vec{\nu}_{vel}$ is the relative velocity field between the crossovers, $\dot{\gamma}_t$ is the in-plane shear strain rate in both sets of tows and in the following calculation is considered constant in time, ω is the relative angular shear rate of the two sets of tows, θ is the material shear angle and X, Y are the position co-ordinates, with the origin at the centre of the crossover. Equation 4.37 suggests that if $\dot{\gamma}_t \neq \omega$ then there is relative motion between crossovers. Equation 4.37 can be used to find the path-line of a given initial position as a function of time, t. Thus, it can be shown that for constant ω, $\theta = \omega t$ and

$$\frac{dX}{dt} = X(\dot{\gamma}_t - \omega)^2 \left\{ \left(t + \frac{\cos\theta}{\omega} \right) (\sin\theta - 1) \right\} - C_1(\dot{\gamma}_t - \omega)(\sin\theta - 1) \tag{4.38}$$

$$\frac{dY}{dt} = Y(\dot{\gamma}_t - \omega)^2 \left\{ \left(t + \frac{\cos\theta}{\omega} \right) (\sin\theta - 1) \right\} + C_2(\dot{\gamma}_t - \omega)(\sin\theta - 1) \tag{4.39}$$

where the constants C_1 and C_2 depend on the initial position of the point, i.e. when $t = 0$, $X(0) = X_0$ and $Y(0) = Y_0$. Thus,

$$C_1 = Y_0 + \frac{\dot{\gamma}_t - \omega}{\omega} X_0 \tag{4.40}$$

$$C_2 = X_0 - \frac{\dot{\gamma}_t - \omega}{\omega} Y_0 \tag{4.41}$$

The energy dissipation due to friction between crossovers is calculated numerically. The method involves discretising the crossover area (see Figure 4.11) with elements numbered 1 to i. Initial positions of the centres of the elements are arranged in a square grid pattern. Equations 4.38 and 4.39 are both non-separable first order differential equations. Thus, to determine $X(t)$ and $Y(t)$ as a function of time, the Runge-Kutta technique is employed [47], where the time steps, t_j, are numbered 1 to j. The distance increment, l_i, of each element's path-line, between times t_j and t_{j+1}, is calculated. If the path-line of a given element meets the condition that it is inside the area of the crossover at time t_j and remains within the new crossover area at time t_{j+1}, then the distance increment of the path-line, l_i, is used in the subsequent energy calculation.

This condition is illustrated in Figure 4.11, which shows how the path-lines of certain elements enter while others leave the crossover area during the course of the simulation. In Figure 4.11(b) two path-lines are circled. The black line circles a path-line about to leave the crossover area, while the grey line circles a path-line that has entered the crossover area during the course of the simulation. In Figure 4.11(c) the initial position of the path-line has left the crossover area (circled) even though the current position of the path-line remains inside the area. Consequently, this path-line is included in the energy calculation at the time step illustrated.

The area of each element, $A(t_j)$, is defined as the crossover area at time, t_j, divided by the number of elements inside the area at time t_j. Energy dissipation is calculated by multiplying the distance increment of each path-line, l_i, that meets the condition described above, by the element area, $A(t_j)$, the normal pressure between crossovers, $P(t_j)$, and the coefficient of dynamic friction, μ. This calculation is summed over all the elements to find the energy dissipation, $U_X(t_j)$, due to friction at the crossovers during a given time increment. Thus,

$$U_{Xj} = P_j X_j \mu \sum_i l_i \tag{4.42}$$

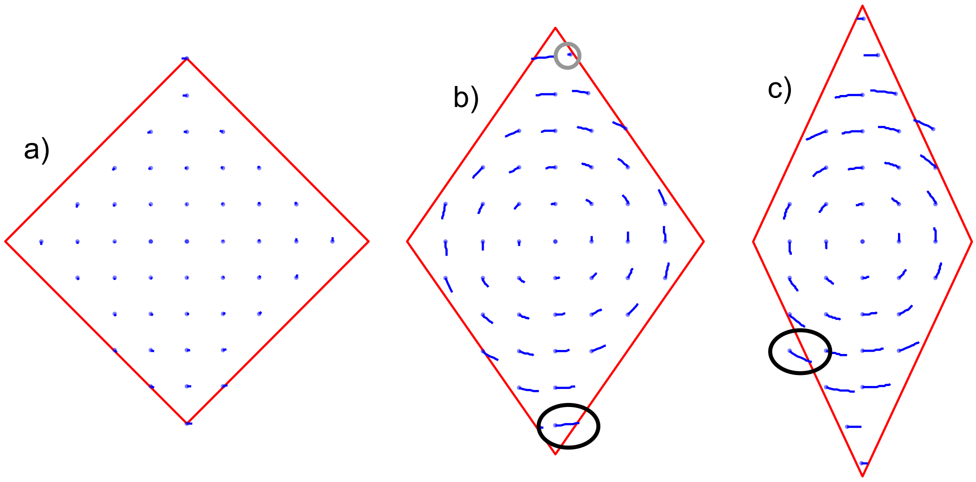

Figure 4.11: Discretised crossover shown at shear angles of (a) 0° (b) 20° and (c) 40°. The points indicate the initial position of the path-line inside the crossover area while the lines indicate the subsequent paths of the path-lines. In this calculation $\dot{\gamma}_t = 0.5\omega$.

where the j subscript indicates the value of the variable at time t_j. The normal pressure can be estimated using the compaction model outlined in Section 4.3.2.1. Using Figure 3.4, this energy can be equated with the work required to displace the top corner of the crossover by a distance, $d(t_j)$ in the time increment t_j to t_{j+1}. For sufficiently small time increments the axial line force, $N_d(t_j)$, can be considered constant and is found by dividing the energy U_{Xj} by the distance increment d_j.

NCF crossover scales

It is interesting at this point to examine the effect of the size of the crossover on the shear force per unit length of the fabric. The relevance for this will become clear when NCF crossovers are considered. For the purposes of the study presented the pressure acting on the surface of the crossover, P_j, was taken to be constant with increasing shear angle (see Figure 4.12 caption). Convergence was obtained using 40 elements. The only parameter varied between calculations was the side length of the crossover. Figure 4.12 shows that for a constant pressure, the crossover contribution to the shear force decreases with increasing shear angle and that the shear force is directly proportional to the side length of the crossover. For woven fabrics this length dependence is a minor point since the size of the crossovers is well defined by the width of the woven tows. However, this is not the case for NCFs. As a consequence, the crossover geometry in NCFs requires investigation.

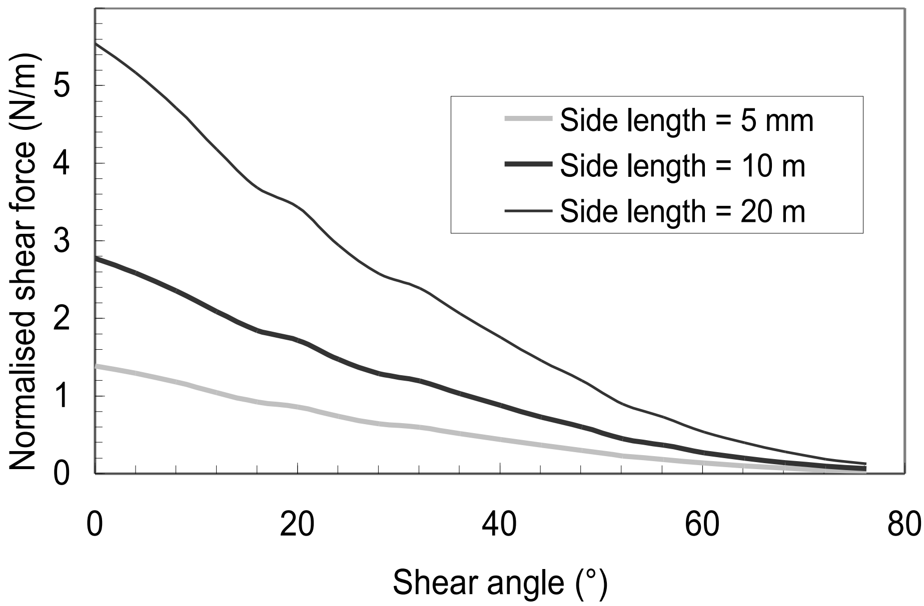

Figure 4.12: Effect of crossover side length on shear force produced by crossover shear, calculated using arbitrary parameters, $\mu = 0.3$, $P_j = 3000\mathtt{Nm}^{-2}$, $\dot{\gamma}_t = 0.5\omega$. The shear force per unit length increases linearly with the side length of the crossover. Oscillations in the predicted shear force result from the spatial discretisation method used in the numerical code

Many NCFs comprise two layers of unidirectional fibres, initially orientated at 90° to each other and stitched together. Each layer of the fabric is originally manufactured using bundles of fibres, or tows, laid in parallel. These tows are then pierced by the stitching thread. Consequently, the stitch appears to define new tows in the fabric. However, the actual situation is often more complicated since fibres within one 'apparent' tow can move across an apparent tow boundary. The degree to which fibres move across apparent tow boundaries is related to the alignment between fibre orientation and stitch pattern. A consequence of this is that the dimensions of the crossovers may span a relatively broad range of length scales and in general will be of initially rectangular form of various length/width aspect ratios, rather than square.

To investigate the effect of crossover shearing on NCFs, measurements were made for a tricot stitch warp knit NCF E-glass fabric, FGE 106hd (see Table 3.2), with an areal density of 936g/m^2. The tricot stitch is illustrated in Figure 4.2 and a photograph of the fabric is shown in Figure 4.5. The tows are initially orientated at $\pm 45^\circ$ to the stitch, with initial stitch lengths s_l = 2.5mm and stitch spacing s_g = 4.17mm. Photographs of both sides of the fabric recorded before and after positive and negative shear, where positive shear refers to stitch extension in the warp direction, are shown Figure 4.13).

Image analysis of the form of the shear strain profile, indicated by the marked line in Figure 4.13 on both sides of the fabric, has provided statistical data on the length scale and shape of the crossovers, along with the shear angle in the tows χ, versus fabric shear angle θ. Results shown in Figure 4.14 show wide distributions of tow width on both surfaces of the fabric following positive and negative shear. Note that tow width is only defined as such for the purposes of defining the size of the cross-section, determined by stochastically distributed preferential slip planes in the fibre mat. These slip planes are created by an interaction of the original tow size, the stitch intersection points, and the local alignment of the fibres. Tow

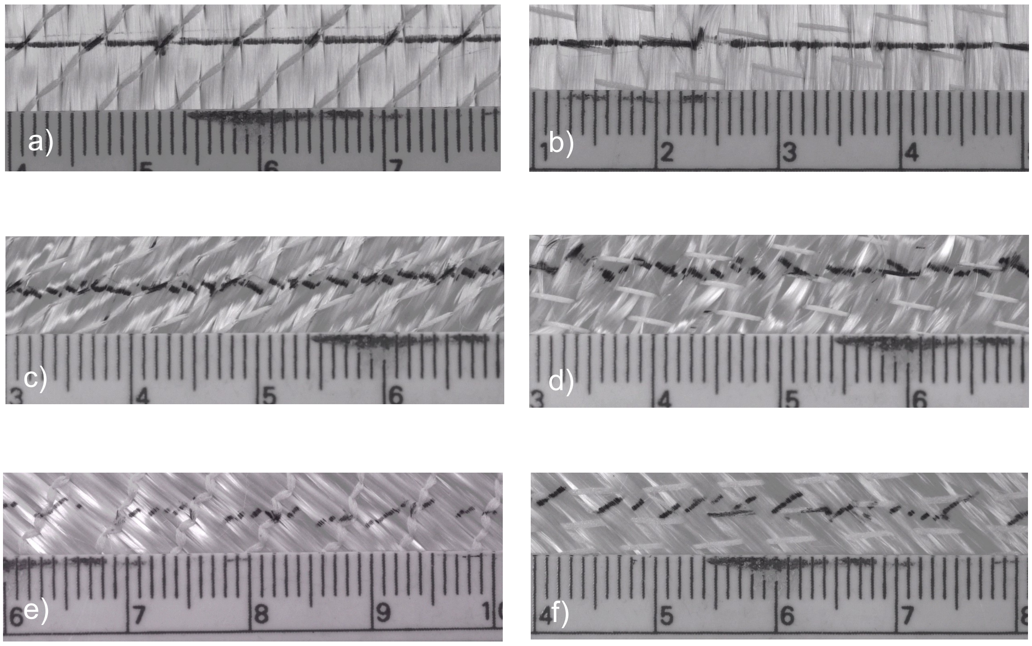

Figure 4.13: A continuous black line was marked across both sides of the fabric surface and photographed following shear.(a) overlap side, unsheared, (b) underlap side, unsheared, (c) overlap side, positive shear, (d) underlap side, positive shear, (e) overlap side, negative shear and (f) underlap side, negative shear. Units of the ruler shown in the pictures are cm.

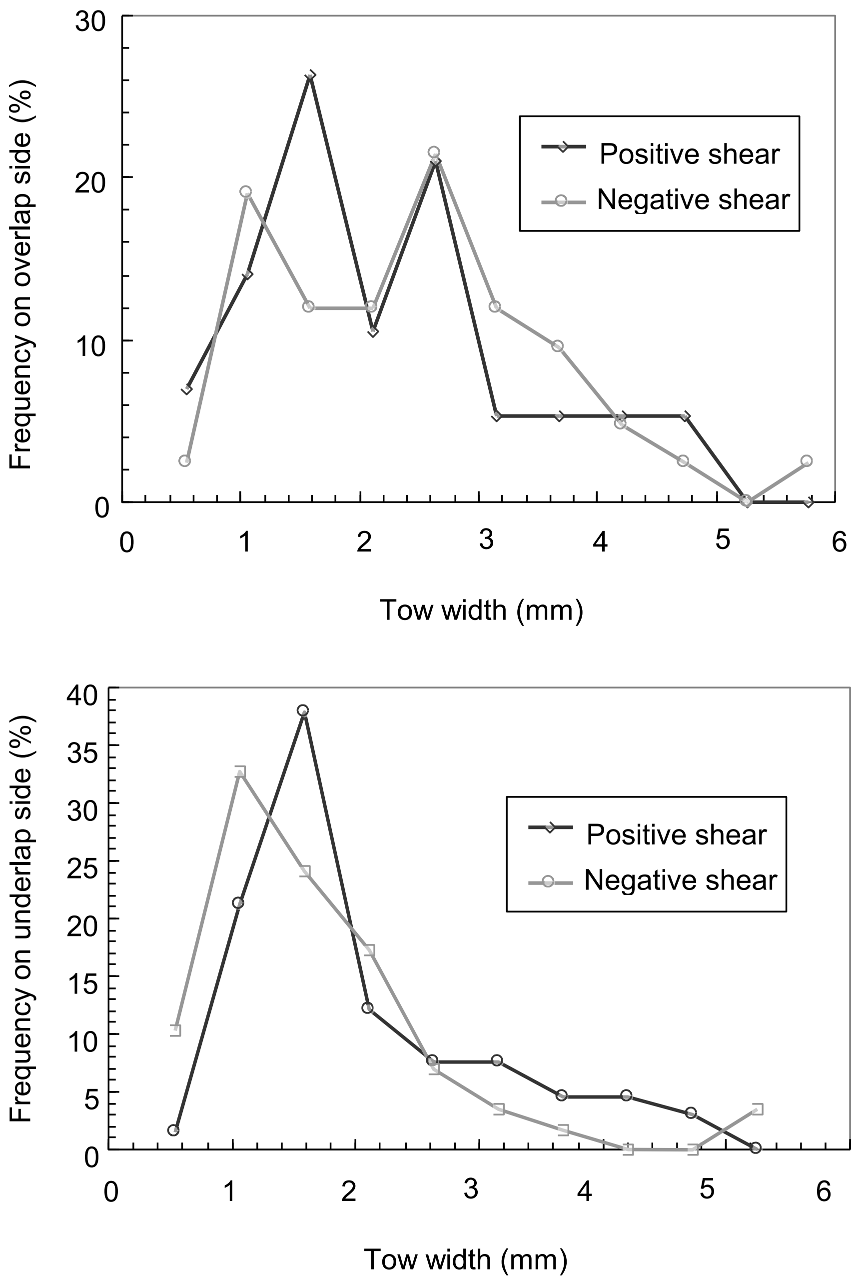

Figure 4.14: Statistical data measured from image analysis (a) tow width on diagonal side, positive shear 57 measurements, negative shear 42 measurements (b) tow width on chain side, positive shear 66 measurements, negative shear 58 measurements.

shear angle measurements in Figure 4.15 also indicate a large amount of scatter. For the purposes of this thesis the average (mean) values of the data are used. This is reasonable, as it has already been established that the shear response is linear with cross-over size, so that modelling for an average crossover size will yield an averaged shear response. Thus, the average crossover side length was calculated to be 1.87

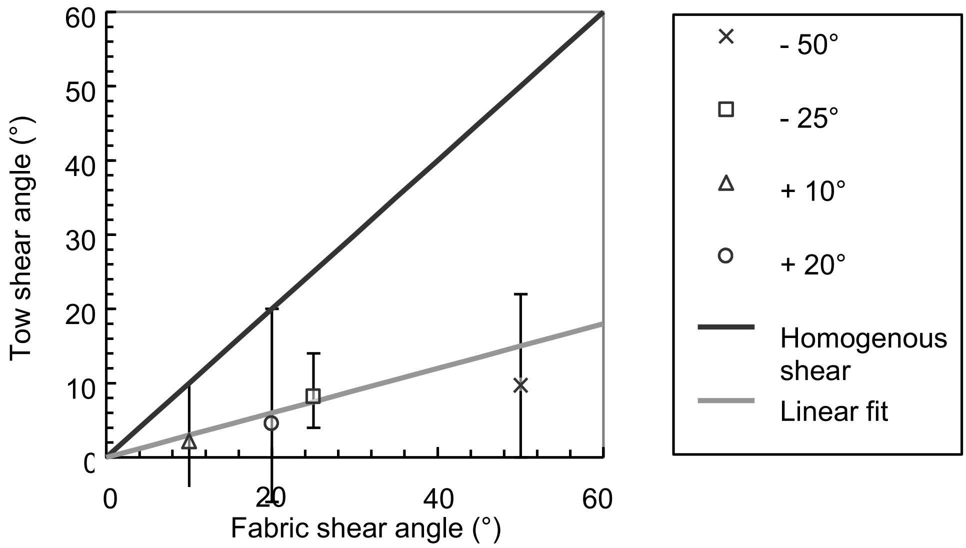

Figure 4.15: Tow shear angle, χ, versus fabric shear angle, θ. Data collected following both positive and negative shear (see legend). Each point is an average of at least 40 measurements and error bars indicate the absolute range of the data. Black line indicates homogeneous shear and grey line indicates a linear fit with $\chi = 0.3\theta$ to the data.

mm and the average tow shear rate, $\dot{\gamma}_t$, was estimated to be approximately 0.3ω.

Note that Figure 4.15 indicates that the tows only shear at 0.3 of the rate of the textile shear. This indicates that tow inter-slip is a substantially lower energy deformation mechanism than tow shear. Thus, even though tow shear stiffness may be significant, other deformation mechanisms allow tow shear to be ignored for dry

NCFs.

Finally, the relative energies associated with the slip of parallel tows past each other, the crossover frictional effects, and tow shear could be added in a more comprehensive model in order to find the minimum energy fraction of tow shear to textile shear. This could be compared to experimental observations demonstrated in Figure 4.15.

4.3.3 Tow - Stitch interactions

So far, stitch tension, stitch friction, tow compaction and inter-tow friction, have been modelled. Tow compaction is the dominating contribution to the shear energy at higher shear angles. Stitch tension and friction dominate more at low shear angle, and cause the shear asymmetry exhibited by these fabrics. It is worthwhile examining interactions between tow and stitch effects. In modelling tow-stitch interactions, the problem can be simplified by considering the fabric thickness, which has so far been assumed to be constant.

If the fabric is considered to be at a constant thickness, the tows will laterally compact until they approach their compaction limit, at which stage the shear force will go up dramatically. Experimental shear tests (see Section 3.3.3) show a more gradual increase in shear force than this would predict, indicating that the fabric thickens as it is sheared, thus counteracting the effect of shear angle on the fibre volume fraction and therefore bulk stress in the composite.

In order to illustrate the connection between tow-stitch interaction and fabric thickness, Figure 4.16 represents a section through a tow in an NCF, with all of the forces in the through-thickness direction indicated. The models for both the com-

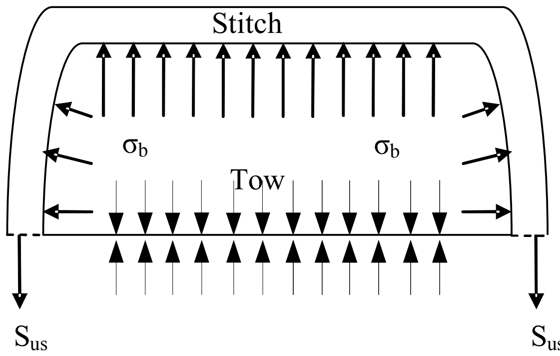

Figure 4.16: Section through a tow with a stitch running over it, showing direction of stitch tension and tow compaction stress.

paction of the tows and the tension placed on the stitching allow these quantities to be expressed as functions of the fabric thickness (t), and the shear angle (θ_s). So far, the thickness of the fabric has been taken to be constant with shear angle, in order that the equations could be expressed solely in terms of the shear angle. This assumption is reasonable for smaller shear angles, and allows other effects to be modelled independently, which is very convenient. At this point, however, a theoretical investigation should be made into the consequences of varying the thickness for any shear angle such that the stitch tension and tow compaction forces are balanced.

The unit stitch in a standard tricot stitch pierces the fabric 4 times. Thus at the crudest level, the tension in the stitch can be made to equate the lateral compaction force, which is calculated as the compaction pressure applied over a quarter of the surface area of the unit cell. As the equations are too complicated to combine for an analytical solution, an MS Visual Basic macro has been written within MS Excel that sets the thickness such that the stitch tension is equal to the tow compaction stress multiplied by a quarter of the unit cell surface area. Figure 4.17 shows the variation of thickness with shear angle for three stitch lengths. The drop in thicknesses seen at positive shear for certain stitch lengths is a result of the increase in stitch tension predicted. The 5mm stitch length fabric shows a sudden jump in thickness at the point at which the stitch fails, modelled as a sudden failure at the breaking strain of 0.17, after which the stitch is assumed to no longer affect the thickness values. This is an unrealistic aspect of the model, in that when the stitch does fail, it only breaks in places, and then slips near to the break points thus only partially relieving the tension felt over most of the textile. The overall fibre volume fraction value of 0.35 is also fairly low for stitched non-crimp fabrics, as the value is taken from V_0 for the compaction equations used. Finally, the compaction model does not restrict out-of-plane thickness increases, leading to entirely unrealistic thicknesses.

4.4 Combined shear model

The model was implemented in an Excel spreadsheet. The energy contribution for each mechanism outlined above was calculated at shear increments of half a degree. Finally, the energy contributions were summed and differentiated to derive the total shear torque and therefore the total shear force.

The shear model combines at the energy level. This is very straight forward, as each energy contribution outlined sums up to give the total energy for shear, and then the same differentiation technique can be applied to derive the total shear force. Whilst this is the most physically appropriate approach for combining the different effects modelled during shear, the linear nature of the differential operator means that it is as valid to differentiate the sum of the energies as it is to sum the differentials of

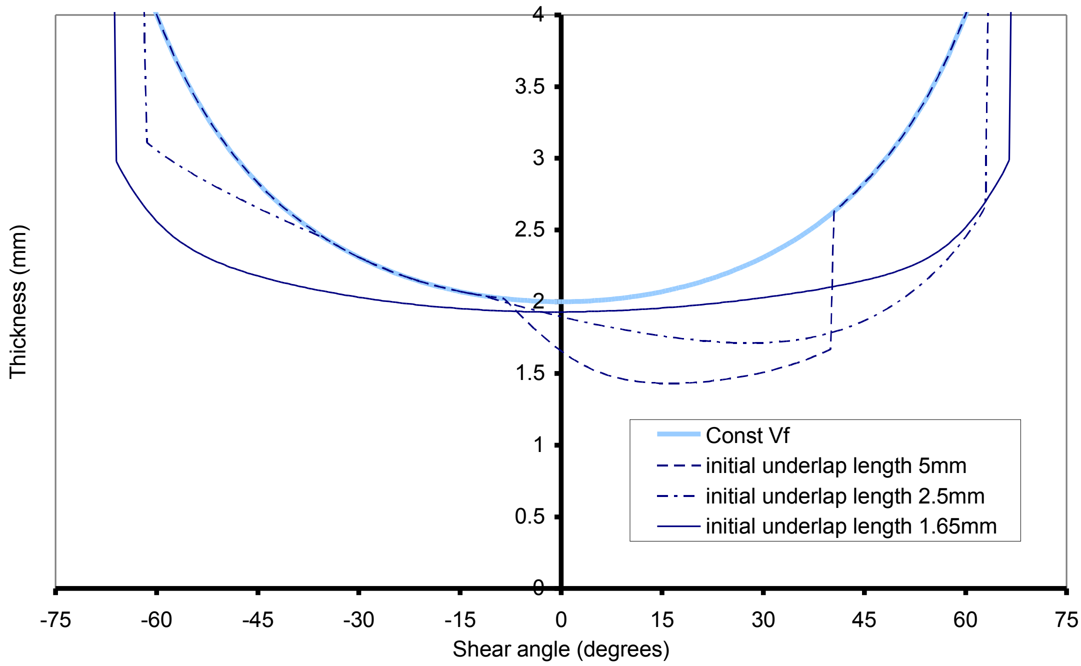

Figure 4.17: Balancing stitch tension and compaction effects: Thickness values such that stitch tension is equal to the bulk compaction stress applied over a quarter of the unit cell, taking the material to have a fibre volume fraction of 0.35 when it is 2mm thick and at zero degrees shear. Constant V_f is given as reference.

the energies (Equation 4.34). This means that the individual normalised shear forces can be added to calculate the total shear force with equal validity. Figure 4.18 compares all four curves for the non-crimp fabric model developed, demonstrating that most of the deformation effects can be addressed independently before summation for the overall shear response. Examination of the different shear force contributions

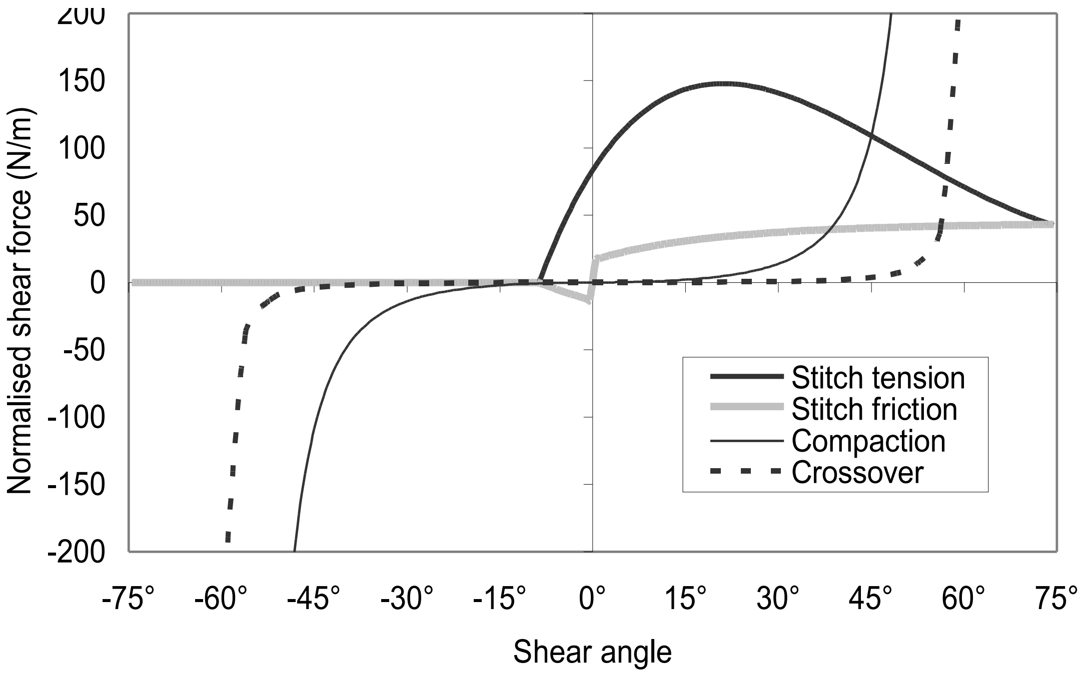

Figure 4.18: Shear contributions for a non crimp, tricot stitch fabric, modelling stitch tension, friction, lateral tow compaction, and inter-tow friction.

shows that at low positive shear angles the stitch dominates the textile shear stiffness. However, as lateral tow compaction increases, this begins to dominate the shear response, and the sample quickly approaches its locking angle. Crossover friction at this crossover size is a small fraction of the lateral compaction force and therefore can be neglected.

Combination at the energy level also allows a more generic shear model to be devised, where different shear contributions are summed according to the fabric architecture undergoing shear. This is illustrated in Figure 4.19. Souter [60], in his

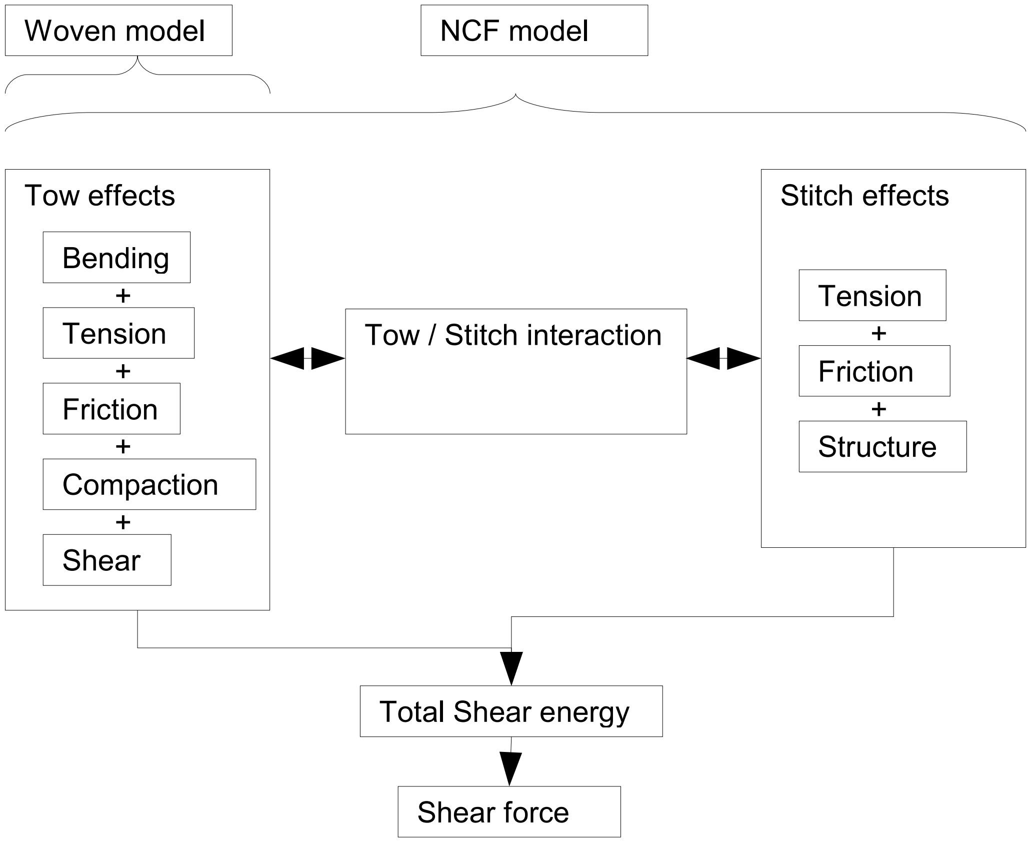

Figure 4.19: The different meso-mechanical deformation mechanisms that control fabric shear.

generic woven shear model used compaction and tow bending models to inform the tow friction. However, by evaluating the *energy* to compact and bend the tows, as well as the crossover frictional energy, a more complete shear model could be devised. Furthermore, combining these effects with those developed here for non-crimp fabrics, and others such as tow shear, would enable a shear model to be developed that can model many textile structures.

4.5 Results and Discussion

In modelling the non-crimp fabric described before, certain material values must be assumed. The initial fabric thickness, t_0, is taken to be 2mm and the coefficient of friction between glass/glass and glass/stitch contacts was taken to be 0.3. The measurement of textile thickness is difficult, as most repeatable experiments tend to involve the measurement of the textile under a given pressure [60]. In the model the initial thickness must not be under a pressure, thus the thickness was chosen such that the given areal weight of the fabric was at a volume fraction that corresponds to the minimum volume fraction stated by McBride [45] in his compaction model. The factor A_sE_s, as discussed in Section 4.3.1.1, has been measured in tensile tests and a sixth order polynomial fitted to data. For the reasons given above, values of stitch run in have been tailored to create a small, consistent amount of stitch tension at 0° shear.

To validate the model, the results for the non-crimp fabric fabric model are first compared to picture frame and bias extension results, normalised according to Section 3.3.2 and Section 3.4.4. Figure 4.20 makes the comparison for results for the constant thickness model and the thickness varying model. The model predictions can be seen to correspond fairly well to measured results, within the variability of the different tests. Varying the thickness seems to be a valid approach up to a certain extent, giving a result somewhere between that for picture frame and that for bias extension, up to about 50° in the positive shear direction. Beyond 50°, the curve dips whereas both picture frame and bias extension do not. This seems to correspond to the point at which *both* stitch tension and tow compaction become very high. The

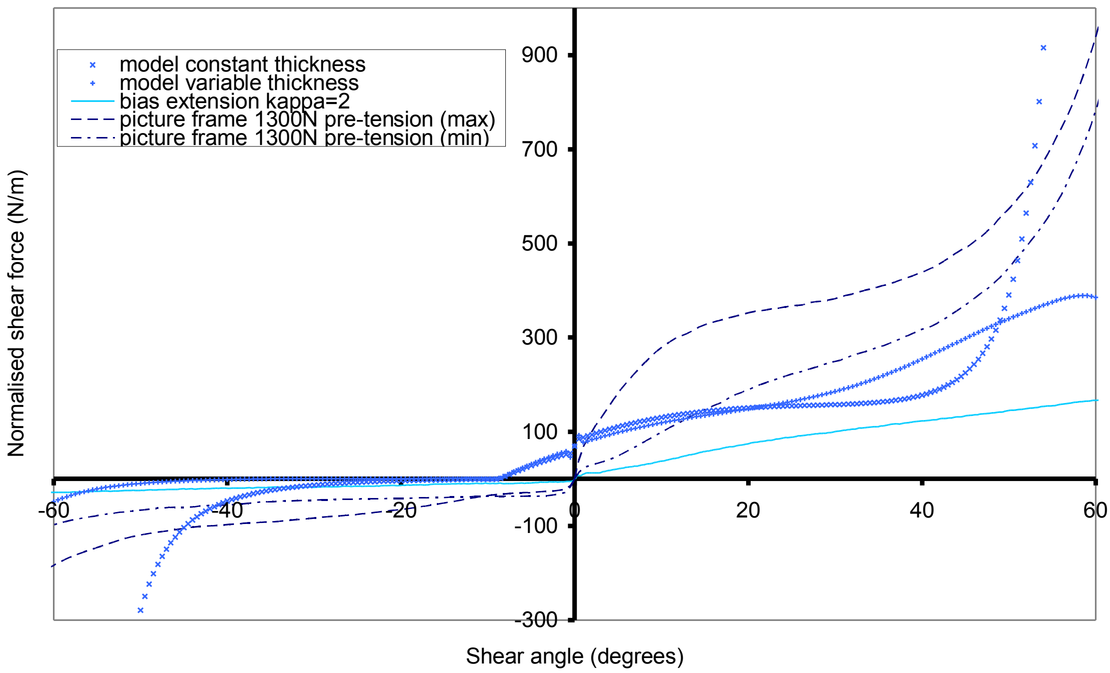

Figure 4.20: Comparison of picture frame, bias extension, constant thickness model, and varying thickness model for FGE 106hd shear response.

approximation that the tow is evenly compressed by the stitch over the entire unit cell must clearly become unrealistic under these conditions, when it is likely that the tow is substantially more compressed directly under the stitch than anywhere else.

Samples of FGE 106hd with different stitch lengths were manufactured to test the non-crimp fabric shear model. Figure 4.21 predicts that if FGE 106hd were to be produced at a stitch length of 1.65mm, it would exhibit symmetric shear properties, whereas with a 5mm stitch it would show extreme shear asymmetry. These

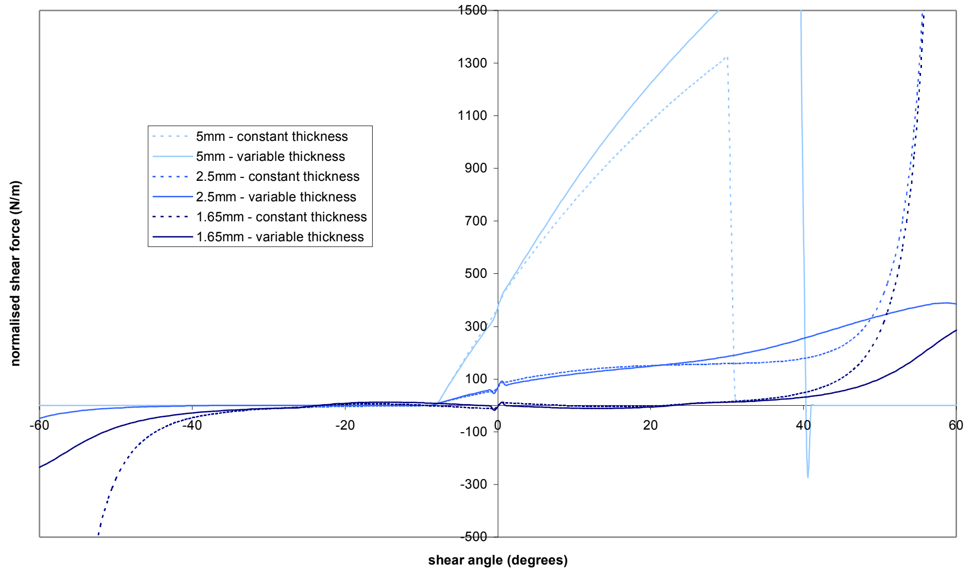

Figure 4.21: FGE 106hd modelled shear response at different stitch lengths - 1.65mm, 2.5mm and 5mm. Thickness was varied to balance stitch tension with compaction, and results were compared to constant thickness predictions.

predictions were compared to bias extension results (Figure 4.22) for the standard material as well as bespoke samples made at 1.65mm and 5mm stitch lengths.

Results for these extreme stitch lengths do not correspond to predictions very well, although trends are replicated. However, it can be seen that the 1.65mm

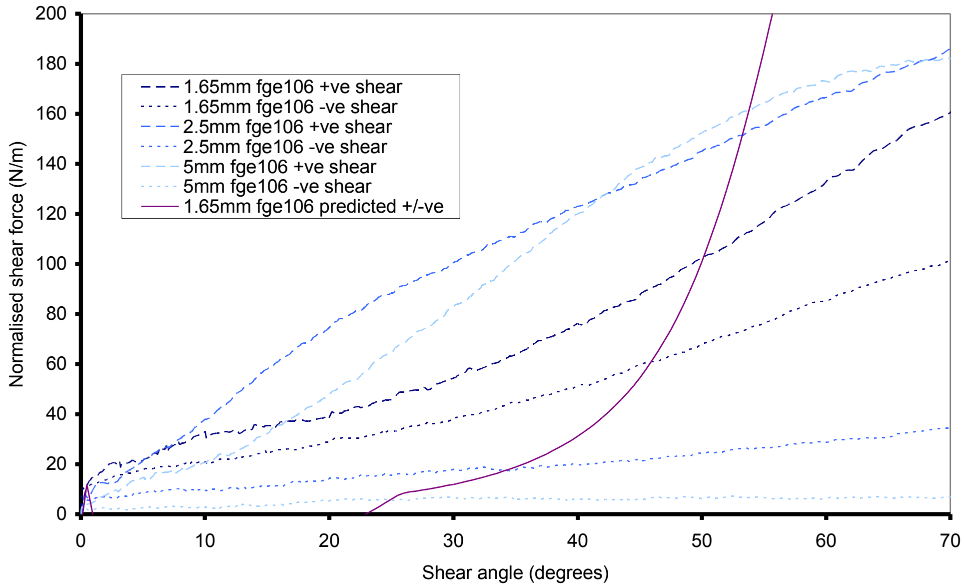

Figure 4.22: Measured FGE 106hd normalised shear response for the material manufactured at different stitch lengths - 1.65mm, 2.5mm and 5mm.

sample does exhibit symmetric shear response, whereas the 5mm sample shows the greatest shear asymmetry. It is interesting to note that the effects of changing the stitch length show during negative shear rather than positive as is predicted by the model. It is possible that the reasons for the errors in positive shear predictions result from the assumptions made in balancing stitch tension and tow compaction - this has already been observed to be inadequate at high tension and compaction situations. It seems likely that the assumptions made in the development of the model do not hold very well for negative shear, where it has been observed that the stitch response to extension parallel to the stitch direction causes the underlap to take a zig-zag form. The current model does not take such stitch deformations into account, neither does it allow for the effects of these on tow deformation.

4.6 Conclusions

The effects of the stitching in non-crimp fabrics on their shear response has been investigated and some simple models have been proposed to predict the shear force curve. An energy based shear model has been proposed for summing the effects of shear, and a range of non-crimp fabrics have been modelled in this manner with predictions subsequently compared to measured results. Results correspond quite well to the baseline fabric shear response: However, fabrics manufactured to test the limits of the model show that there are several factors that need more analysis. Specifically,

- The tow / stitch interactions require a more sophisticated analysis. This particular effect cannot be modelled as a separate energy contribution, rather it is an interaction between other energy terms.
- The current model only assesses the lateral compaction caused by tow shear. The frictional resistance as fibres move past each other should be investigated as a shear response mechanism.
- No model has been offered to predict the average and distribution of crossover length scales in non-crimp fabric shear, rather experimental data for a single textile type has been relied on.

Many preforms for liquid transfer moulding have a binder treatment that allows them to hold their preformed shape during transfer. This could introduce rate dependant effects similar to those found in prepregs, but with the varying V_f that is characteristic of dry fabrics. These effects have not been modelled.

The approach developed here lends itself to further development in allowing textile-architecture specific mechanisms to be modularised. This tactic can allow for inclusion of the ever expanding technologies for creating more complex textiles. Ultimately, fabric architecture understanding should allow the design of a fabric for a specific application, allowing the resulting deformed pattern to correspond optimally to the requirements.

Chapter 5

Further development of energy based kinematic drape model

5.1 Introduction

In moving to an automated manufacturing environment, composite designers need to anticipate the effects of the manufacturing environment and process on the product, and to modify the design to take these factors into account. Whilst FE modelling can represent the entire process including manufacturing concerns, it is slow to run and requires a significant level of resource.

Section 2.3 outlines published progress towards forming models. The energy based kinematic approach developed from Long and Rudd [41] and Souter [60] is taken as the starting point and further developed.

This chapter looks at using a tool much more suited to earlier stages in the design cycle, and looks to adding two important modelling capabilities to this tool. In so doing, manufacturing issues can be predicted and solved much earlier in the design of the part, resulting in a product that can be substantially easier and cheaper to manufacture, whilst performing to design specification. The two factors are the incorporation of a fabric blank-holder and stochastic material variation models to the energy minimisation kinematic drape tool.

5.2 Blank-holder effects on draping patterns

As previously mentioned, a fabric blank-holder is similar in concept to metal forming blank-holders. If composite manufacture is to be automated, an alternative to the hand lay-up technique common in current processes must be found. For small to medium parts for resin transfer moulding (RTM) this can be achieved with a blank-holder that, like metal stamping, holds the fabric in tension while the male tool is punched through the material into the female tool.

It should be pointed out that the use of a blank-holder is not a panacea to the automated draping problem. The use of a blank-holder could result in substantial wastage caused by the excess textile that is held in the blank-holder after moulding. This presents both financial and environmental challenges that have not yet been addressed. Additionally, many complex geometries that may drape successfully by hand may prove more of a challenge when formed with a blank-holder and matched tooling. Hands that tease material into and over sharp corners may maintain a more viable evenness of material distribution, whereas a blank-holder operation may stretch the material excessively in some places and compress it in others. This natural redistribution that occurs in hand lay-up also decreases the chances of wrinkling, as it is possible in some situations to “tease out” wrinkles. Hand lay-up, on the other hand, is even more time consuming if such fiddly jobs are required, adding substantially to the process cost and decreasing its viability in medium and high volume runs. As a result, it is vital that automated draping methods be explored and their limitations better understood.

Previous experiments with such manufacturing approaches within the University of Nottingham have shown that for some component geometries the amount of clamping force applied to the blank by the blank-holder can affect the draping results in terms of wrinkling and shear distribution. Such effects are demonstrated in Section 5.2.4. Thus the use of a blank-holder provides another processing factor that can be adjusted to facilitate better preform manufacture, and so it is desirable to include it in design codes for forming analyses. However, the overriding advantage of draping codes is their ease of use and fast computational times. Any blank-holder models must therefore be incorporated into the code with the same philosophy, so that accuracy may be sacrificed for a simpler, computationally faster, and easier to use approach - a fully accurate blank-holder model can be subsequently included in FEM simulations.

The energy minimisation approach optimises the orientation of the generator paths so as to minimise the energy required to drape the whole part. Previously, in calculating the energy required to drape the part, only two energy contributions have been considered. These were the shear energy (see Section 2.2.2.1, Generic weave shear models) and the fibre bending energy. [Bending energy does not contribute significantly to forming energy in normal circumstances, however it provides an energy penalty that prevents the solution from bending the fibres back on themselves.] To incorporate blank-holder effects, a third energy term can be added to the forming energy, to estimate the energy required to pull the fabric through the blank-holder.

5.2.1 Basis of method

In order to minimise user input, specification of the blank-holder shape has been omitted, and assumptions have been made about the frictional interaction between the blank-holder and the fabric. The user is therefore required to input only two variables: The overall blank-holder force, and the tool/fabric friction. Thus the effects of blank-holder force can be evaluated without requiring a detailed (or in fact any) design of the blank-holder tool to be undertaken.

In order to achieve this, a number of assumptions were made:

- When any part of the blank contacts the tool, it remains there regardless of subsequent actions. This assumption is inherent in the kinematic approach, which maps the fabric onto the geometry rather than undertaking a chronological simulation of the draping process.
- The blank-holder shape can be thought of as being circular at an arbitrary radius, with the centre of the circle being at the first point of contact with the tool, which is taken to be the point at which the kinematic generator paths cross over. This does *not* mean that the part being modelled must be circular, or have rotational symmetry. Any component geometry can be modelled, although it seems likely that the less the similarity of the shape of the blank-holder is to a circle, the more inappropriate the force distribution assumption in Equation 5.3 becomes.
- The blank-holder is assumed to lie in the x-y plane so that the tool moves in the z-direction.
- The parts of the fabric to most recently contact the tool are taken to be level with the blank-holder (i.e. same z-coordinate) at every point, thus ignoring the shape of the fabric between the tool and the blank-holder and (due to

the previous assumption) reducing the blank-holder consideration to a two dimensional problem. Without this assumption the precise geometry of the blank-holder would be required, and the problem would have to be considered in a chronological manner, an approach that is better tackled by FE methods. This is physically inappropriate, and is partly the result of the attempt to model a chronological effect in a non-chronological, mapping approach. However, the significance of the assumption should be assessed by the accuracy of the results.

- The coefficient of friction between the fabric and the blank-holder has been assumed to be 0.2. This is a value based on some characterisation on the fabric within the University of Nottingham, using the same rig reported by Long and Clifford [40]. For different cases the value can be changed.

Projecting the deformed and undeformed boundaries onto the x,y plane, as was done in this case, is particularly easy in that the z component of their position vectors is simply ignored. However, it is relatively simple to project the boundaries onto any plane, if a situation is identified in which the direction of the tool movement is not parallel with the z-axis.

Consider the energy minimisation draping approach, illustrated in Figure 5.1. Each generator path (shown in red) is extended one step away from the initial crossover point. Having calculated the rest of the nodes around the new boundary from geometric constraints, the energy required to drape the fabric up to that step is then evaluated. Finally, the angles of each of these four new generator path segments are chosen so as to minimise the overall forming energy. The generator paths are extended in this way until the geometry has been fully covered.

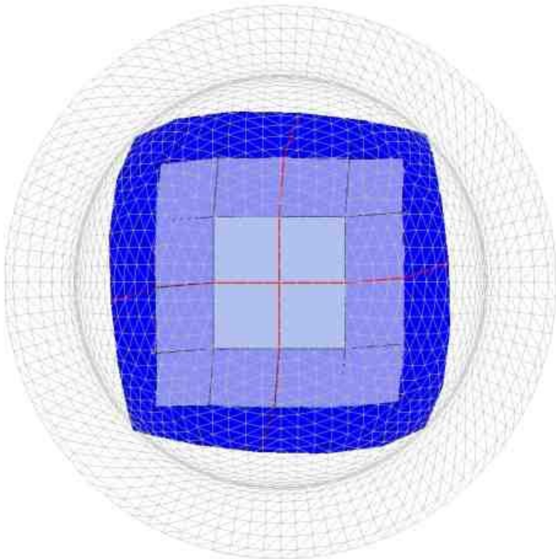

Figure 5.1: The kinematic draping process demonstrated on a hemispherical geometry. After the user has specified the initial crossover point and angles of the generator paths (marked in red), they are extended one step out at a time and any other nodes calculated. The first draping step has been highlighted in light blue, the second in medium blue, and the third in dark blue.

To be incorporated into the minimisation process, the blank-holder energy must be evaluated at each of these steps. To do this, firstly the undeformed blank-shape of the part of the fabric under consideration is calculated. As an example, Figure 5.2 illustrates the draped and undraped positions of the outermost nodes of the fabric at the final draping step of a cone shaped geometry, taken from a Rolls-Royce Tay nose cone component (pictured in Figure 5.7).

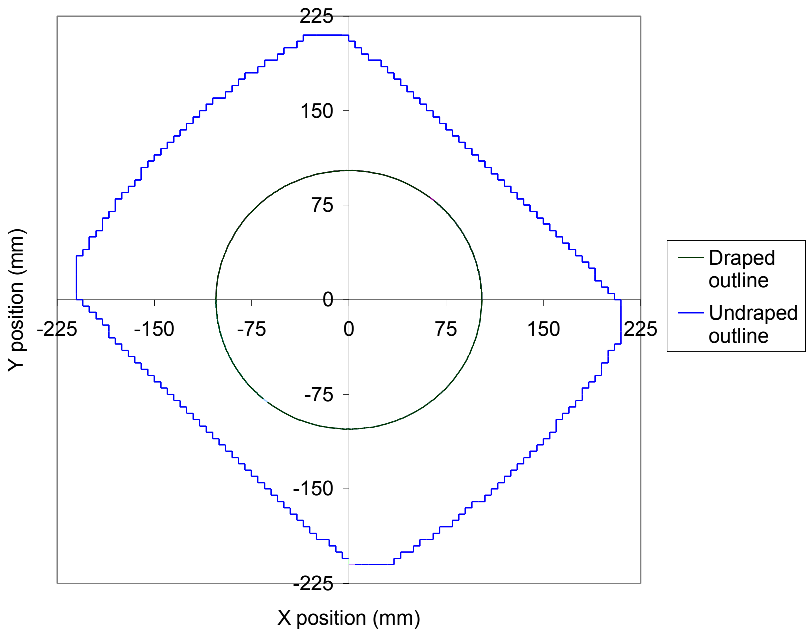

Figure 5.2: The position of the outermost nodes of the fabric, modelled covering a Tay nose cone geometry, projected onto the x-y plane. The energy required to pull the fabric from the undraped to the draped positions through the blank-holder is added to the calculated shear and bending energies to produce an "overall" forming energy. x and y values are in mm.

Consideration of Figure 5.2 reveals that in order for the boundary to have moved from its undeformed state (in blue) to its deformed state, it must have pulled through the blank-holder by a distance similar to the difference in radius of the two boundaries. As both faces of the textile are in contact with the blank-holder, frictional energy to pull it through the blank-holder is taken to be equal to twice the blank-holder force F_{BH} multiplied by the frictional constant μ_{BH}, multiplied by the linear distance pulled through the blank-holder D_{BH}, so that the total energy is doubled

$$U_f = 2\mu_{BH} F_{BH} D_{BH} \tag{5.1}$$

However, Figure 5.2 illustrates a difference in projected area, rather than a change in linear distance. In order to reduce the former to the latter, the boundary drawn by the outermost draped nodes at any draping step is considered in segments defined by the straight lines between adjacent nodes. For each of these the distance ΔD_{BH} can be estimated as the difference between the distance from the generator path crossover to the undraped $D_{undraped}$ and draped D_{draped} boundary segment midpoints, Figure 5.3.

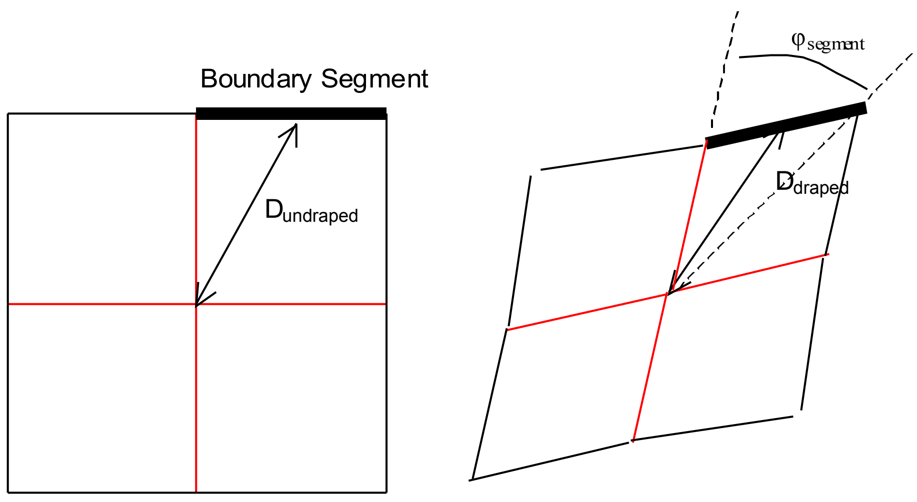

Figure 5.3: The segment distance contribution, $\Delta D_{BH} = D_{undraped} - D_{draped}$

To determine how much the segment contributes to the overall blank-holder energy, an equivalent segment force, ΔF_{BH} needs to be defined. To do this, consider the circular blank-holder of arbitrary radius, with area A_{BH}, in Figure 5.4.

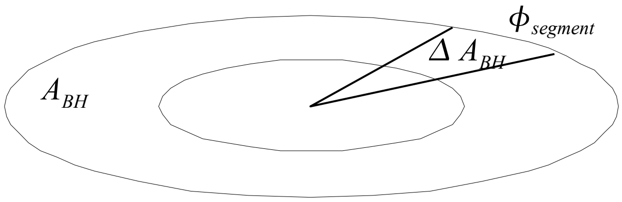

Figure 5.4: Circular blank-holder with arbitrary radius, of area A_{BH}.

The pressure applied by the blank-holder to the fabric is $\dfrac{F_{BH}}{A_{BH}}$, which is the pressure applied to the segment $\phi_{segment}$. If this segment is defined as the average angle subtended by the segment ends to the generator path crossover (Figure 5.3), then the area of the segment, ΔA_{BH}, is equal to A_{BH} multiplied by the angular proportion of the segment:

$$\Delta A_{BH} = \frac{\phi_{segment}}{2\pi} A_{BH} \tag{5.2}$$

Hence the equivalent force that applies to the segment is the pressure multiplied by the area:

$$\Delta F_{BH} = \frac{\phi_{segment}}{2\pi} A_{BH} \frac{F_{BH}}{A_{BH}} = \frac{\phi_{segment}}{2\pi} F_{BH} \tag{5.3}$$

With this the energy contribution of the segment to the overall blank-holder energy can be calculated as

$$\Delta U_f = 2\mu_{BH} \frac{\phi_{segment}}{2\pi} F_{BH} D_{BH} \tag{5.4}$$

so that the total blank-holder energy is the sum of that due to the segment boundaries

$$U_f = \sum_{boundary} \Delta U_f \tag{5.5}$$

This can be calculated for the latest boundary at each step in the kinematic modelling process. Note that at each step, the *total* energy required to pull the textile through the blank-holder from undeformed to deformed is calculated afresh: It is the difference between the fully deformed boundary and the *undeformed* boundary that is calculated, so that the energy calculated is not incremental and does not need to be added to the previous step's blank-holder energy value. It is important to remember this when incorporating the blank-holder energy values to the energy minimisation algorithm, as each energy contribution should be included as the total for the draped pattern so far rather than the incremental amount for each step.

5.2.2 Kinematic demonstration

A simple implementation of the approach is to evaluate the blank-holder energy in the manner outlined above for a traditional kinematic drape in which the generator paths are projected at different inter-fibre angles rather than set according to the energy minimisation algorithms, as illustrated in Figure 5.5. This illustrates the differences in energy resulting from pulling different non-crimp fabric quadrants through the blank-holder. Taking the outline of the draped net, the energy to pull it through the blank-holder can be assessed using the technique outlined above. The energy values are presented in Figure 5.6 as the angle between generator paths is varied from 0° to 55°.

It is very apparent that as the draping pattern is skewed, the total energy required to pull the preform through the blank-holder increases. In the energy minimisation approach, this should result in an energy penalty to shear asymmetry that is dependent on the blank-holder pressure applied.

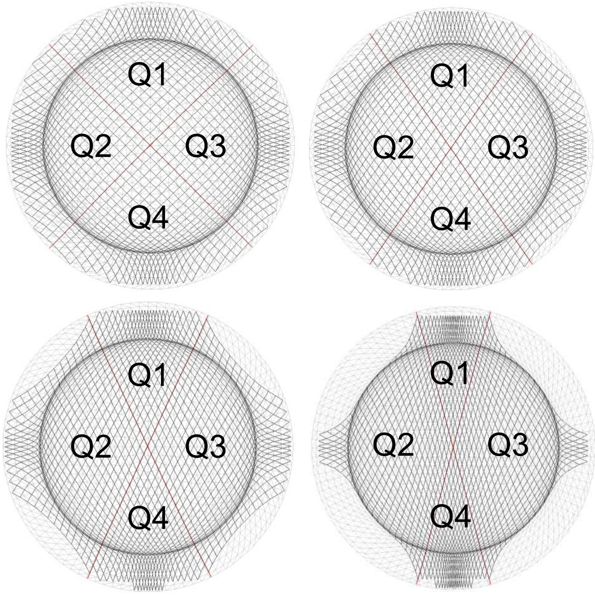

Figure 5.5: Four geodesic kinematic drape results over a hemisphere geometry, with the angle between the geodesic generator paths set to 0°, 20°, 40°, and 60° from left to right respectively.

5.2.3 Experimental method

The demonstrator part used for the experimental verification of blank-holder effects is a Rolls-Royce Tay nose cone geometry. The cone and blank-holder setup are mounted in an Instron test machine, shown in Figure 5.7 The blank-holder used allows the pressure applied to the fabric to be adjusted individually around the rig using a spring and bolt arrangement, however, in this study uniform blank-holder pressure distributions were used. Utilising this, four nose cone drapes were carried out, at progressive blank-holder pressures.

Before draping, the fabric used, EBXhd-936 or FGE 106hd, was marked with an orthogonal grid, with the lines 10mm apart aligned with the fibre directions, as shown in Figure 5.8. The fabric was placed into the blank-holder and the chosen

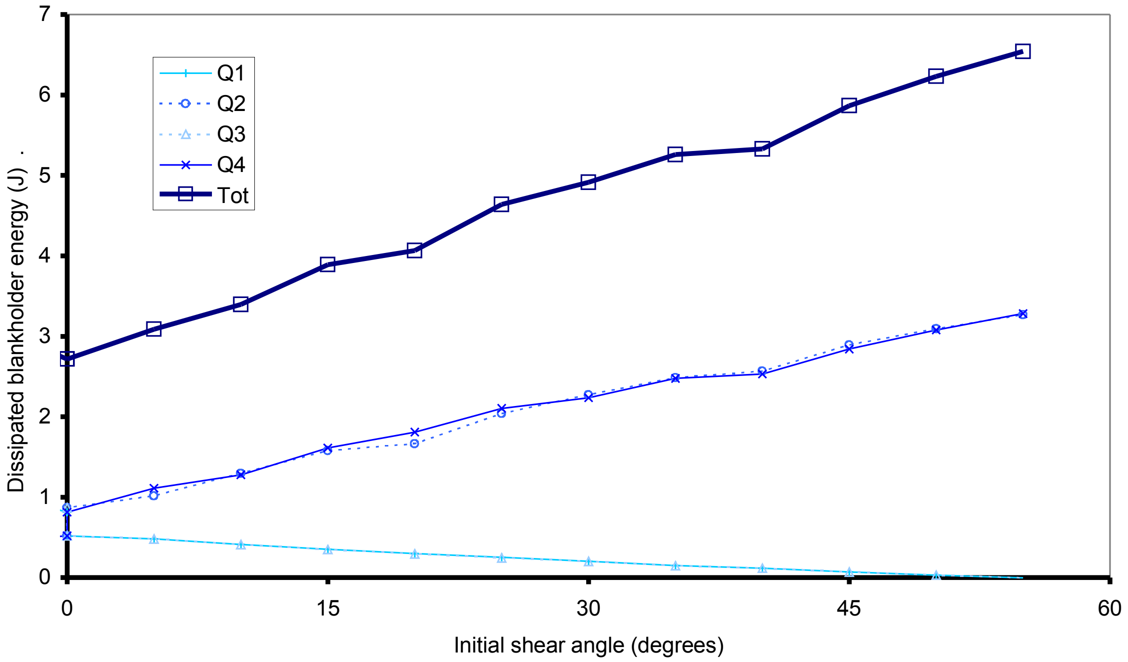

Figure 5.6: Variation of blank-holder energy with initial shear angle for kinematic drape with fibre spacing of 5mm, applying a total blankholder force of 200N with a frictional coefficient of 0.3. Q1,Q2,Q3 and Q4 represent individual quadrant values, whilst their sum, the overall blankholder energy, is shown as Tot.

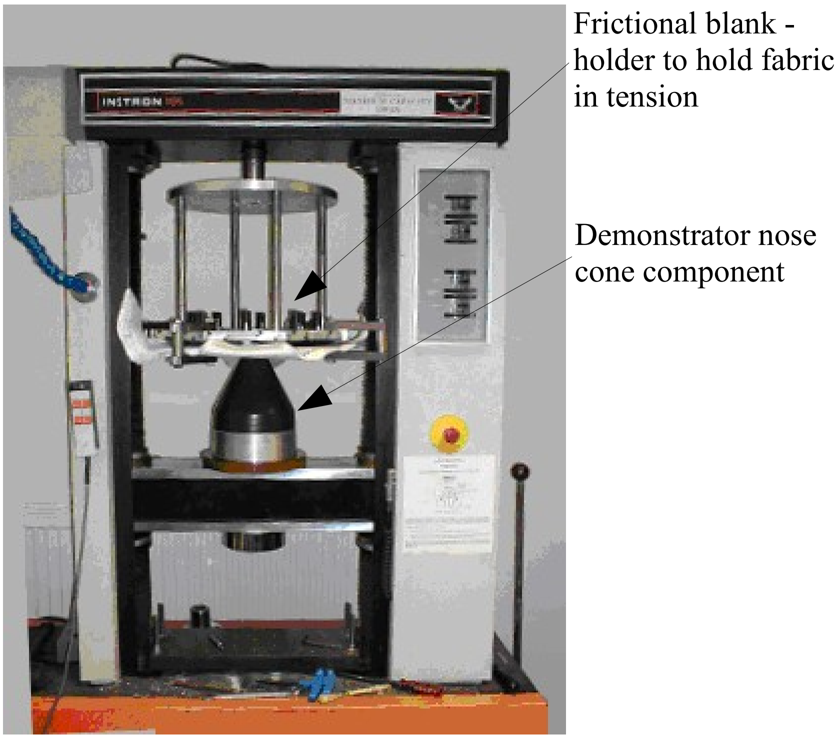

Figure 5.7: Blank-holder setup with the Tay nose cone.

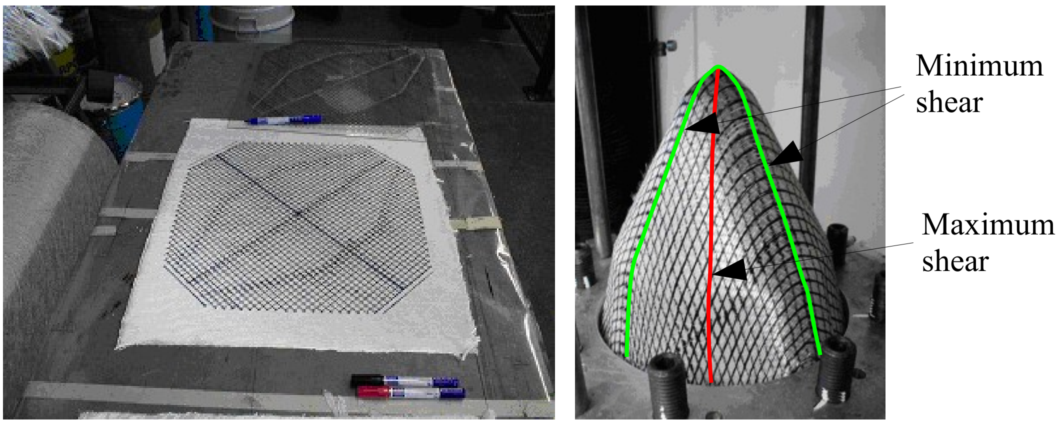

Figure 5.8: Grid marked onto the fabric, before and after forming

blank-holder pressure applied by turning the bolts a fixed number of turns. Four different total blank-holder forces were used: 0N, 128N, 252N, and 378N. The rig was mounted into an Instron test machine, with the blank-holder held at the top and the cone on the moving arm, but without a load cell. The Instron test machine was activated and the cone raised into the blank-holderon displacement control. Once in place, the fabric was painted with a thermoset resin to fix it, and after the resin had set, the formed cone could be removed for analysis. One drape was conducted at each blank-holder level.

Figure 5.8 highlights the lines of maximum and minimum shear for each quadrant of the cone. The difference between the shear angles along the maximum shear lines along different quadrants is a good indicator of the forming symmetry. Accordingly, shear angles were measured along these lines for each of the four cones. The shear angles were measured in two ways. Firstly, the distance between diagonal corners of each grid square was measured using Vernier calipers. Secondly, Photographs were taken and analysed using CamSys, a digital mapping system.

CamSys, originally developed for for the determination of strains induced during forming of metals, uses a system in which the material to be formed is marked with a regular grid in the undeformed condition. After forming photographs with a "target cube" of known dimensions are taken from two positions and analysed in the software. The proprietry analysis software "ASAME" isolates the deformed grid to lines, and triangulates the grid nodes from the two pictures to calculate their 3D coordinates and a strain field. for the component. This was first adapted for composites by Souter [60].

5.2.4 Results

Results are presented such that experimental data can be compared to predictions. The modelled deformation was made using the University of Nottingham kinematic drape programe “DrapeIt”, with modifications to include blank-holder energy in the energy minimisation algorithm. The fabric shear energy was modelled using EBXhd-936 shear data from picture frame tests by Souter [60], similar to those presented in Section 3.3.3. The effect of increased blank-holder pressure in this case is to negate the effect of the asymmetric shear behaviour of the material tested. Thus, the greater the blank-holder pressure, the less skewed the draped pattern. This was also replicated in the modelling approach.

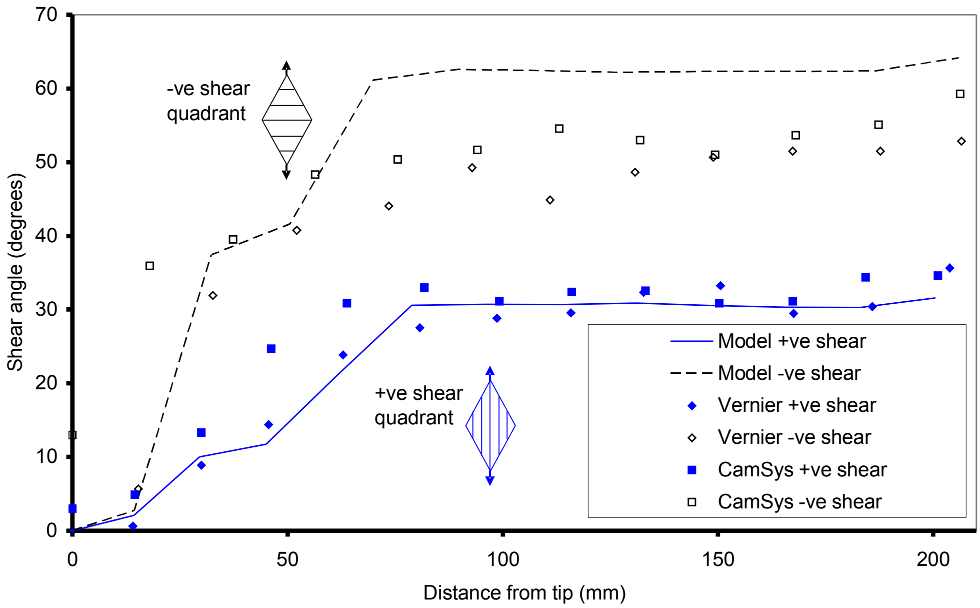

Figure 5.9: Measured and modelled effects of blank-holder on the draping of EBX-hd-936 over the Tay nose-cone. Total blank-holder force is 0N

The results in Figure 5.9 show the typical asymmetric results seen from this fabric.

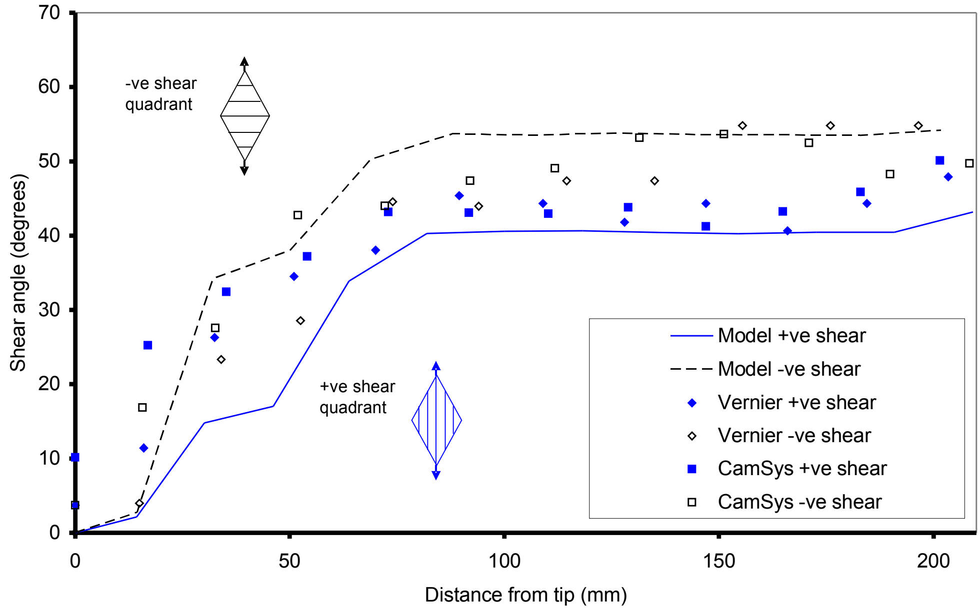

Figure 5.10: Measured and modelled effects of blank-holder on the draping of EBX-hd-936 over the Tay nose-cone. Total blank-holder force is 126N

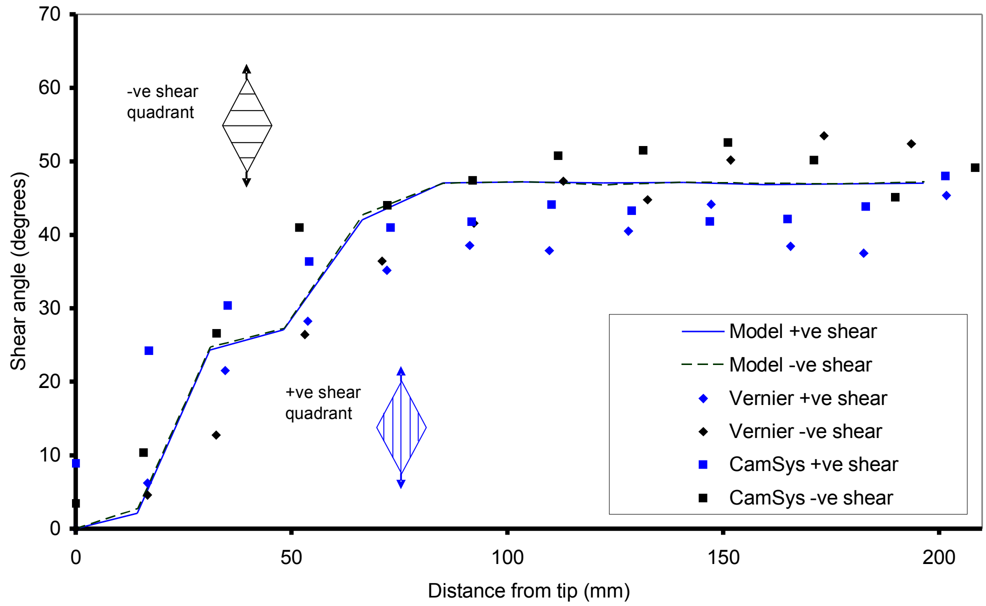

Figure 5.11: Measured and modelled effects of blank-holder on the draping of EBX-hd-936 over the Tay nose-cone. Total blank-holder force is 252N

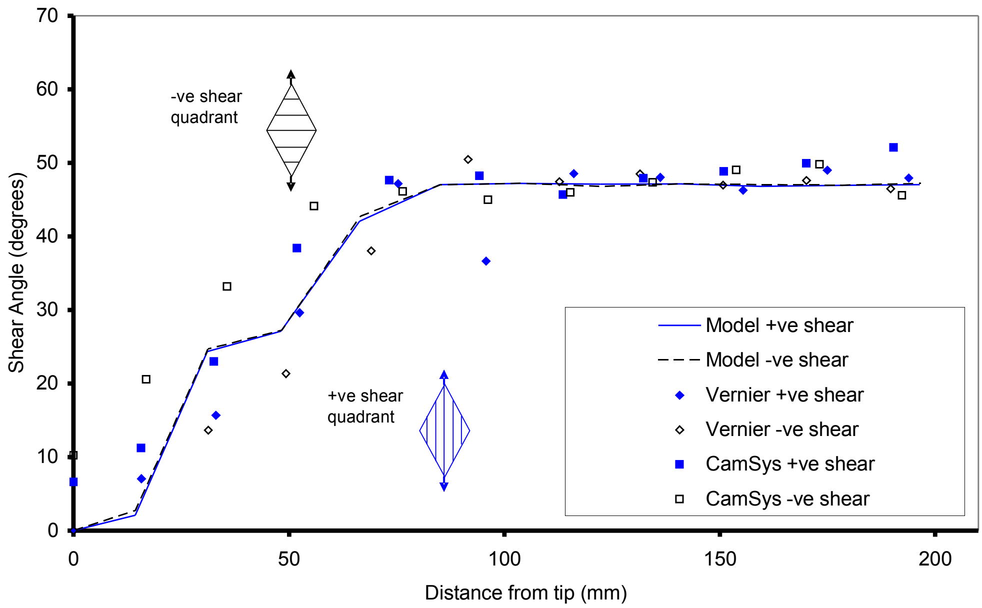

Figure 5.12: Measured and modelled effects of blank-holder on the draping of EBX-hd-936 over the Tay nose-cone. Total blank-holder force is 378N

The reasons for this, arising from the stitching, have been discussed in Section 4.3.1. With the introduction of low blank-holder force in Figure 5.10, it can be seen that the effect of the stitching is decreased, in that the fabric shears more symmetrically. Figure 5.11 shows an almost symmetrical shear pattern as the blank-holder begins to dominate the energy of forming, and Figure 5.12 is entirely symmetric. The errors in the measured results can be seen from the differences in the two measurement techniques.

It can be seen from the results that a skewed draping pattern over the nose cone requires more material to be pulled through the blank-holder than a symmetric pattern. Thus, as the energy cost of pulling the fabric through the blank-holder increases with the blank-holder pressure, it dominates the drape energy so that fabric shear behaviour becomes less prominent. It would be informative to observe the overall drape energy transition from the pattern with zero blank-holder pressure to the point at which an entirely symmetric pattern is established. As what is being observed is the interplay of the two process energies, that from the stitch and that from the blank-holder, the transition between the two extremes could be informative as to the magnitude of the energy that the stitch contributes to the fabric drape. Meanwhile, the close correspondence between the measured and predicted results provides assurance that at the least the drape and blank-holder energy models are proportionate.

It may appear that the use of a blank-holder constricts the fabric from moving circumferentially around the mould, an effect that cannot be adequately modelled by this approach. However, this approach suggests that the more dominant effect of the blank-holder is in achieving a pattern with minimal "radial" movement of the reinforcement, and furthermore that for axisymmetric parts at least, these constrictions achieve the same effect in any case.

Whilst the result over the axisymmetric part approached those of kinematic drape at high blank-holder pressures, several advantages can be seen for using the energy minimisation approach over a kinematic one. The model allows an assessment to be made whether a particular fabric will drape symmetrically at all. Further, it gives an indication of what level of blank-holder pressure is required to achieve that. However, further work should be conducted on expanding this concept, to test it on non axisymmetric components, as well as implementing it with variable pressures, as can be achieved with the nose cone blank-holder.

5.3 Stochastic effects on draping patterns

The object of any virtual process development tool is to reduce the cost of pre-manufacture assessment and optimisation of a product by minimising design iteration and prototyping. One important function already well utilised in other manufacturing environments is the prediction and optimisation of product variability and discard rates. Many composite materials and processes exhibit high variability, which often leads to high failure rates. This in turn increases the per-unit cost of composite manufacture with these materials. Thus, understanding and predicting the effects of variability on the final part should allow stochastic effects to be controlled and minimised, reducing costs.

5.3.1 Sources of variability

In order to model and predict component variability, the processing factors that lead to it must be categorised and individually examined. Such an attempt is made here, and one of these categories is further examined.

Examination of the RTM manufacturing process yields obvious categories for variability according to the manufacturing process itself: Material manufacture, forming, resin transfer, cure, and post-cure. As this thesis concerns itself with the forming stage of the process, sub-categories of the resin-manufacture, resin transfer, cure, and post-cure categories will be left to those more qualified in those areas. Also, textile-manufacture is a process in itself and so lends itself to an independent study, outside the scope of this thesis. Sources of variability for forming could include

- speed. This is particularly of importance in rate-dependent materials such as prepregs.

- temperature. Also of more importance to prepregs, it may also affect frictional constants, lubricant behaviour, and fibre, tow, or stitch moduli (depending on their materials) in dry forming.

- blank-holder pressure. Should a blank-holder be used, the value of the pressure applied, as well as irregularities around the blank-holder (surface and load evenness, load distribution due to material shear compression variations) could affect draping. Alternatively, hand lay-up presents a large potential for variability, depending on the person performing it, the time of day, their working conditions, etc.

- fabric alignment. Fabric misalignment could occur both in terms of in- and out-of-plane rotation and, for example, point of first contact with the tool.

- handling effects. Fabric variability is a consequence not only of the manufacturing process but of subsequent handling prior to forming.

Whilst textile manufacturing variability will not be examined, the resultant fabric variability can be looked at. Thus the variability studied here looks at the effects of variability of the fabrics on the draped results.

5.3.2 Measuring textile variability

Fibre angle variability in turn affects resin transfer and final part characteristics. The more deformable a material is, the more variable it tends to be - hence it is a common practice to use the least deformable material that will drape a part. If quality is particularly important, it is sometimes even deemed preferable to use a fabric that requires cutting, darts etc in return for a more consistent final part quality. This is far from ideal, as darts complicate the manufacturing process and can create resin rich zones in the part. Currently, fibre alignment does not usually form a part of the fabric specification, although that seems likely to change if the composites technology is to be embraced by the mainstream automotive industry.

To assess fabric variability a high-drape non-crimp fabric, FGE 106hd, was measured for tow angle variability. The material was carefully removed from the roll, and samples of local fibre angles (with respect to the weft direction) over the fabric were taken. The angles were measured from digital photographs of the fabric imported into AutoCAD, as illustrated in Figure 5.13. The results, which appear to conform to a Normal distribution, are presented in Figure 5.14, and tabulated in Table 5.1.

Table 5.1: Mean and standard deviation for fibre angles on FGE 106hd taken from 38 different locations over a single sample. All values are in degrees.

Mean fibre angles	42.7
Standard deviation	5.6

The validity of the results is affected primarily by the small, 38 point sample size. However, before using the data other factors must be considered:

- The samples were taken at very regular intervals. If any pattern in the fibre angle distribution has a frequency close to that of the samples, interference between the two intervals could create an apparently random distribution.

- Interactions between fibre angles on the top and bottom of the fabric were not considered as the material was handled between measurements of the top

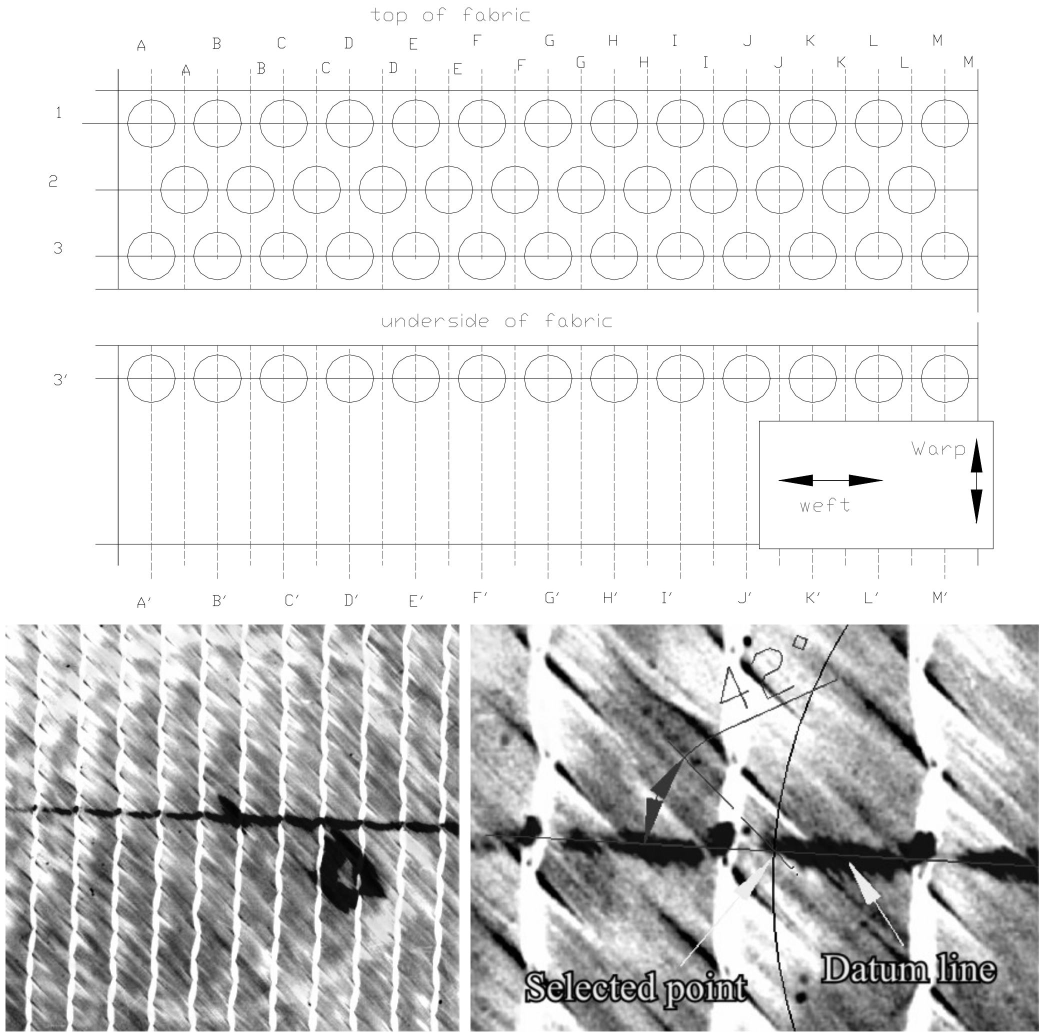

Figure 5.13: Sample areas were marked onto the fabric as shown in the top figure. Bottom left shows a typical sampling area, and bottom right shows angle measurement between the datum line (indicating weft direction) and a selected fibre.

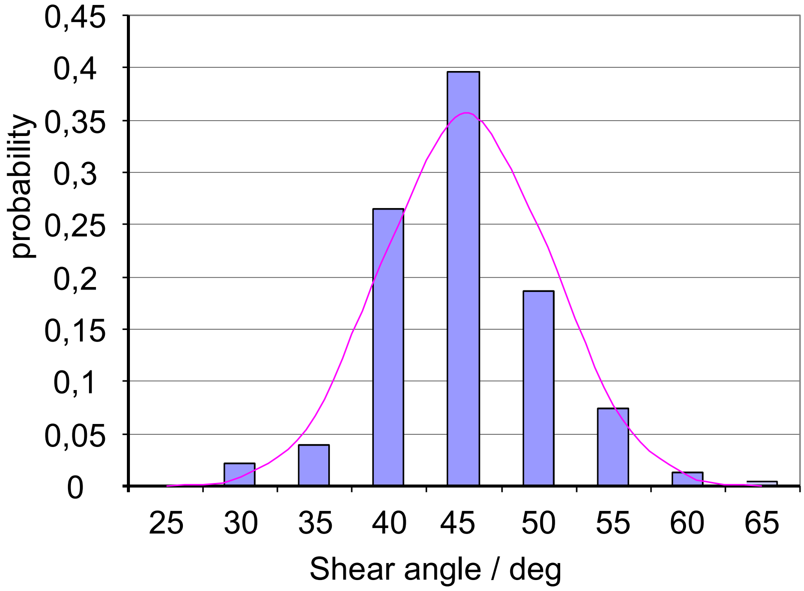

Figure 5.14: Histogram of fibre angles measured over sample with fitted Normal distribution, mean and standard deviation as stated in Table 5.1

and the bottom face. To avoid this, the fabric should in future be placed on a glass surface so that angles can be measured for both top and bottom faces simultaneously.

- Samples were taken from one piece of material taken from one roll, so that variations along the roll or between rolls cannot be taken into account. The scale of the variability measured should be treated with great care, as the graph presented might be seen to suggest that a roll could be received with an average fibre angle of 30° rather than the stated 45°. The angles measured are specifically on a local scale, and not indicative of the global fibre angles or their distribution within a roll or between rolls. Further work should be conducted to measure these, also.

Bearing this in mind, however, the measured distribution can be approximated reasonable well by a Normal distribution, which can therefore be characterised very easily by the mean and standard deviation of the fibre angle. The only significant pattern of local angles observed was that angles were higher at the very edges of the fabric, where it was directly handled as it was removed from the roll.

Note finally that the mean is $2-3°$ below that expected. This can been explained by the shear behaviour model outlined in Section 4.5, as being due to the tension under which the fabric is stitched - shear prediction data shows the shear force only reaches zero at a negative shear value, due to the tension under which the stitch is inserted into the material. The mean shear angle can therefore give a useful indication of the amount of tension initially in the stitch.

5.3.3 Modelling material variability in draping

A simple method is freely available for producing a random variable conforming to a Normal distribution. This requires use of the inverse cumulative Normal distribution, for which very accurate numerical solutions can easily be calculated. The inverse cumulative Normal distribution then allows a pseudo-random variable with a flat distribution to be transformed into one that conforms to the standard Normal distribution.

Hence, using a random number generator, the tow spacing can be varied according to the Normal distribution. Inserting this into the code should create a unique draping solution, for which the resulting shear angle distribution can be analysed and compared to that observed.

5.3.3.1 Varying fibre spacing

Flat plate

One simple scheme for incorporating a stochastic effect within the DrapeIt algorithm is to introduce a variation in tow spacing. In order to investigate how this might affect draping, this spacing variation was initially chosen as conforming to the Normal distribution.

Figure 5.15 shows a typical result for the "draping" of a flat plate using the algorithm implemented. Although the implementation was carried out for both kinematic

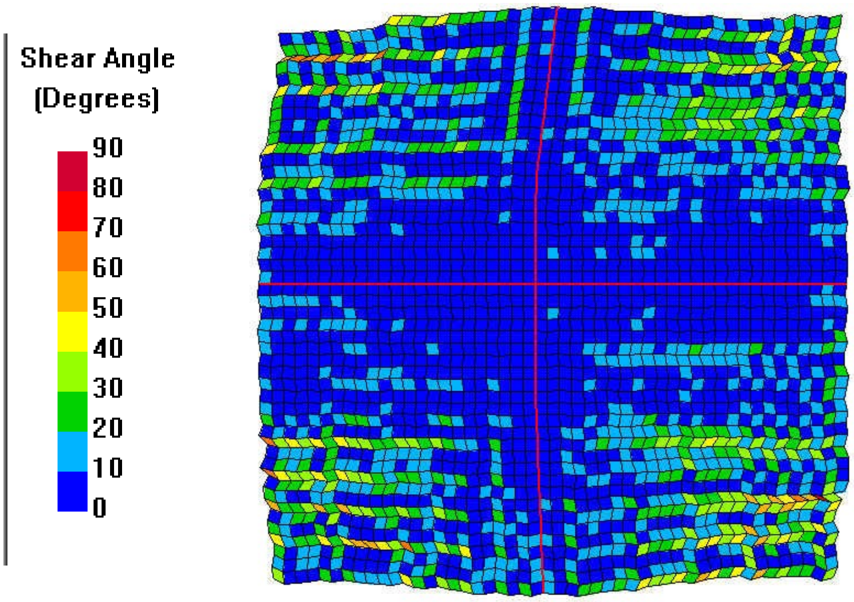

Figure 5.15: Energy-based "drape" results on a flat plate using randomised fibre spacing with a very low standard deviation (1.5% of the mean fibre spacing). The spectrum blue through to red represents low to high shear.

and energy-minimising draping approaches, the energy-minimised approach is presented here, for two reasons. The first is that in a kinematic approach the options for laying generator paths restrict them to lying absolutely straight on a flat plate.

Secondly, although fibre spacing variations represent a departure from the minimum energy, it seems to make sense that once introduced the fabric would tend to deform so as to minimise energy.

It can be observed that due to the nature of the draping approach, the effects of the variable tow spacing are cumulative with respect to the distance of a node from the generator path crossover - this does not correspond to a realistic shear angle distribution.

Nevertheless it is worthwhile observing the resultant shear angle distribution, shown in Figure 5.16. Note the very large angle standard deviation, resulting from

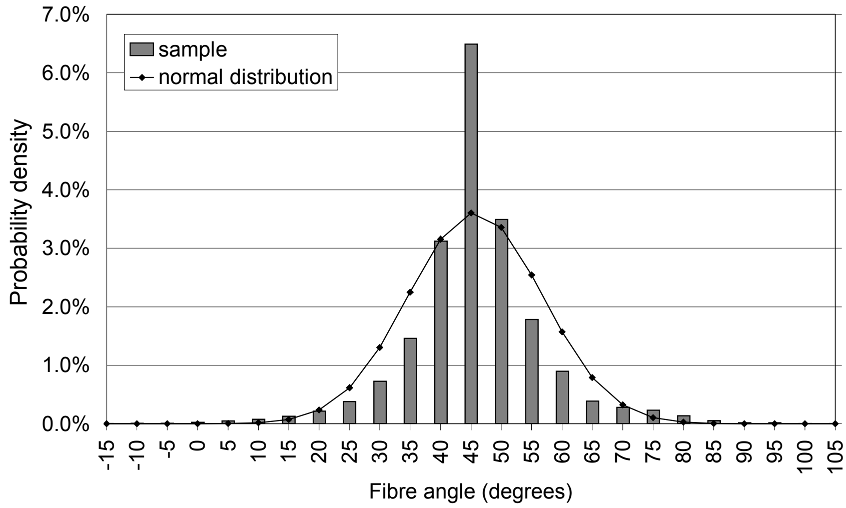

Figure 5.16: Probability distribution for fibre angle taken from results shown in Figure 5.15. The datum line is taken to be at 45° to Figure 5.15 for direct comparison with Figure 5.14, and the fitted Normal distribution uses values for mean of 45.75° and standard deviation of 11.04°.

a very small spacing standard deviation (24% of mean angle arising from only 1.5% of mean spacing). This suggests that the drape response can be *very* sensitive to variations in fibre spacings. However, observed fibre spacing variations tend to be local, so that the cumulative effects seen on the flat plate are not observed. The sensitivity of the drape response to non-cumulative, local spacing variation may not be so strong.

The concentration of 45° fibres is possibly due to the energy minimisation algorithm, as the minimum shear energy for any one node is at 0° and so the minimum energy drape will be such that the most fibres are close to ±45°. A possible fix for this could be to determine the local angles of the generator paths according to a Normal distribution. This may also alleviate the problem of the progression in the angle distribution with distance from the initial crossover point.

Nose Cone

In Section 5.2 a method for predicting blank-holder effects was outlined and compared to results. Consideration of Figures 5.9-5.12 show that as the blank-holder pressure increased, the experimental scatter decreased. Whilst it is not possible at present to model this effect on a mezoscopic level, it would be interesting to see if the degree of scatter observed could be replicated using the method outlined but draping over the nose cone, and incorporating the blank-holder effect.

The result typically looks like Figure 5.17. Whilst the variability in shear angle apparent in Figure 5.17 seems fairly mild, its effect can be seen on the shear angle results in Figure 5.18. The shear angles in the figure are measured from the tip and along the lines of peak shear angle down the length of the cone. They are plotted against the distance on the surface of the geometry from the tip of the cone.

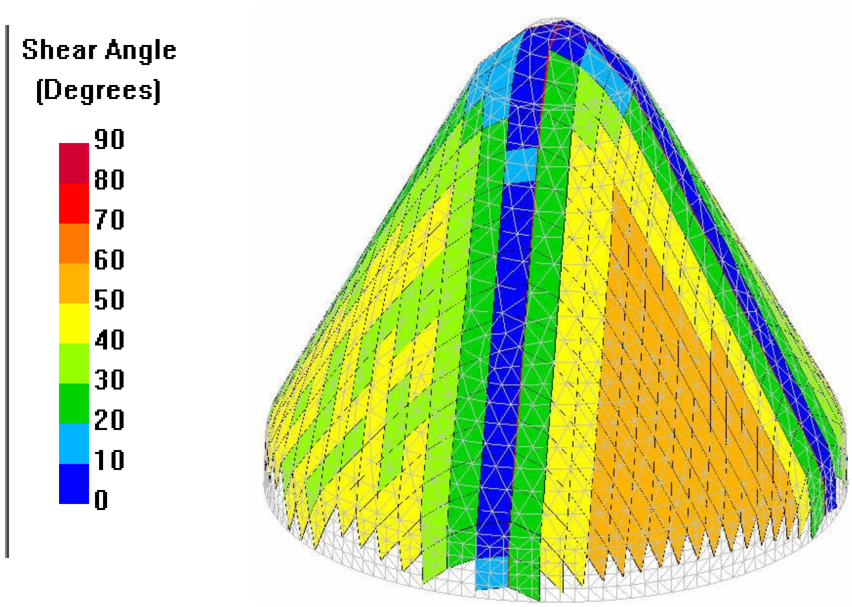

Figure 5.17: A simulation of a cone draped with EBXhd-936at a blank-holder force of 126N and a randomised spacing with a standard deviation of 0.1% of fibre spacing.

5.3.3.2 Varying fibre angle

Varying fibre spacing has limited applicability. A better approach might be to vary the fibre angles according to the Normal distribution presented in Section 5.3.2. However, the fibre angles measured were for the undeformed sheet, rather than for a preform, in which fibre angles have been changed due to the preforming process. In order to link the initial fibre angles with the formed fibre angles, the initial fibre distribution is taken as the *zero energy* shear angle for local regions within the textile. Thus, in a flat plate energy minimising drape, the textile would drape as measured.

In order to model this, the zero energy shear angle for each node in the pin-jointed net is generated according to the Monte-Carlo method, and the value is stored with the other node data. At each point at which the code calculates the node shear energy, the zero energy node angle is subtracted from the calculated shear angle and

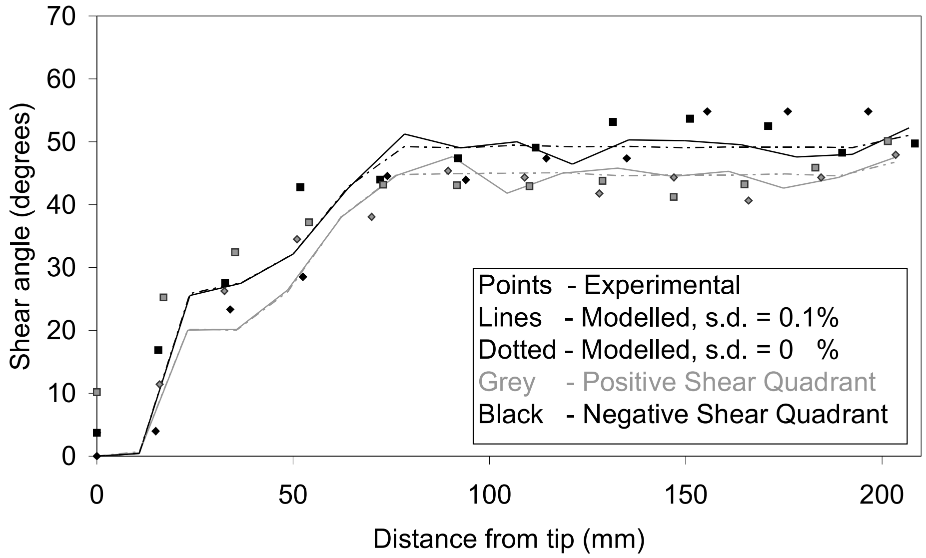

Figure 5.18: Results from randomised cone drape with blank-holder force of 126N. The predicted difference in shear quadrants corresponds fairly well to that experimentally observed, and the spacing standard deviation of 0.1% of the fibre spacing was chosen so that the apparent shear angle scatter would fairly well match experimental scatter.

the resultant angle is used in the shear energy equation.

Nose cone results

The biggest advantage of using an energy-based kinematic code to model stochastic variations is in the speed of the model, which allows large data sets to be created relatively quickly. One representative data set has been generated using the method outlined above embedded into the University of Nottingham "DrapeIt" code. Figure 5.19 shows the variability of results for 127 simulations over the Tay nose-cone geometry. It plots shear angle at each node against distance from the tip of the nose cone, going along the lines of maximum shear.

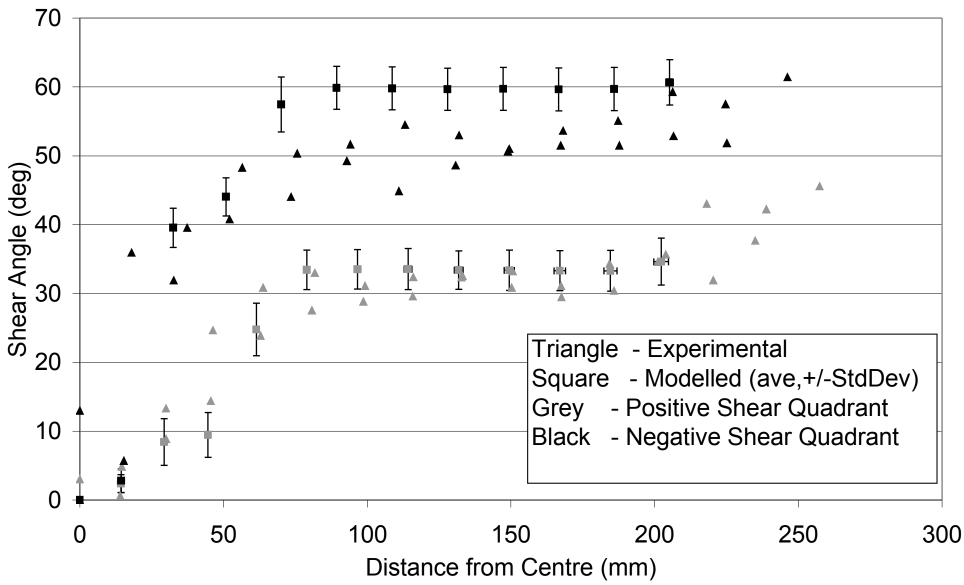

Figure 5.19: Results from drape with randomised energy curve offset. Shear curve zero offset = 5°.

The error bars are set to +/-1 standard deviation for that node, so that they do not give an indication of the shape of the distribution. Figure 5.20 gives an example of that distribution. This study indicates that an experimentally measured,

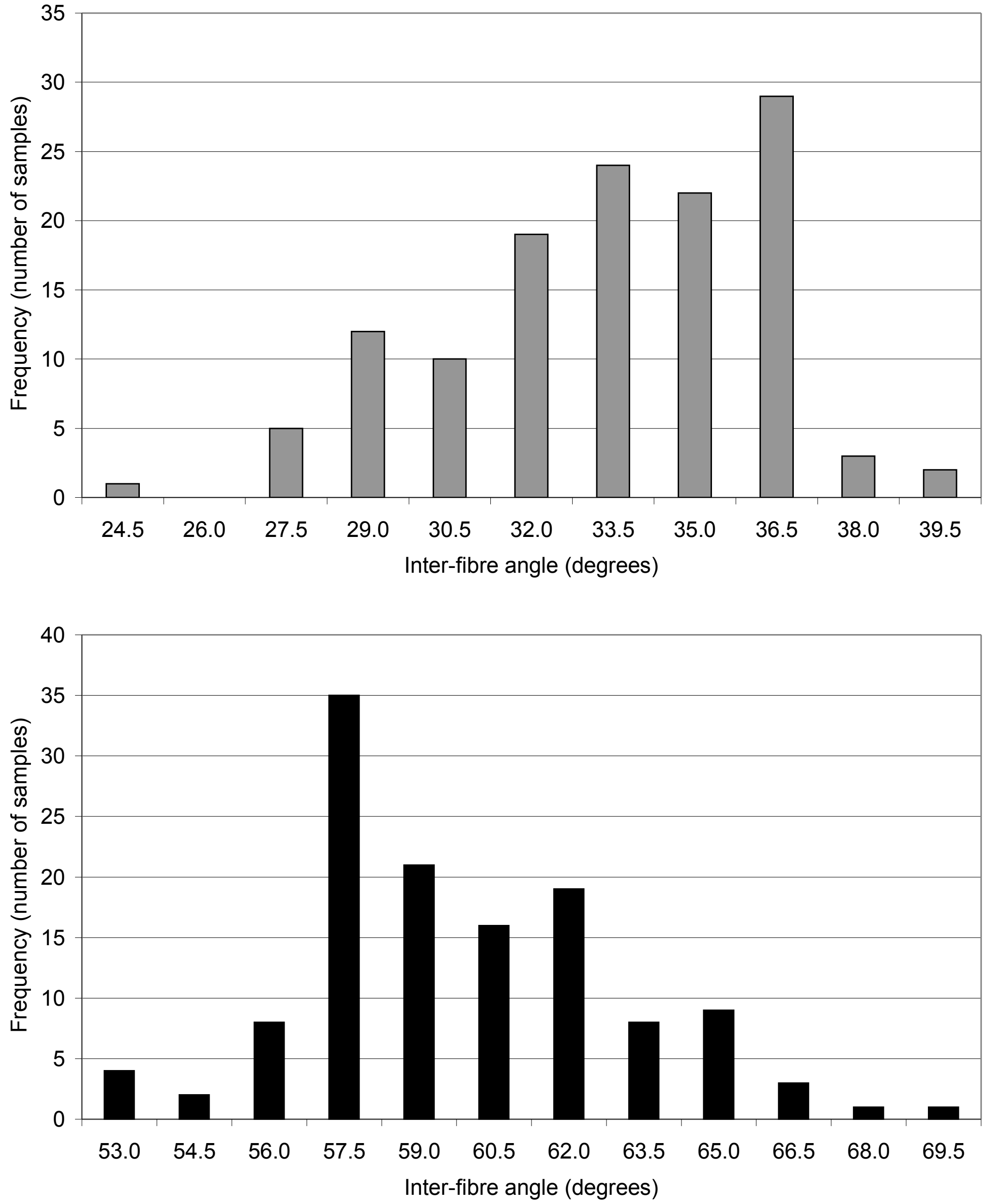

Figure 5.20: Frequency distribution for node 6 along maximum shear line on positive shear quadrant (grey - mean distance from tip = 96.6mm, mean inter-fibre angle = 33.5deg) and negative shear quadrant (black - mean distance from tip = 108mm, mean inter-fibre angle = 59.8deg). No experimental verification of this effect was made.

relatively small variability in fibre angle in the undeformed textile can have quite a substantial effect on the deformed fibre angles and positions. The two distributions presented appear to have a mirrored shape, suggesting that they are related. This is not surprising, as the constraint of constant fibre separation was maintained in the model. This demonstrates that forming variability can be modelled within the environment of kinematic forming models.

5.4 Conclusions

Some concepts for including effects of additional process and material variables have been implemented in the energy based kinematic model that will allow a more appropriate and accurate draping simulation to be conducted with negligible loss of speed (127 simulations in $\approx$ 5 hours) or ease of use. Initial results for the blank-holder modelling approach are promising. However, a more thorough evaluation should be made to fully explore the limits of what is a relatively simple approximation. The potential of using blank-holders intelligently to control the draping pattern should also be explored further. For example, if increased blank-holder pressure was applied to some segments than others around the perimeter, this may have an effect on draped pattern, allowing forming control analogous to that proposed by Hancock and Potter [16] for hand draping. Such controls may allow a previously hard to drape geometry to be reliably and automatically formed.

Adding a stochastic effect to fibre spacing has produced some interesting results. It has indicated that varying the fibre separation in the kinematic drape model by even very small amounts (s.d. $= 0.1\%$) can have a significant effect on the draped angle variation.

Some further direction in this work has been indicated, and this should concentrate on creating a stochastic model that is more physically appropriate. In particular, the following problems should be considered:

- Current spacing variability simulations show a progression of shear angle variability related to the distance from the initial fibre crossover point. This is a direct result of the implementation of the code and needs to be eradicated. This could be achieved by local reorientation of fibres after idealised drape, similar to the fibre reorientation work from Lai and Young [30], to ensure that the fibre spacing variability effect is not cumulative.

- Fibre angles when varying fibre spacing tend to be unrealistically skewed to allow as many to lie at $\pm 45°$ as possible. This may however only be relevant in geometries that require small shear angles. One possibility is to combine the spacing and angle variability models.

- The degree to which adjacent fibre angle or spacing values are interdependent should be addressed.

- The variability simulations should be explored further, with other geometries, and larger experimental samples for comparison.

- Experimental measurements should be made of the variability of draping patterns, and linked to the measured variability of the textile used.

- The effects of blank-holder pressure on variability should be investigated.

In this specific example, it has been shown that even if fibre spacing was found to vary by only a small amount, it could have a substantial effect on the draping behaviour of the textile.

Chapter 6

Discussion and Conclusions

6.1 Discussion

The concern of this thesis is to facilitate the quick and accurate choice of dry textile reinforcement for RTM processes, particularly in the early design stages. As the predominant deformation mechanism observed in non-wrinkling textile forming is shear, much of this thesis concentrates on measuring and predicting the shear response of textiles. Much work has been done on modelling the shear response of woven textiles, so that this work has concentrated on non-crimp fabrics to further the breadth of textiles understood. Some preliminary work has also been conducted to add to kinematic modelling energy minimisation. Specifically, simple models for including the effects of a blank-holder on the draping pattern have been proposed and compared to experiment. Further, some simple approaches to modelling textile and forming variability have been explored.

6.1.1 Textile Shear

Two shear measurement methods were presented in Chapter 3. The relative merits were discussed, and several methods were presented to normalise the shear results for comparison. It was shown that the bias extension test can vary from the idealised shear deformation in many ways, such as non-ideal pure trellis shear or fibre slip. This was demonstrated to occur, and a video analysis tool was developed to monitor the shear deformation of the bias extension sample during the test. Comparisons were made between normalised picture frame results at different pre-tensions and normalised bias extension results at different sample aspect ratios. The differences in normalised results highlighted the importance of boundary conditions on the textile shear response. However, as reinforcement textiles can be processed under very different conditions, it is desirable to understand their behaviour under different boundary conditions.

Non-crimp fabrics were seen to have a lower shear stiffness response than woven fabrics. They also exhibited different shear behaviour in different shear directions. This effect can be controlled by careful choice of the stitch parameters. Stitch length, for example, affects the cost of the fabric produced, as the stitching machines work at a fixed stitching speed. Thus, a 2.5mm stitch length fabric would allow 50% more textile to be produced in a given time than a 1.65mm stitch length fabric. The model suggest that this can be achieved and a relatively balanced fabric still produced by manufacturing at 4-gauge. Woven fabrics generally presented more repeatable shear response. The reasons for this were mostly concerned with the ability to align woven fabrics, in which fibre directions are more readily apparent and consistent. However, this is mostly an artifact of the shear measurement apparatus, as drape results are not as critically sensitive to accurate textile alignment.

Chapter 4 presented a model for the geometric progression of the stitch structure during shear in non-crimp fabrics. The main causes of shear resistance in non-crimp fabrics were explored. The most important of these were the stitch tension and friction, the tow lateral compaction, and the interaction between the stitch tension and tow compaction. The model presented showed good correspondence to experimental results for some cases, and successfully predicted the effect of stitch length on shear asymmetry. However, it did not show good correspondence in two fabrics, FGE 106hd at 1.65mm and 5mm stitch lengths. This was because of the assumptions behind the model, which appear to lose credibility when the material is very compacted or the stitching is highly stressed. The model also did not allow for an observed change in the unit stitch shape during negative shear.

6.1.2 Forming models

The energy minimising kinematic drape simulation was discussed. This takes a geometric approach to drape simulation and iteratively calculates the deformation at which the fabric requires the minimum shear energy. To add to this approach, a method was proposed to model the effects of a blank-holder on the draping results. The use of a blank-holder was shown to affect the draping results of a non-crimp fabric over a nose-cone, and the effect was subsequently predicted with reasonable accuracy. Whilst the method proposed involved many assumptions, it had the advantage of requiring very little input from the user, and did not adversely affect the speed of output of the drape simulation. The method should be tested against a number of different geometries, particularly those without rotational symmetry, to fully explore its limitations.

Finally, some approaches were proposed for the modelling of variability in the textile forming process. These were related to experimental observations of textile variability, and preliminary attempts at modelling the effects of the textile variability on the forming results were made. It was shown that forming results can be very sensitive to small variability in tow spacing and initial shear angles. Further work would systematically measure the relationship between textile variability and forming variability. It would explore the sensitivity of the relationship, and identify the crucial variables for forming quality control.

6.2 Future work

This thesis has further developed work relating to the characterisation and modelling of dry composite reinforcements and their preforming behaviour. Further work should investigate several areas

1. A full statistical analysis should be conducted using the Monte Carlo drape variation tool developed to assess the sensitivity of different geometries to preform variation.

2. The validity of the blank-holder modelling should be further explored, particularly its limits in non-rotationally symmetric geometries. The effects of blank-holder pressure on variability should also be explored.

3. Characterisation and modelling of forming behaviour for new advanced reinforcements, such as 3D weaves, should be undertaken to facilitate acceptance of these materials.

4. A generic, integrated modelling tool incorporating woven and non-crimp fabric models, as well as other textiles should be developed.

5. Shear behaviour prediction models should be used to determine optimised reinforcement forms. These should be integrated with forming models to deter-

mine application specific reinforcement recommendations. Tools could be used to design textiles to specific uses.

6. Further work should be conducted to understand the limits of the shear measurement apparatus. In particular, rigorous approaches to measuring and controlling tension during picture frame tests should be developed. Repeatability continues to cause issues. More work should investigate boundary conditions in picture frame and bias extension tests, shear variability and mitigation, and alignment. Benchmarking should result in best practice guides and a ranking of the merits and pitfalls of different methods.

6.3 Conclusions

1. A rough geometric description of the reinforcement fabric allows an estimation of the fabric formability behaviour to be made. Together with a fast and easy drape modeller, this allows preliminary reinforcement choices to be evaluated quickly. It may also allow fabric architecture to be designed for a specific form.

2. Shear characterisations by different methods can be normalised to compare results. The different boundary conditions of these methods allow different effects within forming to be evaluated.

3. Simple changes in NCF stitch parameters have been demonstrated to affect both the predicted and measured forming behaviour of the textile. This confirms the feasibility of fabric selection or design for specific forming requirements.

4. Kinematic based draping algorithms that take into account some material and processing factors have been demonstrated to possess a legitimate place in the design cycle. Such a model has been extended to allow for the use of a blank-holder, whilst the ease of use and calculation speed when compared to FE solutions has not been adversely affected

5. The use of a blank-holder in forming experiments has been shown to affect the forming results for some textiles. This confirms the importance of more accurate forming simulation such as has been proposed. It also opens up another design parameter for tuning resin injection issues such as dry spots, fibre volume fraction, and final component mechanical behaviour.

6. The effects of textile variability on formed pattern have been modelled. Other textile and forming factors that may affect variability should be modelled. The effects of the forming variability on resin flow should also be investigated.

References

[1] O.K. Bergsma. Computer simulation of 3d forming processes of fabric reinforced plastics. In *Proceedings of the 9th International Conference on Composite Materials (ICCM-9)*, pages 560–567, Madrid, 1993.

[2] R. Blanlot. Simulation of the shaping of woven fabrics. In *Proceedings of the 11th International Conference on Composite Materials (ICCM-11)*, pages V160–V170, Paris, 1997.

[3] P. Boisse. Meso-macro approach for composites forming simulation. *Journal of Materials Science*, 41:6591–5498, 2006.

[4] P. Boisse, M. Borr, K. Buet, and A. Cherouat. Finite element simulations of textile composite forming including the biaxial fabric behaviour. *Composites Part B*, 28B:453–464, 1997.

[5] P. Boisse, J.C. Gelin, and H. Sabhi. Forming of glass fibre fabrics into complex shapes - experimental and computational aspects. *Annals of the CIRP*, 41:327–330, 1992.

[6] P. Boisse, B. Zouari, and J. Daniel. Importance of in-plane shear rigidity in finite element analyses of woven fabric composite preforming. *Composites Part A*, 37:2201–2212, 2006.

[7] U. Breuer and M. Neitzel. Processing technology for mass production of fabric reinforced thermoplastic parts. In *Proceedings of the 35th International Man-Made Fibres Congress*, Austria, 1996.

[8] Z. Cai and T. Gutowski. The 3-d deformation behaviour of a lubricated fiber bundle. *Journal of Composite Materials*, 26(8), 1992.

[9] G.A. Carnaby and N. Pan. Theory of the compression hysteresis of fibrous assemblies. *Textile Research Journal*, 59(5):275–284, 1989.

[10] J. Chen, D.S. Lussier, J. Cao, and X.Q. Peng. Materials characterization methods and material models for stamping of plain woven composites. *International Journal of Forming Processes*, 4:269–283, 2001.

[11] G. Creech and A.K. Picket. Meso-modelling of non-crimp fabric composites for coupled drape and failure analysis. *Journal of Materials Science*, 41:6725–6736, 2006.

[12] J.C. Crookston, A.C. Long, and I.A. Jones. Modelling effects of reinforcement deformation during manufacture on elastic properties of textile composites. *Plastics, Rubber and Composites*, 31(2):58–65, 2002.

[13] M.F. Culpin. The shearing of fabrics: a novel approach. *Journal of the Textile Institute*, 70(3):81–88, 1979.

[14] P. de Luca, P. Lefebure, and A.K. Picket. Numerical and experimental investigation of some press forming promoters of two fibre reinforced thermoplastics: Apc2-as4 and pei-cetex. *Composites Part A*, 29A:101–110, 1998.

[15] J.L. Gorczyca-Cole, J. Chen, and J. Cao. *Composite forming technologies*, chapter 13. Benchmarking of composite forming modelling techniques. Woodhead Publishing Ltd, 2007.

[16] S.G. Hancock and K.D. Potter. The use of kinematic drape modelling to inform the hand lay-up of complex composite components using woven reinforcements. *Composites Part A*, 37:413–422, 2005.

[17] S.G. Hancock and K.D. Potter. Implementation and application of virtual fabric placement in forming fabric reinforcement for production of complex shaped components. In *Proceedings of the 8th International Conference on Textile Composites*, University of Nottingham, UK, 2006.

[18] P. Harrison, M.J. Clifford, and A.C. Long. Shear characterisation of woven textile composites: a comparison between picture frame and bias extension experiments. *Composites Science and Technology*, 64:1453–1465, 2004.

[19] P. Harrison, M.J. Clifford, A.C. Long, and C.D. Rudd. Constitutive modelling of impregnated continuous fibre reinforced composites: a micro-mechanical approach. *Plastics, Rubber and Composites*, 31(2):76–86, 2002.

[20] P. Harrison, M. K. Tan, and A. C. Long. Kinematics of intra-ply slip in textile composites during bias extension tests. In *8th International ESAFORM Conference on Materials Forming*, Cluj-Napoca, Romania, 2005.

[21] P. Harrison, J. Wiggers, A.C. Long, and C.D. Rudd. A constitutive model based on meso and micro kinematics for woven and stitched dry fabrics. In *14th International Conference on Composite Materials (ICCM)*, San Diego, California, 2003.

[22] G. Hivet, F. Dumont, J. Launay, V. Maurel, P. Vacher, and P. Boisse. Optical

analysis of woven fabric's shear behaviour. In *Proceedings of the 7th Esaform Conference on Material Forming*, pages 353–356, Trondheim, Norway.

[23] J.L. HU and ZHANG Y.T. The kes shear test for fabrics. *Textile research journal*, 67(9):654–664, 1997.

[24] S. Kawabata, M. Inoueb, and M. Niwab. Theoretical analysis of the non-linear deformation properties of a triaxial weave under biaxial stress fields. *Composites Science and Technology*, 56:261–271, 1996.

[25] S. Kawabata, M. Niwab, and H. Kawai. The finite-deformation theory of plain-weave fabrics part i: The biaxial-deformation theory. *Journal of the Textile Institute*, 64(2):21–46, 1973.

[26] S. Kawabata, M. Niwab, and H. Kawai. The finite-deformation theory of plain-weave fabrics part ii: The uniaxial-deformation theory. *Journal of the Textile Institute*, 64(2):47–61, 1973.

[27] S. Kawabata, M. Niwab, and H. Kawai. The finite-deformation theory of plain-weave fabrics part iii: The shear-deformation theory. *Journal of the Textile Institute*, 64(2):61–85, 1973.

[28] T. Komori and K. Makishima. Number of fibre-to-fibre contacts in general fibre assemblies. *Textile Research Journal*, pages 13–17, 1977.

[29] J.J. Kutz. *Development of a process for the evaluation of directional fabric formability*. PhD thesis, Drexel University, 1990.

[30] C. Lai and W. Young. Modelling the fibre slippage during preforming process. *Polymer composites*, 20(4):594–603, 1999.

[31] E.A.D. Lamers, R. Akkerman, and S. Wijskamp. Drape modelling of multi layer fabric reinforced thermoplastic laminates. In *6th International conference on textile composites (TexComp 6)*, Philadelphia, USA, 2002.

[32] J. Launay, G. Hivet, A.V. Duong, and P. Boisse. Experimental analysis of in plane shear behaviour of woven composite reinforcements. influence of tensions. In *10th ESAFORM Conference on Material Forming*, pages 1033–1038, 2007.

[33] G.A.V. Leaf, Y. Chen, and X. Chen. The initial shear modulus of plain-woven fabrics. *Journal of the Textile Institute*, 84(3):419–428, 1993.

[34] G.A.V. Leaf and K.H. Kandil. The initial load-extension behaviour of plain-woven fabrics. *Journal of the Textile Institute*, 71, 1980.

[35] G.A.V. Leaf and A.M.F. Sheta. The initial bending behaviour of plain-woven fabrics. *Journal of the Textile Institute*, 75, 1984.

[36] D.H. Lee and J.K. Lee. Initial compressional behaviour of fibre assembly. *The Textile Machinery Society of Japan*, pages 613–622, 1985.

[37] S. V. Lomov and I. Verpoest. Model of shear of woven fabric and parametric description of shear resistance of glass woven reinforcements. *Composites Science and Technology*, 66:919–933, 2006.

[38] S. V. Lomov, I. Verpoest, M. Barburski, and J. Laperre. Carbon composites based on multiaxial multiply stitched preforms. part 2. kes-f characterisation of

the deformability of the preforms at low loads. *Composites Part A*, 34(4):359–370, 2003.

[39] A.C. Long, P.J. Blanchard, C.D. Rudd, and P. Smith. The development of an integrated process model for liquid composite moulding. *Composites Part A*, 29A:847–854, 1998.

[40] A.C. Long and M.J. Clifford. *Composite forming technologies*, chapter 1. Composite forming mechanisms and materials characterisation. Woodhead Publishing Ltd, 2007.

[41] A.C. Long and C.D. Rudd. A simulation of reinforcement deformation during the production of preforms for liquid moulding processes. In *Proceedings of the Institution of Mechanical Engineers. Part B. Journal of Engineering Manufacture*, volume 208, 1994.

[42] A.C. Long, B.J. Souter, F. Robitaille, and C.D. Rudd. Effects of fibre architecture on reinforcement fabric deformation. *Plastics, Rubber and Composites*, 31(2):87–97, 2002.

[43] A.C. Long, J. Wiggers, and P. Harrison. In *The 8th International ESAFORM Conference on Material Forming*, volume 2, page 939, Cluj-Napoca, Romania, 2005.

[44] C. Mack and H.M. Taylor. The fitting of woven cloth to surfaces. *Journal of the textile institute*, 47:T477, 1956.

[45] T.M. McBride. *The Large Deformation Behaviour of Woven Fabric Microstructural Evolution in Formed Textile Composites*. PhD thesis, Boston University College of Engineering, 1997.

[46] U. Mohammed, C. Lekakou, L. Dong, and M. G. Bader. Shear deformation and micromechanics of woven fabrics. *Composites Part A*, 31:299–308, 2000.

[47] P.V. O'Neil. *Advanced Engineering Mathematics*. Wadsworth Publishing Company, Belmont, California, 2 edition, 1987.

[48] N. Pan and G.A. Carnaby. The initial shear modulus of a unit cell of wool fibres. *Wool Research Organisation of New Zealand Comunications*, (C106), 1988.

[49] N. Pan and G.A. Carnaby. Theory of the shear deformation of fibrous assemblies. *Textile Research Journal*, 59(5):285–292, 1989.

[50] X.Q. Peng and J. Cao. Continuum mechanics based non-orthogonal constitutive model for woven composite fabrics. *Composites Part A*, 36:859–874, 2005.

[51] A. K. Pickett, G. Greech, and P. DeLuca. Meso-mechanical modelling of non-crimp fabrics for drape and impact analyses. In *7th International ESAFORM Conference on Materials Forming*, pages 349–352, Trondheim, Norway, 2004.

[52] K. Potter. Bias extension measurements on cross-plied unidirectional prepreg. *Composites Part A*, 33:63–73, 2002.

[53] K.D. Potter. The influence of accurate stretch data for reinforcements on the production of complex structural mouldings: Part 1. deformation of aligned sheets and fabrics. *Composites*, (10):161–167, 1979.

[54] A.G. Prodromou and J. Chen. On the relationship between shear angle and wrinkling of textile composite preforms. *Composites Part A*, 28A:491–503, 1997.

[55] R.E. Robertson, E.N. Hsiue, E.N. Sickafus, and G.S.Y. Yeh. Fiber rearrangements during the molding of continuous fiber composites. 1. flat cloth to a hemisphere. *Polymer composites*, 2(3):126–131, 1981.

[56] F. Robitaille and R. Gouvin. Compaction of textile reinforcements for composites manufacturing. i: Review of experimental results. *Polymer composites*, 19:198–216, 1998.

[57] S.B. Sharma, M.P.F. Sutcliffe, and S.H. Chang. Characterisation of material properties for draping of dry woven composite material. *Composites Part A*, 34:1167–1175, 2003.

[58] M. Sherburn. *Geometric and mechanical modelling of textiles.* PhD thesis, University of Nottingham, 2007.

[59] J. Skelton. Fundamentals of fabric shear. *Textile Research Journal*, 46:862–869, 1976.

[60] B.J. Souter. *Effects of Fibre Architecture on Formability of Textile Preforms.* PhD thesis, University of Nottingham, 2001.

[61] S.M. Spivak. The behavior of fabrics in shear, part i: The instrumental method and the effect of test conditions. *Textile research journal*, 36(12), 1966.

[62] S.M. Spivak and L.R.G. Treloar. The behavior of fabrics in shear, part iii: The relation between bias extension and simple shear. *Textile research journal*,

37:963–971, 1968.

[63] A.S. Tam and T.G. Gutowski. The kinematics for forming ideal aligned fibre composites into complex shapes. *Composites Manufacturing*, 1990.

[64] F. Van der Weeen. Algorithms for draping fabrics on doubly-curved surfaces. *International journal for numerical methods in engineering*, 31:1415–1426, 1991.

[65] B.P. van West, M. Keefe, and R.B. Pipes. The draping of bidirectional fabric over three-dimensional surfaces. In *American Society for Composites 4th technical conference*, Blacksburg, Virginia, 1989.

[66] B.P. van West, R.B. Pipes, and M. Keefe. A simulation of the draping of bidirectional fabrics over an arbitrary surface. *Journal of the textile instite*, 81(4):448–460, 1990.

[67] C. Van Wyk. Note on the compressibility of wool. *Journal of the Textile Institute*, 37:T285–T292, 1946.

[68] J Wang, J.R. Page, and R. Paton. Experimental investigation of the draping properties of reinforcement fabrics. *Composites Science and Technology*, 58:229–237, 1998.

[69] A. Willems, S.V. Lomov, I. Verpoest, and D. Vandepitte. Picture frame shear tests on woven textile composite reinforcements with controlled pretension. In *10th ESAFORM Conference on Material Forming*, pages 999–1004, 2007.

[70] L. Ye and H.R. Daghyani. Characteristics of woven fibre fabric reinforced composites in forming process. *Composites Part A*, 28A:869–874, 1997.

[71] W.R. Yu, P. Harrison, and A.C. Long. Finite element forming simulation for non-crimp fabrics using a non-orthogonal constitutive equation. *Composites Part A*, 36:1079–1093, 2005.

Appendix A

Publications arising from this work

1. J. Wiggers, A.C. Long, P.Harrison, C.D. Rudd. "The effects of stitch architecture on the shear compliance of non-crimp fabrics", Proc. 6th Int. European Scientific Association for Material Forming (ESAFORM) Conf., Salerno, Italy, April 2003, pp 851-854.

2. P. Harrison, J. Wiggers, A.C. Long, C.D. Rudd. "A constitutive model based on meso and micro kinematics for woven and stitched dry fabrics", Proc. 14th Int. Conf. on Composite Materials (ICCM-14), San Diego, July 2003, 10 pp.

3. P. Harrison, W.R. Yu, J. Wiggers, A.C. Long. "Finite element simulation of fabric forming, incorporating predictions of a meso-mechanical energy model", Proc. 7th Int. European Scientific Association for Material Forming (ESAFORM) Conf., Trondheim, Norway, April 2004, pp. 139-142.

4. A.C. Long, J. Wiggers, P. Harrison. "Modelling the effects of blank-holder pressure and material variability on forming for textile preforms", Proc. 8th Int. European Scientific Association for Material Forming (ESAFORM) Conf., Cluj-Napoca, Romania, April 2005, pp. 939-942.

5. P. Harrison, J. Wiggers, A.C. Long. "Normalisation of shear test data for rate-independent compressible fabrics", Proc. 10th Int. European Scientific Association for Material Forming Conf., Zaragoza, Spain, April 2007, 6 pp.

Appendix B

Picture frame and bias extension results

B.1 Picture frame results

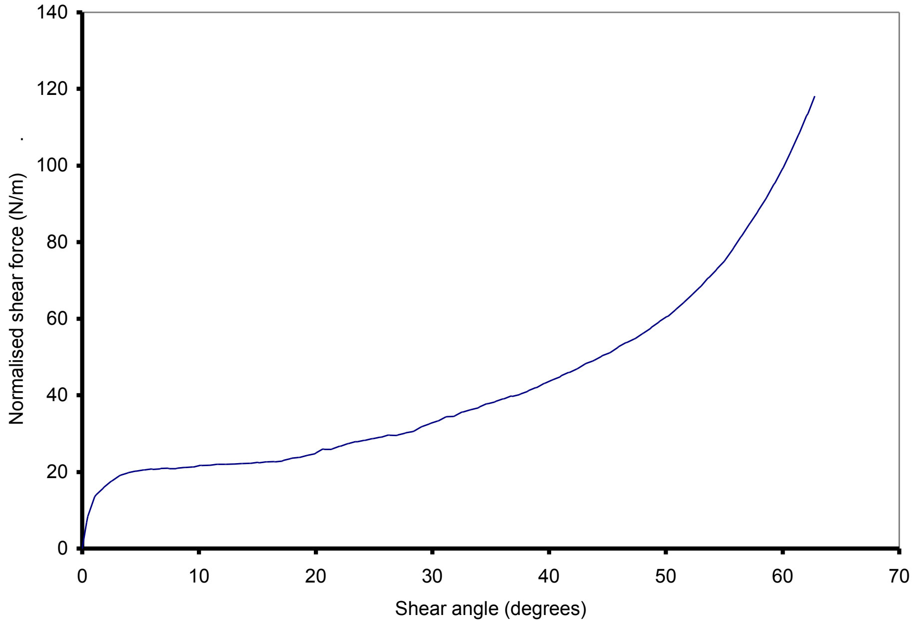

Figure B.1: EBXhd-936 at 62N pre-tension, sheared in the negative direction

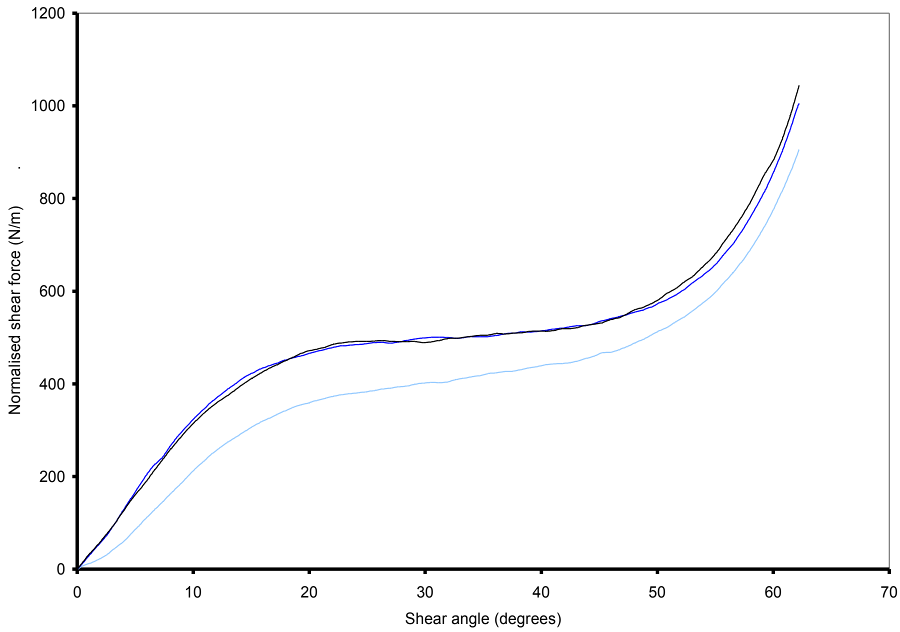

Figure B.2: EBXhd-936 at 375N pre-tension, sheared in the positive direction

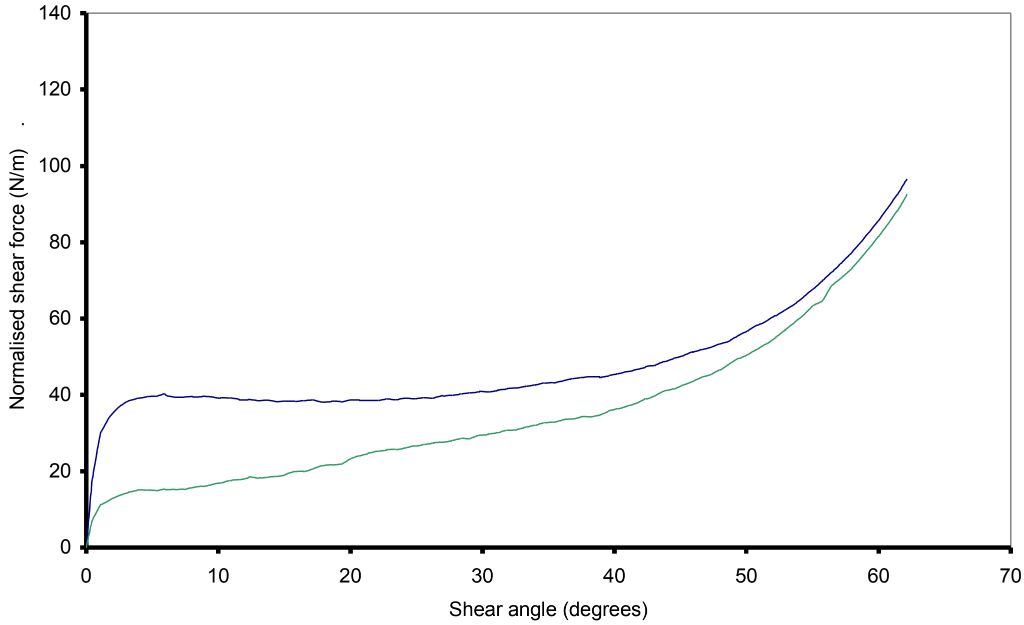

Figure B.3: EBXhd-936 at 375N pre-tension, sheared in the negative direction

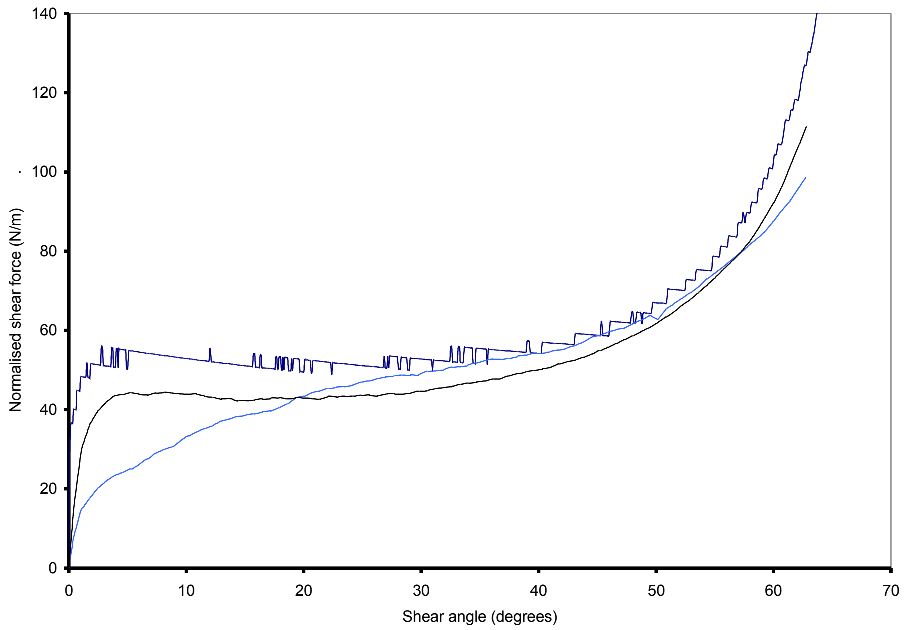

Figure B.4: EBXhd-936 at 1300N pre-tension, sheared in the negative direction

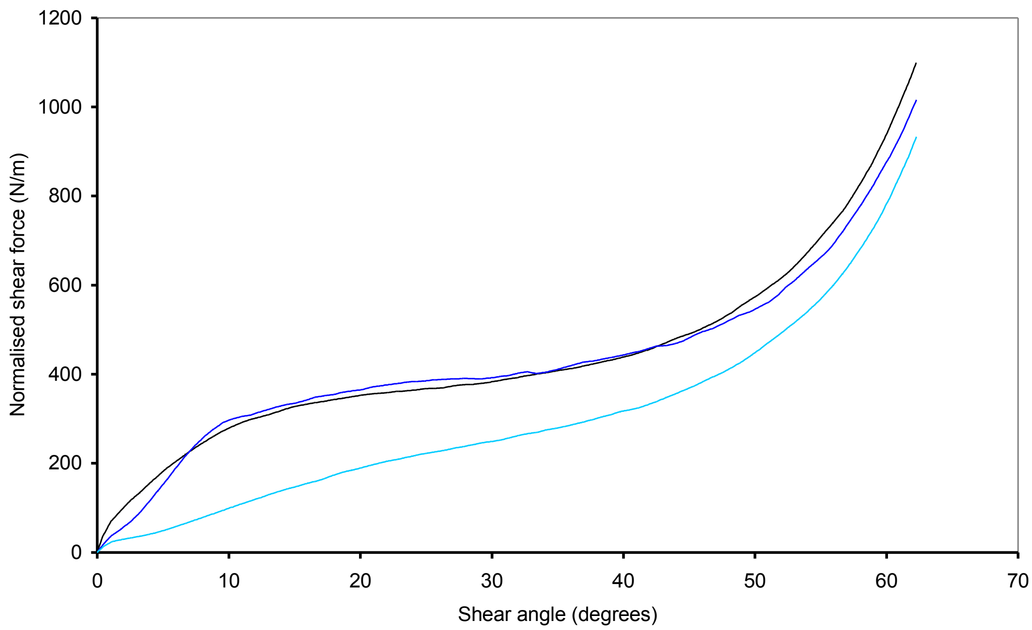

Figure B.5: FGE 106hd at 1300N pre-tension, sheared in the positive direction

B.2 Bias extension results - comparison of normalisation techniques

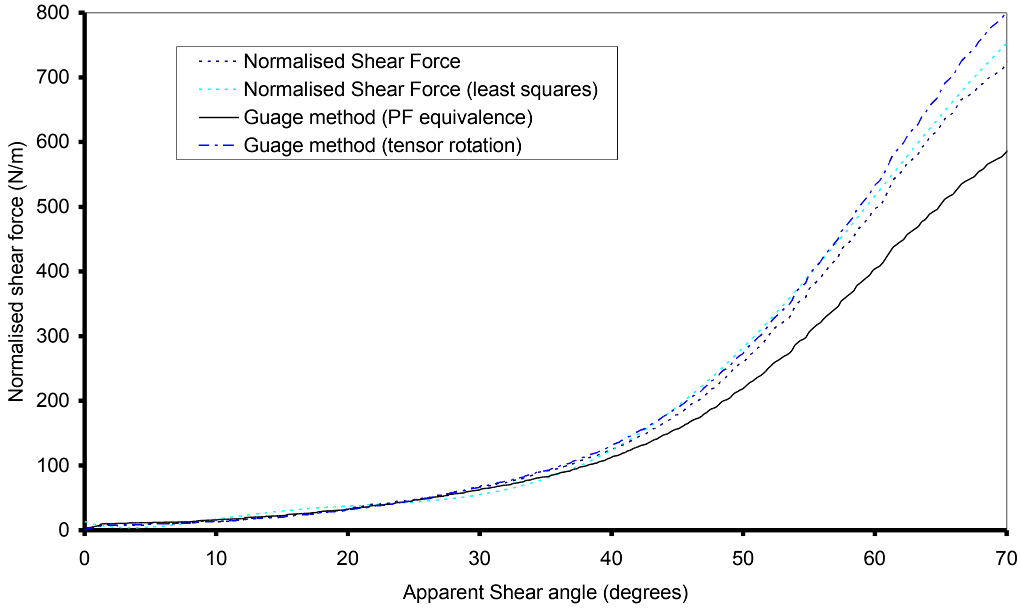

Figure B.6: Bentley mat2 at $\kappa = 2$. Sample width $=$ 100mm

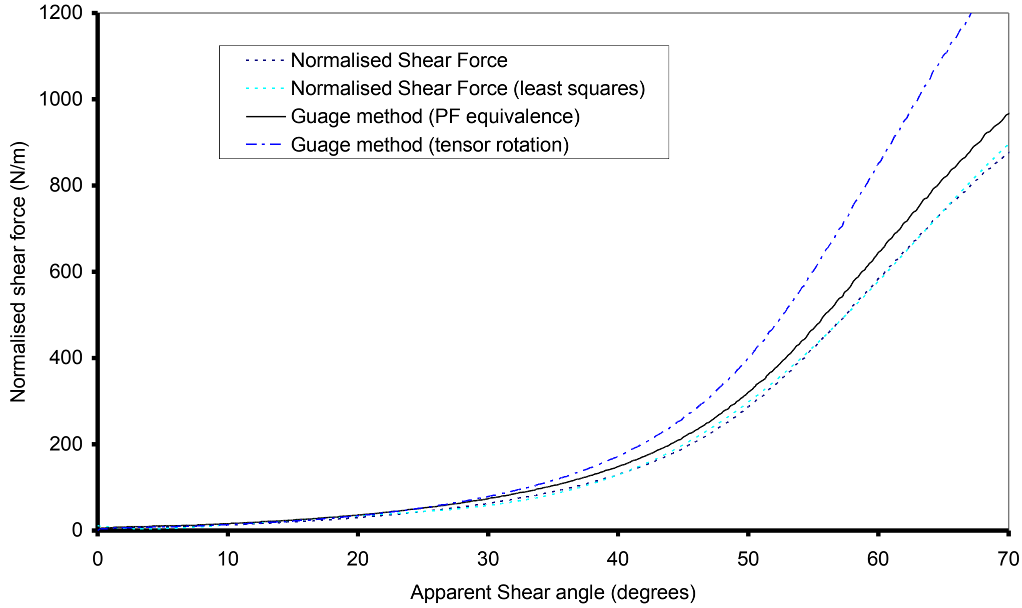

Figure B.7: Bentley mat2 at $\kappa = 3$. Sample width = 100mm

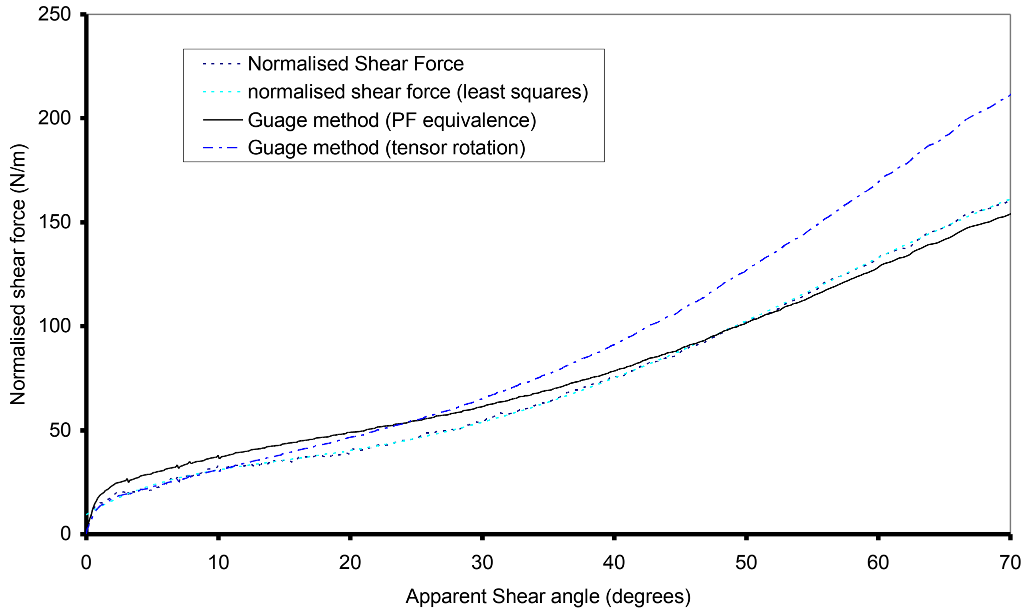

Figure B.8: FGE 106hd:1.65 at $\kappa = 2$, positive shear direction. Sample width = 90mm

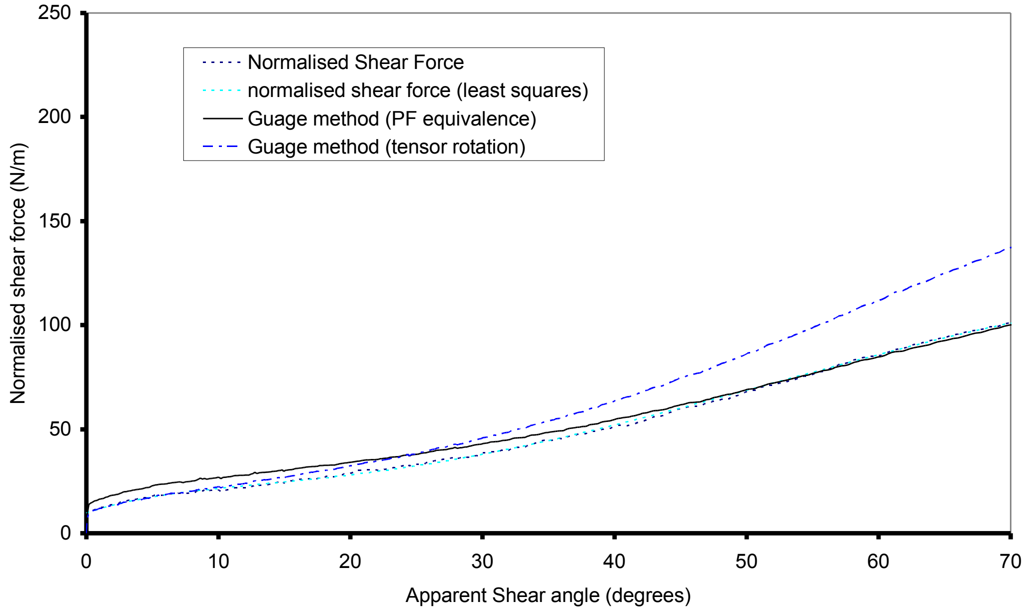

Figure B.9: FGE 106hd:1.65 at $\kappa = 2$, negative shear direction. Sample width = 90mm

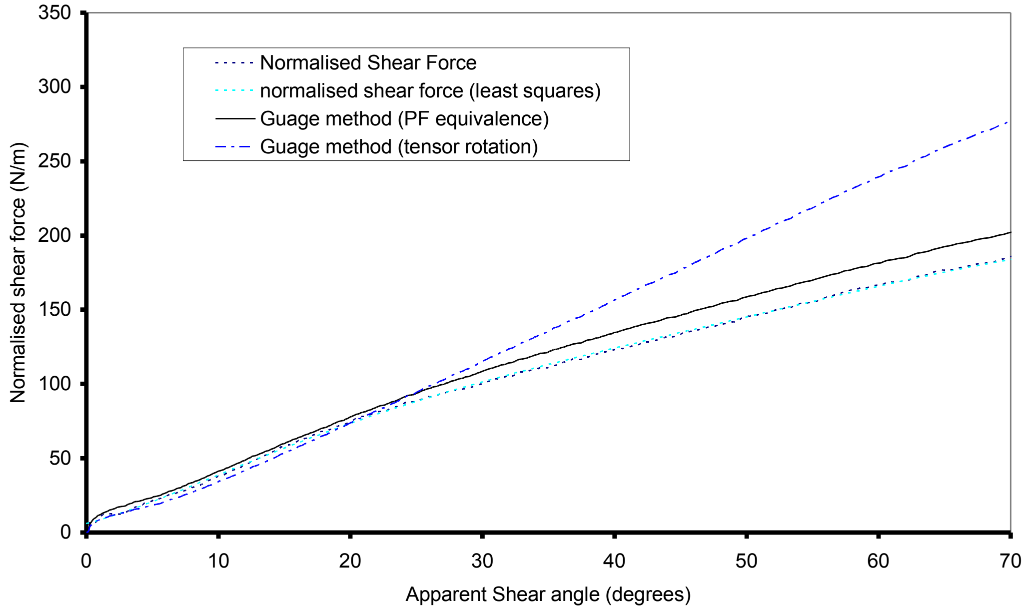

Figure B.10: FGE 106hd at $\kappa = 2$, positive shear direction. Sample width = 90mm

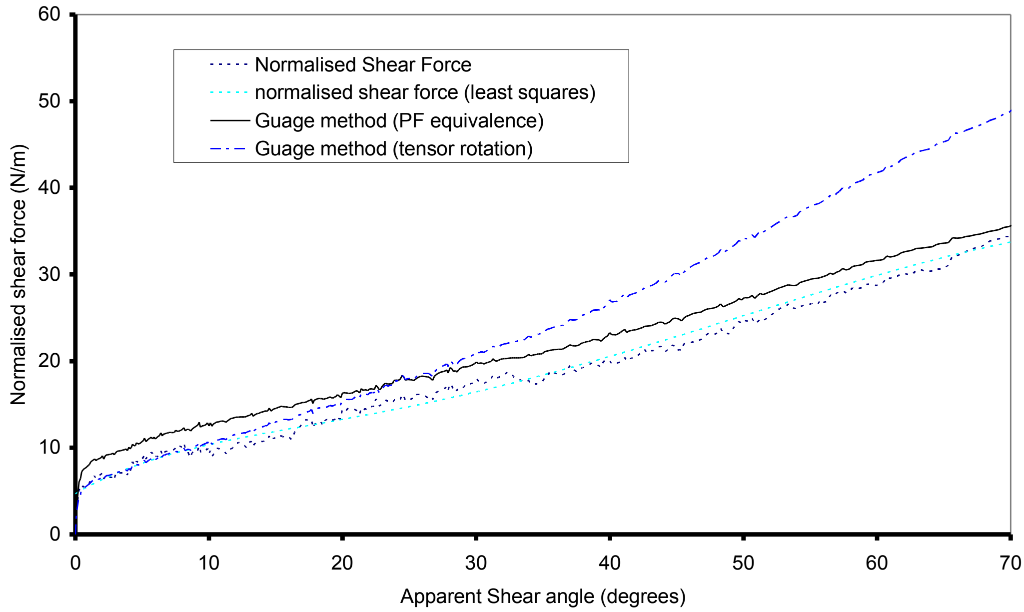

Figure B.11: FGE 106hd at $\kappa = 2$, negative shear direction. Sample width = 90mm

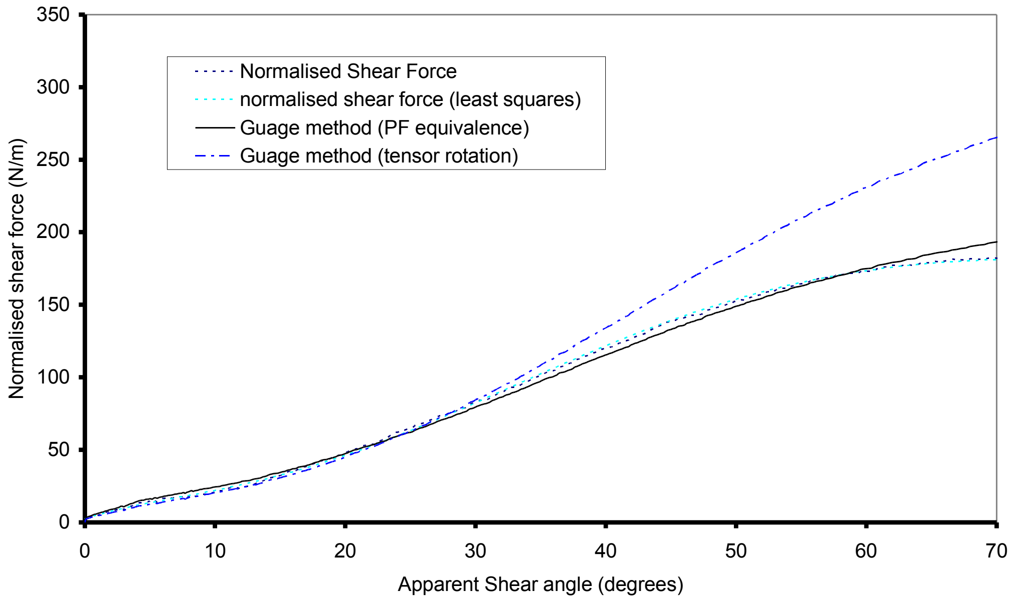

Figure B.12: FGE 106hd:5 at $\kappa = 2$, positive shear direction. Sample width = 90mm

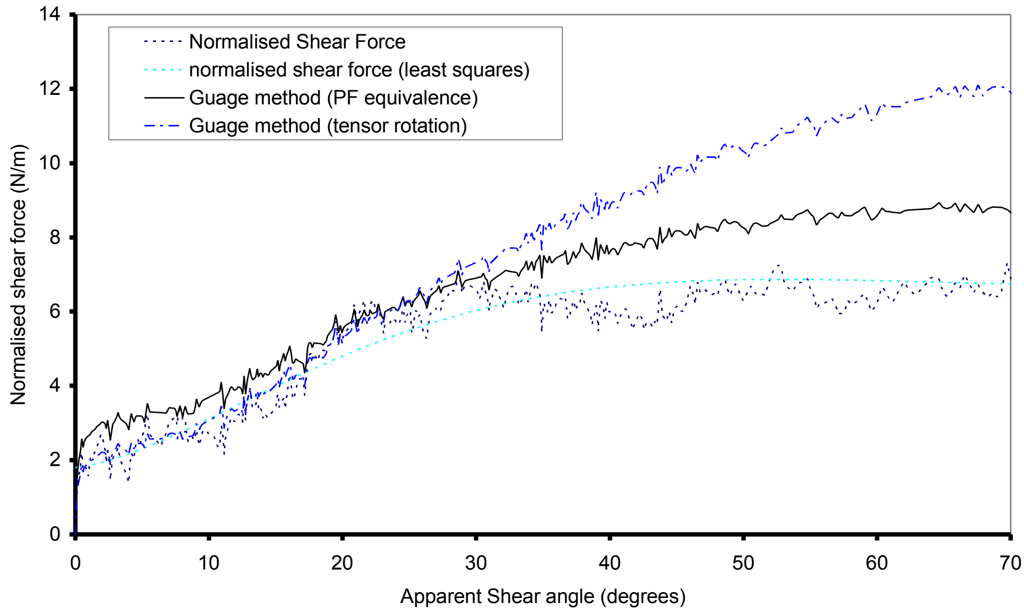

Figure B.13: FGE 106hd:5 at $\kappa = 2$, negative shear direction. Sample width = 90mm

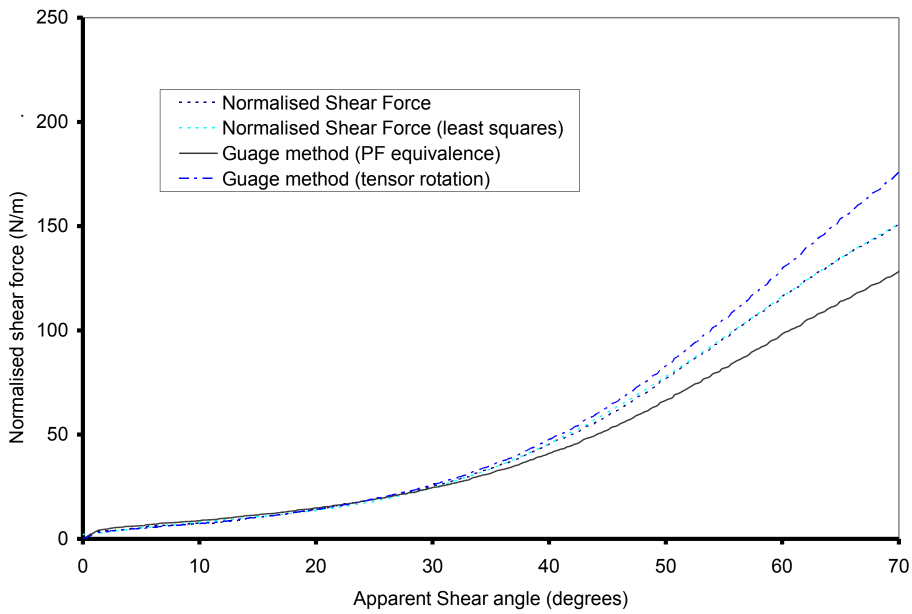

Figure B.14: Twintex$^{\text{TM}}$ 3 at $\kappa = 2$. Sample width = 99mm

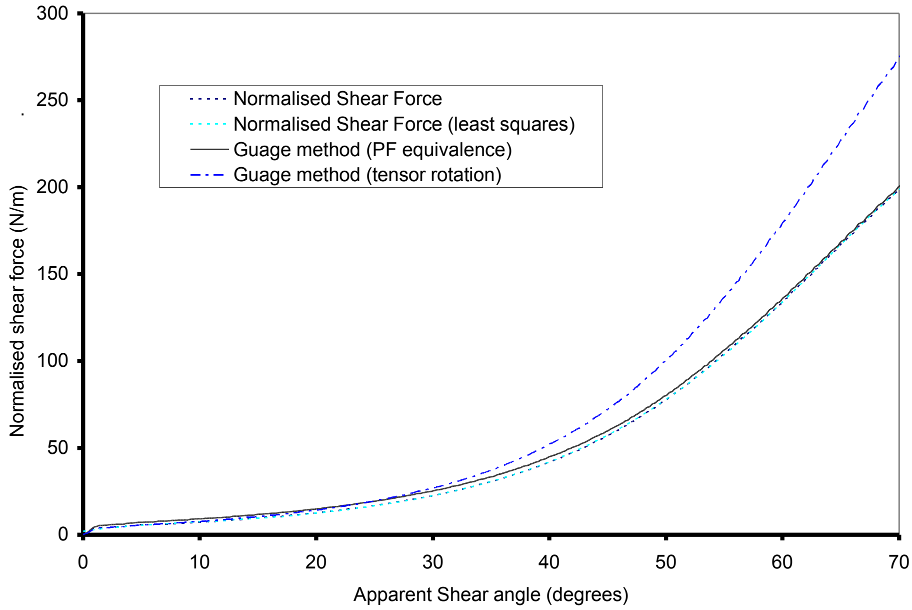

Figure B.15: Twintex$^{\text{TM}}$ 3 at $\kappa = 2.5$. Sample width = 99mm

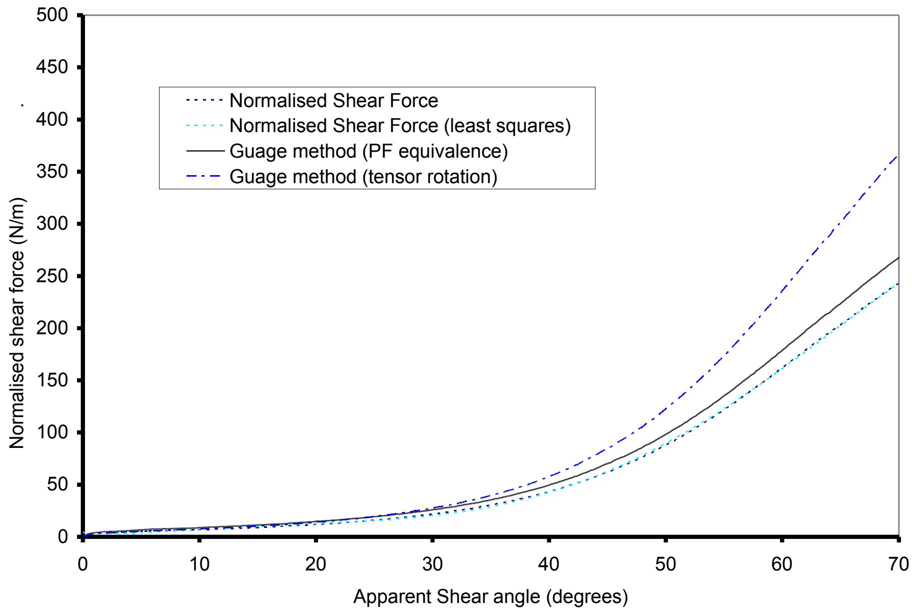

Figure B.16: Twintex$^{\text{TM}}$ 3 at $\kappa = 3$. Sample width = 99mm

B.3 Comparisons of normalised results from different tests

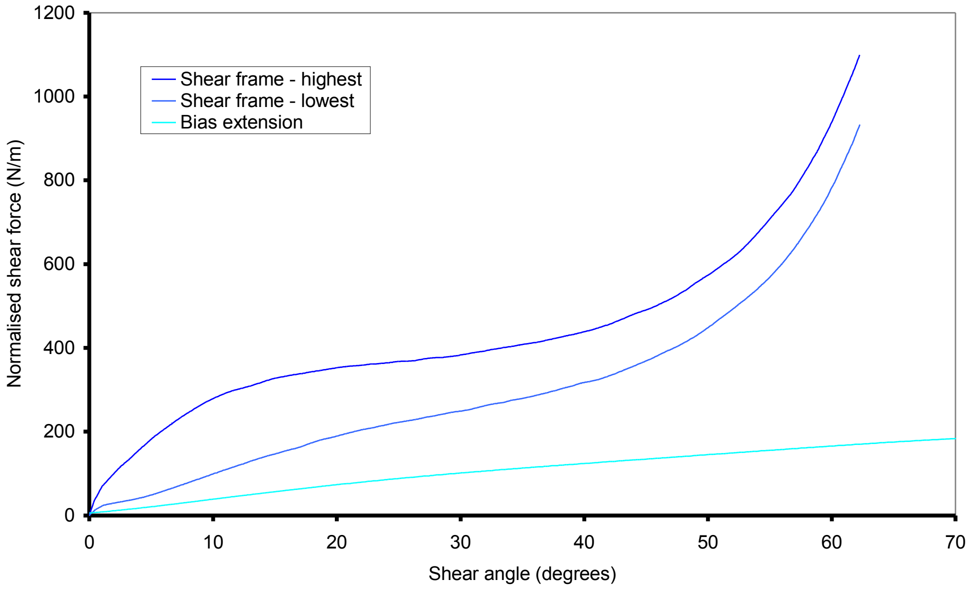

Figure B.17: Comparison of picture frame (at 1300N pre-tension) and bias extension ($\kappa = 2$) normalised test results for FGE 106hd. Shear direction is positive (extending in the stitch direction)

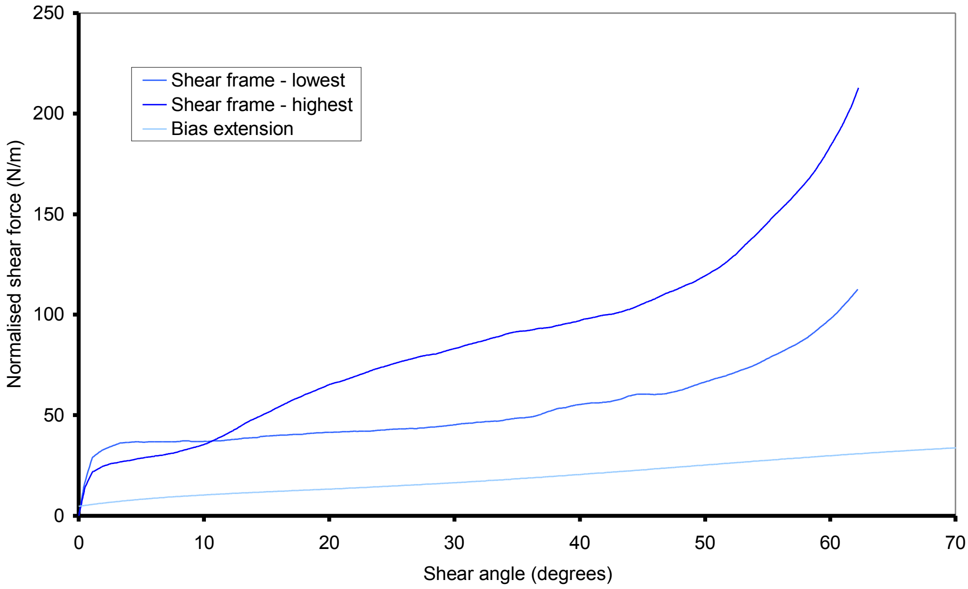

Figure B.18: Comparison of picture frame (at 1300N pre-tension) and bias extension ($\kappa = 2$) normalised test results for FGE 106hd. Shear direction is negative (extending transverse to the stitch direction)

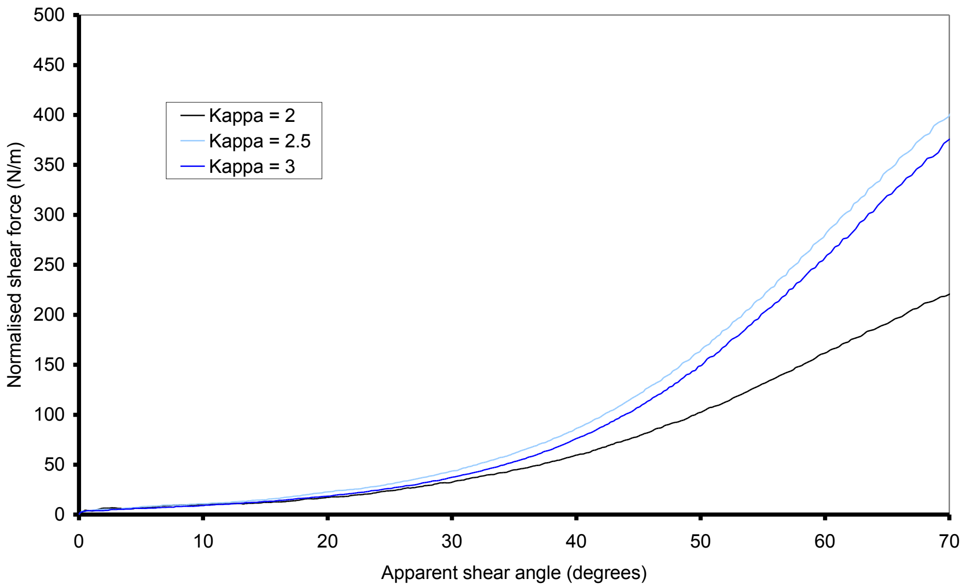

Figure B.19: Comparison of bias extension normalised test results for Twintex$^{\text{TM}}$ 1 at different aspect ratios $\kappa = 2, 2.5, 3$

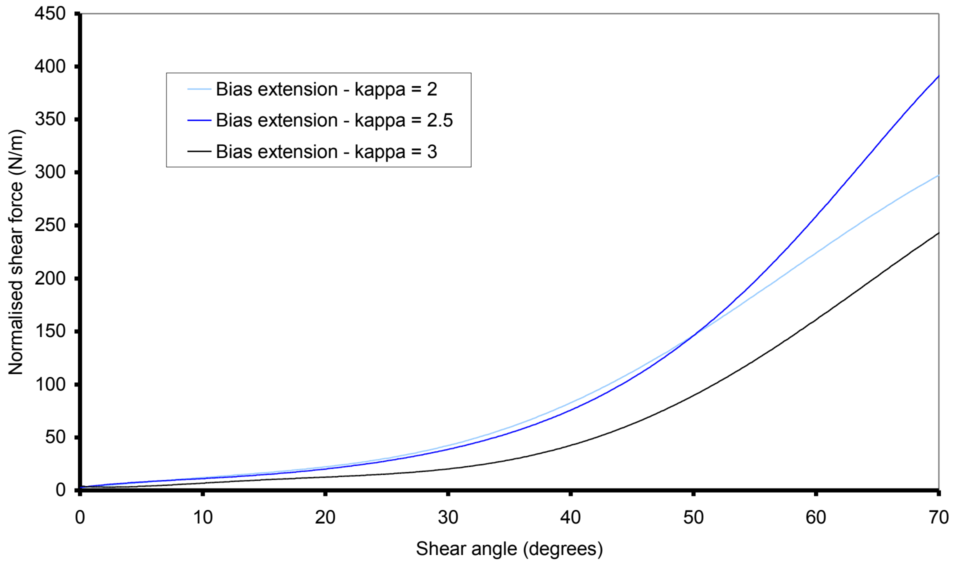

Figure B.20: Comparison of bias extension normalised test results for Twintex^{TM} 3 at different aspect ratios $\kappa = 2,\ 2.5,\ 3$

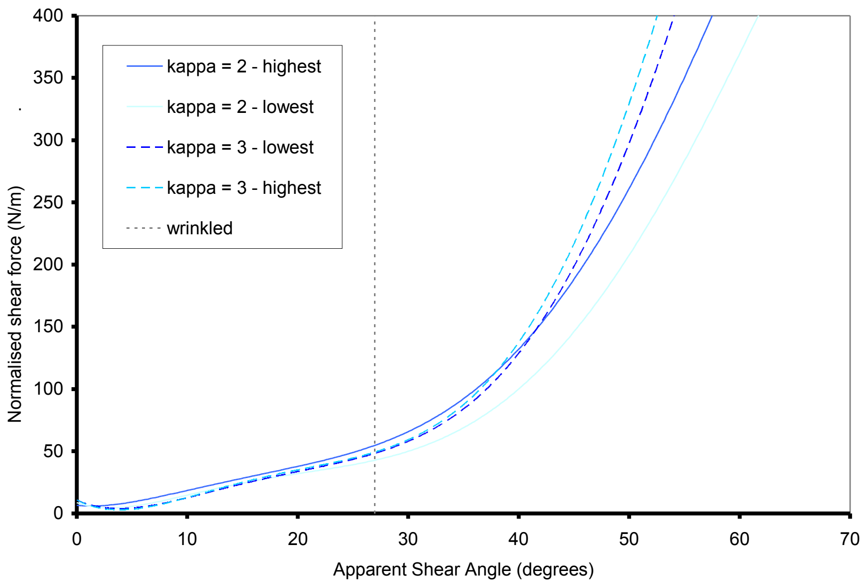

Figure B.21: Comparison of bias extension normalised test results for Bentley mat2 at different aspect ratios $\kappa = 2$ and 3

Appendix C

Bias extension angle results from video analysis

Results are presented after offsetting the displacement according to the axis intersection point, but before further offsetting according to the average value. A large number of results were generated for Twintex$^{\mathrm{TM}}$ 3 so that the trends and variability of the shear results could be examined.

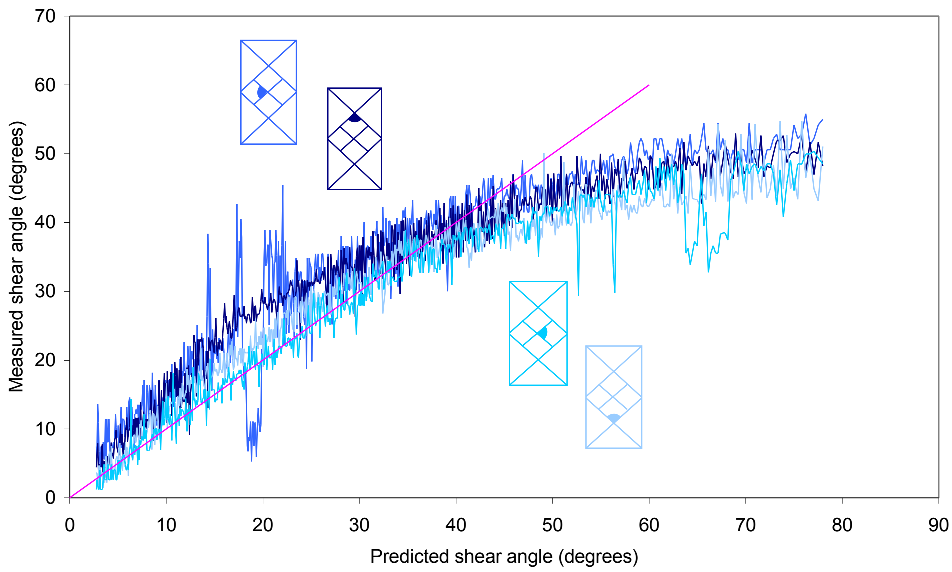

Figure C.1: Angles measured from video taken of a bias extension test of Bentley mat1 with sample ratio factor $\kappa = 2$.

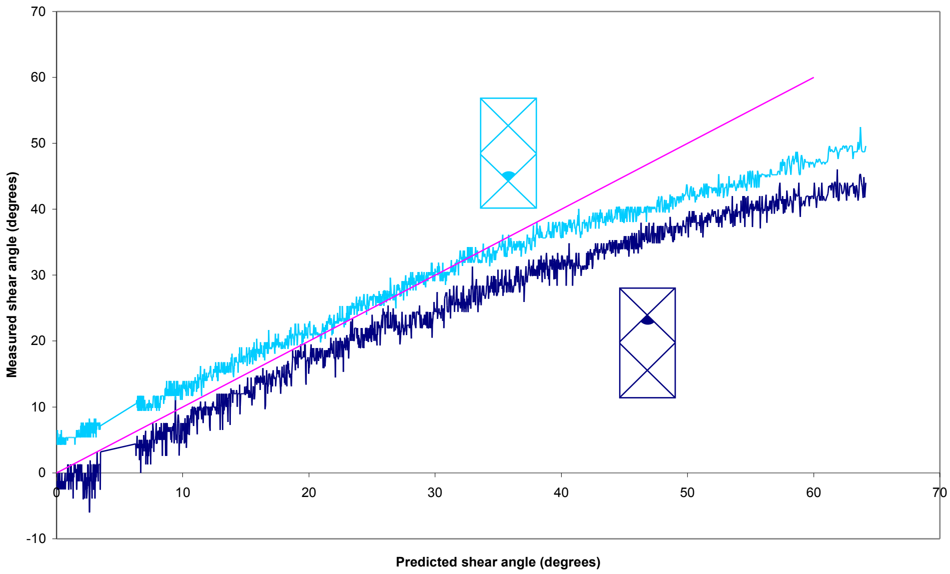

Figure C.2: Angles measured from video taken of a bias extension test of Twintex^{TM} 3 with sample ratio factor $\kappa = 2$ (1).

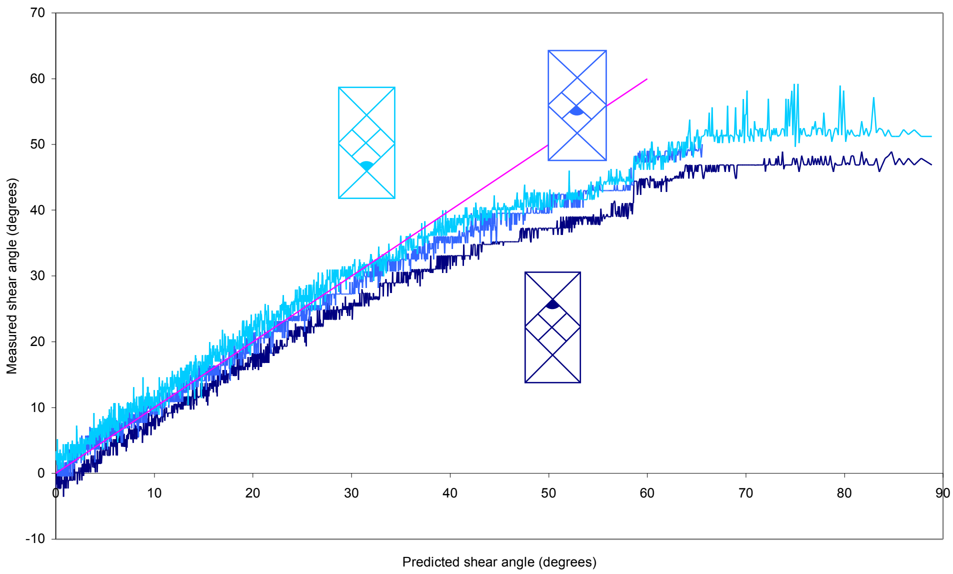

Figure C.3: Angles measured from video taken of a bias extension test of Twintex^{TM} 3 with sample ratio factor $\kappa = 2$ (2).

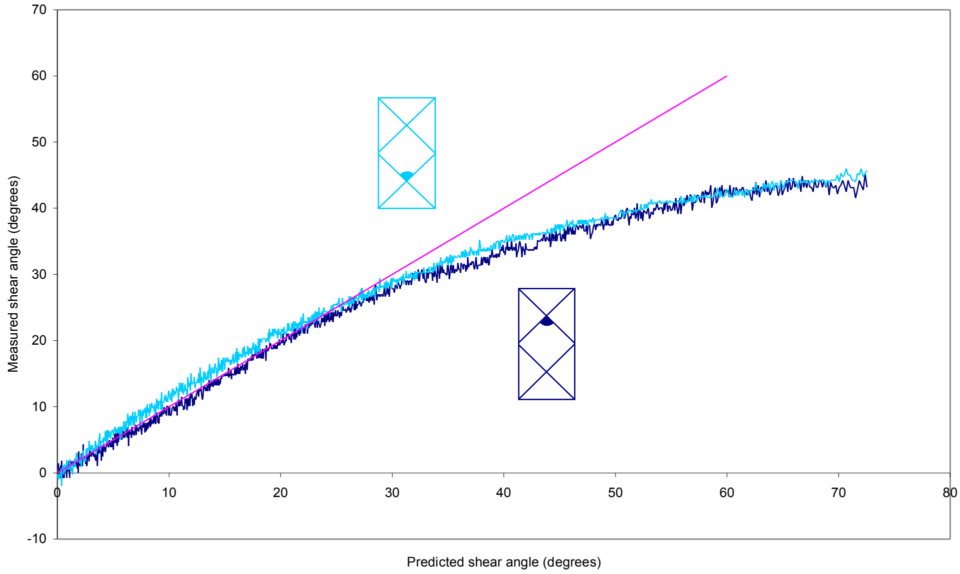

Figure C.4: Angles measured from video taken of a bias extension test of Twintex$^{\text{TM}}$ 3 with sample ratio factor $\kappa = 2$ (3).

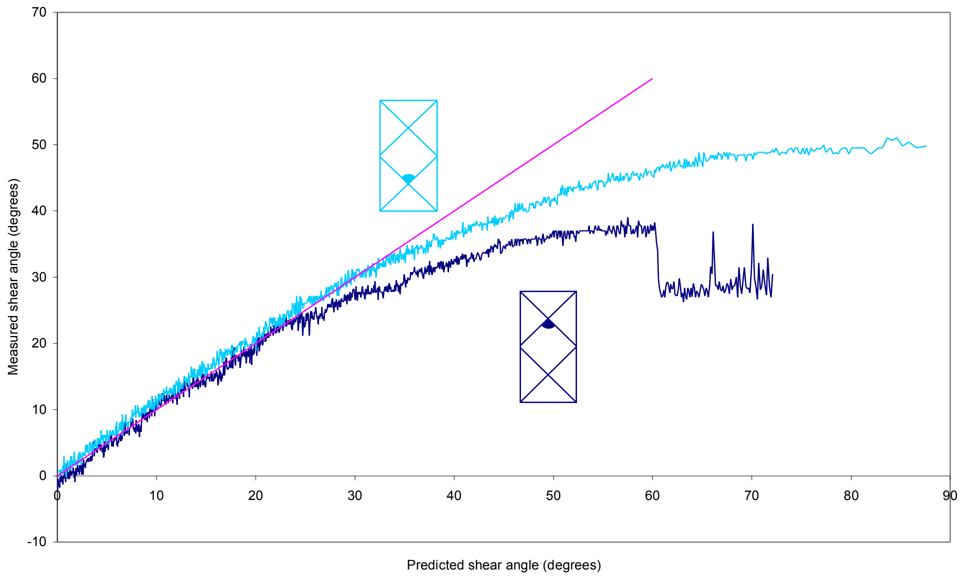

Figure C.5: Angles measured from video taken of a bias extension test of Twintex$^{\text{TM}}$ 3 with sample ratio factor $\kappa = 2$ (4).

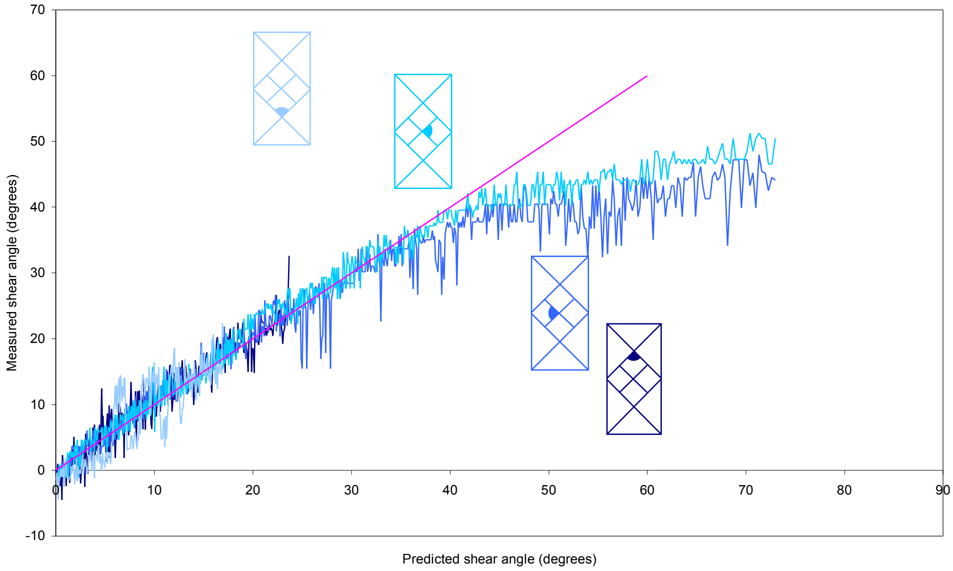

Figure C.6: Angles measured from video taken of a bias extension test of Twintex^{TM} 3 with sample ratio factor $\kappa = 2$ (5).

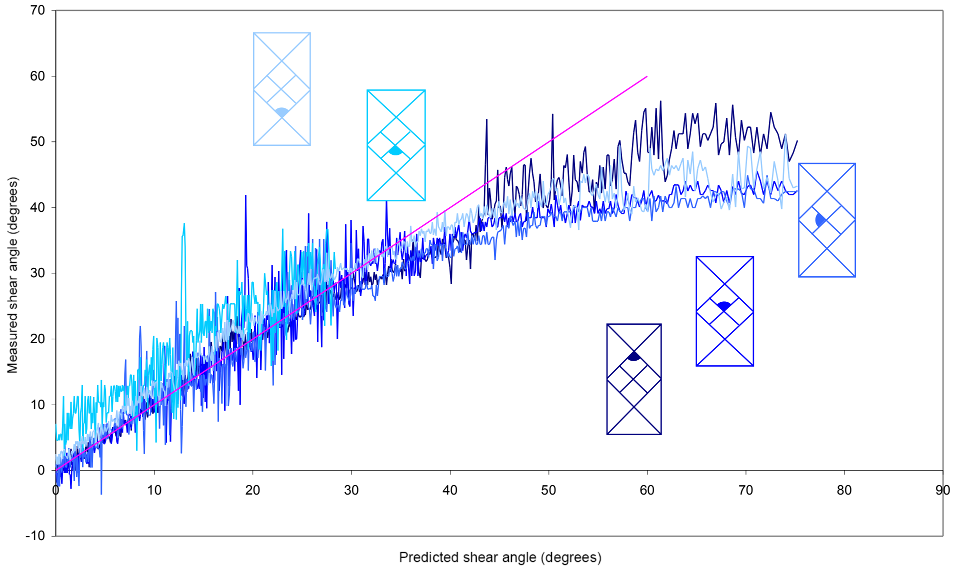

Figure C.7: Angles measured from video taken of a bias extension test of Twintex^{TM} 3 with sample ratio factor $\kappa = 2$ (6).

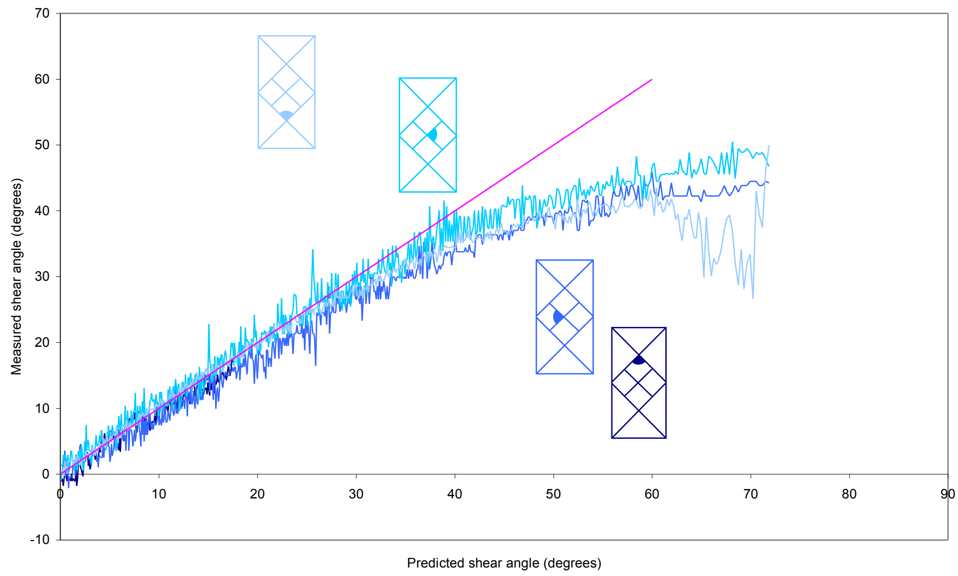

Figure C.8: Angles measured from video taken of a bias extension test of Twintex™ 3 with sample ratio factor $\kappa = 2$ (7).

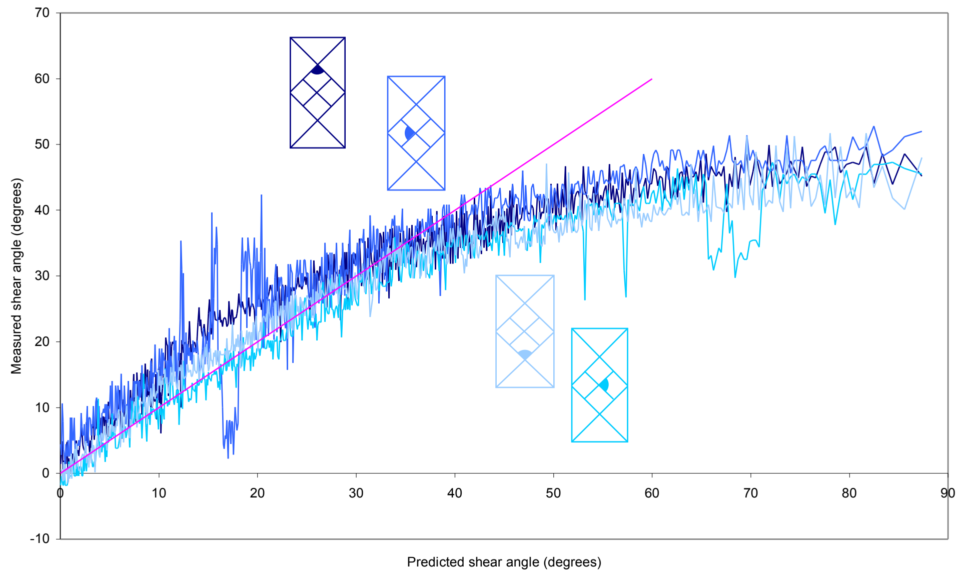

Figure C.9: Angles measured from video taken of a bias extension test of Twintex™ 3 with sample ratio factor $\kappa = 2$ (8).

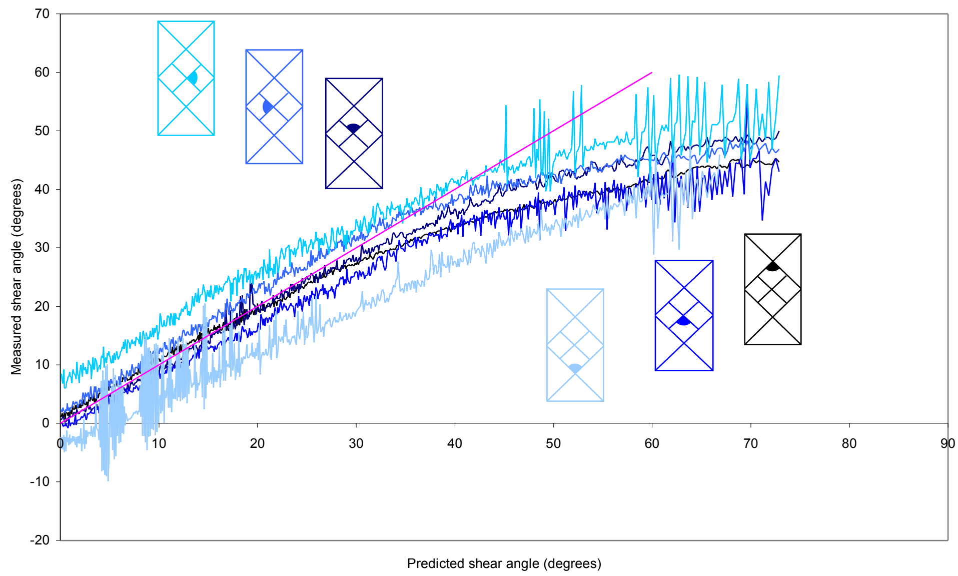

Figure C.10: Angles measured from video taken of a bias extension test of Twintex$^{\mathrm{TM}}$ 3 with sample ratio factor $\kappa = 2$ (9).

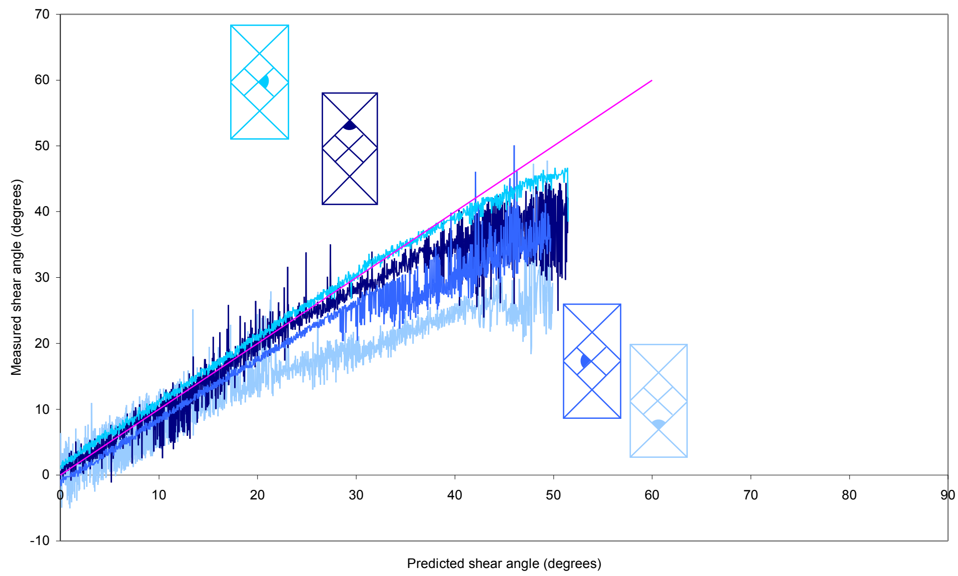

Figure C.11: Angles measured from video taken of a bias extension test of Twintex$^{\mathrm{TM}}$ 3 with sample ratio factor $\kappa = 2.5$.

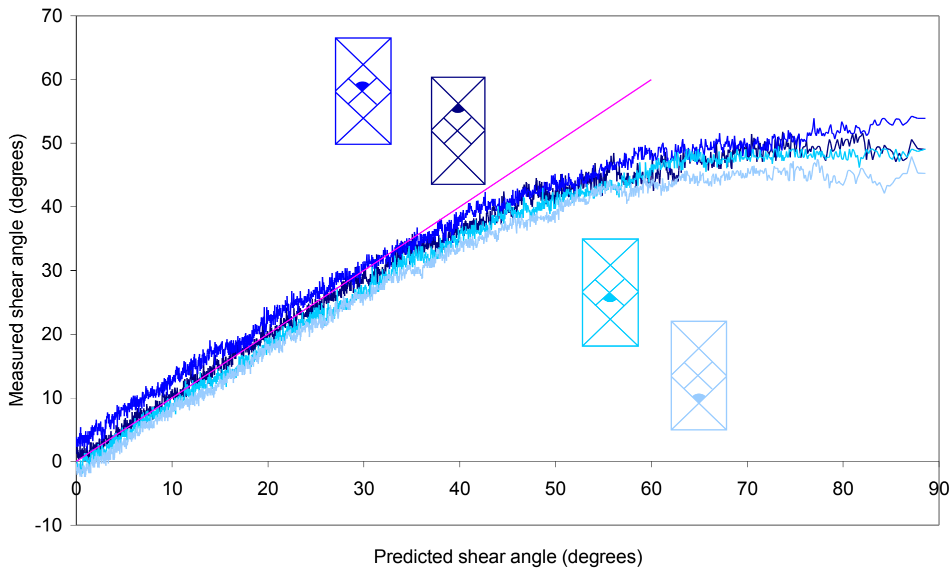

Figure C.12: Angles measured from video taken of a bias extension test of Twintex™ 3 with sample ratio factor $\kappa = 3$.